Institut für Geodäsie und Geoinformation der Universität Bonn
Astronomisch-Physikalische und Mathematische Geodäsie

Simulated Satellite Formation Flights for Detecting the Temporal Variations of the Earth's Gravity Field

Inaugural–Dissertation zur
Erlangung des akademischen Grades
Doktor–Ingenieur
(Dr.–Ing.)
der Hohen Landwirtschaftlichen Fakultät
der Rheinischen Friedrich–Wilhelms–Universität
zu Bonn

vorgelegt am 26. 04. 2010
von

M.Sc. Basem Abd Elkareem Anwar Elsaka

aus
El Mansoura, Ägypten

D 98

Referent:	Univ. Prof. Dr.–Ing. Karl-Heinz Ilk
Korreferent:	Univ. Prof. Dr.–Ing. Jürgen Kusche
Korreferent:	Univ. Prof. Dr.–techn. Wolf-Dieter Schuh
Tag der mündlichen Prüfung:	05. 07. 2010.
Publikation:	Diese Dissertation ist auf dem Hochschulschriftenserver der ULB Bonn http://hss.ulb.uni-bonn.de/fakultaet/landw/ elektronisch publiziert.
Erscheinungsjahr:	2010.

Acknowledgement

Foremost, I would like to express my deepest heart gratitude to **ALLAH** for life itself and for all his uncounted graces. One of these graces is this thesis, which is a milestone in my life, and yet, it is not the thesis itself or its contents that will remain imprinted in my mind, it is the journey and the accompany of the inspiring people who have motivated me during this period and for whom I have eternal gratitude.

The initial idea for this work came from my academic advisor **Prof. Dr.-Ing. Karl Heinz Ilk**. I was actually very lucky to join his research group. So, I really want to thank him from my deep heart for accepting me to accomplish my Ph.D. research in his institute, his instant and continuous guidance, his constructive criticism as well as for his critical reading and discussions of this work, which were really so valuable to me. I would like also to express my deep gratitude to **Prof. Dr.-Ing. Jürgen Kusche** for giving me his inestimable advices and opinions through my thesis, his continuous remarks and valuable suggestions for improving the results of this work and also for criticizing this thesis as a second referent. My thank goes also to **Prof. Dr.-techn. Wolf-Dieter Schuh** for his evaluation of my thesis as a third referent and also I would like to thank him deeply for writing during three years the recommendation letters required for extending my Ph.D. scholarship.

I would like to acknowledge the help of **Prof. Dr.-Ing. Nico Sneeuw** at the Institute of Geodesy, Stuttgart University for his nice guiding e-mails that have surely been an enlightening at the begin of my Ph.D. research. I gratefully acknowledge the assistance of **Dr. Frank Flechtner** at GFZ Potzdam for supporting me with the atmospheric and oceanic data which helped me a lot in my study.

My straightforward gratitude to the German Academic Exchange Service, **DAAD** (Deutscher Akademischer Austausch Dienst) for selecting me as one of its scholarship holders and for granting me the financial support to proceed my education in Germany, the country I have really loved. A special thank among the DAAD community goes to **Ms. Margret Leopold**, from the DAAD office in Bonn, who was particularly helpful in all administrative stuff and supportive during the years of my scholarship. I gratefully acknowledge also the financial support of the German Federal Ministry for Education and Research, **BMBF** (Bundesministerium für Bildung und Forschung) under the project BMBF – Geotechnologien Future Missions during the year 2010.

Very special thanks go to my family especially my father **Abd Elkareem** and my mother **Ahlam**, who always wished to see this day, as well as my mother-in-law **Fatema** for their heartily feelings, great supports and continuous prayers.

Last but not least, an endless thank goes to my beloved wife **Mona Taha** for her support in pursuing my goals, her endless love, her encouragement and her patience with me during the hard days and also to my beloved sons **Youssef** and **Malik** for their lovely smiles that could mitigate any sort of tiredness. I owe a lot to their support.

Basem Elsaka

Bonn, Germany
April, 2010

Simulated Satellite Formation Flights for Detecting the Temporal Variations the Earth's Gravity Field

Abstract

In this thesis, the concept of satellite formation flight (SFF) is studied by means of simulated satellite observations. With various formation types enabling inter-satellite measurements in various directions (e.g. along-track, cross-track or radial), the principal tasks in global gravity field recovery are tackled: the determination of the static gravity field and the detection of its temporal variations. The investigated formation flight types include GRACE, Pendulum, GRACE-Pendulum, Radial wheel and Inclined wheel configurations. For each formation type, appropriate orbit parameters are determined to receive homogeneous subsatellite track patterns required for a high spatial resolution. In addition, orbit designs are developed which allow an enhancement of the temporal resolution (i.e. sub-month solutions). The investigated formation flight types of this case include GRACE-24days, GRACE-12days, Multi-GRACE ΔM and Multi-GRACE $\Delta\Omega$ configurations.

In the static gravity field analysis, the test scenarios cover different spectral ranges of the Earth's gravity field up to the spherical harmonics degree 180. The detection of the temporal variations is performed using physical models from ocean tides, atmosphere, ocean and continental hydrology. The numerical computations show that significant improvements are achieved from the formation flights for the recovery of the global static gravity field and the detection of its temporal variations. Thus, the study provides an outlook on the progress in the gravity field modeling that is achievable by future satellite missions.

Simulierte Satellitenformationsflüge zur Bestimmung der temporalen Variationen des Erdgravitationsfeldes

Zusammenfassung

In der vorliegenden Arbeit wird mit Hilfe simulierter Satellitenbeobachtungen das Konzept des Satellitenformationsflugs (SFF) untersucht. Mit verschiedenen Formationstypen, mit denen Intersatellitenmessungen in verschiedenen Richtungen gesammelt werden können (z.B. along-track, cross-track oder radial), werden die beiden wesentlichen Aufgaben der globalen Gravitationsfeldbestimmung bearbeitet, die Bestimmung des statischen Gravitationsfeldes und die Bestimmung seiner zeitlichen Variationen. Die untersuchten Formationstypen umfassen GRACE, Pendulum, GRACE-Pendulum, Radial wheel and Inclined wheel Konfigurationen. Für jeden Formationstyp werden geeignete Bahnparameter ermittelt, um die für eine hohe räumliche Auflösung notwendige gleichmäßige Überdeckung der Erde mit Subsatellitenbahnen zu erreichen. Außerdem werden Formationsdesigns entworfen, die eine Verbesserung der zeitlichen Auflösung erlauben (submonatliche Lösungen). Die untersuchten Formationstypen dieses Falls umfassen GRACE-24days, GRACE-12days, Multi-GRACE ΔM und Multi-GRACE $\Delta\Omega$ Konfigurationen.

Bei der Bestimmung des statischen Schwerefeldes werden den Testszenarien unterschiedlich hoch aufgelöste Feldmodelle bis Grad 180 der Kugelfunktionsentwicklung zugrunde gelegt. Die Simulation der zeitlichen Variationen erfolgt mit physikalischen Modellen für die Ozeangezeiten, für die Massenverlagerungen in Atmosphäre und Ozeanen und für die kontinentale Hydrologie. Die numerischen Untersuchungen zeigen, dass signifikante Verbesserungen sind von Satellitenformationsflügen zur Bestimmung des statischen Gravitationsfeldes und der Bestimmung seiner zeitlichen Variationen erreicht. Die Arbeit liefert damit einen Ausblick auf den Fortschritt in der Gravitationsfeldbestimmung, der mit zukünftigen Satellitenmissionen möglich sein wird.

Table of Contents

Acknowledgement . . . iii

Abstract . . . iv

Zusammenfassung . . . iv

1 Introduction **1**

2 The Determination of the Earth's Gravity Field from Satellite Missions **4**

2.1 Current Methods of Satellite Geodesy . . . 4

2.1.1 Precise Orbit Determination (POD) – CHAMP Mission . . . 4

2.1.2 Low-Low Satellite-to-Satellite Tracking (ll-SST) – GRACE Mission . . . 5

2.1.3 Satellite Gravity Gradiometry (SGG) – GOCE Mission . . . 6

2.2 Motivation for Satellite Formation Flights based on ll-SST . . . 7

2.2.1 GRACE-type FF . . . 9

2.2.2 Radial wheel-type FF . . . 9

2.2.3 Inclined wheel-type FF . . . 10

2.2.4 Pendulum-type FF . . . 10

2.2.5 Enhanced Temporal and Spatial Sampling SFF Types . . . 11

2.2.5.1 GRACE-Pendulum-type FF . . . 11

2.2.5.2 Multi-GRACE-type Constellation . . . 11

3 Satellite's Motion in Static Gravity Field **15**

3.1 Defining the Systems and Frames of Reference . . . 15

3.1.1 Transformation between Reference Frames . . . 15

3.2 Potential Theory and Spherical Harmonics . . . 16

3.2.1 Attraction and potential . . . 17

3.2.2 Spherical Harmonics, Laplace Equation and Legendre Function . . . 18

3.2.3 Spherical Harmonics Analysis in Geodesy Applications . . . 20

3.3 Satellite Motion – Elliptic and Circular Motion . . . 23

3.3.1 Kaula's Solution of Linear Perturbation Equations . . . 23

3.3.1.1 Perturbations in the Satellite Directions . . . 25

3.3.2 Hill's Equations of Satellite Motion . . . 25

4 Temporal Variations of the Gravity Field and Other Effects 28

4.1 Introduction . . . 28

4.2 Gravitative Forces . . . 29

4.2.1 Direct Tidal Effects . . . 29

4.2.1.1 Solid Earth Tides . . . 31

4.2.1.2 Ocean Tides . . . 31

4.2.1.3 Pole Tides . . . 32

4.2.2 Atmosphere and Ocean Mass Effects . . . 33

4.2.2.1 Atmospheric Mass Effects . . . 33

4.2.2.2 Oceanic Mass Effects . . . 34

4.2.2.3 Atmospheric and Oceanic De-aliasing . . . 34

4.2.3 Hydrological Effects . . . 35

4.3 Non-Gravitative Forces . . . 35

4.3.1 Atmospheric Drag . . . 36

4.3.2 Solar Radiation Pressure and Earth Albedo . . . 36

4.4 Relativistic Effects . . . 36

5 Recovery of the Earth's Global Gravity Field 38

5.1 From Observations to Gravity Field Parameters . . . 38

5.1.1 Physical Model for Low-low Satellite-to-Satellite Tracking . . . 38

5.1.2 Linearized Functional Model for Low-low Satellite-to-Satellite Tracking . . . 39

5.1.3 Stochastic Model . . . 41

5.1.4 Least squares Solution based on a Gauss-Markov Model . . . 41

5.1.5 Accumulation of the Observation Equations . . . 42

5.2 Gravity Recovery Object Oriented Programming System (GROOPS) . . . 42

5.2.1 Observation Simulations . . . 43

5.2.1.1 Observation Generating Steps . . . 43

5.2.1.1.1 Orbit Integration . . . 44

5.2.1.1.2 Inter-Satellite Observations . . . 45

5.2.1.1.3 Accelerometer Data . . . 46

5.2.1.1.4 Star Camera Data . . . 48

5.2.1.2 Observations Processing Steps . . . 48

5.2.1.2.1 Short Arc Approach . . . 48

5.2.1.2.2 Gravity Field Representation . . . 48

5.2.2 Applied Physical Models for Temporal Gravity Field . . . 50

6 Simulation Scenarios of Satellite Formation Flight Missions 51

6.1 Introduction . . . 51

6.1.1 Shortcomings of Current Satellite Gravity Missions . . . 51

6.1.2 Feasibility of the Formation Flight Concept in Gravity Recovery . . . 52

6.2 Orbit Design . . . 52

6.2.1 Inclination and Subsatellite Track Variability . . . 53

6.2.2 Orbit Altitude and Subsatellite Track Variability . . . 57

6.2.3 Inter-satellite Range . . . 60

6.2.3.1 Inter-satellite Range Geometry . . . 60

6.2.3.2 Inter-satellite Range Metrology . . . 62

6.3 Satellite Formation Flights . . . 64

6.3.1 Introduction . . . 64

6.3.2 Approximation of the Relative Motion . . . 64

6.3.3 The Use of Keplerian Parameters Difference . . . 70

6.4 Different Missions Simulation Scenarios . . . 70

6.4.1 GRACE-type Mission Simulation Scenario . . . 71

6.4.2 Radial wheel-type Mission Simulation Scenario . . . 74

6.4.2.1 East-West Radial wheel-type FF . . . 74

6.4.2.2 Controlling the Stability of the Radial wheel-type FF . . . 74

6.4.2.3 Radial wheel-type FF as a Gravity Gradiometry . . . 75

6.4.2.4 North-South Radial wheel-type FF . . . 76

6.4.2.5 Combined Radial wheel-types . . . 76

6.4.3 Inclined wheel-type Mission Simulation Scenario . . . 80

6.4.4 Pendulum-type Mission Simulation Scenario . . . 83

6.4.5 GRACE-Pendulum-type Mission Simulation Scenario . . . 83

6.4.6 Multi-GRACE-type Mission Simulation Scenario . . . 86

7 Test Computations and Results **89**

7.1 Simulation Scenario of Formation Flights . . . 89

7.2 Gravity Field Solutions . . . 91

7.2.1 Static Gravity Field Solutions of Satellite Formation Flights . . . 92

7.2.1.1 Simulation Study: Scenario 1 . . . 92

7.2.1.2 Effects of Different Noises on the Monthly Mean Gravity Field Solution . . . 93

7.2.1.3 Simulation Study: Scenario 2 . . . 101

7.2.2 Time Variable Influences on the Gravity Field Solutions of Satellite Formation Flights 107

7.2.2.1 Introduction . . . 107

7.2.2.2 Time Variable Effects on the Gravity Field Solution at Different Noise Levels 107

7.2.2.3 Effects of Time Variable Elements on Monthly Mean Gravity Field Solutions as Determined by Satellite Formation Flights . . . 109

7.2.2.3.1 Ocean Tides Effects . . . 111

7.2.2.3.2 Processing of Atmospheric, Oceanic and Hydrological Effects . . . 116

7.2.2.3.3 Atmospheric Effects . . . 116

7.2.2.3.4 Oceanic Effects . . . 123

7.2.2.3.5 Combined Atmospheric-Oceanic Effects . . . 129

7.2.2.3.6 Hydrological Effects . . . 131

7.2.2.3.7 Monthly Hydrological Influences on the SFFs gravity solutions . . . 138

8 Summary and Conclusions **144**

8.1 Summary . . . 144

8.2 Conclusions . . . 145

8.3 Recommendations . . . 147

A Keplerian Motion, Keplerian Anomalies and Kepler's Equation **148**

A.1 Kepler Motion . . . 148

A.1.1 Kepler Problem and the Gravity Field . . . 150

A.1.2 The Motion of a Satellite . . . 150

A.2 The Relationship between the Three Keplerian Anomalies . . . 151

A.3 Solution of Kepler's Equation . . . 153

Acronyms **156**

List of Figures **157**

List of Tables **162**

References **164**

1. Introduction

Geodesy was defined by Helmert (1880) as *the science of the measurement and mapping of the Earth's surface*. During the last century, the definition of geodesy was modified many times driven by the technological advancements. Geodetic networks were established, precise terrestrial geodetic angle measurements, distances and leveled height differences became feasible. The accuracy of determination of the locations of the geodetic networks' points has been raised significantly. Moreover, the use of the astronomical and gravimetry measurements to correct the datum surfaces was introduced. According to this, Vaníček and Krakiwsky (1986) defined geodesy to be *the discipline that deals with the measurement and representation of the Earth, including its gravity field, in a three-dimensional time varying space*. This definition underlines that the Earth's gravity field in the outer space is considered as a main task of interest for geodesy.

Five decades ago with the launch of the first artificial satellite SPUTNIK-1 in 1957, it became possible to use satellites to monitor the spatial variations of the Earth's static gravity field. This application was useful for different scientific and practical aspects that are related to the Earth's structure and the Earth's surface variation. The tracking of SPUTNIK-1 helped in the determination of the Earth's oblateness giving the largest difference of the real Earth from fluid equilibrium. The first determination of a gravity term not associated with the Earth rotation with the help of satellites was established in 1959 by determination of the pear shape (odd zonal harmonics) of the Earth. In 1965, Doppler tracking from U.S. Navy TRANET network included in the Earth's gravity field determination was developed supplying at this time a significantly improved gravity field accuracy of ± 12 meters RMS error in the geoid. Three years later, an effective Earth-to-Lunar Tracking was accomplished. The first altimetric satellite for improving the ocean's geoid by measuring the sea-level at the 1-m level was launched in 1975. An analysis of monthly gravity data from LAGEOS was achieved by the year 1987. JGM3 model was released in 1993 to estimate the geoid accuracy of ± 0.5 meters from altimetry, surface gravimetry and GPS tracking. In 1995, ERS-1 provided a global map of the oceanic gravity field with a resolution of 20 km.

With the launch of the CHAMP (CHAllenging Minisatellite Payload) satellite mission in 2000, a new era in modeling the Earth's gravity field has been arisen. Twenty months after the launch of CHAMP, in the year 2002, unprecedented accuracy estimates of the global high-resolution models of the Earth's gravity field was achieved by the launch of the twin-satellite GRACE (Gravity Recovery And Climate Experiment). The modeling of the Earth's gravity field with an extremely high accuracy and a spatial resolution of down to 100 km will be achieved in the course of the next years after the analysis of GOCE (Gravity field and steady-state Ocean Circulation Explorer) mission data.

The innovative sensor technologies such as an advanced accelerometer, a high accuracy of Satellite-to-Satellite Tracking (SST) and Satellite Gravity Gradiometry (SGG) of the previously mentioned three missions opened the way to dramatic improvements in the Earth's gravity field recovery results. Despite this progress and the first exciting results of the Earth's system research, it becomes clear that new perspectives of future gravity satellite missions are necessary. The demand for future missions and satellite formation flights (addressed later as SFF) hence is required not only for the Earth's gravity field investigations related to geodesy, but also for all fields of Earth's sciences including solid Earth physics (from core to crust), hydrology, oceanography, glaciology, sea level changes, Glacial-Isostatic Adjustment (GIA) and the physics of the atmosphere. An overview of these processes is given by Ilk et al. (2005). The improvements can be achieved by future missions in terms of higher precision by considering advanced scientific sensors e.g. optical ranging system (of laser accuracy). Additionally, the improvements can be also achieved in terms of higher spatial resolution by having e.g. sufficient and homogeneous ground track pattern as well as in terms of higher resolution in time by improving the temporal sampling (e.g. investigation of Multi-GRACE-type). These suggestions for such improvements can solve the current limitations of CHAMP, GRACE and GOCE gravity missions. These limitations include insufficient data sampling and poor resolution, aliasing and weak components of the gravity signal (Sneeuw and Schaub 2005). Identification and isolation of individual effects can be combined to form interdisciplinary and complementary information. Therefore, a demand for new observation techniques is required for the development of the new analysis strategies (Aguirre-Martinez and Sneeuw 2002). For instance, future flying missions utilizing several satellites in either coplanner or non-coplanner

orbits provide a better understanding of the global knowledge of the dynamic ocean topography because of their supply of several elements (along-track, cross-track and radial) of the gradient tensor. They provide also a better understanding of the hydrological cycle, an improved monitoring of continental waters from space determining secular changes of the geoid (e.g. of continental water) and monitoring and modeling the evolution of ice sheets and GIA. Hence, the future satellite missions advance the state of knowledge and define a new starting point for new developments.

The proposed future missions will be able not only to improve the physical models related to the previous mentioned ones, but also to solve other mis-modeled and not-modeled phenomena that distort the Earth's gravity field estimates. In addition, they address some key limitations that restrict the current missions such as the adversely systematic (aliased) signals which affect the interpretation of truly long-periodic signals. For this reason, this investigation is related to examining the static and time-dependent gravitational field of the Earth from the feasibility of the proposed and future satellites' configurations. These configurations are planned from different space agencies like NASA (National Administration Space Aeronautics), ESA (European Space Agency), DLR (Deutsches Zentrum für Luft und Raumfahrt or German Aerospace Center) and CNES (Centre National d'Etudes Spatiales).

The goal of this thesis is the study of future satellite formations to improve the Earth's gravity field and to point out which formation flight provides the best possibility to determine the gravity field parameters. This thesis will be restricted only to a simulation study of the future satellite missions. This study includes numerous numerical simulations which are generated between two satellites based on the analysis of the low-low Satellite-to-Satellite Tracking (ll-SST) observables for various formations of Low Earth Orbiter (LEO) type. This investigation should give a motivation for the design of future satellite clusters (meant here 2, 3 and 4 satellites) as a step for substantially improving the Earth's gravity field recovery results.

The main differences between this investigation and other ones presented recently e.g. by Sharifi et al. (2007), Sneeuw et al. (2008) and Wiese et al. (2008) are that this study applies the approved short arc method to SFF configurations, tailored especially to the recovery of Earth's gravity field solutions. The process includes the analysis of the satellite's positions and range observations in the Line-Of-Sight (LOS) direction for each arc. Therefore, different results in terms of only level of error accuracies are expected, since the former investigations are applying different approaches to gravity field modeling (e.g. simplified approach and variational equations approach). Secondly, this study takes into consideration most of the time-variable elements of the gravity field adapting the current available physical models for detecting and mapping the time variations in the Earth's gravity field. Thirdly and more important, incorporation and combination of some of these formations for additional improvement of the gravity field recovery are investigated. We should note here, that all our investigated SFFs do not exhaust the total complex topic; i.e. there may be other SFFs which may improve the Earth's gravity field recovery in addition. For instance, a combination of polar and inclined orbits in one constellation (more than one SFF) is pointed out within this thesis but will not be applied for gravity field analysis.

This dissertation is organized as follows: In the ***second chapter***, various satellite geodesy techniques are presented with a view on the current and planned spaceborne missions. Also an overview of the proposed SFF mission concepts, which is the main objective of this thesis, is given.

The focus of the ***third chapter*** is the motion of satellites under the assumption that no external perturbation forces exist in space, i.e. Keplerian motion. Firstly, a review of potential theory with a discussion of the spherical harmonics with its feasibility in geodetic applications is presented. After that, satellite's motion under the existence of the disturbances will be reviewed. Computational aspects for perturbed satellite's motion is included in this chapter.

The ***fourth chapter*** deals with the different time variable elements which influence the satellite's motion in orbit. These time variation elements are caused by the tidal phenomenon including the solid Earth, pole and ocean tides, atmospheric and oceanic mass variations and the continental water storage changes (i.e hydrological effect). These are the major gravitational forces affecting the satellite's motion. Beside these forces, there are non-gravitational forces that have to be considered as well, including all surface forces induced by atmospheric drag, solar radiation and Earth albedo. A short review of the small effect caused by relativity theory is also discussed.

The numerical tools required for performing the determination of the potential coefficients of the Earth's gravity field are introduced in the ***fifth chapter***. A description of the applied programming system GROOPS, which was developed at the Department of Astronomical, Physical and Mathematical Geodesy at the University of Bonn, for the Earth's gravity field recovery is given with a review of its numerical steps.

The ***sixth chapter*** presents the dedicated satellite mission scenarios that are introduced in the second chapter. It makes use of the analysis of ll-SST observables of the different SFF types. A review of selecting the reference orbit for a comparison study is introduced. Furthermore, comparative aspects of the different formation flights with their innovative characteristics are presented.

In the ***seventh chapter***, comparative numerical results of the dedicated mission scenarios are given. Furthermore, monthly solutions of the Earth's gravity field for each satellite configuration of different satellite clusters are investigated.

Finally, the results of all simulation scenarios are summarized in the ***eighth chapter***. A conclusion for this new development relevant for the analysis of the observations of the new gravity satellite missions is outlined. An outlook to further investigations concludes this chapter.

In order to implement our objectives, different satellite formations have been identified as well as their orbital options. In addition, numerical simulation campaigns have been carried out in order to recover the Earth's gravity field with detection of temporal variations. Some issues are not to be considered in this thesis such as the technological feasibilities concerning e.g. the optimal design of the spacecraft to the selected SFF (e.g. wedge shaped or disk shape), its on-board scientific sensors (e.g. the accelerometer or laser sensors).

The technical implementations are not considered also e.g. the SST meteorology (for cross-track and radial SST) and attitude and orbit control concept. Other remaining topics are not considered within this thesis concerning, for example, the cost aspects. For instance, if the conservative and simpler SFF launched by only a joint launch vehicle was chosen, this leads to in a cost efficient design of low complexity. On the contrary if a more complex SFF was chosen, this will require for example two launchers and hence will be a cost challenge.

An important issue that has not been also taken into account and should be mentioned here is the consideration of smoothing techniques. In other words, no filtering methods such as Gaussian isotropic filter by Jekeli (1981) or the decorrelated and non-isotropic one by Kusche (2007) have been applied for improving all dedicated gravity field solutions obtained in this thesis and for minimizing the error level of these solutions.

2. The Determination of the Earth's Gravity Field from Satellite Missions

Since the beginning of this decade, the information of the Earth's gravity field has been improved by several orders of magnitudes due to the new missions in satellite geodesy. The satellite missions CHAMP, GRACE and the recently launched GOCE showed significant improvements in our knowledge of the gravitational field. The purpose of this chapter is to review the concepts related to the determination of the Earth's gravity field from the current satellite missions. In the first sections, different satellite missions characterized by individual measurement principles and their innovative character are described. It is followed by the motivation of future satellite missions for the Earth's gravity determination. Hence, a review of the proposed future SFF missions treated within this thesis will be given with pointing out their characteristic features.

2.1 Current Methods of Satellite Geodesy

In the last decade, the observations based on different techniques and satellite configurations have led to an improved modeling of the Earth's global gravity field. The design of these satellite missions, especially for observing the gravity field, should have two main facets. On the one hand it is necessary to achieve a high resolution in the spatial and temporal domains of the gravity field and at low costs on the second hand. The first aspect should fulfill three fundamental criteria. Firstly, the orbit altitude should be as low as possible. Secondly, the orbital arcs should be tracked uninterruptedly in the three spatial dimensions. This latter issue has already been achieved by the concept of spaceborne GNSS tracking (e.g. GPS of USA and GLONASS of Russia), which provides a precise orbit determination in the three dimensions. Thirdly, discrimination between gravitational and non-gravitational forces acting on the satellite should be realized (Seeber 2003).

In the following, an overview of the current missions that are successfully applied in satellite geodesy is given. Firstly, a short preview of the CHAMP mission based on Precise Orbit determination (POD) is introduced; then the GRACE mission, based on the satellite-to-satellite tracking (SST) concept is described. At last, GOCE mission with its gradiometry concept is reviewed. Fig. 2.1 illustrates these three missions.

2.1.1 Precise Orbit Determination (POD) – CHAMP Mission

CHAMP (Reigber et al. 1999) was one of the three satellite missions especially designed for the study of the Earth's gravity and magnetic fields. The mission was proposed by the German Research Center (GeoForschungsZentrum, GFZ) as a primary investigator in cooperation with the German Aerospace Center (DeutschesZentrum für Luft- und Raumfahrt, DLR). GFZ is responsible for the mission scheduling, command preparation, mission and orbit analysis, while DLR is responsible for the mission operating system to receive and download the raw data at his data center stations. The CHAMP's spacecraft (Fig. 2.2) was launched on July 15, 2000 from Plesetsk, Russia originally designed for a five-year mission. Due to the successful execution of two orbit rises (one was performed on June 10/11, 2002 by about 16 km and the second rise was on December 9/10, 2002 by about 20 km) and the availability of sufficient cold gas, the mission could be extended till mid 2010 (see Reigber et al. 2006).

For scientific objectives such as optimizing the aerodynamic behavior and magnetic field observation environment, CHAMP was designed and built as a trapezoid body. It contains a total mass of 522 kg at the beginning of the mission (it will lose 34 kg of cold gas at the end of the mission) and has the dimensions 404 (length) x 162 (width) x 75 (height) cm^3. The orbit is almost circular (the initial eccentricity was 0.004. It became an almost perfect circular orbit by the mid of 2005 on with an eccentricity of e=0.0002). The orbit of CHAMP is characterized by near polar (initial inclination of 87°) with an initial altitude of 454 km. CHAMP lost 100 km of its altitude by the mid of 2005 and decayed to 300 km by the year 2007 till to the

end of the mission.

The measurement principle is based on the fact that the satellite itself can be considered as a test mass moving in the gravity field. The CHAMP satellite carries an on-board GPS antenna; this enables the determination of precise orbits. As the gravity field is always disturbed by the various processes that mentioned e.g. in Ilk et al. (2005), the satellite's orbit is influenced accordingly. The determination of these influences and orbit perturbations provides information about the structure of the gravity field. The measurement principle is known as satellite-to-satellite in the high-low mode (hl-SST). This means that an orbit of the low flying CHAMP satellite is continuously and precisely determined by high flying satellites of the Global Positioning System (GPS). The on-board star cameras provide high precision attitude information. The non-gravitational forces acting on the CHAMP satellite are measured in three dimensions by the on-board accelerometers. More details for mission objectives, description and results can be found at the web site: *http://www.gfz-potsdam.de/pb1/op/champ/*.

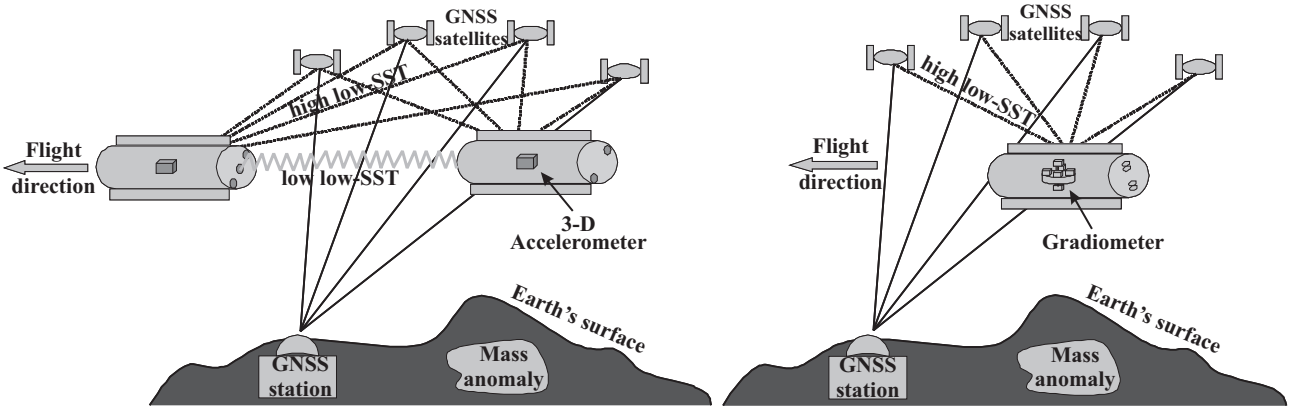

Fig. 2.1: Satellite-to-Satellite Tracking by GNSS satellites: high low-SST combined with low low-SST concept (left) and SGG with high low-SST concept (right).

2.1.2 Low-Low Satellite-to-Satellite Tracking (ll-SST) – GRACE Mission

The GRACE mission is based on satellite-to-satellite tracking in the low-low mode (ll-SST) and composed of two LEO satellites. This concept represents the basic measurement principle applied to the formation flights treated in this thesis, where two satellites are flying in identical low orbit, several hundred kilometers apart. The inter-satellite distances are controlled and measured by a microwave link with a highest accuracy. The two LEO spacecrafts are continuously tracked also by the GPS satellites; this enables a precise orbit determination for the two LEO satellites. The acceleration differences between the two satellites are measured by 3-D accelerometer (placed in the satellite's center of mass). The ll-SST and hl-SST concepts can be combined as shown in Fig. 2.1.

On Sunday, 17 March 2002 at 10.21 am, the twin satellites of the GRACE mission were successfully brought into orbit. It is an international cooperative US-German (NASA/DLR) project. The mission was proposed in 1996 by the University of Texas at Austin, Center for Space Research (UTCSR), GFZ, JPL, Space Systems/Loral (SSL), DLR, and Astrium GmbH. It was selected in 1997 as a second mission in NASA's Earth System Science Pathfinder (ESSP) project. GRACE surpassed CHAMP by providing unprecedented accuracy estimates of the medium-resolution models of the Earth's mean and time variable gravity field. Besides this primary task of GRACE, the second objective is to obtain tropospheric and ionospheric profiles by the feasibility of GPS radio occultation measurements. Some other scientific objectives based on gravity field information can be realized from the GRACE observables such as to enable a better understanding of ocean surface currents and ocean heat transport. Also to measure changes in the sea-floor pressure, to study ocean mass changes, to measure the mass balance of ice sheets and glaciers, and to monitor changes in the water storage and snow on the continents are primary scientific applications of the results of GRACE.

Based on the structure of the CHAMP satellite, the both GRACE twin-satellites (Fig. 2.2) are of identical design. The shape of each satellite is trapezoidal in cross section of length=312 cm, height=72 cm, bottom width=194 cm and top width=69 cm. The GRACE satellites are orbiting with a semi-circular polar coplanner orbit with an initial altitude of 485 km and orbital inclination is 89° at the beginning of the mission with a relative velocity of the leader satellite of about 0.5 m/s. The nominal inter-satellite distance between the leader satellite and the follower one is 220 km. A detailed description for the GRACE mission can be found in Tapley et al. (2004b).

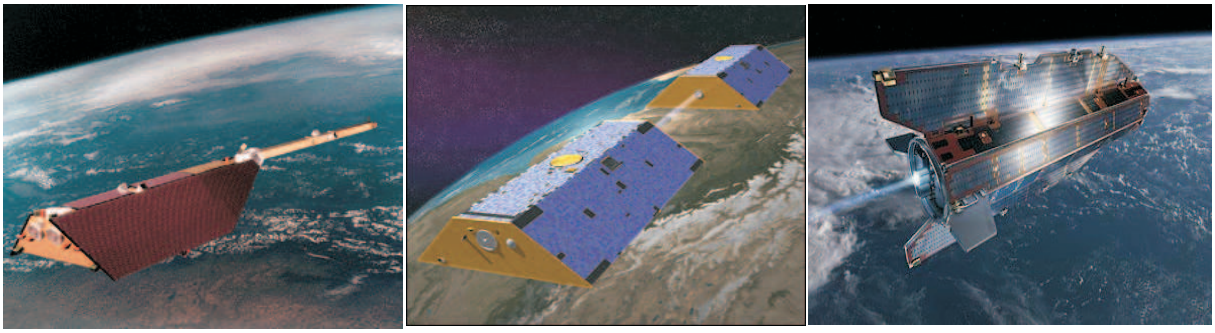

Fig. 2.2: The current applied satellites' missions (from left to right: CHAMP, GRACE and GOCE).

2.1.3 Satellite Gravity Gradiometry (SGG) – GOCE Mission

The first Earth explorer core mission GOCE, which is considered as part of ESA's (European Space Agency) Living Planet program (ESA 1999), is the first satellite equipped with a satellite gravity gradiometer (SGG) (see Fig. 2.1). This gradiometer is a sensor that can measure the differences in gravity acceleration directly in all three spatial dimensions. It is located inside the satellite's center of mass (CoM) over a short baseline of about 50 cm. GOCE (Fig. 2.2) brings an unprecedented significant gravity field resolution and surpasses the current SST missions of both high-low and low-low modes (CHAMP and GRACE). An important advantage is that the non-gravitational accelerations are the same for all measurements inside the GOCE spacecraft and hence disappear by differentiating. GOCE is flying in a near-Sun-synchronous and lowest orbit (of 280 km altitude) of all dedicated satellites, has an inclination of 96.7° and will operate only for a mission period of about 20 months. The maximum spatial resolution that GOCE achieves can reach up to degree n=250 (corresponding to a half wavelength ≈ 80 km).

Like CHAMP and GRACE, GOCE will be tracked by GPS in the 3-D mode. The data will be of two types, the geometrical type using GPS satellite-to-satellite tracking in the high-low mode (hl-SST) and physical type using satellite gravity gradiometry (SGG). GOCE was launched on 17 March 2009 having two separate phases of observation each of which is 6 months separated by a hibernation phase of about 5 months and with a calibration phase at the beginning of the mission of about 3 months. For improving the GOCE gravity field solution, Abrikosov et al. (2006) proposed possible solutions for eliminating the time variable influences (which can be computed using the available physical models) from GRACE observations. This can be done by transforming all these temporal variations into the same form (represented as a spherical harmonic expansion). As a second step is to separate the effect of each time-variable element.

To sum up the last three satellite techniques, the first derivatives of the gravitational potential are obtained from the first mission CHAMP (hl-SST). In the second case of GRACE (ll-SST), the difference of the first derivatives over the inter-satellite distance is determined. The second derivatives of the gravitational potential are directly and accurately measured in the last case (SGG), realized with GOCE.

2.2 Motivation for Satellite Formation Flights based on ll-SST

The contribution of the last mentioned satellite missions covers model developments by measuring the spatial and temporal variations of the Earth's gravity and magnetic fields as well as the atmospheric mass density. New gravity field models have been estimated from CHAMP and GRACE observations that surpass previous models in accuracy for long and medium wavelengths. But still some restrictions exist that confine these successful missions (see Sneeuw and Schaub 2005). For instance, by considering CHAMP, as a first successful gravity field mission, the restriction to derive higher spatial and temporal resolutions plays the important key limitation. For the GRACE mission, the benefit of relative measurements between two satellites is already achieved. Despite the fact that GRACE has displayed an invaluable data set for observing mass changes and mass variations in the Earth's system (e.g. continental water storage and oceanic mass variations) of long-wavelength resolution, still a mismodeling of the periodic ocean and atmospheric signals exists (see e.g. Rummel et al. 2003, Rummel 2007 and van Dam et al. 2008). This issue is called aliasing problem which results from the undersampling of the high frequency time-variable signals that take place at short time periods or may result also from the limited de-aliasing products used for correcting the high-frequency signals of the atmosphere and ocean tides. This aliasing problem distorts the GRACE gravity field monthly solutions. According to the GOCE mission and its scientific rationale, the higher spatial resolution is achieved with a higher static gravity field accuracy. However, it is still not possible to determine the temporal variations of the Earth's gravity field which is the main perspective due to the limited mission duration ($\approx$ one year of observations).

New and improved technologies are currently under progress like laser metrology as an optical ranging system, accelerometry and drag-free control and micro propulsion systems. These activities open the door to an effective employment of these improved sensors towards future satellite gravity missions. Another aspect for the motivation of new missions is the necessity of understanding and describing all the signals affecting the retrieval of the Earth's gravity field in time and space. The most problematic issue when designing future satellite missions is the simultaneous combination of a higher spatial resolution with a higher temporal one. This is impossible nowadays with the current gravity field missions. This becomes clear from the so-called bubble plot (Fig. 2.3), which explains the limitations of the current missions with the requirements of different geophysical processes in terms of temporal and spatial resolutions as well as mission duration. The impact of the current deficiencies can be mitigated and/or solved by choosing the satellite configuration with properly selected orbital parameters. This issue has been discussed by numerous studies for reducing the gravity field retrievals errors (see e.g. Sneeuw and Schaub 2005, Sharifi et al. 2007, Sneeuw et al. 2008 and Elsaka and Ilk 2008a). A significant improvement can be achieved by lowering the noise levels of the sensor systems (see e.g. Wiese et al. 2008).

For this reason and as a main objective of this study, we are going to investigate the different satellite configurations that are flying in a satellite formation; this is a topic of intensive discussion nowadays to achieve further progress in the Earth's system research. We decided to investigate SFFs because they are considered as an important technology for future space-based science missions and astronomical observations. Our investigation includes various mission concepts in order to improve the gravity field recovery coefficients and to detect the time variable mass variations caused by different solid and environmental Earth processes as explained by Ilk et al. (2005). The detection of these temporal variations will serve the analysis of mass transports in the Earth's system and to reduce the systematic errors of the physical models (e.g. ocean tides and atmosphere). The above mentioned investigations showed that it seems to be possible to provide better field parameters by selecting different satellite configurations.

As a simple definition, satellite formation flights (SFFs) mean those satellites that orbiting around the Earth in various geometrical configurations. The concept of SFF may confuse with that of a satellite constellation. As defined by NASA Goddard Space Flight Center, a constellation is composed of two or more satellites in similar orbits that are not maintaining a relative position with each other. Xiang and Jørgensen (2005) made a brief comparison between the satellite's constellation and the FF as:

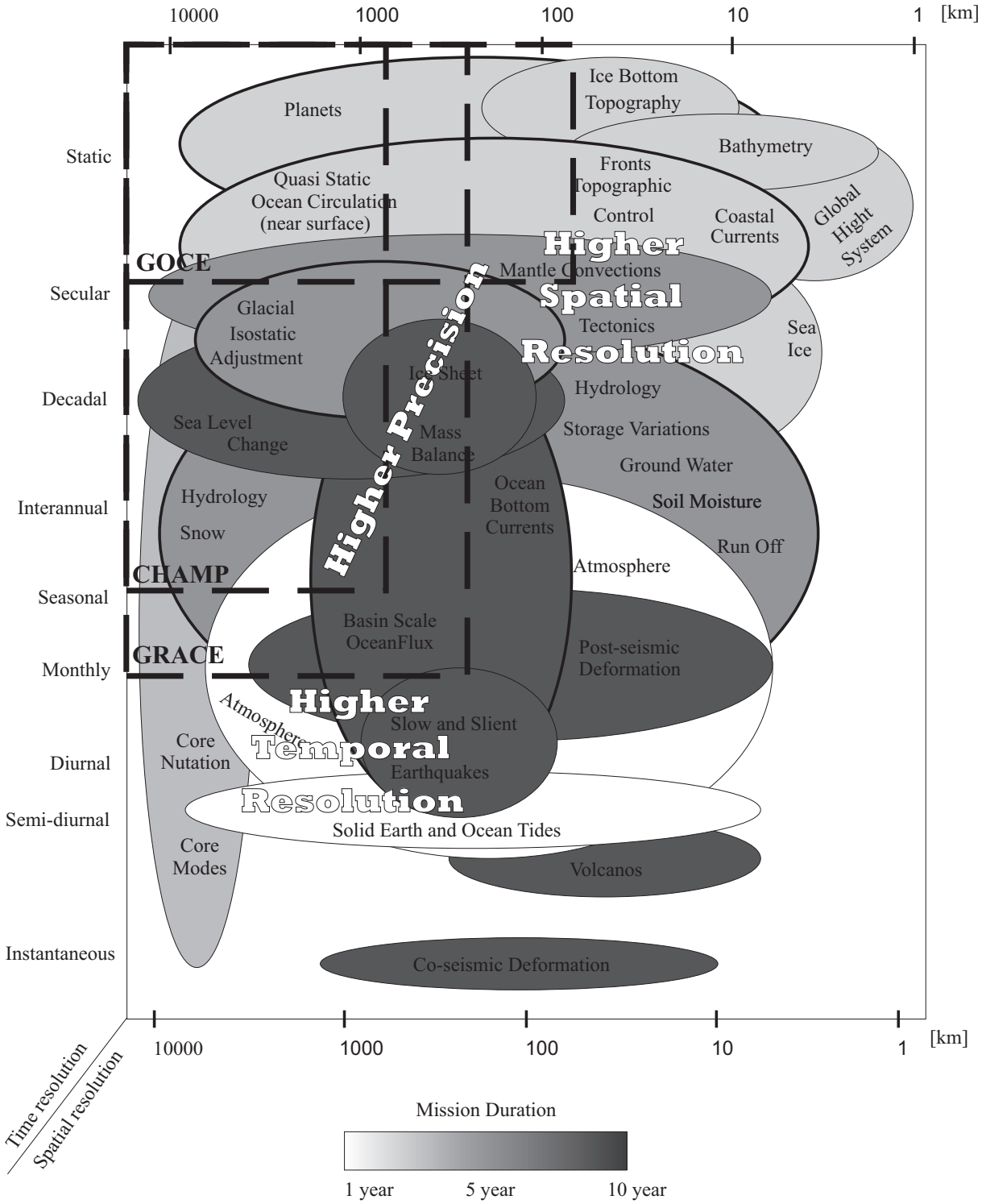

Fig. 2.3: The requirements for future FF missions for different scales of geophysical processes at both scales; resolution and mission duration (after Rummel 2007).

- For constellation, the relative position and relative velocity between the satellites are not controlled except to orbital station keeping points predefined at mission design. For the FF, the relative position and relative velocity between the two satellites are controlled and also the relative attitudes can be controlled at certain parts.
- For constellation, there is no plane defined for the inter-satellite positions other than the orbital planes. For the FF, a plane is defined for the inter-satellite positions with an arbitrary orientation in space with respect to a possible local orbit frame.

This study concentrates on the SFF concept based on the satellite-to-satellite measurement principle. The focus is on accuracy requirements for detecting temporal and spatial Earth's system variations. We are seeking to achieve satellite missions that have higher spatial and temporal resolution with a higher accuracy for mapping the different signals related to the Earth's gravity field than with the preceding missions. This will be executed based on the measurement of the satellites' positions and the inter-satellite observations in the LOS direction. In the following, different satellite configurations for improved and comprehensive gravity field retrieval are to be examined. The SFFs are commonly characterized by near-circular to circular and semi-polar orbits for a better coverage of the Earth. The individual orbital parameters will be discussed later in Chapter 6.

2.2.1 GRACE-type FF

The GRACE mission is based on a mission architecture consisting of a leader-follower formation in a simple collinear satellite configuration and is considered as the simplest realization of a SFF concept. In this satellite-to-satellite tracking mission, the difference of the first derivatives of the gravitational potential between the two GRACE satellites is measured. The disadvantage of this configuration is that the observable is sensitive only in along-track (or in-track) direction, providing (approximately) a projection multiplied by the inter-satellite distance of the signal of the gradient tensor onto the baseline between the GRACE twin-satellites. So it does not carry neither radial nor cross-track information of the gravitational forces. This leads to numerous problems such as undersampling and distortion. The former problem causes what is called aliasing effect that occurs when the gravity signal at higher frequencies becomes indistinguishable from that at certain lower frequencies. These higher frequencies either distort or create signals at lower frequencies and consequently they are said to become aliases of each other. The distortion problem is already seen in the monthly gravity solutions represented by longitudinal striping. This striation may occur due to the geographic systematic effects resulting from the propagation of errors in the observations due to the collinearity of GRACE configuration. This induces a non-isotropy of the error structure, i.e. the error structure of the sampling form is not identical in all directions. Another source for this striation is the variability behavior of the subsatellite-track patterns.

For this reason and in order to significantly improve the gravity recovery capability, the observation geometry should include the radial and/or cross-track gravitational signals. In this thesis, we are going to investigate the GRACE-type FF (see Fig. 2.4) as a reference formation for the other proposed formations. Consequently, the obtained gravity solutions can be also used as a reference gravity field solution for comparison purposes.

2.2.2 Radial wheel-type FF

An alternative to the GRACE-type FF, named Cartwheel (in the following labeled as Radial wheel), was first proposed by Massonnet (1998) when he discussed an interferometric constellation of passive micro-satellites to produce coherently combined radar images. This configuration has been investigated as a possibility for an Earth's gravity satellite mission by e.g. Sharifi et al. 2007, Sneeuw et al. 2008, Wiese et al. 2008 and Elsaka and Ilk 2008a. The Radial wheel formation consists of one or more satellite pairs performing a 2:1 relative elliptical motion (i.e. the semi-major axis is twice the semi-minor one) about their center of mass providing both along-track and radial gravity information (Fig. 2.5). Despite the slight discrepancy

between the along-track and radial measurements, however, the radial components are more sensitive to the gravitational signal. Two investigated interferometric Radial wheel formations are selected in this thesis, each of them are composed of two satellites without differences in the orbital elements except in the arguments of perigee and the mean anomalies of the satellites by an amount π (for more discussions of orbital parameters and the formation design refer to Sec. 6.4.2).

Fig. 2.5(a) shows two satellites adopting a Radial wheel formation oriented in the east-west direction with respect to (w.r.t.) only the Earth's equator (not the orbital plane). The satellite S_1 is located at the perigee of its orbit while S_2 is located at the apogee of its orbit forming a significant component in radial direction. This type collects per one orbital revolution two pure along-track measurements over the pole regions and two pure redial measurements over the equator ones. The measurements during the majority of time are composed of a combination of along-track and radial components. Two satellites adopting a Radial wheel formation oriented in the north-south direction w.r.t. the Earth's equator are indicated in Fig 2.5(b). This formation is different from the former one, in so far as the pure radial information is collected over the pole regions, while the pure along-track information is taken over the equator. It is worthwhile to note, that the aforementioned Radial wheel concept can be extended to form a four-satellite Radial wheel formation, either with two pairs of satellites as described by Wiese et al. (2008) or to form a six-satellite Radial wheel formation with three pairs of satellites as introduced by Sneeuw and Schaub (2005) (defined as the wheel configuration). Although, the six-satellites Radial wheel formation seems to be extremely expensive.

2.2.3 Inclined wheel-type FF

An out-of-plane formation, namely LISA (Laser Interferometer Space Antenna) (referred in this thesis as Inclined wheel), is already investigated for the recovery of the Earth's gravity field by Sneeuw et al. (2008) by imposing differential orbital elements including the right ascension of ascending nodes ($\Delta\Omega$) or the orbit inclination (Δi). The latter assumption, with non-zero differential inclination is not guaranteed to fly in a stable formation within the Earth's gravity field because of the drift that occurred in the orbit elements leading to drastic variations in the SST links (refer to Chapter 6).

This configuration was chosen in this investigation as a trade-off to improve the accuracy of the gravity field solutions by combining the three components: along-track, cross-track and radial. A set of conditions of different orbital elements are used including eccentricity (e), right ascension of ascending node (Ω) with a selection of a particular geometry of the argument of perigee (ω) or the mean anomaly (M) for maintaining the radial component (as given before in Radial wheel-type). These initial requirements can perform a relative circular out-of-plane motion known as Inclined wheel-type formation. In this thesis, we will consider only two satellites as shown in Fig. 2.6. The mission scenario and the synthesized data will be described later in Sec. 6.4.3.

2.2.4 Pendulum-type FF

A dedicated space-time sampling strategy is needed to obtain a reasonable coverage of the various systems within a time period compatible with the time scales of the gravity field variations. This can be achieved by the Pendulum-type mission which was proposed by DLR (for the TerraSAR-L mission). Two formations investigated by DLR (see Zink et al. 2003) are presented: The Cross-Track Pendulum and the Trinodal Pendulum. The satellite-to-Satellite baseline sweeps the cross-track direction at the equator providing the maximum inter-satellite distance and sweeps the in-track direction at pole giving the minimum distance. At the majority of time, the measurements are made in a combination of the along-track and cross-track directions.

An example of this type is the Swarm mission which was approved by ESA implemented as the fifth Earth Explorer mission. The Swarm mission is composed of a space segment of three satellites, two of them (Swarm A and Swarm B) are flying side-by-side in the east-west direction causing a cross-track inter-satellite distance of 160 km at the same low orbit altitude of 450 km, while the initial orbit altitude of the third satellite (Swarm

C) is 530 km. An overview of the Swarm mission objectives can be found in detail in Schönenberg et al. (2005). Sharifi et al. (2007) and Elsaka and Ilk (2008a) studied Swarm-like Pendulum configurations that are corresponding to Swarm A and Swarm B for the recovery of the static gravity field but with different inter-satellite distances of approximately 10-20 km and 100-200 km, respectively.

Fig. 2.7 shows the two proposed formation flights of the Pendulum concept investigated in this thesis. One of them (Fig. 2.7(a)) has no differential orbital elements except for the right ascension of the ascending node ($\Delta\Omega$) representing only a cross-track Pendulum-type. The other formation (Fig. 2.7(b)) represents a cross-along-track Pendulum-type with a differential right ascension of ascending node ($\Delta\Omega$) and mean anomaly (ΔM). A simulation scenario for this concept will be discussed later in Sec. 6.4.4.

2.2.5 Enhanced Temporal and Spatial Sampling SFF Types

2.2.5.1 GRACE-Pendulum-type FF

An alternative mission scenario for improving the temporal and the spatial sampling at the same time is to integrate different satellite formations. One choice describes a combination of two types of observations. This combination is given by joining along-track observations of GRACE-type with cross-track ones of Pendulum-type. This type of integration forms the so-called GRACE-Pendulum-type FF (see Fig. 2.8(a)). Elsaka et al. (2009) investigated this SFF for the first time showing a noticeable improvement of the gravity field on the both scales, the static scale and the temporal one using the combined observations. It helped also in mitigation of the temporal aliasing issue. This improvement is already expected as long as along-track information and cross-track one are incorporated together into the observables. Therefore, this formation type is considered as a modified form of the aforementioned cross-along-track Pendulum-type formation consisting of three satellites rather than two satellites.

2.2.5.2 Multi-GRACE-type Constellation

As addressed in Sec. 2.2.1, the collinear GRACE-type flies in a loose formation. This type suffers from both the undersampling of temporal signals and a leakage in the spatial sampling due to an insufficient and inconsistent coverage of the Earth's surface in short periods (i.e. the inhomogeneity of the subsatellite-track pattern). Hence, a trade-off has to be made between temporal and spatial resolution for gravity mapping satellites. A single gravity satellite mission cannot accomplish the global temporal resolution at such level. For this reason, an alternative mission configuration making use of multiple-satellite sensors is highly demanded. One implementation involves the use of two or more multiple satellites' orbits of GRACE-type, flying simultaneously, which can be accounted for combining two or more one-dimensional (along-track) observations as introduced by Elsaka and Ilk (2008b). Multiple orbits can solve or mitigate these problems. For instance, we do not know how many and which orbital frequencies alias into each other. For this reason, a demand for improved spatial data coverage is required. Examples for Multi-GRACE-type orbits are represented in Figs. 2.8(b), 2.9(a) and 2.9(b) with three postulations: One of them represents two GRACE-type formations in one constellation having different temporal resolution with the same spatial resolution. Another one concerning two GRACE-type formations flying also in one constellation with different spatial resolution with the same temporal resolution. The last Multi-GRACE-type represents a multiple formation having different inclinations at semi-polar and relatively lower latitudes. The detailed description of this formation with the characteristic nodal longitudes are given later in the Chapter 6 (see Sec. 6.4.6).

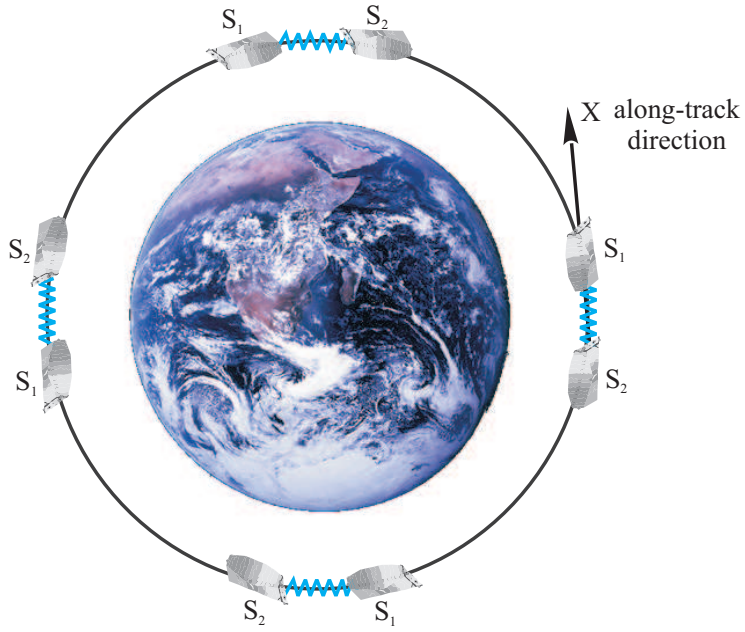

Fig. 2.4: GRACE-type FF as a reference configuration in this study.

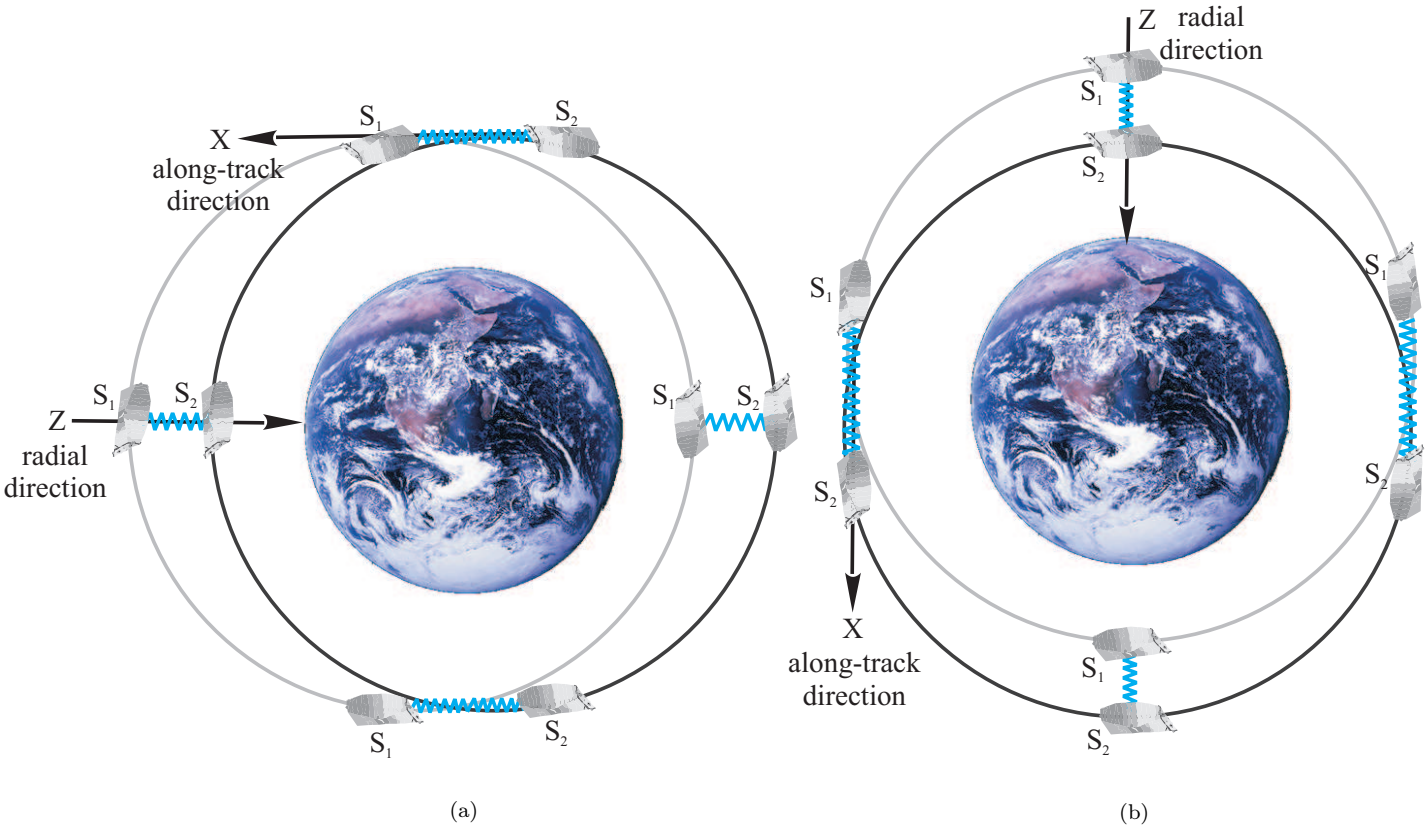

Fig. 2.5: Radial wheel-type FF, (a) East-West Radial wheel-type and (b) North-South Radial wheel-type.

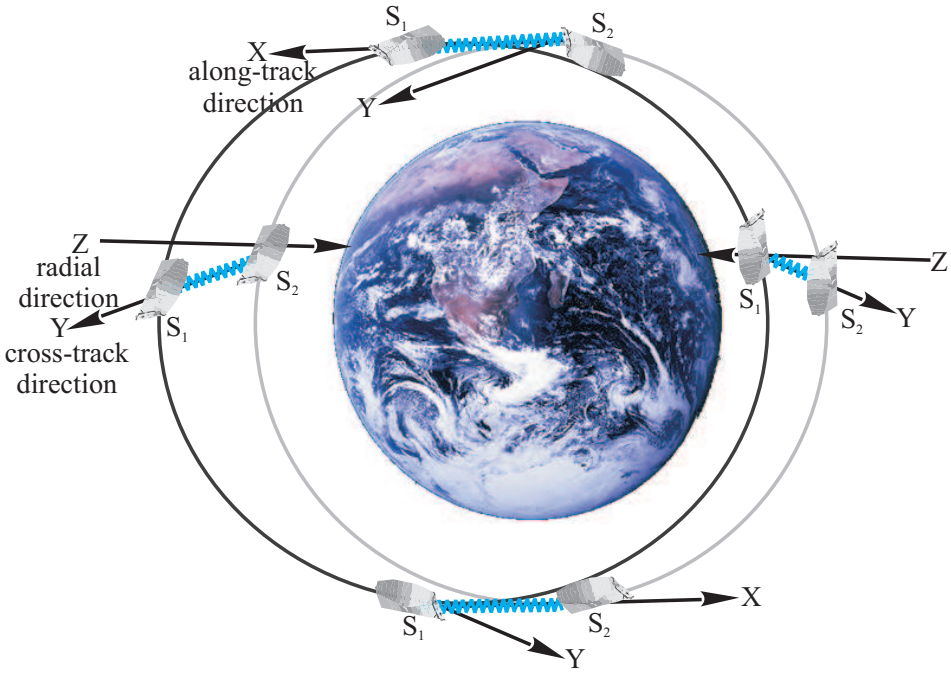

Fig. 2.6: Inclined wheel-type FF.

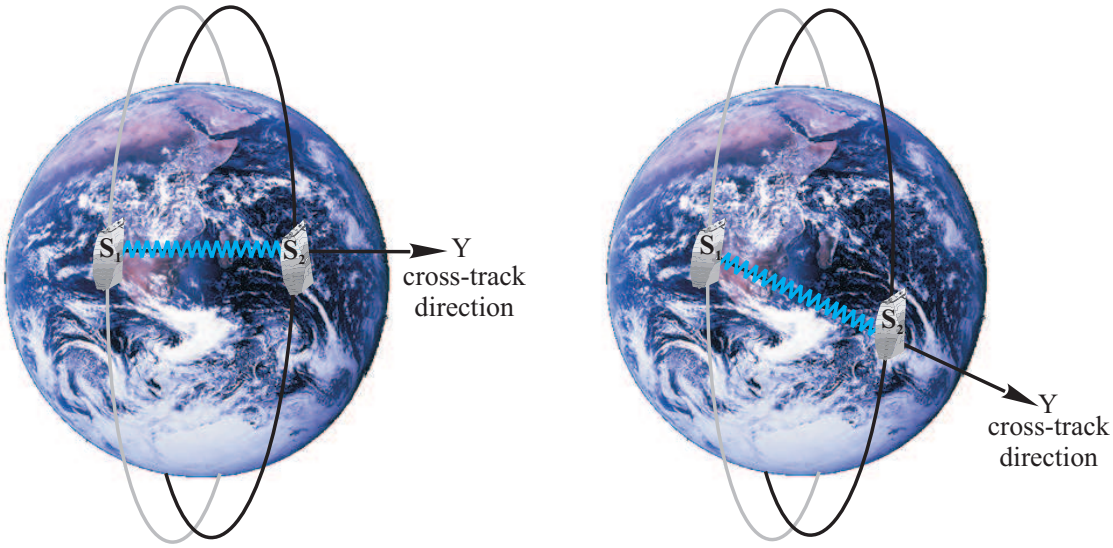

(a) (b)

Fig. 2.7: Pendulum-type FF, (a) cross-track Pendulum-type and (b) cross-along-track Pendulum-type.

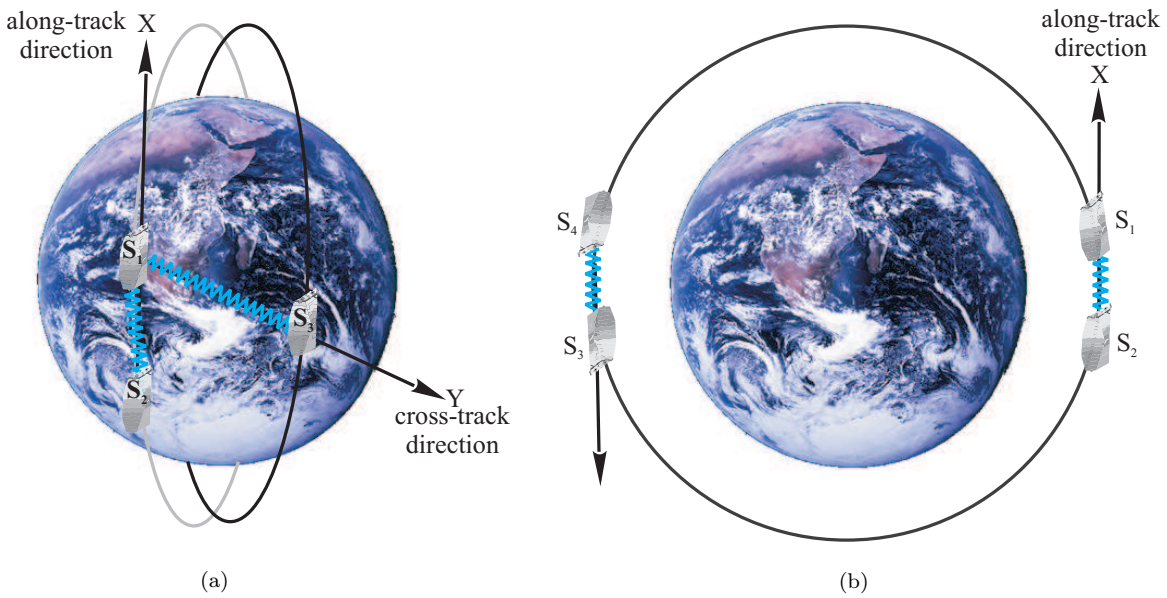

Fig. 2.8: (a) Combined GRACE-Pendulum-type FF and (b) Multi-GRACE-type with different temporal resolution and same spatial one.

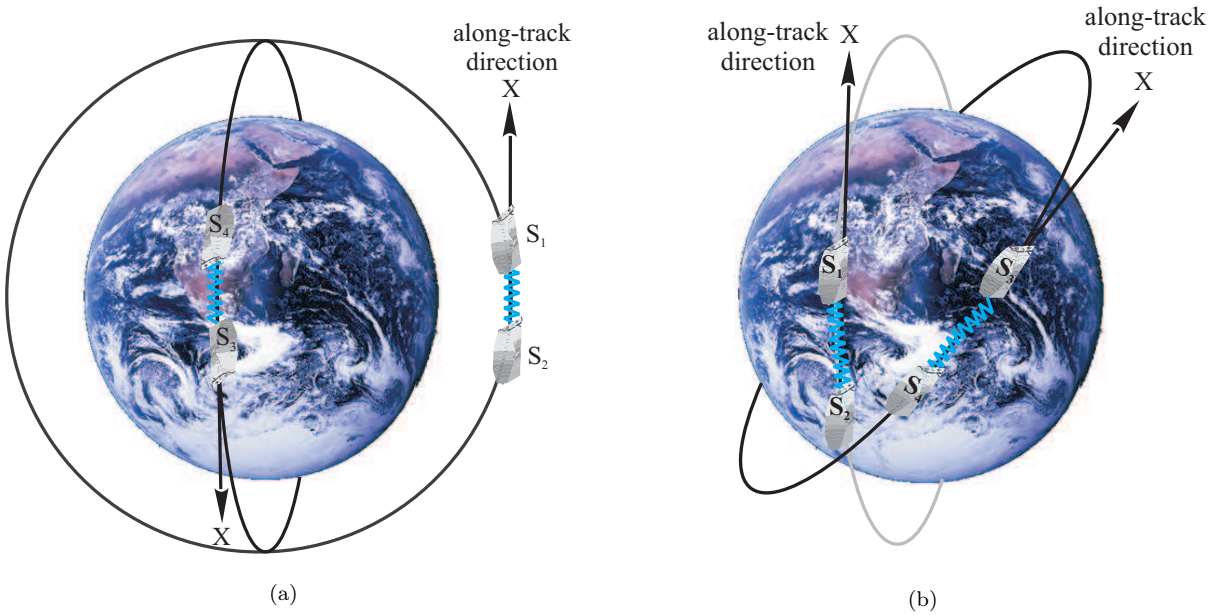

Fig. 2.9: (a) Multi-GRACE-type constellation with different spatial resolution and same temporal one and (b) Multi-GRACE-type with different inclinations.

3. Satellite's Motion in Static Gravity Field

In this chapter, we are going to consider the satellite motion in the Earth's gravity field from two points of view. Since the ideal non-perturbed motion does not exist in practical applications, we will treat the satellite motion according to the perturbation theory. First, we will discuss the relation between the celestial reference system and the terrestrial one. An overview on the transformation between the two reference systems is included in the following sections. For our task to recover the gravity field from satellite data, a preview of the potential theory and the determination of the unknown gravity field parameters in terms of spherical harmonic coefficients outside the Earth from satellite's positions concludes the second part of this chapter. In the last sections, the ecliptic and circular satellite motion is discussed.

3.1 Defining the Systems and Frames of Reference

When representing the satellite's orbits, we retain the name inertial system as a reference system, attached to the Earth's center, moving in free-fall without a rotation referred to the inertial space. The *Inertial system* is considered as the most fundamental reference system in geodesy with a translational motion (rigorously) along a straight line with a constant velocity. The term *quasi-Inertial* is preferred as the Earth-centered frame accelerating (but not rotating) around the sun. On the other hand, modeling the gravity field of the Earth is performed in an Earth-fixed or *terrestrial system*. For the relation between the equation of motion in the inertial system and the force models in the terrestrial system, one needs transformations between these systems. Therefore, a transformation is carried out between the standardized systems, the International Celestial Reference Frame (ICRF) and the International Terrestrial Reference Frame (ITRF). The former frame (ICRF) realizes a (quasi-)Inertial system, while the latter one (ITRF) realizes the terrestrial system as established by the International Earth Rotation and Reference System Service (IERS). They are based on the IERS standards contain a set of constants and models published in McCarthy and Petit (2004).

3.1.1 Transformation between Reference Frames

The transformation between the conventional CRF and the conventional TRF could be performed by three rotations in space encompassing Universal Time 1 (UT1), polar motion, and the phenomena of precession and nutation. The total rotational matrix for the total transformation from the Cartesian coordinates referred to the CRF at epoch t_0 to the Cartesian coordinates referred to the TRF at epoch t reads

$$\begin{pmatrix} x \\ y \\ z \end{pmatrix}_{CTRF_t} = \mathbf{S}(x_p, y_p, GAST)\mathbf{N}(\epsilon, -\Delta\psi, -\epsilon - \Delta\epsilon)\mathbf{P}(-\zeta, \vartheta, -z) \begin{pmatrix} x \\ y \\ z \end{pmatrix}_{CCRF_{t_0}} . \tag{3.1}$$

Due to the gravitational interaction of the Moon and the Sun with the Earth, the Earth's equatorial plane rotates. The total motion is composed of a mean secular component (precession) represented by the matrix $\mathbf{P}(-\zeta, \vartheta, -z)$ and a periodic component (nutation) represented by the matrix $\mathbf{N}(\epsilon, -\Delta\psi, -\epsilon - \Delta\epsilon)$. The last rotation matrix, $\mathbf{S}(x_p, y_p, GAST)$, includes the polar motion and the daily rotation.

When only the precession is taken into account, one transforms the mean celestial reference positions from an epoch t_0 in days since J2000.0 (1 January 2000 12:00= 51545.0) to the required mean celestial positions at epoch t using the precession matrix,

$$\mathbf{P}(-\zeta, \vartheta, -z) := \mathbf{R}_z(-z)\mathbf{R}_y(\vartheta)\mathbf{R}_z(-\zeta). \tag{3.2}$$

The three precession angles $(-\zeta, \vartheta, -z)$ for are given by McCarthy and Petit (2004) as

$$\begin{aligned} \zeta &= 2.5976176'' + 2306.0809506''T + 0.3019015''T^2 + 0.0179663''T^3 - 0.0000327''T^4 - 0.0000002''T^5, \\ \vartheta &= 2004.1917476''T - 0.4269353''T^2 - 0.0418251''T^3 - 0.0000601''T^4 - 0.0000001''T^5, \\ z &= -2.5976176'' + 2306.0803226''T + 1.094779''T^2 + 0.0182273''T^3 + 0.000047''T^4 - 0.0000003''T^5, \end{aligned} \tag{3.3}$$

with,

$$T = (t - t_0)/36525.0, \tag{3.4}$$

the time difference between the actual epoch (t) and the reference epoch J2000.0 counted in Julian centuries.

When nutation is taken into account, then one transforms the mean celestial reference positions at the epoch t to the instantaneous true celestial positions using the nutation matrix,

$$\mathbf{N}(\epsilon, -\Delta\psi, -\epsilon - \Delta\epsilon) := \mathbf{R}_x(-\epsilon - \Delta\epsilon)\mathbf{R}_z(-\Delta\psi)\mathbf{R}_x(\epsilon), \tag{3.5}$$

with ϵ obliquity of the ecliptic, $\Delta\epsilon$ nutation in obliquity and $\Delta\psi$ nutation in longitude (counted in the ecliptic). The obliquity of the ecliptic at epoch t, which represents the rotation angle from the ecliptic system to the equator system, is computed from:

$$\epsilon = 23^\circ 26' 21.448'' - 46.815'' T - 0.00059'' T^2 + 0.001813'' T^3. \tag{3.6}$$

Based on the precession-nutation model adopted by the International Astronomical Union (IAU) in 2000, $\Delta\psi$ and $\Delta\epsilon$ are computed using an expansion series. The first terms read

$$\begin{aligned} \Delta\psi &= (-17.1996'' - 0.01742'' T)\sin(\Omega) + (0.2062'' + 0.00002'' T)\sin(2\Omega) + \cdots, \\ \Delta\epsilon &= (9.2025'' + 0.00089'' T)\cos(\Omega) + (-0.0895'' + 0.00005'' T)\cos(2\Omega) + \cdots, \end{aligned} \tag{3.7}$$

with Ω the mean ecliptic longitude of the lunar ascending node. The complete series terms can be found in the technical report of the IERS conventions 2003 (see McCarthy and Petit 2004).

The final rotation from the true celestial system at epoch t to a conventional terrestrial system at the same epoch t is given by three further parameters which are contained in the rotational matrix,

$$\mathbf{S}(x_p, y_p, GAST) := \mathbf{R}_y(-x_p)\mathbf{R}_x(-y_p)\mathbf{R}_z(GAST). \tag{3.8}$$

GAST is the Greenwich Apparent (=true) Sidereal Time and expressed as the difference between the Universal Time 1 and the Universal Time Coordinated (UT1-UTC). UT1 is the time determined by the rotation of the Earth and is computed by correcting UT0[1] for the effect of polar motion on the longitude of the observing site. The other two terms x_p and y_p represent the polar coordinates. The rotation matrix for this last rotation reads

$$\mathbf{S}(x_p, y_p, GAST) := \begin{pmatrix} 1 & 0 & x_p \\ 0 & 1 & 0 \\ -x_p & 0 & 1 \end{pmatrix} \begin{pmatrix} 1 & 0 & 0 \\ 0 & 1 & -y_p \\ 0 & y_p & 1 \end{pmatrix} \begin{pmatrix} \cos(GAST) & \sin(GAST) & 0 \\ -\sin(GAST) & \cos(GAST) & 0 \\ 0 & 0 & 1 \end{pmatrix}. \tag{3.9}$$

Unlike Eq. (3.2) and Eq. (3.5), the parameters of Eq. (3.8) cannot be described through a theory (as e.g. precession and nutation) but must be determined from actual observations by an international time and latitude service (Seeber 2003, p. 20). The observation techniques include laser ranging to satellites and to the Moon (SLR and LLR) as well as Very Long Baseline Interferometry (VLBI).

3.2 Potential Theory and Spherical Harmonics

The purpose of the following sections is to summarize shortly the fundamental concepts of potential theory including spherical harmonics as far as they are relevant in this thesis to assure adequate understanding of the following chapters. The *Laplace equation* and *Legendre functions* are reviewed because of their beneficial application in geodesy.

[1] UT0 is the Universal Time determined at an observatory by observing the diurnal motion of stars or extragalactic radio sources, and also from ranging observations of the Moon and artificial Earth satellites

3.2.1 Attraction and potential

The mutual attraction force of a mass point m_2 (the attracted point) with a gravitating mass m_1 (e.g. the attracting point) separated by a distance r (measured between the two mass points) has been described by Newton's law of universal gravitation (see Fig. 3.1) as

$$\mathbf{F}_{21} = -Gm_1m_2\frac{\mathbf{r}_2 - \mathbf{r}_1}{||\mathbf{r}_2 - \mathbf{r}_1||^3}, \tag{3.10}$$

with the universal gravitational constant $G = (6672 \pm 4)\,10^{-14}m^3s^{-2}kg^{-1}$ and the position vectors $\mathbf{r}_1$ and $\mathbf{r}_2$. By regarding the attracting mass as a source point, written as m_Q, then the gravitational strength of the gravity field of this mass reads

$$\mathbf{g}_Q(\mathbf{r}) = -Gm_Q\frac{\mathbf{r} - \mathbf{r}_Q}{||\mathbf{r} - \mathbf{r}_Q||^3}, \tag{3.11}$$

and the gravity force acting on a mass m located at the position $\mathbf{r}$ within this force field can be expressed as

$$\mathbf{F}_Q(\mathbf{r}) = m\mathbf{g}_Q(\mathbf{r}). \tag{3.12}$$

The gravity force function is a vector for one point mass, so the gravity field of more than one point mass can be superimposed by adding the individual components of $\mathbf{g}(\mathbf{r})$. Thus for the total mass distribution, the gravity force function can be given as an integral over the total volume v with a vector length $\mathbf{l}$ and a continuous density function $\rho(\mathbf{r}_Q)$,

$$\mathbf{g}(\mathbf{r}) = -G\iiint\limits_v \rho(\mathbf{r}_Q)\frac{\mathbf{l}}{l^3}dv. \tag{3.13}$$

It is well known that the gravity force is a conservative force, this means that it can be derived as the gradient vector of a scalar function V,

$$\mathbf{g}(\mathbf{r}) = \nabla V(\mathbf{r}). \tag{3.14}$$

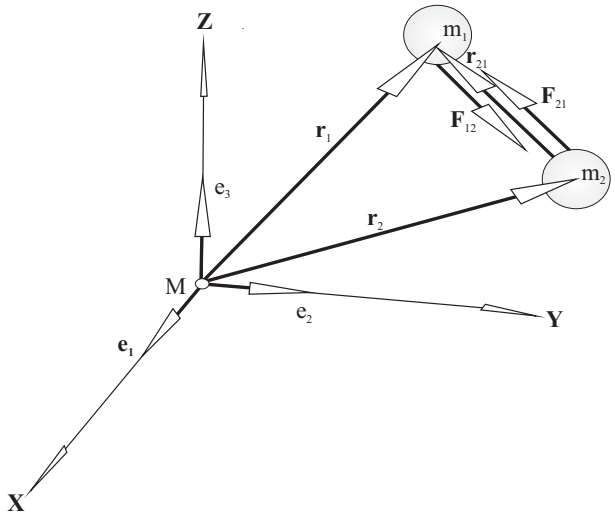

Fig. 3.1: The universal law of gravitation as described by Newton.

The gravitational potential V can be determined by

$$V(\mathbf{r}) = G\iiint\limits_v \rho(\mathbf{r}_Q)\frac{1}{l}dv. \tag{3.15}$$

This potential V is continuous throughout the whole space and vanishes ($V = 0$) at infinity because it holds $1/l = 0$ for $l \to \infty$.

3.2.2 Spherical Harmonics, Laplace Equation and Legendre Function

Spherical harmonics are the eigenfunctions of the *Laplace operator* Δ or the solution of the *Laplace equation*. Considering the potential V of an attracting mass at any point with the Cartesian coordinates (x, y, z), outside the masses, then the gravity potential V must satisfy the differential operator Δ applied to V, i.e., representing the sum of the second partial derivatives (*Laplace equation*),

$$\Delta V = \nabla^2 V = \frac{\partial^2 V}{\partial x^2} + \frac{\partial^2 V}{\partial y^2} + \frac{\partial^2 V}{\partial z^2} = 0. \tag{3.16}$$

When introducing to spherical coordinates (r, ϑ, λ) by writing $r \sin\vartheta \cos\lambda$ for x, $r \sin\vartheta \sin\lambda$ for y and $r \cos\lambda$ for z (see Fig. 3.2), then Eq. (3.16) reads

$$\Delta V = \frac{1}{r^2}\frac{\partial}{\partial r}\left(r^2 \frac{\partial V}{\partial r}\right) + \frac{1}{r^2 \sin\vartheta}\frac{\partial}{\partial \vartheta}\left(\sin\vartheta \frac{\partial V}{\partial \vartheta}\right) + \frac{1}{r^2 \sin^2\vartheta}\frac{\partial^2 V}{\partial \lambda^2} = 0. \tag{3.17}$$

Solutions of *Laplace equation* are called *harmonic functions*, and therefore, the solutions in spherical coordinates are *spherical harmonics*. For a detailed mathematical discussion please refer to Heiskanen and Moritz (1979).

Two different cases have to be considered separately when dealing with the gravitational field: it is the question whether the attracting point is inside or outside of the attracting masses. If the mass point is outside the attracting masses (the Earth), then *Laplace equation* holds and if the mass point is inside the attracting mass then *Poisson equation*, which reads

$$\Delta V = \nabla^2 V = \frac{\partial^2 V}{\partial x^2} + \frac{\partial^2 V}{\partial y^2} + \frac{\partial^2 V}{\partial z^2} = -4\pi G\rho, \tag{3.18}$$

has to be applied. Our interest here is the determination of the gravitational potential outside the Earth, therefore, *Laplace equation* is relevant.

By separating the variables (r, ϑ, λ) in Eq. (3.17), one obtains

$$V(r, \vartheta, \lambda) = f(r)Y(\vartheta, \lambda). \tag{3.19}$$

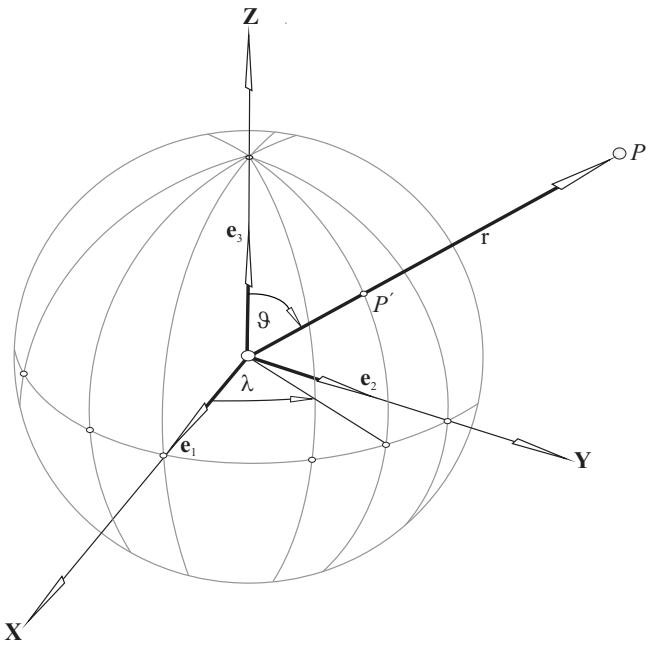

Fig. 3.2: Representation of spherical coordinates

The right-hand side is composed of two functions, f is a function dependent only on r and Y is a function dependent only on ϑ and λ. The solution of the function $f(r)$ is indicated by

$$f(r) = \begin{cases} r^n \\ \frac{1}{r^{n+1}} \end{cases}, \tag{3.20}$$

where n is integer constant. Therefore, Eq. (3.17) can be solved as

$$V = r^n Y_n(\vartheta, \lambda), \tag{3.21a}$$

or

$$V = \frac{1}{r^{n+1}} Y_n(\vartheta, \lambda). \tag{3.21b}$$

The functions $Y_n(\vartheta, \lambda)$ are known as surface harmonic functions. As known, if the differential equation is linear and has several solutions, then the sum of these solutions is also a solution. Hence one concludes that

$$V = \sum_{n=0}^{\infty} r^n Y_n(\vartheta, \lambda), \tag{3.22a}$$

and

$$V = \sum_{n=0}^{\infty} \frac{1}{r^{n+1}} Y_n(\vartheta, \lambda), \tag{3.22b}$$

are also solutions of the *Laplace equation* and are harmonic functions as well.

The Laplace surface harmonics $Y_n(\vartheta, \lambda)$ can again be split into two functions each depend on one variable only as

$$Y_n(\vartheta, \lambda) = g(\vartheta) h(\lambda). \tag{3.23}$$

The solutions of the second term of the right-hand side of Eq. (3.23) are represented by the two functions

$$h(\lambda) = \begin{cases} \cos m\lambda, \\ \sin m\lambda, \end{cases} \tag{3.24}$$

while the solutions of the first term of the right-hand side of Eq. (3.23) is given by the so-called *associated Legendre functions*[2] $P_{nm}(\cos\vartheta)$. The *associated Legendre functions* are defined as functions on the interval [-1,+1] for any $n \geq 0$ and $0 < m \leq n$. Since ϑ is defined on the interval [π,0], the *Legendre functions* can be easily written as

$$g(\vartheta) = P_{nm}(\cos\vartheta). \tag{3.25}$$

Then the surface spherical harmonic functions $Y_n(\vartheta, \lambda)$ read

$$Y_n(\vartheta, \lambda) = \begin{cases} P_{nm}(\cos\vartheta)\cos m\lambda, \\ P_{nm}(\cos\vartheta)\sin m\lambda. \end{cases} \tag{3.26}$$

Since this equation is linear in the associated Legendre polynomials, any linear combination of the solutions is also a solution. The linear combination reads

$$Y_n(\vartheta, \lambda) = \sum_{m=0}^{n} [c_{nm} P_{nm}(\cos\vartheta)\cos m\lambda + s_{nm} P_{nm}(\cos\vartheta)\sin m\lambda], \tag{3.27}$$

[2]Legendre functions are called associated Legendre functions if the order m≠0 - that is, m= 1,2,$\cdots$,n.

where c_{nm} and s_{nm} are arbitrary constants. By inserting Eq. (3.26) into Eq. (3.22a) and Eq. (3.22b), we obtain two sets of general solutions,

$$V(r,\vartheta,\lambda) = \sum_{n=0}^{\infty} r^n \sum_{m=0}^{n} [c_{nm} P_{nm}(\cos\vartheta)\cos m\lambda + s_{nm} P_{nm}(\cos\vartheta)\sin m\lambda], \tag{3.28a}$$

and

$$V(r,\vartheta,\lambda) = \sum_{n=0}^{\infty} \frac{1}{r^{n+1}} \sum_{m=0}^{n} [c_{nm} P_{nm}(\cos\vartheta)\cos m\lambda + s_{nm} P_{nm}(\cos\vartheta)\sin m\lambda]. \tag{3.28b}$$

Every function which is harmonic inside a certain sphere can be expanded into a series (3.28a), while any function which is harmonic outside a certain sphere (such as the Earth's gravitational potential) can be expanded into a series (3.28b).

3.2.3 Spherical Harmonics Analysis in Geodesy Applications

Spherical harmonics have powerful properties especially for Earth related applications as an orthogonal set of solutions to the *Laplace equation*. This property of orthogonality allows a simplified forward and inverse transformation between a function and its spectrum. The spherical harmonics are a preferred tool for many theoretical and practical applications in geodesy, particularly for the representation of gravitational field. Therefore, most of the existing gravity field models are formulated in terms of spherical harmonic coefficients.

In Satellite geodesy, Eq. (3.28b) is written in the following form (e.g. Heiskanen and Moritz (1979))

$$V(r,\vartheta,\lambda) = \frac{GM}{R_e}\left[\sum_{n=2}^{\infty}\sum_{m=0}^{n}\left(\frac{R_e}{r}\right)^{n+1}(c_{nm}C_{nm}(\lambda,\vartheta) + s_{nm}S_{nm}(\lambda,\vartheta))\right], \tag{3.29}$$

with GM the gravitational constant times the Earth's mass, R_e the mean radius of the Earth and the base functions

$$C_{nm}(\vartheta,\lambda) = P_{nm}(\cos\vartheta)\cos(m\lambda), \tag{3.30a}$$

$$S_{nm}(\vartheta,\lambda) = P_{nm}(\cos\vartheta)\sin(m\lambda), \tag{3.30b}$$

with the associated Legendre functions $P_{nm}(\cos\vartheta)$. There are different normalizations used in the literature, the fully normalized harmonics seem to be the most convenient and widely used in geodesy. The orthogonality property on the sphere's area reads (see Heiskanen and Moritz 1979, p. 29-31)

$$\frac{1}{4\pi}\int_{\lambda=0}^{2\pi}\int_{\vartheta=0}^{\pi} C_{nm}^2(\vartheta,\lambda)\sin\vartheta\, d\vartheta\, d\lambda = \frac{1}{4\pi}\int_{\lambda=0}^{2\pi}\int_{\vartheta=0}^{\pi} S_{nm}^2(\vartheta,\lambda)\sin\vartheta\, d\vartheta\, d\lambda = 1. \tag{3.31}$$

The gravity force $\mathbf{g}$ can be obtained, as discussed before, from the potential V as the gradient of V,

$$\mathbf{g}(\mathbf{r}) = \nabla V(\mathbf{r}). \tag{3.32}$$

For the gravity field determination from satellite's data, the potential V and the gravity vector $\mathbf{g}$ are needed at several positions along an orbit's arc in dependency of the estimated potential coefficients c_{nm} and s_{nm}. Both, the potential and the gravity have the same linear form in terms of the unknown coefficients. Therefore, the computation can be expressed by a matrix-vector-product (i.e. a matrix that has only one column). The following parameter vector $\mathbf{x}$ contains the potential coefficients up to the maximum desired degree and order n_{max} (instead of the indefinite limit ∞ in Eq. (3.29)) as described by Mayer-Gürr (2006)

$$\mathbf{x} = \left(c_{20}, c_{21}, s_{21}, \ldots, c_{nm}, s_{nm}\right)^T. \tag{3.33}$$

It should be mentioned here that the matrix-vector-product of Eq. (3.33) begins with the term c_{20} because the term c_{00} is defined to be exactly 1 and the terms c_{10}, c_{11} and $s_{11}$are defined to be exactly 0.

The potential at positions $\mathbf{r}_i(r_i, \lambda_i, \vartheta_i)$ along the orbit's arc is then calculated from

$$\begin{pmatrix} V(\mathbf{r}_1) \\ \vdots \\ V(\mathbf{r}_N) \end{pmatrix} = \mathbf{V}\mathbf{x}, \tag{3.34}$$

with the matrix

$$\mathbf{V} = \frac{GM}{R_e} \begin{pmatrix} \dots & \left(\frac{R_e}{r_1}\right)^3 C_{21}(\lambda_1, \vartheta_1) & \left(\frac{R_e}{r_1}\right)^3 S_{21}(\lambda_1, \vartheta_1) & \dots & \left(\frac{R_e}{r_1}\right)^{n+1} S_{nm}(\lambda_1, \vartheta_1) \\ \dots & \left(\frac{R_e}{r_2}\right)^3 C_{21}(\lambda_2, \vartheta_2) & \left(\frac{R_e}{r_2}\right)^3 S_{21}(\lambda_2, \vartheta_2) & \dots & \left(\frac{R_e}{r_2}\right)^{n+1} S_{nm}(\lambda_2, \vartheta_2) \\ & \vdots & \vdots & & \vdots \\ \dots & \left(\frac{R_e}{r_N}\right)^3 C_{21}(\lambda_N, \vartheta_N) & \left(\frac{R_e}{r_N}\right)^3 S_{21}(\lambda_N, \vartheta_N) & \dots & \left(\frac{R_e}{r_N}\right)^{n+1} S_{nm}(\lambda_N, \vartheta_N) \end{pmatrix}. \tag{3.35}$$

For computing this matrix, the positions must be given in a terrestrial coordinates system. Correspondingly, the gravity forces along the orbit's arcs can be expressed by a matrix-vector-product as

$$\begin{pmatrix} \mathbf{g}(\mathbf{r}_1) \\ \vdots \\ \mathbf{g}(\mathbf{r}_N) \end{pmatrix} = \bar{\mathbf{G}}\mathbf{x}. \tag{3.36}$$

As the gravity forces are defined in the terrestrial system and the functionals of the satellite's motion are referred to the inertial system, the gravity has to be transformed with the help of the rotational matrix of the Earth's rotation through the transformation

$$\mathbf{G} := \mathbf{R}\bar{\mathbf{G}}, \tag{3.37}$$

with the block diagonal matrix $\mathbf{R}$ as

$$\mathbf{R} = \begin{pmatrix} \mathbf{R}_e(t_1) & \mathbf{0} & \cdots & \mathbf{0} \\ \mathbf{0} & \mathbf{R}_e(t_2) & \cdots & \mathbf{0} \\ \vdots & \vdots & \ddots & \vdots \\ \mathbf{0} & \mathbf{0} & \cdots & \mathbf{R}_e(t_N) \end{pmatrix}, \tag{3.38}$$

where $\mathbf{R}_e(t_i)$ describes the rotational matrix from the terrestrial to the inertial system at time t_i (see Section 3.1.1). One obtains the gravity in the inertial system in Eq. (3.36) by replacing the matrix $\bar{\mathbf{G}}$ with $\mathbf{G}$.

In General, the potential V itself is not the main issue for further investigations, instead the disturbing potential T is introduced. The disturbing potential is the difference between the potential V and a reference potential U,

$$T = V - U. \tag{3.39}$$

The equipotential surface corresponding (approximately) with the sea level, the geoid, has a special consideration in geodesy for its importance in modeling the figure of the Earth's gravity field. The geoidal undulations N referred to the reference ellipsoid can be calculated from the disturbing potential T by applying Bruns's formula as (see Heiskanen and Moritz 1979, p.85)

$$N = \frac{T}{\gamma}. \tag{3.40}$$

The disturbing potential T in Eq. (3.40) is defined by the difference of the gravity potential at sea level and the potential coefficients of a level ellipsoid (e.g. GRS80) and can be formulated as

$$T(r,\vartheta,\lambda) = \frac{GM}{R_e}\left[\sum_{n=2}^{n_{max}}\sum_{m=0}^{n}\left(\frac{R_e}{r}\right)^{n+1}\left(\Delta c_{nm}C_{nm}(\lambda,\vartheta)+\Delta s_{nm}S_{nm}(\lambda,\vartheta)\right)\right], \tag{3.41}$$

with the corrections $\Delta c_{nm}, \Delta s_{nm} \in \Delta\mathbf{x}$ to the reference potential coefficients $c_{nm}, s_{nm} \in \mathbf{x}_0$. The term γ in Eq. (3.40) represents the normal gravity calculated on the surface of the ellipsoid. For simplicity, the normal gravity is determined approximately by $\gamma = GM/R_e^2$ in spherical approximation[3]. It is worthwhile noting that the term $(R_e/r)^n$ becomes smaller with increasing distance from the Earth and hence the gravity field becomes smoother and so will the orbit perturbations.

Hence, the geoid undulations can be approximately computed from the spherical harmonic coefficients referred to the potential coefficients $\Delta c^0_{nm}, \Delta s^0_{nm}$ and of the level ellipsoid as (see Ilk et al. 2005, p. 127)

$$\begin{aligned} N(r,\vartheta,\lambda) &= T(r,\vartheta,\lambda)\frac{R_e}{GM} = \\ &= R_e\left[\sum_{n=2}^{n_{max}}\sum_{m=0}^{n}\left(\Delta c^0_{nm}C_{nm}(\lambda,\vartheta)+\Delta s^0_{nm}S_{nm}(\lambda,\vartheta)\right)\right]. \end{aligned} \tag{3.42}$$

The estimation of the degree variances of the spherical harmonic coefficients c_{nm} and s_{nm} (or any differences) is a very powerful tool in the gravity analysis to show the discrepancies between the different solutions of the disturbing potential on the Earth's surface,

$$\sigma^2(T) = \frac{1}{4\pi R_e^2}\int_{\lambda=0}^{2\pi}\int_{\vartheta=0}^{\pi} T^2(\lambda,\vartheta)\sin\vartheta\, d\lambda\, d\vartheta = \frac{GM}{R_e}\sum_{n=0}^{n_{max}}\sum_{m=0}^{n}\left(c_{nm}^2+s_{nm}^2\right) = \frac{GM}{R_e}\sum_{n=0}^{n_{max}}\sigma_n^2, \tag{3.43}$$

with

$$\sigma_n^2 = \sum_{m=0}^{n}\left(c_{nm}^2+s_{nm}^2\right). \tag{3.44}$$

The variance of the geoid heights can be determined as well by

$$\sigma^2(N) = \frac{1}{4\pi R_e^2}\int_{\lambda=0}^{2\pi}\int_{\vartheta=0}^{\pi} N^2(\lambda,\vartheta)\sin\vartheta\, d\lambda\, d\vartheta = R_e^2\sum_{n=0}^{n_{max}}\sigma_n^2. \tag{3.45}$$

Accordingly, the variance of the difference of two solutions can be derived in order to obtain a measure of the consistency of the two solutions (see Mayer-Gürr 2006, p.26)

$$\sigma^2(\Delta N) = \frac{1}{4\pi R_e^2}\int_{\lambda=0}^{2\pi}\int_{\vartheta=0}^{\pi}\left(N(\lambda,\vartheta)-\bar{N}(\lambda,\vartheta)\right)^2\sin\vartheta\, d\lambda\, d\vartheta = R_e^2\sum_{n=0}^{n_{max}}\Delta\sigma_n^2, \tag{3.46}$$

with

$$\Delta\sigma_n^2 = \sum_{m=0}^{n}\left((c_{nm}-c'_{nm})^2+(s_{nm}-s'_{nm})^2\right). \tag{3.47}$$

This equation has been intensively applied in this thesis for representing our results in terms of the degree variances of geoid heights to show the difference in the spectral domain between the applied model and our solutions of different formation flights (see Sec. 5.2.1.2.2).

[3]Close to the Earth's surface, r= R_e (in the spherical approximation).

3.3 Satellite Motion – Elliptic and Circular Motion

A near-Earth satellite's orbit differs slightly from the ideal Keplerian motion (see Appendix A). After few days, one finds that the slight differences became easily recognizable. Regarding this fact, one can say that the Keplerian orbit is gradually perturbed. The difference between the true satellite's orbit and the Keplerian one is caused by the fact that the Earth is not spherically symmetrical and other forces act on the satellites.

These forces are categorized into conservative and non-conservative forces. The first conservative forces can be derived from the potential such as the gravitational attraction of the Earth and the other heavy celestial bodies (e.g. Sun, Moon and other planets) and the tidal effects. The other non-conservative forces include atmospheric drag, Sun radiation pressure and Earth's reflected radiation (Earth Albedo).

Satellites' observations are composed of information about the satellite orbit perturbations, i.e. the changes in the satellite's position and velocity relative to the reference Kepler orbit. Therefore, these changes or perturbations must be computed in order to be able to process the satellite observations. In our interest and since these perturbations are caused by the change of the gravity field, we are going to discuss the relation between them and the Earth's gravitational potential. Two well established and widely applied methods in celestial mechanics and satellite geodesy are to derive the relation between these orbital perturbations and the gravity potential in form of the disturbing potential. One method is based on the Kaula's solution of the Lagrange planetary equations (LPE) and the other one is originating from the Hill's equations.

3.3.1 Kaula's Solution of Linear Perturbation Equations

Many textbooks of celestial mechanics and satellite geodesy have treated the solution of the linear perturbational motion of a satellite. The forces acting onto the satellites cover a very broad spectrum beginning from the very large central gravitational forces till very small gravitational inhomogeneities and small surface forces, which are summarized as disturbing forces. Since these disturbing forces are relatively weak, so the motion of the satellite orbit remains close to an elliptic motion. Kaula (1966) formulated the perturbation equations in terms of classical Keplerian elements as

$$\frac{da}{dt} = \frac{1}{\mathrm{n}a}\left(2\frac{\partial R}{\partial M}\right), \tag{3.48a}$$

$$\frac{de}{dt} = \frac{1}{\mathrm{n}a^2}\left(\frac{1-e^2}{e}\frac{\partial R}{\partial M} - \frac{\sqrt{1-e^2}}{e}\frac{\partial R}{\partial \omega}\right), \tag{3.48b}$$

$$\frac{di}{dt} = \frac{1}{\mathrm{n}a^2}\left(\frac{\cos i}{\sin i\sqrt{1-e^2}}\frac{\partial R}{\partial \omega} - \frac{1}{\sin i\sqrt{1-e^2}}\frac{\partial R}{\partial \Omega}\right), \tag{3.48c}$$

$$\frac{d\Omega}{dt} = \frac{1}{\mathrm{n}a^2}\left(\frac{1}{\sin i\sqrt{1-e^2}}\frac{\partial R}{\partial i}\right), \tag{3.48d}$$

$$\frac{d\omega}{dt} = \frac{1}{\mathrm{n}a^2}\left(\frac{\sqrt{1-e^2}}{e}\frac{\partial R}{\partial e} - \frac{\cos i}{\sin i\sqrt{1-e^2}}\frac{\partial R}{\partial i}\right), \tag{3.48e}$$

$$\frac{dM}{dt} = \mathrm{n} - \frac{1-e^2}{\mathrm{n}a^2 e}\frac{\partial R}{\partial e} - \frac{2}{\mathrm{n}a}\frac{\partial R}{\partial a}. \tag{3.48f}$$

Where R is the perturbing potential, $\mathrm{n} = \sqrt{GM/a^3}$ is known as the mean motion of the satellite and G is the gravitational constant and M is the total mass of the Earth. The elements (a, e, i, Ω, ω and M) are the Keplerian elements (semi-major axis, eccentricity, inclination, right ascension of ascending node, argument of perigee and the mean anomaly, respectively) (see Appendix A for definitions). One should mention here that Eqs. (3.48d) – (3.48f) will be used later in Sec. 6.2.1.

Kaula (1966) expressed the perturbing potential R in terms of spherical harmonics similar to Eq. (3.29) but w.r.t. the Keplerian elements instead of spherical coordinates of the satellite positions,

$$R = \sum_{n=0}^{\infty} \sum_{m=0}^{n} R_{nm}, \tag{3.49a}$$

$$\begin{aligned} R_{nm} &= \frac{GMR_e}{a^{n+1}} \sum_{p=0}^{n} F_{nmp}(i) \sum_{q=-\infty}^{\infty} G_{npq}(e) S_{nmpq}(\omega, M, \Omega, \Theta), \\ &= \sum_{n=2}^{\infty} \sum_{m=0}^{n} \sum_{p=0}^{n} \sum_{q=-\infty}^{\infty} \frac{GMR_e}{a^{n+1}} F_{nmp}(i) G_{npq}(e) S_{nmpq}(\omega, M, \Omega, \Theta), \end{aligned} \tag{3.49b}$$

with $F_{nmp}(i)$ being the inclination function, $G_{npq}(e)$ the eccentricity function and

$$S_{nmpq}(\omega, M, \Omega, \Theta) = \begin{bmatrix} \Delta C_{nm} \\ -\Delta S_{nm} \end{bmatrix}_{(n-m)\text{odd}}^{(n-m)\text{even}} \cos\psi_{nmpq} + \begin{bmatrix} \Delta S_{nm} \\ \Delta C_{nm} \end{bmatrix}_{(n-m)\text{odd}}^{(n-m)\text{even}} \sin\psi_{nmpq}, \tag{3.49c}$$

where,

$$\psi_{nmpq} = (n-2p)\omega + (n-2p+q)M + m(\Omega - \Theta), \tag{3.49d}$$

Θ represents here the angle between the equinox and the Greenwich meridian, known as Greenwich sidereal time GAST (see Sec. 3.1.1), n and m indicate degree and order of the spherical harmonic representation (n must not be confused with the orbital mean motion n indicated before in Eqs. (3.48)). The indices p and q are summation indices. More details on the functions $F_{nmp}(i)$ and $G_{npq}(e)$ can be found in Kaula (1966) (see p. 34 and p. 37).

Due to the difficulty to find an analytical solution of Eqs. (3.48), a linearization is required. This linearized solution is performed firstly by a direct substitution of the disturbing potential R (Eq. (3.49)) in Eqs. (3.48) and secondly by an integration w.r.t. ψ_{nmpq} (not the time t).

The assumption for the integration is (in a sense of a perturbation theory) that the Keplerian elements as well as the Greenwich sidereal time Θ are only linearly time dependent, so $\ddot{\omega} = \ddot{\Omega} = \ddot{M} = \ddot{\Theta} = 0$. According to these conditions, the linear solution of the perturbations of the Keplerian elements can be written for the terms n, m, p and q as

$$\begin{aligned} \Delta a_{nmpq} &= \frac{GMR_e^n}{\mathrm{n}a^{n+2}} \left[2F_{nmp}G_{npq}(n-2p+q)\right] \frac{S_{nmpq}}{\dot{\psi}_{nmpq}}, \\ \Delta e_{nmpq} &= \frac{GMR_e^n}{\mathrm{n}a^{n+3}e} \left[F_{nmp}G_{npq}(1-e^2)^{1/2} \left((1-e^2)^{1/2}(n-2p+q) - (n-2p)\right)\right] \frac{S_{nmpq}}{\dot{\psi}_{nmpq}}, \\ \Delta i_{nmpq} &= \frac{GMR_e^n}{\mathrm{n}a^{n+3}(1-e^2)^{1/2}\sin i} \left[F_{nmp}G_{npq}\left((n-2p)\cos i - m\right)\right] \frac{S_{nmpq}}{\dot{\psi}_{nmpq}}, \\ \Delta\Omega_{nmpq} &= \frac{GMR_e^n}{\mathrm{n}a^{n+3}(1-e^2)^{1/2}\sin i} \left[F'_{nmp}G_{npq}\right] \frac{\bar{S}_{nmpq}}{\dot{\psi}_{nmpq}}, \\ \Delta\omega_{nmpq} &= \frac{GMR_e^n}{\mathrm{n}a^{n+3}} \left[(1-e^2)^{1/2}e^{-1}F_{nmp}G'_{npq} - \cot i(1-e^2)^{-1/2}F'_{nmp}G_{npq}\right] \frac{\bar{S}_{nmpq}}{\dot{\psi}_{nmpq}}, \\ \Delta M_{nmpq} &= \frac{GMR_e^n}{\mathrm{n}a^{n+3}} \left[F_{nmp}\left(-(1-e^2)e^{-1}G'_{npq} + 2(n+1)G_{npq}\right)\right] \frac{\bar{S}_{nmpq}}{\dot{\psi}_{nmpq}}, \end{aligned} \tag{3.50}$$

where,

$$\dot{\psi} = \frac{d\psi}{dt} = (n-2p)\dot{\omega} + (n-2p+q)\dot{M} + m(\dot{\Omega} - \dot{\Theta}), \qquad F'_{nmp} = \partial F/\partial i, \qquad G'_{npq} = \partial G/\partial e, \tag{3.51}$$

and $\bar{S}_{nmpq}$ is the same as shown in Eq. (3.49c) but with permuted cosine and sine functions due to the integration of these functions

$$\bar{S}_{nmpq}(\omega, M, \Omega, \Theta) = \begin{bmatrix} \Delta C_{nm} \\ -\Delta S_{nm} \end{bmatrix}_{(n-m)\text{odd}}^{(n-m)\text{even}} \sin\psi_{nmpq} - \begin{bmatrix} \Delta S_{nm} \\ \Delta C_{nm} \end{bmatrix}_{(n-m)\text{odd}}^{(n-m)\text{even}} \cos\psi_{nmpq}. \tag{3.52}$$

Specific examples of the linear perturbations (Eq. (3.50)), using the inclination function $F_{nmp}(i)$, the eccentricity function $G_{npq}(e)$ and the function $S_{nmpq}(\omega, M, \Omega, \Theta)$ can be found in e.g. Kaula (1966).

3.3.1.1 Perturbations in the Satellite Directions

The satellite observations provide us with the information about the positions and velocity perturbations in the three main satellite directions; the in-track or along-track direction (in the same direction of the satellite's velocity vector), the radial (in the direction along the vector connecting the Earth's geocenter with the satellite) and cross-track one (completing a right-hand coordinate system). Therefore, it is convenient to transform the satellite orbital element variations into the perturbations in these directions.

Visser (1992) introduced the relation between the radial, along-track and cross-track perturbations and the Kepler element perturbations as

$$\begin{aligned} \Delta r &= (\Delta a - a\Delta e\cos M + ae\Delta M\sin M), \\ \Delta l &= a(\Delta\omega + \Delta\Omega\cos i + \Delta M + 2\sin M\Delta e + 2e\cos M\Delta M), \\ \Delta c &= a(\Delta i\sin(\omega + M) - \Delta\Omega\sin i\cos(\omega + M)). \end{aligned} \tag{3.53}$$

These relations between these satellite directions (radial (r), along-track (l) and cross-track (c)) and the orbit perturbations are now derived also by using the functions $F_{nmp}(i)$, $G_{npq}(e)$ and $S_{nmpq}(\omega, M, \Omega, \Theta)$. The solution for the terms with the indices n, m and p reads

$$\Delta r_{nmp} = a\left(\frac{R_e}{a}\right)^n F_{nmp}\left[\frac{2(n-2p)}{\gamma_{nmp}} + \frac{4p-3n-1}{2(\gamma_{nmp}+1)} + \frac{4p-n+1}{2(\gamma_{nmp}-1)}\right] S_{nmp0}, \tag{3.54a}$$

$$\Delta l_{nmp} = a\left(\frac{R_e}{a}\right)^n F_{nmp}\left[\frac{2(n+1)-3(n-2p)\gamma_{nmp}^{-1}}{\gamma_{nmp}} + \frac{4p-3n-1}{\gamma_{nmp}+1} + \frac{n-4p-1}{\gamma_{nmp}-1}\right] \bar{S}_{nmp0}, \tag{3.54b}$$

$$\begin{aligned} \Delta c_{nmp} = a\left(\frac{R_e}{a}\right)^n \frac{1}{2\gamma_{nmp}} \Bigg[&\left(\frac{F_{nmp}}{\sin i}((n-2p)\cos i - m) - F'_{nmp}\right)\bar{S}_{(n+1)mp0} - \\ &- \left(\frac{Fnmp}{\sin i}((n-2p)\cos i - m) + F'_{nmp}\right)\bar{S}_{(n-1)mp0}\Bigg], \end{aligned} \tag{3.54c}$$

where,

$$\gamma_{nmp} = n - 2p - m\frac{\lambda_a - \Omega + \Theta}{\omega + M} = n - 2p - m\frac{1}{\beta}, \tag{3.55}$$

with λ_a the longitude at an ascending node passage and β the number of satellite revolutions per day. It should be mentioned that the perturbations in the satellite directions (Eqs. (3.54a) – (3.54c)) have not been considered in this thesis but have been only pointed out.

3.3.2 Hill's Equations of Satellite Motion

Kepler parameters are less suitable when dealing with circular orbits or orbits with small eccentricities because singularities may occur in the elements Ω, ω and M of Eqs. (3.48d) – (3.48f). In such cases, alternative sets

of orbital parameters are advisable, such as Hill's elements. These corresponding equations were derived by Hill (Hill 1878) and were first applied to describe the lunar motion in a rotating Cartesian triad. They have been applied several times for numerous other purposes. For geodetic purposes, these equations become really simpler and exactly handable when the reference motion is taken as uniform circular. Fig. 3.3 shows the relation of the Hill parameters and the Kepler elements.

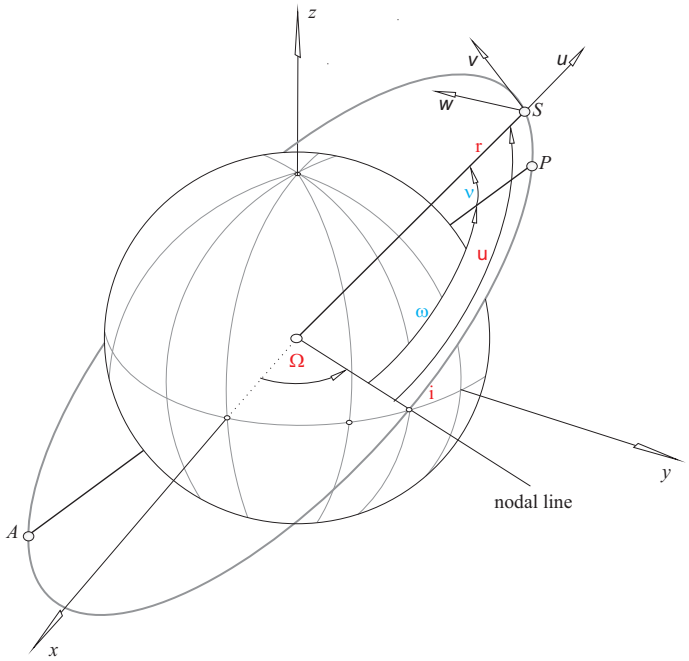

Fig. 3.3: Relation between Kepler orbital parameters and Hill orbital parameters (u, Ω, i, r). The coordinates (u, v, w) represent the Hill coordinates.

The orbital perturbations referred to an orbital frame can be described based on Hill's equations with a harmonic force term (Schaub and Junkins 2003)

$$\begin{aligned} \ddot{\mathrm{u}} - 2\mathrm{n}\dot{\mathrm{v}} \quad -3\mathrm{n}^2\mathrm{u} &= f_\mathrm{u} = \frac{\partial R}{\partial \mathrm{u}}, \\ \ddot{\mathrm{v}} + 2\mathrm{n}\dot{\mathrm{u}} \qquad\quad\ \ &= f_\mathrm{v} = \frac{\partial R}{\partial \mathrm{v}}, \\ \ddot{\mathrm{w}} \qquad\quad +\mathrm{n}^2\mathrm{w} &= f_\mathrm{w} = \frac{\partial R}{\partial \mathrm{w}}. \end{aligned} \tag{3.56}$$

Where n is the mean motion and (u, v, w) are the Hill's elements in the satellite radial, along-track and cross-track directions, respectively (Fig. 3.3). The right hand side terms f_u, f_v and f_w denote the disturbing forces in these three directions and R denotes the perturbing potential. It is noted here that the third equation of (3.56) is uncoupled from the other two, therefore, it can be treated independently. These Hill equations, especially the third w-equation, resemble a mass-spring system oscillating at the natural frequency n (see Schrama 1989, p. 55).

The disturbing forces f_u, f_v and f_w must be known to solve Eq. (3.56). The perturbing potential R can be expressed as a function of the orbit parameters (Eq. (3.49b)). Therefore, the partial derivatives of this potential w.r.t. u, v and w may be translated into partial derivatives w.r.t. the orbital parameters. The

following expressions can be obtained using Eq. (3.54) for circular reference orbits (e= 0) and with a radius r of the satellite orbit approximating the semi-major axis a

$$\begin{aligned}
\Delta \mathrm{u} &= \Delta r, \\
\Delta \mathrm{v} &= \Delta l = r(\Delta(\omega + M) + \Delta\Omega \cos i), \\
\Delta \mathrm{w} &= \Delta c = r(\Delta i \sin(\omega + M) - \Delta\Omega \sin i \cos(\omega + M)).
\end{aligned} \tag{3.57}$$

Similar to Eqs. (3.54a) – (3.54c), a particular solution of the perturbation equations in the radial and along-track is equal to the formulas of Eq. (3.54a) and Eq. (3.54b). But for the perturbations in the cross-track direction, a particular solution of the third part (f_w) of Eq. (3.56) reads (Schrama 1989)

$$\begin{aligned}
\Delta c_{nmp} = \frac{r}{2}\left(\frac{R_e}{r}\right)^n \Bigg[&\frac{1}{\gamma_{nmp}(\gamma_{nmp}+2)}\left(\frac{F_{nmp}}{\sin i}((n-2p)\cos i - m) - F'_{nmp}\right)\bar{S}_{(n+1)mp0} + \\
&+ \frac{1}{\gamma_{nmp}(\gamma_{nmp}-2)}\left(\frac{Fnmp}{\sin i}((n-2p)\cos i - m) + F'_{nmp}\right)\bar{S}_{(n-1)mp0}\Bigg].
\end{aligned} \tag{3.58}$$

It is concluded here, that in general Hill's equations are not solvable, but they can be analytically solved for some special cases to lead to particular solutions. A homogeneous part resembles a force free oscillation of the system (f_u= f_v= f_w= 0). The homogeneous solution is obtained by (f_u, f_v, f_w)= $\vec{0}$. It describes the response of the system to an initial state vector effect, i.e. it represents the orbit perturbations caused by the initial condition errors. For the initial position error (u_0, v_0, w_0) and the initial velocity error ($\dot{\mathrm{u}}_0$, $\dot{\mathrm{v}}_0$, $\dot{\mathrm{w}}_0$) without perturbing forces, the homogeneous solution is given by the following expressions (Schrama 1989, p. 55)

$$\begin{aligned}
\mathrm{u}(t) &= \left(-3\mathrm{u}_0 - \frac{2}{\mathrm{n}}\dot{\mathrm{v}}_0\right)\cos \mathrm{n}t + \frac{\dot{\mathrm{u}}_0}{\mathrm{n}}\sin \mathrm{n}t + \left(4\mathrm{u}_0 + \frac{2}{\mathrm{n}}\dot{\mathrm{v}}_0\right), \\
\mathrm{v}(t) &= \frac{2}{\mathrm{n}}\dot{\mathrm{u}}_0 \cos \mathrm{n}t + \left(6\mathrm{u}_0 + \frac{4}{\mathrm{n}}\dot{\mathrm{v}}_0\right)\sin \mathrm{n}t - (6\mathrm{n}u_0 + 3\dot{\mathrm{v}}_0)t + \left(\mathrm{v}_0 - \frac{2}{\mathrm{n}}\dot{\mathrm{u}}_0\right), \\
\mathrm{w}(t) &= \mathrm{w}_0 \cos \mathrm{n}t + \frac{\dot{\mathrm{w}}_0}{\mathrm{n}}\sin \mathrm{n}t.
\end{aligned} \tag{3.59}$$

Other particular solutions representing the non-resonant solution and the resonant ones are described in Balmino et al. (1996).

4. Temporal Variations of the Gravity Field and Other Effects

The time variations of the Earth's gravitational field are attributed to the environmental and climate related processes that take place at the Earth's surface as well as processes inside the Earth's surface. These time variation elements can be determined from satellite's observations by modeling different force functions that affect the LEO satellite. Gravity field variations from sub-days to several years are classified into two categories; gravitative and non-gravitative forces. The gravitative forces arise from tidal phenomena and mass transport phenomena inside the Earth and on its surface besides the effect of the non-tidal signals of atmospheric and oceanic mass loading. This chapter reviews also the other non-gravitational forces including atmospheric drag, directed Sun radiation pressure and the not directed one (Earth albedo). A short review of the relativistic effects will be introduced but will not be applied in this thesis due to their infinitesimal influence on the LEO satellites. In the following, we shall introduce the relation between the acceleration and the working forces on a satellite.

4.1 Introduction

The second Newton's axiom which describes the relation between the force $\mathbf{F}$ and the impulse $\mathbf{p}$ of a body reads

$$\dot{\mathbf{p}}(t) = \mathbf{F}(t, \mathbf{r}, \dot{\mathbf{r}}). \tag{4.1}$$

The impulse $\mathbf{p}$ is the product of the body mass and its velocity as

$$\mathbf{p}(t) = m(t)\dot{\mathbf{r}}(t). \tag{4.2}$$

After differentiating the impulse and substitution in Eq. (4.1), one obtains

$$m(t)\ddot{\mathbf{r}}(t) + \dot{m}(t)\dot{\mathbf{r}}(t) = \mathbf{F}(t, \mathbf{r}, \dot{\mathbf{r}}). \tag{4.3}$$

By neglecting the impulse change that arises from a mass change, which is very small for a satellite and caused by the fuel consumption, one obtains the so-called Newton-Euler's equation of motion as

$$m(t)\ddot{\mathbf{r}}(t) = \mathbf{F}(t, \mathbf{r}, \dot{\mathbf{r}}). \tag{4.4}$$

If one introduces a specific force function $\mathbf{f}$ referred to a unit mass $\mathbf{f} := \mathbf{F}/m$, Eq. (4.4) simplifies,

$$\ddot{\mathbf{r}}(t) = \mathbf{f}(t, \mathbf{r}, \dot{\mathbf{r}}). \tag{4.5}$$

By considering Eq. (4.5), one finds that $\mathbf{f}$ is composed of a set of force constituents that act on the LEO satellite. For precise orbit determination of the LEO satellite, the total acceleration vector $\mathbf{a}_{total} = \mathbf{F}/m_s$, with m_s the satellite's mass, has to be determined (see Seeber 2003, p.83 and Reigber 1989, p.201) including the components

$$\mathbf{F}/m_s = \mathbf{a}_{total} = \mathbf{a}_C + \mathbf{a}_T + \mathbf{a}_S + \mathbf{a}_M + \mathbf{a}_{ET} + \mathbf{a}_{OT} + \mathbf{a}_{AT} + \mathbf{a}_O + \mathbf{a}_D + \mathbf{a}_{SP} + \mathbf{a}_A + \mathbf{a}_{RE} + \mathbf{a}_{others}, \tag{4.6}$$

where all vectors at the right-hand side model are accelerations caused by:

$\mathbf{a}_C$	:	the Earth as Central force term,
$\mathbf{a}_T$	:	anomalous mass distribution,
$\mathbf{a}_S$	:	the Sun as a third celestial body (direct tide effect by the Sun),
$\mathbf{a}_M$	:	the Moon as a third celestial body (direct tide effect by the Moon),
$\mathbf{a}_{ET}$	:	solid Earth tides,
$\mathbf{a}_{OT}$	:	ocean tides,
$\mathbf{a}_{AT}$	:	atmospheric mass effects,
$\mathbf{a}_O$	:	oceanic mass effects,
$\mathbf{a}_D$	:	atmospheric drag,
$\mathbf{a}_{SP}$	:	solar radiation pressure,
$\mathbf{a}_A$	:	Earth albedo (solar radiation reflected from the Earth's surface),
$\mathbf{a}_{RE}$	:	relativistic effects,
$\mathbf{a}_{others}$	:	other perturbations.

The gravitational influences of these force components are expressed by models. As described in Chapter 3, the dominant part is caused by the gravitation potential function in terms of a spherical harmonic expansion (Eq. (3.29)) (Heiskanen and Moritz (1979)).

The investigation of the time variable gravity variations is the most important goal that we are seeking, especially, those arising from the gravitational forces, e.g. tidal effect, atmospheric and its oceanic reaction and the continental water storage variations. The other non-gravitational forces are of less importance of their interest and will not be treated in this thesis, but will be pointed out.

4.2 Gravitative Forces

4.2.1 Direct Tidal Effects

Gravitational forces of a third body (Sun, Moon, planets) affect the Earth on the one hand and the LEO satellite on the other hand. The resulting force effect acting on the satellite is called direct tidal force. Direct tidal forces influence the motion of the satellite relative to the center of the Earth.

The most significant orbit perturbations arise from the Sun and the Moon. The disturbing acceleration affecting a LEO satellite due to the gravitational attraction from the Sun and the Moon is given by Seeber (2003) as

$$\ddot{\mathbf{r}}_S = Gm_S \left(\frac{\mathbf{r}_S - \mathbf{r}}{||\mathbf{r}_S - \mathbf{r}||^3} - \frac{\mathbf{r}_S}{||\mathbf{r}_S||^3} \right) \qquad ,\ddot{\mathbf{r}}_M = Gm_M \left(\frac{\mathbf{r}_M - \mathbf{r}}{||\mathbf{r}_M - \mathbf{r}||^3} - \frac{\mathbf{r}_M}{||\mathbf{r}_M||^3} \right), \tag{4.7}$$

with m_S and m_M the masses of the Sun and the Moon, respectively. For this tidal fields, it is possible to formulate a potential function which can be expressed in terms of a spherical harmonic expansion referred to the terrestrial reference frame as Eq. (3.29)

$$V_{tide,j}(\lambda, \vartheta, r) = \left[\sum_{n=2}^{n_{max}} \left(\frac{R_e}{r} \right)^n \sum_{m=0}^{n} P_{nm}(\cos\vartheta) \left(c_{nm,j}(\lambda_j, \vartheta_j, r_j) \cos m\lambda + s_{nm,j}(\lambda_j, \vartheta_j, r_j) \sin m\lambda \right) \right], \tag{4.8}$$

where,

$$
\begin{aligned}
c_{nm,j}(\lambda_j, \vartheta_j, r_j) &= \frac{GM_j}{r_j} \frac{1}{2n+1} \left(\frac{R_e}{r_j}\right)^n \cos(m\lambda_j) P_{nm}(\cos\vartheta_j), \\
s_{nm,j}(\lambda_j, \vartheta_j, r_j) &= \frac{GM_j}{r_j} \frac{1}{2n+1} \left(\frac{R_e}{r_j}\right)^n \sin(m\lambda_j) P_{nm}(\cos\vartheta_j),
\end{aligned}
\tag{4.9}
$$

are coefficients that depend on the position $\mathbf{r}_j$ and mass M_j of the third body j. Analogously to Eq. (3.32), the gravitational force of any third body can be derived by applying the Nabla operator (∇),

$$
\mathbf{g}_{tide}(\mathbf{r}, t) = \nabla V_{tide}(\mathbf{r}, t). \tag{4.10}
$$

If the coefficients (Eq. (4.9)) are inserted into the spherical harmonic expansion (Eq. (4.8)) and the spherical harmonic series is limited at the degree $n = 2$, then it holds,

$$
\begin{aligned}
V_{tide,2}(\lambda, \vartheta, r) = GM_j \frac{r^2}{r_j^3} \frac{1}{5} \Big[& \bar{P}_{2,0}(\cos\vartheta) \bar{P}_{2,0}(\cos\vartheta_j) + \\
& + \bar{P}_{2,1}(\cos\vartheta) \bar{P}_{2,1}(\cos\vartheta_j) \cos(\lambda - \lambda_j) + \\
& + \bar{P}_{2,2}(\cos\vartheta) \bar{P}_{2,2}(\cos\vartheta_j) \cos(2(\lambda - \lambda_j)) \Big].
\end{aligned}
\tag{4.11}
$$

The difference $(\lambda - \lambda_j)$ with the time variable longitudinal λ_j of the tide generating body j has a period of approximately one day because of the Earth's rotation. Apart from the Earth's rotation, the movement of the Sun and the Moon are considered also as periodic functions allowing the tidal potential to be expanded into a Fourier-series. Mayer-Gürr (2006) combines the coefficients of Eq. (4.9) from degree $n = 2$ referring to the Sun and the Moon into the complex coefficient h_m with the imaginary unit i (with no real numbers) according to

$$
h_m(t) = \sum_j c_{2mj}(\lambda_j(t), \vartheta_j(t)) - i \cdot s_{2mj}(\lambda_j(t), \vartheta_j(t)), \tag{4.12}
$$

where m describes the order of three different frequency bands ($m = 0, 1, 2$) as represented in the first, middle and last sum of Eq. (4.11), respectively. Eq. (4.11) separates the period of the lunar tidal potential into three terms with periods near 14 days (long period), 24 hours (diurnal), and 12 hours (semi-diurnal). The functions (4.12) can be expanded into a discrete Fourier-series as

$$
h_m(t) = \sum_s H_{ms} e^{i\omega_s t}, \tag{4.13}
$$

with H_{ms} the amplitudes of the corresponding frequencies ω_s. The discrete frequencies are described after Doodson (1921) as a linear combination of six parameters β_i (*Doodson-Elements*) of the movement of the Sun and the Moon represented in a terrestrial reference system

$$
\omega_s t = \sum_{i=1}^{6} n_{is} \beta_i(t), \tag{4.14}
$$

where β_i represents the so-called *Doodson-Elements*:

$\beta_1 = \tau$: local mean lunar time (Period: 1,0351 days),
$\beta_2 = s$: Moon's mean longitude (Period: 27,322 days),
$\beta_3 = h$: Sun's mean longitude (Period: 365,242199 days),
$\beta_4 = p$: mean longitude of Moon's perigee (Period: 8,847 years),
$\beta_5 = N'$: mean longitude of Moon's ascending node (Period: 18,613 years),
$\beta_6 = p_s$: mean longitude of Sun's perigee (Period: 20926 years).

The six multipliers n_{is} for a certain frequency ω_s are usually coded in only one expression called *Doodson number A*

$$A = n_1(n_2 + 5)(n_3 + 5)(n_4 + 5)(n_5 + 5)(n_6 + 5). \tag{4.15}$$

As n_1= 1, 2, 3 and $n_2, \cdots, n_6$ are between -5 and +5, *Doodson* added 5 to $n_{2,\cdots,6}$ to avoid negative numbers. Each tidal constituent, sometimes called a partial tide, has a *Doodson number*. For example, the principal, semi-diurnal lunar tide (M_2) has the number A= 255.555. Because of the very long-term modulation of the tides by the small change in Sun's perigee, the last *Doodson number* n_6 is usually ignored (n_6= 0).

4.2.1.1 Solid Earth Tides

It is well known that the Earth itself as an extended body responds to luni-solar gravitational attraction. As a consequence, the Earth deforms because of a certain degree of elasticity; in case of a perfect rigidity, there would be no Earth tides. The solid Earth tide deformations amount up to 20 cm, and can exceed 30 cm. Solid Earth tides are easily measured only with satellite systems or sensitive gravimeters. This is due to the fact that the solid Earth tide is a very smooth function around the Earth. This phenomenon is a time-variant one and the gravitational potential can be expressed in terms of time dependent geopotential coefficients similar to Eq. (3.29) as

$$V_E(t) = \frac{GM}{R_e} \sum_{n=0}^{n_{max}} \sum_{m=0}^{n} \left(\frac{R_e}{r}\right)^{n+1} P_{nm}(\cos\vartheta) \left(\Delta c_{nm}(t) \cos m\lambda + \Delta s_{nm}(t) \sin m\lambda\right). \tag{4.16}$$

The contributions Δc_{nm} and Δs_{nm} denote the deformation coefficients, describing the elasticity of the Earth's body and they are expressed in terms of the k_{nm} Love number[1]. Changes of the tide generating potential in the normalized geopotential coefficients are given in the time domain by *IERS Conventions (2003)* (McCarthy and Petit 2004, p.59) as

$$\Delta c_{nm} - i\Delta s_{nm} = \frac{k_{nm}}{2n+1} \sum_{j=2}^{3} \frac{GM_j}{GM} \left(\frac{R_e}{r_j}\right)^{n+1} P_{nm}(sin\Phi_j) e^{-im\lambda_j}, \tag{4.17}$$

where,

k_{nm}	:	are nominal Love numbers for degree n and order m,
j	:	is a third body (for Moon j= 2 and for Sun j= 3),
GM	:	are the gravitational constant for the Earth,
GM_j	:	are the gravitational constant for a third body,
r_j	:	is the distance from the geocenter to the Moon or the Sun,
Φ_j	:	is the body fixed geocentric latitude of the Moon or the Sun,
λ_j	:	is the body fixed east longitude (from Greenwich) of the Moon or the Sun.

The parameter values of the solutions of Eq. (4.17) and also their corrections are given by the *IERS Conventions (2003)* (McCarthy and Petit 2004, p.60 and 64) as nominal values of solid Earth tide external potential Love numbers.

4.2.1.2 Ocean Tides

Ocean tides are another time-variable phenomenon occurring in the ocean and causing cyclic variations in local sea level that can exceed 10 meters in some places. The dynamical effects of ocean tides are most easily

[1] Augustus Edward Hough Love (1863-1940) was one of the pioneers of Geodynamics. He introduced these numbers in 1909.

incorporated by periodic variations in the normalized spherical harmonic coefficients (see McCarthy and Petit 2004, p.67). These variations can be written as

$$\Delta C_{nm} - i\Delta S_{nm} = F_{nm} \sum_{s(n,m)} \sum_{+}^{-} (C^{\pm}_{snm} \pm S^{\pm}_{snm}) e^{\pm i\vartheta_f}, \tag{4.18}$$

where,

$$F_{nm} = \frac{4\pi G\rho_\omega}{g_e} \sqrt{\frac{(n+m)!}{(n-m)!(2n+1)(2-\delta_{om})}} \left(\frac{1+k'_n}{2n+1}\right), \tag{4.19}$$

with g_e the mean equatorial gravity (9.780 ms^{-2}), ρ_ω the density of seawater (1025 kg m^{-3}), k'_n load Love numbers (e.g. k'_2= -0.3075, k'_3= -0.195, k'_4= -0.132, k'_5= -0.1032, k'_6= -0.0892) and ϑ_f argument of the tide constituent s (for semi-diurnal, diurnal and long-period tides) with frequency f. The $C^{\pm}_{snm}$ and $S^{\pm}_{snm}$ are coefficients of a spherical harmonic decomposition of the ocean tide height for the ocean tide due to the constituent s of the tide generating potential. The + sign denotes the respective addition of the prograde waves and the - sign for the retrograde waves.

4.2.1.3 Pole Tides

Pole tides are generated due to the centrifugal effect of polar motion. The variation of station coordinates caused by the pole tide can amount up to a couple of centimeters and needs to be taken into account. The centrifugal potential caused by the Earth's rotation corresponding to *IERS Conventions (2003)* is

$$V = \frac{1}{2}[r^2||\vec{\Omega}||^2 - (\vec{r}\cdot\vec{\Omega})^2], \tag{4.20}$$

with

$$\vec{\Omega} = \Omega(m_1\hat{x} + m_2\hat{y} + (1+m_3)\hat{z}),$$

where,

Ω	:	the mean angular velocity of the rotation of the Earth,
m_1, m_2	:	describe the time dependent offset of the instantaneous rotation pole from the mean,
m_3	:	the fractional variation in the rotation rate,
r	:	the geocentric distance to the station,
$\hat{x}$, $\hat{y}$, $\hat{z}$	:	the coordinates referring to a terrestrial system of reference.

Wahr (1985) introduced a first order perturbation in the potential V through m_1 and m_2 terms as

$$\Delta V(r,\vartheta,\lambda) = -\frac{\Omega^2 r^2}{2} \sin 2\vartheta (m_1\cos\lambda + m_2 \sin\lambda). \tag{4.21}$$

The radial displacement S_r and the horizontal displacements S_ϑ and S_λ (positive upwards, south and east respectively in a horizon system at the station) due to ΔV are obtained using the formulation of tidal Love numbers[2](Munk and MacDonald 1960)

$$S_r = h_2\frac{\Delta V}{g}, \qquad S_\vartheta = \frac{l_2}{g}\partial_\vartheta \Delta V, \qquad S_\lambda = \frac{l_2}{g}\frac{1}{\sin\vartheta}\partial_\lambda \Delta V. \tag{4.22}$$

[2]Besides tidal Love number h_n, there are also Shida numbers l_n (Eq. 4.22) that relate for horizontal displacements to the potential.

Using Love number values appropriate to the frequency of the pole tide (h_2= 0.6027, l_2= 0.0836) and r= R_e= 6.378137×10^6m, one finds

$$S_r = -32 \sin 2\vartheta (m_1 \cos\lambda + m_2 \sin\lambda) mm,$$
$$S_\vartheta = -9 \cos 2\vartheta (m_1 \cos\lambda + m_2 \sin\lambda) mm,$$
$$S_\lambda = 9 \cos\vartheta (m_1 \sin\lambda - m_2 \cos\lambda) mm.$$

The deformation which constitutes this tide produces a perturbation in the external potential, which is equivalent to changes in the geopotential coefficients c_{21} and s_{21}. Using the complex love number k_2, the value 0.3077 + 0.0036 for the anelastic Earth appropriate to the polar tide yields (McCarthy and Petit 2004, p.65)

$$\begin{aligned} \Delta c_{21} &= -1,333 \cdot 10^{-9}(m_1 - 0,0115 m_2), \\ \Delta s_{21} &= 1,333 \cdot 10^{-9}(m_2 + 0,0115 m_1), \end{aligned} \tag{4.23}$$

with m_1 and m_2 given in seconds of arc.

4.2.2 Atmosphere and Ocean Mass Effects

Another well known source of the Earth's time-variable gravity field effects after the previously mentioned tidal phenomena are caused by changes of atmospheric and oceanic masses. The high frequency mass variations in the atmosphere have an impact to all gravity measurements. Therefore, the observations of the satellite missions CHAMP, GRACE and GOCE have to be reduced very carefully. The high frequency mass variations in the oceans are much smaller than in the atmosphere, but still have an impact on the satellite's observations.

4.2.2.1 Atmospheric Mass Effects

The atmospheric mass variations have two important effects: firstly, in driving the ocean circulation (e.g. by computing wind stress/velocity and atmospheric air pressure firstly from the atmospheric data analysis), the terrestrial cryosphere and the continental hydrology. Secondly, atmospheric mass variations influence the satellites estimates of geoid and gravity anomalies, and thus, they have to be separated from the total gravity signal before studying mass variations in the oceans and continental hydrology. The variation in the atmospheric mass has different time-variable scales, i.e. short-term (daily) variations and long-term (seasonal) ones. For more precise computations of the gravity field from satellite's observations, the vertical structure of the atmosphere has to be taken into consideration. A vertical integration of the spatial and time-variable atmospheric mass was described and formulated by Flechtner et al. (2006) based on a spherical harmonic expansion,

$$\begin{aligned} c_{nm} &= -\frac{1}{(2n+1)Ma^{n+2}} \int\int_{Earth} \left[\int_{P_S}^{0} \left(\frac{a}{1-\frac{\Phi}{a}} + \xi \right)^{n+4} dP \right] P_{nm}(\cos\vartheta) \cos m\lambda \sin\vartheta d\vartheta d\lambda, \\ s_{nm} &= -\frac{1}{(2n+1)Ma^{n+2}} \int\int_{Earth} \left[\int_{P_S}^{0} \left(\frac{a}{1-\frac{\Phi}{a}} + \xi \right)^{n+4} dP \right] P_{nm}(\cos\vartheta) \sin m\lambda \sin\vartheta d\vartheta d\lambda, \end{aligned} \tag{4.24}$$

where,

a	:	mean Earth radius,
M	:	Earth's mass,
P_S	:	surface pressure,
ξ	:	height of the mean geoid above the mean sphere,
Φ	:	orthometric height.

The elastic deformation of the solid Earth must be taken into account under the variable load via the load Love number k_n for loading of the harmonic degree n. Also for analyzing the gravity variations caused by atmospheric vertical integrated pressure variations, a corresponding mean pressure field $\bar{P}_{VI}$ has to be subtracted from the inner integral of the last formula. This means that the residual data of the pressure field represents the mass variations w.r.t. the mean field. The final formula reads

$$\begin{pmatrix} c_{nm} \\ s_{nm} \end{pmatrix} = -\frac{a^2(1+k_n)}{(2n+1)Mg} \int\int_{Earth} \left[\int_{P_S}^{0} \left(\frac{a}{a-\Phi} + \frac{\xi}{a} \right)^{n+4} dP - \overline{P}_{VI} \right] P_{nm}(\cos\vartheta) \begin{pmatrix} \cos m\lambda \\ \sin m\lambda \end{pmatrix} \sin\vartheta d\vartheta d\lambda, \tag{4.25}$$

with g the mean gravity acceleration. Before this integration can be numerically performed, the orthometric heights Φ for all levels have to be computed. Also the mean geoid above the mean sphere (ξ/a) has to be approximated by the orthometric height at the Earth's surface. The detailed derivation of these formulas and their numerical computations can be found in Flechtner (2007).

4.2.2.2 Oceanic Mass Effects

The high-frequency mass variations in the oceans are much smaller than in the atmosphere, but still have an impact on the determined gravity field solutions from LEO satellites observations. The relations between the mass redistribution of the oceans and the atmosphere, as response of the former due to the forcing of the latter, can be classified into barotropic and baroclinic. An oceanic model of the barotropic kind takes into consideration that the whole water column has the same density and it is forced by wind and pressure only. The barotropic motions are fast with time scales from fractions of a day to weeks. The second baroclinic model includes vertical density changes and their effects. The latter model requires additional forcing such as evaporation minus precipitation or radiation flux to handle thermodynamic effects. Its motions are slow (weeks to centuries). The best example of a barotropic motion are the tides, while El Niño is considered as a baroclinic phenomenon.
Two barotropic models PPHA[3] provided by the Jet Propulsion Laboratory (JPL) and MOG2D[4] which was developed in Toulouse, France, are applied and used for monthly gravity field determinations from satellite observations (e.g. from GRACE mission). The PPHA computes the components of oceanic mass redistribution due to wind stress and atmospheric pressure for the area 65° N and 75° S on a 1.125° grid. This model has a deficiency such as the exclusion of the Arctic Ocean. In this case, it is preferred to use the global 2D finite element model, MOG2D. This latter model gives a high resolution of the coastline. Another baroclinic Ocean Model for Circulation and Tides (OMCT) is provided on a global scale. It allows to take into account the effects arising from loading and self-attraction, atmospheric pressure forcing and continental freshwater fluxes.

4.2.2.3 Atmospheric and Oceanic De-aliasing

Flechtner (2007) combined the atmosphere and ocean fields to get the global residual pressure field used as an input for the spherical harmonic expansion applied for GRACE observations. The output harmonic coefficients are called AOD1B (Atmospheric and Oceanic De-aliasing). This was done firstly by transforming the meteorological input data of the European Center for Medium-range Weather Forecast (ECMWF) from a gaussian grid to a 0.5° grid. Then, the barotropic PPHA ocean model is used to produce 24 hourly, 1.125° gridded files. The later combination represents a vertical integration of the atmosphere at synoptic times 0h, 6h, 12h, 18h for each 0.5 grid point.

The ocean and atmosphere actual and mean fields are combined to get the global residual pressure field, used as input for the calculation of the spherical harmonic series. This is performed in the following way (see Flechtner 2007):

[3]This model is called PPHA because it was developed by Pacanowski, Ponte, Hirose and Ali.
[4]MOG2D was provided by GRGS (Groupe de Recherche de Géodésie Spatiale).

1. Build the difference between the actual 6h barotropic sea level and the mean barotropic sea level which defines the residual barotropic sea level.

2. In case of PPHA, undefined ocean areas (e.g. ocean areas above 65° and -75° latitude) are filled with 0 values.

3. Build the difference between the actual 6h surface or vertical integrated pressure and the atmospheric mean field which defines the residual atmospheric pressure.

4. Over the oceans, the residual barotropic sea level and the residual atmospheric pressure are added.

5. The land and ocean residual pressure values are the input to calculate spherical harmonic series, which are stored in an ASCII file (the AOD1B product).

Besides the 6-hourly atmosphere, ocean and combined mass variations, RL04 (the fifth available release of the AOD1B product after RL00, RL01, RL02 and RL03) also provides the variations in the ocean bottom pressure.

4.2.3 Hydrological Effects

Continental hydrology or continental water storage includes the following constituents of the terrestrial part of the hydrological cycle: open freshwater bodies (e.g., river stretches and active volumes of lakes, ponds, reservoirs and wetlands) active groundwater storage, snow cover, interception storage, soil moisture, climate, agriculture and ecosystem. Lakes and swamps keep 102500 km^3 corresponding to 0,29% of total freshwater on Earth, while rivers keep 1220 km^3 corresponding to 0.006% of total freshwater. The groundwater storage has a volume of about 23,4 Million km^3 of water corresponding to 1,7% of total water on Earth. About 46% are fresh groundwater and 54% are saline groundwater (Gruber 2009). The variations in continental water storage affect the global circulation of both atmosphere (e.g. weather and climate) and oceans of the Earth and hence affect the global Earth's gravity field. Yet observation and understanding of continental water storage in space and time became possible nowadays to be obtained with sufficient accuracy. There are no extensive networks currently existent for monitoring large-scale variations of continental water storage and its individual components. However, the seasonal variations of the hydrological effects are nowadays derivable from satellites' observations (e.g. GRACE mission). These observations enhance the knowledge about the continental water storage variations (a reason for mass changes) and contribute to closing the water balance at different scales in space and time. In addition, the direct measurement of water storage changes for large areas by satellite-based gravity field measurements is very important to validate and improve the predictive capacity of large-scale hydrological models such as the WaterGap Global Hydrology Model (WGHM) (Döll et al. 2003). This model is considered at present as the best estimate of the global-scale long-term average diffuse groundwater recharge (i.e. renewable groundwater resources) that has been calculated with spatial resolution of 0.5° by 0.5° and with daily time steps.

4.3 Non-Gravitative Forces

In addition to the previous mentioned gravitational forces due to the Earth, the Sun, the Moon and the planets, other forces working on the LEO satellite are considered as non-gravitational forces. In spite of their orders of magnitude that are much weaker than the gravity, these non-gravitational forces must be modeled for precise orbit determination. These are briefly discussed in the following sections.

4.3.1 Atmospheric Drag

The most dominant non-gravitational perturbation is resulted from a drag force (i.e. atmospheric resistance). Tapley (1989) indicated the usual form for modeling the drag force as

$$\bar{F}_D = -\frac{1}{2}\rho\left[\frac{C_D A}{m}\right] V_r^2 \bar{u}, \tag{4.26}$$

with ρ the atmospheric density near the satellite, C_D the drag coefficient, A the cross-sectional area of the satellite, m the satellite's mass, V_r the relative velocity of the satellite w.r.t. the atmosphere, $\bar{u}$ the unit vector pointing in the V_r direction. The drag coefficient C_D depends on the geometry of the satellite and Mach number[5]. C_D ranges from 1.5 to 3.0, and is approximated as 2 for a spherical satellite. For more complicated surfaces like a cylinder or a plane, C_D becomes larger (Seeber 2003). The (-) sign denotes that the drag acceleration is in an opposite direction to the satellite movement.

4.3.2 Solar Radiation Pressure and Earth Albedo

A small force is produced by the Sun due to the particle radiation from the Sun to the satellite. The resulting perturbing acceleration is given by Seeber (2003) as

$$\ddot{a}_{SP} = \nu P_S \frac{C_r O}{m}(AU)^2 \frac{\mathbf{r} - \mathbf{r}_S}{||\mathbf{r} - \mathbf{r}_S||^3}, \tag{4.27}$$

with P_S Sun-constant, (AU) the Astronomical Unit (1.5×10^8km), O/m cross-section area of the satellite divided by its mass, C_r factor of reflectivity for the satellite surface, ν shadow function and $\mathbf{r}$, $\mathbf{r}_S$ geocentric position vector of satellite and the Sun in the inertial system, respectively.

Part of solar radiation is reflected by the Earth. The ratio between the reflected radiation and the incoming one is called ***Earth albedo***. As mentioned by Seeber (2003), the albedo part of the radiation pressure for GPS satellites is very small (4×10^{-10}) so the effect is usually neglected. For a near-Earth satellite, the force cannot be neglected and should be taken into consideration.

4.4 Relativistic Effects

For very precise orbit determinations, further perturbations should be taken into account. The individual contributions of these perturbations are usually far below 10^{-8}. One of these perturbations are caused by relativistic effects, if objects such as satellites travel at speeds that are substantial fractions of the speed of light. These effects include time dilation, mass increase, and length contraction. Time dilation would, in principle, allow astronauts to travel vast distances within their own lifetimes. However, relativistic mass increase would make it more and more difficult to continue to accelerate a spacecraft. The factor that determines the amount of mass increase and other relativistic effects is called (γ) given by

$$\gamma = \frac{1}{\sqrt{1 - v^2/c^2}} \tag{4.28}$$

with v the satellite's velocity and c the light's velocity. The relativistic treatment of the LEO satellite orbit determination problem includes corrections to the equations of motion, the time transformations, and the

[5]Mach number is the ratio of the satellite's velocity to the speed of sound.

measurement model. The relativistic correction to the acceleration of an artificial Earth satellite as given by McCarthy and Petit (2004) is

$$\begin{aligned}\Delta\ddot{\mathbf{r}} = &\frac{GM_E}{c^2 r^3}\left[\left(2(\beta+\gamma)\frac{GM_E}{r} - \gamma\dot{\mathbf{r}}\cdot\dot{\mathbf{r}}\right)\mathbf{r} + 2(1+\gamma)(\mathbf{r}\cdot\dot{\mathbf{r}})\dot{\mathbf{r}}\right] \\ &+ (1+\gamma)\frac{GM_E}{c^2 r^3}\left[\frac{3}{r^2}(\mathbf{r}\times\dot{\mathbf{r}})(\mathbf{r}\cdot\mathbf{J}) + (\dot{\mathbf{r}}\times\mathbf{J})\right] \\ &- (1+2\gamma)\frac{GM_S}{c^2 R^3}\dot{\mathbf{R}}\times\mathbf{R}\times\dot{\mathbf{r}},\end{aligned} \tag{4.29}$$

where,

β, γ	:	parameterized post-Newtonian parameters equal to 1 in General Relativity,
c	:	the light's velocity,
r	:	the satellite's distance from the geocenter,
$\mathbf{r}, \dot{\mathbf{r}}$	:	position and velocity vectors of the satellite w.r.t. the Earth,
$\mathbf{R}, \dot{\mathbf{R}}$	:	position and velocity vectors of the Earth w.r.t. the Sun (in the inertial space),
$\mathbf{J}$	:	Earth's angular momentum per unit mass ($\|\mathbf{J}\| = 9.8 \times 10^8 m^2/s$),
GM_E	:	geocentric gravitational constant,
GM_S	:	heliocentric gravitational constant.

5. Recovery of the Earth's Global Gravity Field

To precisely recover the gravitational field of the Earth with its time dependency, the satellites' observations must be related to the unknown gravity field parameters. This can be performed via a functional model which connects the particular satellite observations with the modeling parameters of the gravity field. For the present application, the low-low satellite-to-satellite tracking (ll-SST) between two satellites, the kinematic positions of the satellite and highly precise LOS (line-of-sight) range and range-rate measurements between two satellites are of interest. After establishing this deterministic relation and properly selected stochastic model, the different observation equations at the different observation times are combined yielding a linearized system of equations. In the first part of this chapter, the physical model of the gravity field recovery technique based on Newton-Euler's equation of motion, formulated as a boundary value problem in the form of a Fredholm type integral equation is described. The principal characteristics of using the short arc method of the satellite's orbit is outlined. Subsequently, the stochastic model that relates the observations to the unknown parameters is presented. At the end of this chapter, a detailed description of the Gravity Recovery Object Oriented Programming System (GROOPS) that is applied in the calculations and developed at the Department of Astronomical, Physical and Mathematical Geodesy at the University of Bonn is introduced.

5.1 From Observations to Gravity Field Parameters

In satellite geodesy, satellites are used as high targets, as test bodies following the force function acting on the satellites and as platform carrying scientific sensors to detect various features of the Earth's system. The analysis of accumulated orbit perturbations of the satellites, considered as best masses, enables the derivation of the gravitational potential. This is the classical approach to derive the gravity field of the Earth. Our approach applied for the present investigation will be tailored to the recovery of the gravity field based on the low low satellite-to-satellite tracking technique. The gravity field recovery tailored to two satellites in the low-low mode is based on the Newton-Euler's equation of motion, formulated as a boundary value problem in the form of a Fredholm type integral equation. Schneider (1968) has proposed this idea in 1967 as a general method for orbit determination. After that, this idea has been modified by Schneider and Reigber (1969) for the gravity field determination (investigated in detail by Reigber 1969). Consequently, the idea has been applied by Ilk (1984) to the satellite-to-satellite problem. In the following, this method has been developed and tested, e.g. by Ilk et al. (1995), based on various simulation scenarios. As a first real data application, the method has been applied to the analysis of kinematical short arcs of CHAMP by Mayer-Gürr et al. (2005), in which a series of CHAMP gravity models (ITG-CHAMP01, ITG-CHAMP02, etc.) have been successfully derived. This method has been applied by Mayer-Gürr et al. (2006) and Mayer-Gürr et al. (2007) to the analysis of the relative measurements of the GRACE twin-satellite mission. As a result, a series of high precession GRACE gravity field models (ITG-GRACE01s and ITG-GRACE02s) have been successfully derived. The fundamental properties of this technique is the use of short arcs for regional and global recovery of the Earth's gravity field. For the processing and calculation used in this thesis, satellite-to-satellite tracking data in low low mode as provided by the range and range-rate measurements in the LOS direction between two satellites flying in a formation is used. The *Integral Equation* approach is one possibility among different approaches (e.g. *Energy Integral*, *Acceleration Approach* and *Hammerstein-Schneider Method*). This approach is achieved by formulating a boundary value problem to Newton-Euler's equation of motion in form of an integral equation of Fredholm type for setting up the observation equation as described in detail in Mayer-Gürr (2006). The success of applying the integral equation approach for the analysis of precise inter-satellite distances, as used for the GRACE mission, makes this technique the proper one also for the analysis of the observations of a future SFF missions.

5.1.1 Physical Model for Low-low Satellite-to-Satellite Tracking

In this section, the mathematical formulation is presented as used for the data analysis in this thesis. Firstly, the mathematical-physical model for a single satellite is based on the formulation of Newton-Euler's equation

of motion (Eq. (4.5)). When integrating this equation of motion two times and applying a partial integration, then it reads

$$\mathbf{r}(t) = \mathbf{r}_A + \dot{\mathbf{r}}_A(t - t_A) + \int_{t_A}^{t} (t - t')\mathbf{f}(t')dt', \tag{5.1}$$

with $\mathbf{r}_A$ and $\dot{\mathbf{r}}_A$ the initial position and velocity vectors, respectively. It can be formulated in form of a boundary value problem as

$$\mathbf{r}(\tau) = \mathbf{r}_A(1 - \tau) + \mathbf{r}_B\tau - T^2 \int_0^1 K(\tau, \tau')\mathbf{f}(\tau')d\tau', \tag{5.2}$$

with the boundary values

$$\mathbf{r}_A := \mathbf{r}(t_A), \qquad \mathbf{r}_B := \mathbf{r}(t_B), \qquad t_A < t_B,$$

the normalized time variable

$$\tau = \frac{t - t_A}{T}, \qquad T = t_B - t_A, \qquad t \in [t_A, t_B],$$

and the integral kernel

$$K(\tau, \tau') = \begin{cases} \tau'(1 - \tau) & \text{for } \tau' \leq \tau, \\ \tau(1 - \tau') & \text{for } \tau' > \tau. \end{cases}$$

The functional model, e.g. for range observations, can be derived by projecting the baseline vector onto the LOS direction between two satellites, if the precise inter-satellite range or/and range-rate measurements are available,

$$\rho(\tau) = \mathbf{e}_{12}(\tau) \cdot (\mathbf{r}_2(\tau) - \mathbf{r}_1(\tau)), \tag{5.3}$$

with the unit vector in the LOS direction

$$\mathbf{e}_{12}(\tau) = \frac{\mathbf{r}_{12}(\tau)}{||\mathbf{r}_{12}(\tau)||}, \qquad \mathbf{r}_{12} = \mathbf{r}_2(\tau) - \mathbf{r}_1(\tau). \tag{5.4}$$

The vectors $\mathbf{r}_1(\tau)$ and $\mathbf{r}_2(\tau)$ are the two satellites' positions. The relative vectors between the two satellites (Eq. (5.3)) can also be formulated as a boundary value problem as

$$\mathbf{r}_{12}(\tau) = (1 - \tau)\mathbf{r}_{12,A} + \tau\mathbf{r}_{12,B} - T^2 \int_{\tau'=0}^{1} K(\tau, \tau') \left[\mathbf{e}_{12} \cdot \mathbf{f}_{12} + \frac{\left(\dot{\mathbf{r}}_{12}^2 - \dot{r}_{12}^2\right)}{||\mathbf{r}_{12}||} \right] d\tau'. \tag{5.5}$$

Analogously, the solution of the equation of motion can be derived not only for the inter-satellite ranges but also for the range-rates and range-accelerations through differentiation (see Mayer-Gürr 2006 and Mayer-Gürr et al. 2007). In the following, only inter-satellite ranges between the satellites of a FF mission are used for the gravity field recovery.

5.1.2 Linearized Functional Model for Low-low Satellite-to-Satellite Tracking

The last physical model describes the dependency of the satellite observations from the gravity field and hence a column vector $\bar{\mathbf{x}}$ that represents the number of unknown parameters, which should be estimated with the help of the observations. The observations $\bar{\rho}$ can be linked to the unknown parameters $\bar{\mathbf{x}}$ via a functional model $f(\bar{\mathbf{x}})$ and the additional measurement noise ϵ as

$$\bar{\rho} := f(\bar{\mathbf{x}}) + \epsilon. \tag{5.6}$$

As usual to achieve at a sufficient redundancy, the numbers of unknown parameters shall be considerably smaller than the number of observations. If this model is non-linear, a linearization becomes necessary. In this case, it is advisable to begin with the well-known approximate values (i.e. initial values[1] ($\mathbf{x}_0$)) for the unknown model parameters and to compute their influence on the observations,

$$\rho_0 = f(\mathbf{x}_0). \tag{5.7}$$

This linearization procedure can be accomplished by a Taylor-expansion, truncated after the linear term,

$$\bar{\rho} = \rho_0 + \left.\frac{\partial f(\bar{\mathbf{x}})}{\partial \bar{\mathbf{x}}}\right|_{\mathbf{x}_0} (\bar{\mathbf{x}} - \mathbf{x}_0) + \cdots . \tag{5.8}$$

Then the reduced observations can be calculated as

$$\rho = \bar{\rho} - \rho_0, \tag{5.9}$$

and the unknown parameters are computed according to the reduced observations between the final unknown parameters ($\bar{\mathbf{x}}$) and the initial ones ($\mathbf{x}_0$) as

$$\mathbf{x} = \bar{\mathbf{x}} - \mathbf{x}_0. \tag{5.10}$$

The partial derivatives of the model ($\partial f(\bar{\mathbf{x}})/\partial \bar{\mathbf{x}}$) can be combined in the design matrix $\mathbf{A}$. These partial derivatives are derived by applying the chain rule, firstly, by differentiating the range measurements w.r.t. the positions of the two satellites. Then the positions are differentiated w.r.t. the unknown parameters,

$$\frac{\partial \rho}{\partial \mathbf{x}} = \frac{\partial \rho}{\partial \mathbf{r}_1}\frac{\partial \mathbf{r}_1}{\partial \mathbf{x}} + \frac{\partial \rho}{\partial \mathbf{r}_2}\frac{\partial \mathbf{r}_2}{\partial \mathbf{x}}. \tag{5.11}$$

The first term at the right hand side can be derived by differentiating Eq. (5.3) as

$$\frac{\partial \rho}{\partial \mathbf{r}_1} = -\mathbf{e}_{12}, \qquad \frac{\partial \rho}{\partial \mathbf{r}_2} = \mathbf{e}_{12}. \tag{5.12}$$

The second part is split into two linearized relationships, the positions are differentiated w.r.t. the force function $\mathbf{f}$ and, finally, the force function w.r.t. the unknown parameters as

$$\frac{\partial \mathbf{r}_1}{\partial \mathbf{x}} = \frac{\partial \mathbf{r}_1}{\partial \mathbf{f}}\frac{\partial \mathbf{f}}{\partial \mathbf{x}}, \qquad \frac{\partial \mathbf{r}_2}{\partial \mathbf{x}} = \frac{\partial \mathbf{r}_2}{\partial \mathbf{f}}\frac{\partial \mathbf{f}}{\partial \mathbf{x}}. \tag{5.13}$$

The first terms at the right hand side of both equations can be derived by differentiating Eq. (5.2). The specific force function along the satellite orbits in the last term can be separated into three parts,

$$\mathbf{f}(t; \mathbf{r}, \dot{\mathbf{r}}; \mathbf{x}) = \mathbf{f}_d(t; \mathbf{r}, \dot{\mathbf{r}}) + \nabla V(t; \mathbf{r}; \mathbf{x}_0) + \nabla T(t; \mathbf{r}; \Delta\mathbf{x}), \tag{5.14}$$

where $\mathbf{f}_d$ is the disturbance part that represents the non-conservative disturbing forces, ∇V the reference part, which represents the long wavelength gravity field features $\mathbf{x}_0$ as formulated previously in terms of spherical harmonics expansion as

$$V = \frac{GM}{R_e}\left[\sum_{n=0}^{n_{max}}\sum_{m=0}^{n}\left(\frac{R_e}{r}\right)^{n+1}\left(c_{nm}C_{nm}(\lambda,\vartheta) + s_{nm}S_{nm}(\lambda,\vartheta)\right)\right], \tag{5.15}$$

and ∇T the anomalous part, which models the short wavelength refinements $\Delta\mathbf{x}$ to the parameters $\mathbf{x}_0$ of the global gravity field as referred to Eq. (3.41). The last term of Eq. (5.13) can then be derived from Eq. (5.14) with Eq. (5.15).

Finally, if all observation equations for one short arc of the satellite orbits are collected, a linear system of equations can be represented in a Gauss-Markov model in matrix form as

$$\mathbf{l} = \mathbf{A}\mathbf{x} + \epsilon, \qquad \text{with} \qquad \mathcal{C}(\epsilon) = \sigma^2\mathbf{P}^{-1}, \tag{5.16}$$

[1] Therefore, one needs a reference gravity model in the gravity field estimation process to start with these values.

with $\mathbf{l}$ the range observations and $\mathbf{x}$ the unknown parameters which are written as follow

$$\mathbf{l} = \begin{pmatrix} \rho(\tau_1) - \rho_0(\tau_1) \\ \rho(\tau_2) - \rho_0(\tau_2) \\ \vdots \\ \rho(\tau_N) - \rho_0(\tau_N) \end{pmatrix}, \qquad \mathbf{x} = \begin{pmatrix} c_{2,0} \\ c_{2,1} \\ \vdots \\ s_{n_{max},m} \end{pmatrix}, \tag{5.17}$$

where ϵ is the error vector, $\mathcal{C}(\epsilon)$ is its corresponding covariance matrix, σ^2 stands for the unknown variance factor for each satellite arc and $\mathbf{P}$ represents the weight matrix of the observations. The design matrix $\mathbf{A}$ is composed of the partial differentials as given in Eq. (5.11) and Eq. (5.13),

$$\mathbf{A} = \frac{\partial \rho}{\partial \mathbf{r}} \frac{\partial \mathbf{r}}{\partial \mathbf{f}} \frac{\partial \mathbf{f}}{\partial \mathbf{x}}. \tag{5.18}$$

5.1.3 Stochastic Model

As described for the calculations of the gravity field model ITG-GRACE02s (Mayer-Gürr et al. 2007), the reduced ranges between the twin satellites are strongly correlated: the same holds for the range-rates and the range accelerations. Therefore, an adapted stochastic model has to be introduced by a variance-covariance matrix

$$\mathcal{C}(\mathbf{l}) = \sigma^2 \mathbf{P}^{-1}, \tag{5.19}$$

The consideration of this variance-covariance matrix acts as a decorrelation of the observations and the decorrelated adjusted residuals should show white noise. The derivation of a realistic variance-covariance matrix is very important to achieve a correct decorrelation. Then one can claim that the solution is optimal in the statistical sense and it is not necessary to introduce calibration parameters for the inter-satellite measurements. The formal errors of the adjustment results should not require any calibration. The variance-covariance matrix is composed of two parts

$$\mathcal{C}(\mathbf{l}_{range}) = \sigma_P^2 \mathbf{F}_{range} \mathcal{C}(\mathbf{p}) \mathbf{F}_{range}^T + \sigma_a^2 \mathbf{F}_{Acc} \mathcal{C}(\mathbf{a}) \mathbf{F}_{Acc}^T. \tag{5.20}$$

The first part at the right hand side describes the noise of the range measurements, while the second one describes the noise of the accelerometer measurements. The matrix $\mathbf{F}_{range}$ represents the filtering of the phase observations and the matrix $\mathbf{F}_{Acc}$ represents the corresponding filtering matrix for the accelerometer measurements. For more details about the filtering matrices and the stochastic model please refer to Mayer-Gürr (2006).

5.1.4 Least squares Solution based on a Gauss-Markov Model

In general, the set of residuals ϵ contains measurement errors. One can introduce a standard Gauss-Markov model (Eq. (5.16)) based on the assumption that these measurement errors have an expectation $\mathcal{E}(\epsilon)$ of zero and the variance-covariance matrix of the observations $\mathcal{C}(\epsilon)$ is a-priori known,

$$\mathcal{E}(\epsilon) = \mathbf{0} \qquad \text{and} \qquad \mathcal{C}(\epsilon) = \mathcal{C}(\mathbf{l}) = \sigma^2 \mathbf{P}^{-1}. \tag{5.21}$$

The optimal solution of the unknown parameters $\mathbf{x}$ of Eq. (5.16) can be obtained by a least squares adjustment, leading to the following system of normal equations,

$$\mathbf{N}\mathbf{x} = \mathbf{n} \qquad \text{with} \quad \mathbf{N} = \mathbf{A}^T\mathbf{P}\mathbf{A} \quad \text{and} \quad \mathbf{n} = \mathbf{A}^T\mathbf{P}\mathbf{l}. \tag{5.22}$$

The solution of the normal equations yields the estimation of the unknown parameters as

$$\mathbf{x} = \mathbf{n}\mathbf{N}^{-1} = \mathbf{A}^T\mathbf{P}\mathbf{l}(\mathbf{A}^T\mathbf{P}\mathbf{A})^{-1}. \tag{5.23}$$

The variance-covariance matrix of the unknown parameters can be derived similar to Eq. (5.21) as

$$\mathcal{C}(\mathbf{x}) = \sigma^2 \mathbf{N}^{-1}. \tag{5.24}$$

5.1.5 Accumulation of the Observation Equations

For each orbit arc, the observation equations are established individually giving an observation vector and a design matrix as

$$\mathbf{l} = \begin{pmatrix} \mathbf{l}_1 \\ \mathbf{l}_2 \\ \vdots \\ \mathbf{l}_m \end{pmatrix} \qquad \text{and} \qquad \mathbf{A} = \begin{pmatrix} \mathbf{A}_1 \\ \mathbf{A}_2 \\ \vdots \\ \mathbf{A}_m \end{pmatrix}. \tag{5.25}$$

It is impossible in many cases to set up the design matrix $\mathbf{A}_{n\times m}$ completely in the memory of a computer, with millions of positions and thousands of unknown gravity parameters. Fortunately, this is not required. The normal set of equations can be directly accumulated from the individual blocks as

$$\mathbf{N} = \sum_{i=1}^{m} \mathbf{A}_i^T \mathbf{P}_i \mathbf{A}_i \qquad \text{and} \qquad \mathbf{n} = \sum_{i=1}^{m} \mathbf{A}_i^T \mathbf{P}_i \mathbf{l}_i. \tag{5.26}$$

This is possible because the observations of different blocks are not correlated, so that the weight matrix is block diagonal

$$\mathbf{P} = \begin{pmatrix} \mathbf{P}_1 & \mathbf{0} & \cdots & \mathbf{0} \\ \mathbf{0} & \mathbf{P}_2 & \cdots & \mathbf{0} \\ \vdots & \vdots & \ddots & \vdots \\ \mathbf{0} & \mathbf{0} & \cdots & \mathbf{P}_m \end{pmatrix}. \tag{5.27}$$

Then a block of the design matrix $\mathbf{A}_i$ is set up. The product $\mathbf{A}_i^T \mathbf{P}_i \mathbf{A}_i$ is added to the normal equation matrix and the product $\mathbf{A}_i^T \mathbf{P}_i \mathbf{l}_i$ is added to the right side and, finally, the memory for the block of the design matrix is controlled. The computation can be significantly accelerated in case of using computer clusters and parallel computing. A part of the blocks of the design matrix is set up on any computer and accumulated to a subtotal. At the end the subtotals must be sent and added to the master-computers. For equation systems with many unknown parameters, the formation of the product matrices $\mathbf{A}^T\mathbf{PA}$ is the costly computation step and requires much memory space. The set-up of the design matrices $\mathbf{A}$ is much less computing intensive. For effective successfully calculations, the product $\mathbf{q} = \mathbf{A}^T\mathbf{PAp} = \mathbf{Np}$ has to be estimated, so $\mathbf{s} = \mathbf{Ap}$ is formed, then $\mathbf{t} = \mathbf{Ps}$ and finally, $\mathbf{q} = \mathbf{A}^T\mathbf{t}$ is expressed as

$$\mathbf{q} = \sum_{i=1}^{m} \mathbf{A}_i^T [\mathbf{P}_i (\mathbf{A}_i \mathbf{p})]. \tag{5.28}$$

5.2 Gravity Recovery Object Oriented Programming System (GROOPS)

This section describes the procedures used for the numerical simulations of the gravity field recovery using the utilized **G**ravity field **R**ecovery **O**bject **O**riented **P**rogramming **S**ystem (GROOPS). It has been developed and implemented at the Department of Astronomical, Physical and Mathematical Geodesy (APMG), Institute of Geodesy and Geoinformation (IGG) at the University of Bonn. It summarizes all the concepts and calculation procedures applied within this thesis including two major parts, generating simulated observations and processing them for gravity field estimation. These two parts use different models, one is a pseudo-real model for generating the measurements, and the other one is a linearized functional model for processing the observations. The software GROOPS is implemented in C++ language and features an object-oriented design implying a completely modularized structure. It consists of various modules allowing the combination of different types of observations (precise satellite orbits, satellite-to-satellite tracking, gradiometry, altimetry, airborne and terrestrial data) with different types of gravity field representations (global modeling by spherical harmonics and regional parameterization by space localizing basis functions) in a very flexible way. The actual status of GROOPS can be characterized as follows:

- Gravity field recovery based on kinematically precisely determined orbits (KPOD) of low flying satellites,
- Gravity field recovery based on precise inter-satellite observations, such as distances, relative velocities and relative accelerations (low-low SST data),
- Gravity field recovery based on gravity field functionals such as gravitational tensor components,
- Regional gravity field solutions represented by space-localizing base functions (spherical splines),
- Directly derived global gravity field solutions represented by base functions with global support,
- Global gravity field solutions by merging regional focusing patches and represented either by base functions with global or local support,
- Static and temporal gravity field models,
- Use of real data or data based on simulation scenarios.

With GROOPS, various gravity field models (static and temporal ones) have been derived in the course of the years. Based on the analysis of precise kinematical orbits of the satellite CHAMP, static gravity field models ITG-CHAMP01E, K, S (Mayer-Gürr et al. 2005) have been derived using observations from 03.2002 to 02.2003, up to a spherical harmonic degree 75. After that, static gravity field models based on three different regularization models: ITG-CHAMP02E, K, S using observations from 03.2002 to 02.2004, up to a spherical harmonic degree 90, have been derived. Based on the analysis of high-precise range and range-rate K-band measurements of GRACE, four different gravity field models have been determined. A static (non-regularized) gravity field model ITG-GRACE01S has been derived using observations from 07.2003 to 06.2004, up to a spherical harmonic degree 160, together with temporal gravity field models (temporal variations modeled by spline functions, up to a spherical harmonics degree 30). Then a static (non-regularized) gravity field model ITG-GRACE02S has been estimated using observations from 01.2003 to 12.2005, up to a spherical harmonic degree 160, together with temporal gravity field models (temporal variations modeled by spline functions, up to a spherical harmonic degree 40). A static (non-regularized) gravity field model ITG-GRACE03s (which is used in this study as a reference model) has been calculated using observations from 08.2003 to 04.2007, up to a spherical harmonic degree 180, together with temporal gravity field models (temporal variations modeled by spline functions), up to a spherical harmonics degree 40 and complete variance-covariance matrix available for this model as well. The last static gravity field model ITG-GRACE-SPLINE03 has been derived using observations from 08.2003 to 04.2007, up to a spherical harmonic degree 180, but no temporal variations has been modeled. In the following sections, only the implemented parts of the software system that are directly used in the calculation of static and temporal global gravity field solutions are reviewed.

5.2.1 Observation Simulations

5.2.1.1 Observation Generating Steps

The simulation procedure starts with generating the simulated observations for each satellite at specific time instants with a sufficient sampling rate, orbit data (positions, velocities and accelerations) and SST observables (range, range-rate and range acceleration). These measurements are simulated using a precise gravity field model ITG-GRACE03s (considered as the true field). In addition to the satellite measurements, the disturbing forces acting on each spacecraft have to be considered. A short summary of the different disturbing forces (as formerly discussed in Chapter 4) and the applied models is given in Section 5.2.2. GROOPS has the option to either directly include these models at the generating steps (at the satellite's positions) or alternatively they can be calculated afterwards at the processing step. A tailored noise model implemented for each of the observation types allows to create simulation scenarios that are as realistic as possible. The simulation procedure covers the generation of the accelerometer measurements that represent the non-gravimetric forces and also the star cameras measurements that are responsible of the satellite's rotation in the inertial frame. Fig. 5.1 explains the procedure steps for the simulation scenarios. In the following, each step with its mathematical background will be individually described.

5.2.1.1.1 Orbit Integration

Satellite orbits can be integrated either analytically or numerically. The analytical methods, which are also called general perturbation methods, are suffering from some disadvantages such as the complexity of algebraic expressions when dealing with the perturbation forces acting on LEO satellites and the deficiency of modeling these perturbations with analytical expressions. Moreover, singularities of orbital elements such as eccentricity and inclination appear in case of circular orbits or equatorial orbits (see Seeber 2003, p. 116). The numerical methods which are also called special perturbation methods are characterized by its simplicity when compared with the analytical ones for orbit determination. This is the reason that the latter techniques are applied in most of the applications. The main task for determining an orbit is to calculate the satellite state (position and velocity vectors) for the desired epoch. The basic idea for doing this is to solve the equation of motion including all perturbations for a step-wise integration (Seeber 2003)

$$\ddot{\mathbf{r}} = -\frac{GM}{r^3}\mathbf{r} + \mathbf{R}, \tag{5.29}$$

with $\mathbf{r}$ and $\ddot{\mathbf{r}}$ the inertial position and acceleration vectors and $\mathbf{R}$ vector of the perturbation forces per unit mass acting on the satellite.

In celestial mechanics, many numerical orbit determination methods besides the well-known methods, *method of Encke* (1857) and *method of Cowell* (1910) (see Seeber 2003) have been developed. They are categorized depending on the applied algorithms into *single-step* and *multi-step* integrators that are depending on the number of points that are used by proceeding to the next point. Both integrators may either have a *fixed* or a *variable* step size. When *multi-step* integrators are carried out, they are then grouped into *summed* and *non-summed* forms, which refers to whether the integration is performed from epoch or step-by-step. Finally, both *single-step* and *multi-step* integrators can be performed either as single-integration integrators, or double integration integrators.

These integrators (*single-step* and *multi-step*) require an orbit propagator which gives the satellite's state at some time before or after an epoch state. This integration is done by fitting a proper polynomial to a limited series of successive points in order to generate an additional point through this polynomial based on the equation of motion (5.29). The most widely used methods of type *single-step* are *Euler* and *Runge-Kutta* methods, while frequently used methods of type *multi-step* integrators are e.g. *Adams*, *Summed Adams*, *Shampine-Gordon*, *Störmer-Cowell* and *Gauss-Jackson* methods. Detailed explanations of all these methods are given e.g. in Berry (2004).

In the following, we will introduce the most common applied integrators used within GROOPS, the *Runge-Kutta method*, which is a family of *single-step* integrators that forward integrate to the next point $\mathbf{P}_{i+1}$ using only a priori information (i.e. from a previous point $\mathbf{P}_i$). They have the general form

$$\mathbf{P}_{i+1} = \mathbf{P}_i + h\boldsymbol{\alpha}, \tag{5.30}$$

with $\boldsymbol{\alpha}$ having a form of a linear function of weighted slope estimates over the interval $h = t_{i+1} - t_i$ as

$$\boldsymbol{\alpha} = \sum_{j=1}^{m} a_j \mathbf{k}_j, \tag{5.31}$$

where $\mathbf{k}_j$ are slope estimates found by evaluation of $\mathbf{f}(t, \mathbf{P})$ (where $\mathbf{f}(t, \mathbf{P}) = d\mathbf{P}/dt$), m is the number of estimates and a_j represent the weighting constants.

The ***tenth order Runge-Kutta method*** has been applied to the integrated orbits of all simulation scenarios in this study as it leads to a better approximation and accuracy. It reads (Xu 2007)

$$\mathbf{P}_{i+1} = \mathbf{P}_i + \frac{1}{840}\left(41\mathbf{k}_1 + 27\mathbf{k}_4 + 272\mathbf{k}_5 + 27\mathbf{k}_6 + 216\mathbf{k}_7 + 216\mathbf{k}_9 + 41\mathbf{k}_{10}\right), \tag{5.32}$$

where the ten slope estimates $\mathbf{k}_1, \cdots, \mathbf{k}_{10}$ are indicated as

$$
\begin{aligned}
\mathbf{k}_1 &= h\mathbf{f}\left(t_i, \mathbf{P}_i\right), \quad \mathbf{P}_i = \mathbf{P}(t_i), \\
\mathbf{k}_2 &= h\mathbf{f}\left(t_i + \frac{4}{27}h, \mathbf{P}_i + \frac{4}{27}\mathbf{k}_1\right), \\
\mathbf{k}_3 &= h\mathbf{f}\left(t_i + \frac{2}{9}h, \mathbf{P}_i + \frac{1}{18}\mathbf{k}_1 + \frac{1}{6}\mathbf{k}_2\right), \\
\mathbf{k}_4 &= h\mathbf{f}\left(t_i + \frac{1}{3}h, \mathbf{P}_i + \frac{1}{12}\mathbf{k}_1 + \frac{1}{4}\mathbf{k}_3\right), \\
\mathbf{k}_5 &= h\mathbf{f}\left(t_i + \frac{1}{2}h, \mathbf{P}_i + \frac{1}{8}\mathbf{k}_1 + \frac{3}{8}\mathbf{k}_4\right), \\
\mathbf{k}_6 &= h\mathbf{f}\left(t_i + \frac{2}{3}h, \mathbf{P}_i + \frac{1}{54}(13\mathbf{k}_1 - 27\mathbf{k}_3 + 42\mathbf{k}_4 + 8\mathbf{k}_3)\right), \\
\mathbf{k}_7 &= h\mathbf{f}\left(t_i + \frac{1}{6}h, \mathbf{P}_i + \frac{1}{4320}(389\mathbf{k}_1 - 54\mathbf{k}_3 + 966\mathbf{k}_4 - 824\mathbf{k}_5 + 243\mathbf{k}_6)\right), \\
\mathbf{k}_8 &= h\mathbf{f}\left(t_i + h, \mathbf{P}_i + \frac{1}{20}(-231\mathbf{k}_1 + 81\mathbf{k}_3 - 1164\mathbf{k}_4 + 656\mathbf{k}_5 - 122\mathbf{k}_6 + 800\mathbf{k}_7)\right), \\
\mathbf{k}_9 &= h\mathbf{f}\left(t_i + \frac{5}{6}h, \mathbf{P}_i + \frac{1}{288}(-127\mathbf{k}_1 + 18\mathbf{k}_3 - 678\mathbf{k}_4 + 456\mathbf{k}_5 - 9\mathbf{k}_6 + 576\mathbf{k}_7 + 4\mathbf{k}_8)\right), \\
\mathbf{k}_{10} &= h\mathbf{f}\left(t_i + h, \mathbf{P}_i + \frac{1}{820}(1481\mathbf{k}_1 - 81\mathbf{k}_3 + 7104\mathbf{k}_4 - 3376\mathbf{k}_5 + 72\mathbf{k}_6 - 5040\mathbf{k}_7 - 60\mathbf{k}_8 + 720\mathbf{k}_9)\right).
\end{aligned}
\tag{5.33}
$$

As mentioned before that GROOPS has the property to implement a tailored noise model for imitating the realistic state. In this way, the generated satellite orbits were contaminated in all scenarios with an error level of 2 cm, which corresponds to the errors in a precise orbit determination (POD) that range from 2 cm to 5 cm.

5.2.1.1.2 Inter-Satellite Observations

For the recovery of the Earth's gravity field, the satellite-to-satellite tracking observations in the low low mode between the LEO satellites have to be calculated. The benefits of these inter-satellite measurements including the inter-satellite range, range-rate and range acceleration are their pronounced sensitivity to the satellite's perturbing forces, including conservative forces and non-conservative ones. For instance, a non-conservative force error of $3{\times}10^{-10}\mathrm{m/s}^2$ (on board accelerometer error accuracy in case of GRACE) can cause centimeter level inter-satellite range error. However, the corresponding inter-satellite range-rate is comparably less sensitive to the perturbing forces to mm/s or sub-mm/s level error. For this reason, it is less useful to improve the gravity field due to only enhanced range-rate measurements, and therefore, it is helpful to use the range observations for recovering the gravity field. In our investigation, we will show how the gravity field can be improved by increasing the distance between the two LEO satellites (see Chapter 6). Decreasing the range error level from the microwave ranging system to that of laser interferometer level plays also an important role for significantly improving the global gravity field solutions. The satellite range in LOS direction can be numerically calculated according to the simple form of Eq. (5.3) as

$$
\rho = ||\mathbf{r}_2 - \mathbf{r}_1|| = \mathbf{e}_{12} \cdot \mathbf{r}_{12} = \sqrt{x_{12}^2 + y_{12}^2 + z_{12}^2}, \tag{5.34}
$$

with $\mathbf{r}_1$ and $\mathbf{r}_2$ the two satellites position vectors. The satellite's range-rate with the two satellite velocity vectors is then calculated by the formula

$$
\dot{\rho} = \mathbf{e}_{12} \cdot \dot{\mathbf{r}}_{12} = \frac{1}{\rho}\left(x_{12}\dot{x}_{12} + y_{12}\dot{y}_{12} + z_{12}\dot{z}_{12}\right), \tag{5.35}
$$

correspondingly the range acceleration reads

$$\begin{aligned}\ddot{\rho} &= \mathbf{e}_{12} \cdot \ddot{\mathbf{r}}_{12} + \frac{1}{\rho}\left(\dot{\mathbf{r}}_{12}^2 - \dot{\rho}^2\right) = \\ &= \frac{1}{\rho}\left(x_{12}\ddot{x}_{12} + y_{12}\ddot{y}_{12} + z_{12}\ddot{z}_{12}\right) + \frac{1}{\rho}\left[\left(\dot{x}_{12}^2 + \dot{y}_{12}^2 + \dot{z}_{12}^2\right) - \dot{\rho}^2\right].\end{aligned} \tag{5.36}$$

5.2.1.1.3 Accelerometer Data

As indicated in the last section, the gravity signal is attenuated with increasing altitude. For this reason, the satellite orbits for investigating the gravity field must be as low as possible. The atmosphere at these low altitudes considerably influences the satellite orbital motion, where the non-conservative forces take place (see Chapter 4). In order to isolate the gravitational signals from the non-gravitational ones, these forces have to be measured and compensated. A powerful technological progress of extreme relevance to gravity field determination from satellite missions is the use of accelerometer. The accelerometer measurement depicts the sum of the non-gravitational accelerations including the atmospheric-drag, direct solar radiation and the indirect one (Earth albedo) and is contaminated by biases, random noise and unknown scale factors in addition. A simple measurement model as introduced by Kim (2000)

$$\mathbf{f}^{obs} = \mathbf{M}\mathbf{f}^{acc} + \mathbf{B} + \mathbf{N}, \tag{5.37}$$

with

$\mathbf{f}^{obs}$	:	vectorial accelerometer measurements,
$\mathbf{f}^{acc}$	:	vector of the sum of the true non-gravitational accelerations (in accelerometer coordinates),
$\mathbf{M}$	:	scale factor matrix,
$\mathbf{B}$	:	bias vector,
$\mathbf{N}$	:	random noise vector.

The scale factor matrix $\mathbf{M}$ is a matrix of nine elements with only diagonal elements different from zero. The bias $\mathbf{B}$ differs from the random noise in a such way that it has constant values while the random noise has a frequency dependent characteristic. It should be mentioned here that the accuracy of the scale factors and the bias estimates are more important than their size. The accelerometer measurements $\mathbf{f}^{acc}$ and $\mathbf{f}^{obs}$ refer to the accelerometer coordinate frame and hence some coordinate transformations are essential for expressing these measurements in the inertial coordinate system.

In the simulation process, firstly the non-gravitational accelerations are computed along the integrated satellites' trajectories by a transformation matrix using the applied true models referring to the inertial frame

$$\mathbf{f}^S = R_{I\to S}\mathbf{f}^I, \tag{5.38}$$

with $\mathbf{f}^S$ and $\mathbf{f}^I$ the accelerations given in the satellite and inertial coordinate systems, respectively and $R_{I\to S}$ the rotation matrix from the inertial to the satellite coordinate frame. Subsequently, the satellite coordinates are multiplied by a small angle rotation matrix to transform them into the accelerometer coordinate frame

$$\mathbf{f}^{acc} = R_{S\to A}\mathbf{f}^S, \tag{5.39}$$

where $R_{S\to A}$ the rotation matrix from the satellite coordinate frame to the accelerometer coordinates. The accelerometer coordinates are finally multiplied by the scale factor $\mathbf{M}$, then the biases and the random noise are added to get the accelerometer output $\mathbf{f}^{obs}$ (Eq. (5.37)). More details of all these transformations are given in Kim (2000). We have to mention here that a white noise of $3 \times 10^{-10} ms^{-2}$, which is as same as the twin satellites of GRACE mission error level, has been applied in order to generate noisy accelerometer measurements.

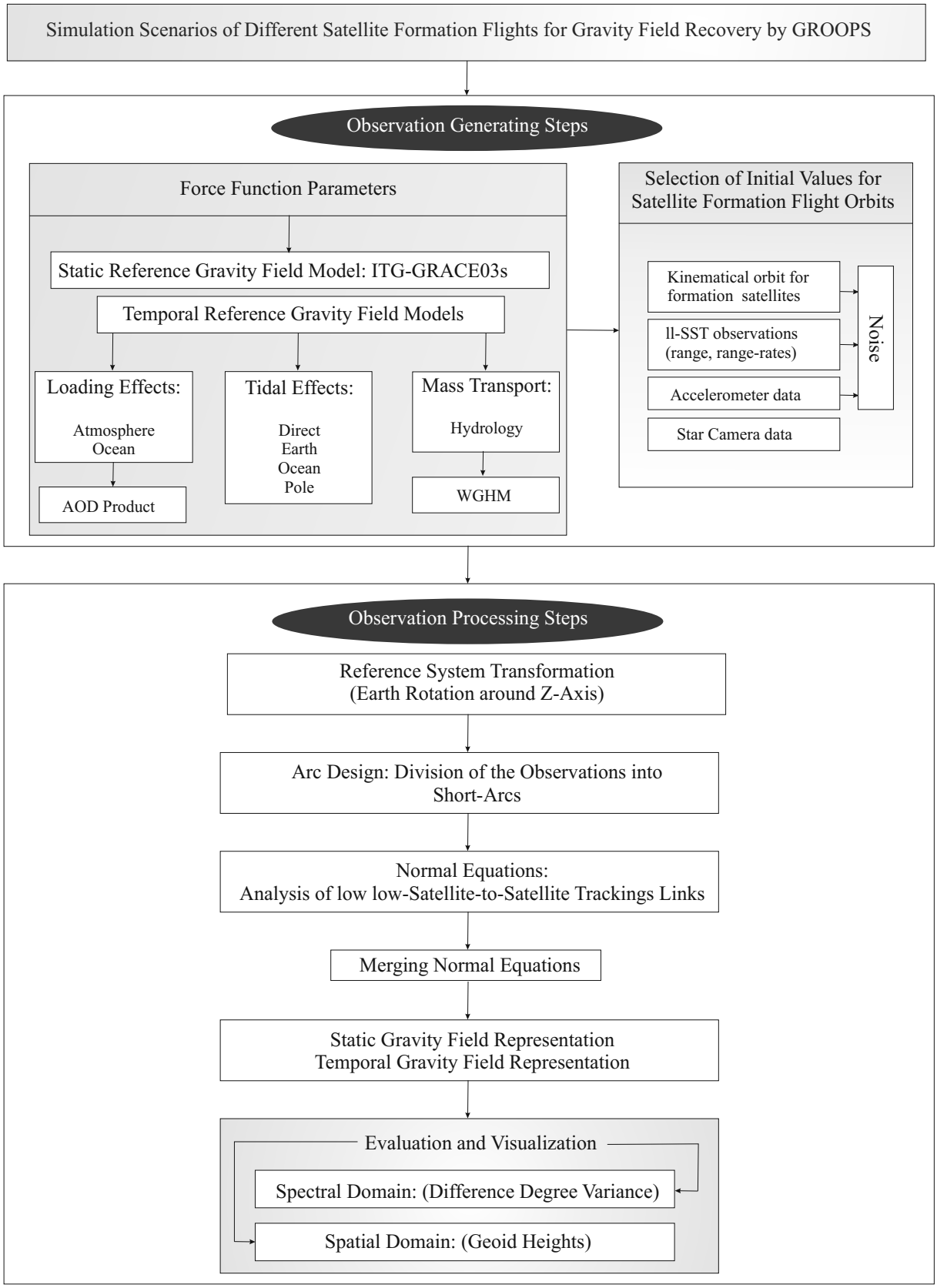

Fig. 5.1: Flowchart describing the procedures of the simulation scenarios by GROOPS.

5.2.1.1.4 Star Camera Data

Another error source already mentioned is caused by the uncertainty between the satellite coordinate system and the inertial coordinate system. This is related to the accuracy of the attitude determination but it should be pointed out that this is different from the satellite's attitude control. The attitude control of the satellite uses different satellite sensors such as cold-gas thruster systems with magneto-torques in addition to the star cameras for a fine correction of the satellite position (see Feucht et al. 2003 for more details). The star cameras are used for a precise determination of the satellites' orientation by tracking them relative to the position of the stars. This determination includes a computation of a rotation matrix between these two coordinate systems (satellites and inertial ones) to accurately adjust the satellite attitude in the inertial space as indicated by Eq. (5.38).

5.2.1.2 Observations Processing Steps

5.2.1.2.1 Short Arc Approach

The main focus of this study is the use of the short arc approach of the different investigated SFFs tailored especially to the recovery of the Earth's global gravity field solutions. This method has been developed at the APMG Department, Institute of Geodesy and Geoinformation of the University of Bonn. In simple words, a short arc means a portion of a satellite orbit significantly less than one revolution. This new analysis technique has same advantages when compared to the gravity field determination from satellite orbits over a long period of time. This is because of the fact that the division of the satellite orbit into short pieces reduces the accumulated effects of the perturbing forces. Moreover, the short arc approach uses the positions and the range measurements as observations directly allowing data gaps and data interruptions to be handled by starting a new arc after the occurrence of a data gap.

As discussed in Section 5.2, series of gravity field models have been derived based on the short arc approach. On the one hand, the arc length should be not too small ($<$ 10 minutes) to allow no data deficiency and to provide a safe redundancy and on the other hand, it should be not too long to avoid accumulated unmodeled disturbances. For the recovery of the Earth's gravity field, an arc length of approximately 30 minutes has been recently displayed to be sufficient for determining the complete spectrum of the gravitational field of the Earth. Consequentially, all investigated simulation scenarios within this thesis are restricted to this arc length type for the analysis of the Earth's global gravity field.

5.2.1.2.2 Gravity Field Representation

After splitting the observations into short arcs, the observation equations for each short arc are set up by the applied GROOPS software. This composes a system of normal equations (Eq. (5.22)) which are accumulated according to Eq. (5.26). In a next step, the normal equations are directly solved via Cholesky decomposition (see e.g. Koch 1988, p. 36). The output of the accumulated normal equations is a set of spherical harmonic coefficients (see Eq. (3.29)). The number of unknown parameters (n_p) (up degree n= 2) is related to the maximum spherical harmonic degree (n_{max}) by

$$n_p = n_{max}^2 + 2n_{max} - 3. \tag{5.40}$$

Spectral Domain In order to represent the gravity recovery results, several quantities were used to describe the spherical harmonic spectrum. One of a frequently used measure is the degree variance and the difference the degree variance, respectively, that characterizes the errors and uncertainties in the estimation of the gravity coefficients,

$$\sigma_n^2 = \sum_{m=0}^{n} \sigma_{nm}^2 = \sum_{m=0}^{n} \left(c_{nm}^2 + s_{nm}^2\right). \tag{5.41}$$

The subscripts n and m are the degrees and orders, respectively. The corresponding root mean square per degree n (RMS_n) is given by

$$RMS_n = \sqrt{(2n+1)^{-1} \sum_{m=0}^{n} \sigma_{nm}^2}. \tag{5.42}$$

For the discrepancies of two gravity solutions, the difference degree variance (DDV) is used, which is defined by the difference between the estimated gravity coefficients $((c_{nm})_{est}, (s_{nm})_{est})$ and the reference gravity field $((c_{nm})_{ref}, (c_{nm})_{ref})$ as introduced before (Eq. (3.47)),

$$\Delta\sigma_n^2 = \sum_{m=0}^{n} \left(\Delta c_{nm}^2 + \Delta s_{nm}^2\right). \tag{5.43}$$

where,

$$\begin{aligned} \Delta c_{nm} &= (c_{nm})_{est} - (c_{nm})_{ref}, \\ \Delta s_{nm} &= (s_{nm})_{est} - (s_{nm})_{ref}. \end{aligned} \tag{5.44}$$

This DDV are used in all simulation scenarios for comparisons and are defined for each degree (i.e. they depend on the degree n not the order m), but sometimes it is better for the interpretation to use a scalar quantity that characterizes to a gravity coefficients set. Therefore, the cumulative geoid error (or commissioning error) from n= 2 up to n_{max} is used

$$\Delta\sigma_{cum}^2 = R_e \sum_{n=2}^{n_{max}} \sum_{m=0}^{n} \left(\Delta c_{nm}^2 + \Delta s_{nm}^2\right). \tag{5.45}$$

Another representation of the gravity field solution are the formal errors (discussed later in Chapter 7) which read

$$\sigma_n^2 = \sum_{m=0}^{n} \left(\sigma_{c_{nm}}^2 + \sigma_{s_{nm}}^2\right). \tag{5.46}$$

Spatial Domain The output of the spherical coefficients are transformed onto potential coefficients and then represented in terms of gravity anomalies or geoid heights. The results within this thesis are of interest with the geoid height spectrum.

It should be noted that for different purposes such as applying different temporal resolutions (more than one month, a month and sub-month), an appropriate degree of the spherical harmonic expansion has to be selected. Correspondingly, the spatial resolution will be changed as well. For instance, spherical harmonic degrees of n_{max}= 60, n_{max}= 90 and n_{max}= 180 are used for the static gravity recovery in order to recover different wavelengths of the gravity field spectrum. For the recovery of the temporal gravity signals, also different spherical harmonic degrees are used corresponding to the applied physical model. These different analysis degrees from 60, 90 and 180 correspond to spatial resolutions of 333 km, 222 km and 111 km, respectively, as a result of the approximation,

$$n_{max} \approx \frac{2\pi R_e}{\lambda} \approx \frac{20000}{\mathrm{D}}, \tag{5.47}$$

where,

n_{max}	:	maximum spherical harmonic degree,
R_e	:	mean radius of the Earth,
λ	:	wavelength in km,
D	:	resolution (half-wavelength) in km.

5.2.2 Applied Physical Models for Temporal Gravity Field

A short summary of the physical models that have to be accounted for during the simulation scenarios of the future SFFs besides the "true" gravity field model ITG-GRACE03s is given in the following:

Direct Tides: It is well-known that the satellite's orbit in addition to the Earth's gravitational force is influenced by third-body tidal forces (mainly the Sun, the Moon, and the other planets). These tidal forces which affect the satellite orbit can be estimated from the positions of the third bodies that are given in the Ephemerides DE 405 by the JPL (see Standish 1998).

Solid Earth Tides: As illustrated in Chapter 4 that the tidal forces cause a deformation of the Earth. This deformation causes mass displacement which changes the gravitational potential of the solid Earth. The corresponding specifications are given in *the IERS conventions (2003)* (McCarthy and Petit 2004).

Ocean Tides The periodic variations occurring in the oceans caused by the tidal forces and their correspondingly variations in the gravitational potential are considered using the ocean tide model FES2004 (Le Provost 2001). The errors in the tidal models were estimated using different tidal model such as EOT08a (Bosch and Savcenko 2008).

Pole Tides: Due to the centrifugal force of the polar motion, a deformation of the Earth takes place and thus a change in the gravitational potential in the polar regions occurs. This phenomena is donated as polar tides. The related specifications can again be obtained from the *IERS conventions (2003)* (McCarthy and Petit 2004).

De-aliasing: The high frequency signals with short periods induce observable variations of the atmospheric masses. In addition, the reaction of the ocean due to these changes have to be added to our simulations for detecting and mapping the aliasing effects and their impacts on the gravity field solutions. The models to account for the short periodic variations are therefore taken from the so-called de-aliasing product (AOD1B), as specified in Flechtner (2007).

Hydrological Effects: As the continental water storage varies, the mass variations occur and hence the gravity field changes. Thus, the effect of the hydrology should be taken into considerations as a tool of improving the hydrological signal using different information of various satellite configurations.

6. Simulation Scenarios of Satellite Formation Flight Missions

The calculation of the Earth's global gravity field from satellites' missions meets some proper requirements. Properly chosen satellite configurations flying in a formation and equipped with a precise sensor instrumentation and sophisticated satellite technologies play an important role for a precise determination of the gravity field. The objective of this chapter is to establish a mission architecture concept for a SST mission, which shall provide an optimal recovery of the Earth's variable gravity field. This is done by analyzing numerous SFF scenarios based on the SST measurements principle. For doing this, proposed future satellite missions from different space agencies are considered. Firstly, an overview of the key limitations that face the current satellite missions and how future satellite missions are used as an option for providing a higher gravity field accuracy and also as a solution for mitigating these limitations. The parameters that affect the gravity field recovery such as orbit selection and the noise levels are outlined. Furthermore, each proposed SFF with its innovative characteristics is introduced.

6.1 Introduction

6.1.1 Shortcomings of Current Satellite Gravity Missions

The current space-based observation missions opened a new chance in satellite geodesy for improved understanding of the Earth's system from space. This contribution appears in model development by measuring the spatial and temporal variations of the Earth's shape, gravity and magnetic fields as well as the atmospheric mass density. Some shortcomings still confine these successful missions. Considering only the ll-SST mission (i.e. GRACE mission), which represents the simplest SFF, it does only provide a single gravity gradient component in the along-track direction given by the baseline established by its two spacecrafts. Some error sources of the GRACE mission accuracy arise from the satellite configuration, the altitude control and from instrument noise like the three noise sources in the accelerometer, the Ultra Stable Oscillator (USO) and the microwave ranging system. From GRACE twin-satellites' configuration point of view, its observable seems to have a relatively weak gravity signal component due to measuring observations in solely in-track direction. Also the GRACE mission does not have an altitude control since its orbit is decaying with a rate of 1.1 km/month due to the atmospheric drag. Hence, controlling the altitude for the future missions in addition to defining a better satellite configuration allows a better observable improvement. In addition, the improvement of the used optical tracking equipment (e.g. laser ranging rather than microwave ranging) leads to a mission performance which has to be considered for studying such future gravity missions as outlined by e.g. Aguirre-Martinez and Sneeuw (2002) and studied by e.g. Bender et al. (2003) and Wiese et al. (2008). This allows a higher accuracy to be achieved when the ranges between the satellites are measured.

On the other hand, the mass variations in the Earth system that occur on various temporal and spatial scales influence the satellite observations causing the so-called temporal variations. Insufficient sampling of short-term/small-scale mass change and mass transport processes (e.g. atmosphere and ocean tides) may lead to signal aliases in the mean gravity field solutions that are calculated as a compromise between temporal and spatial resolution. To avoid aliasing, short-term mass variability has to be dealiased with numerical models before calculating mean gravity fields from the satellite observations. Besides tidal variability in the atmosphere, oceans and solid Earth, non-tidal mass variations associated with short-term dynamics in atmosphere and oceans have to be considered. Due to the various deficits in these models, residual short-term variability remains uncorrected and aliases e.g. into the monthly mean solution, where it manifests itself in the case of the GRACE constellation in characteristic north-south (i.e. along orbit) oriented stripes. Since the amplitude of the short-term variability can be large compared to the monthly mean signals, aliasing can significantly degrade the accuracy of the mean solutions. This is one reason why the predicted GRACE baseline accuracy has not been achieved so far. Therefore, new SFF missions are necessary to overcome the above mentioned shortcomings.

6.1.2 Feasibility of the Formation Flight Concept in Gravity Recovery

Many technical and scientific reports are proposed and introduced for establishing different sets of mission requirements and for identifying the related technical requirements (see Rummel et al. 2003, Rummel 2007, Bender et al. 2008 and van Dam et al. 2008). They introduce the pre-requisites for future missions and how they can improve the state-of-art after the current missions in form of different strategies. One of them is to achieve a higher precision without the necessity for improving the spatial or temporal resolution. Another strategy is to increase the spatial resolution for studying e.g. coastal currents, ocean bottom topography and/or to increase the temporal resolution for hydrology and solid Earth geophysics. Also another strategy is to improve the spatial and temporal resolution together with a higher precision and a longer experiment duration. This would also help to separate and isolate of individual error effects as previously shown in Fig. 2.3.

One of the science requirement recommendations pointed out e.g. in Rummel et al. (2003) for understanding the gravity and geoid issue and separating them from various physical and geophysical phenomena is the selection of a SFF mission type. A future SFF should overcome the aforementioned limitations in Sec. 6.1.1. A Selection of the SFF that either contains a single-arm component or multi-arms component is the uppermost important point. In addition, a future satellite gravimetry mission should therefore be designed in a SFF that enables improvements in spatial and temporal resolution and largely minimizes the aliasing effects. Establishment of satellite orbits, number of the required satellites in addition to the type of SFF and observational pattern of the mission scenarios are the main topics when designing a new mission concerning the recovery of Earth's gravity field variations. In the following sections, an overview for the selection and the design of the orbital parameters, which affect the accuracy of the gravity estimation, is introduced.

6.2 Orbit Design

The subsatellite track pattern and hence the Earth's coverage with observations are determined by the orbits of the SST pair around the Earth causing variable spatial and temporal sampling. The selection of an orbit requires an understanding of the orbital characteristics that influence the accuracy of the satellite's measurements including the temporal and spatial distribution of the measurements. Some orbital parameters determine the temporal and spatial characteristics of the satellite and hence determine the accuracy of the recovered gravity field. These parameters can be summarized into the selection of the satellite orbital elements including inclination, eccentricity and altitude, in addition to the separation between the two satellites which influences also the accuracy of the gravity field recovery. Furthermore, the level of the measurement noise affects especially the accuracy of the gravity determination. The orbit repeat period is also one of the parameters that affect the temporal and spatial sampling characteristics of the satellite. But since the repetition of the orbital period is dependent on the orbital parameters, particularly, the orbital inclination and altitude, it will be introduced during the discussion of these two elements. In the following, an analysis of the critical orbit parameters used for the orbit selection including the orbital inclination and altitude as well as inter-satellite separation is introduced by numerical simulations. For this task, the applied simulation scenarios have been selected of along-track observation type of a collinear formation (e.g. GRACE-like) as a reference SFF. The eccentricity was chosen very small (e= 0.001) for these test scenarios for providing better gravity field recovery using approximate circular orbits, and therefore, its effect was ignored as mentioned before. So, the choice of the initial orbit parameters of a satellite cluster to be discussed in the following should

- have a common inclination of all satellites,
- have a common altitude of the satellites,
- show an inter-satellite separation of the satellites that includes different distance geometries and metrologies.

6.2.1 Inclination and Subsatellite Track Variability

An ideal case for obtaining a complete global Earth coverage is a polar orbit (i= 90°), although the realistic satellite gravity missions don't fly at this inclination but still don't differ much from this ideal case. There are some reasons for this. One of them is the restriction in the launcher system itself as mentioned by Kim (2000). The maximum launch inclination of the CHAMP mission was only 87° due to the safety area restriction of the launch site (a submarine base is in the direct north of the site). For the GRACE mission, the launch vehicle performed additional maneuvers to get 89°, which required additional fuel and reduced the total payload weight. Other aspects are physical and/or numerical ones. Koop (1993) gave an example related to gradiometer measurements. He showed that the zonal coefficients in case of polar orbits cannot be estimated from the cross-track gravity components. This is due to the fact that the cross-track direction is always orthogonal to the direction of zonal coefficient variations along the meridians. From the numerical point of view, numerical singularities in the normal matrices may also be encountered. This means that certain coefficients are not estimable any more from the observations especially for low orders, which constitute the largest sub-blocks of the normal matrix. Another aspect is related to the inclination function of the cross-track gravity components, which becomes zero for polar orbits (i= 90°) and zonal coefficients (m= 0). More discussion of the effect of the polar orbits on the cross-track inclination function is discussed in detail in Koop (1993).

Non-polar orbits do not provide measurements in the polar regions causing a so-called polar gap (an area which is not covered with subsatellite tracks of the satellite's orbit). The size of this polar gap is given by $2 \times (i - 90)°$. Fig. 6.1 shows some of the applied inclinations that are implemented for investigating the effect of the polar gaps on the gravity field recovery: one retrograde orbit at i= 95°, one polar orbit at i= 90° and some prograde orbits at i= 89.5°, 89°, 85° and 80°. At a first view, one expects a polar gap to disturb the gravity field solution. As seen from the *DDV* (difference degree variances) in terms of geoid heights (Fig. 6.2), which represents the geoid height differences between the gravity solutions and the "true" gravity model ITG-GRACE03s, as well as from the cumulative geoid errors (Fig. 6.3) that some of the non-polar orbits (e.g. 95°, 89.5°, 89° and 85°) provide gravity solutions better than the polar one. The interpretation for this phenomenon is attributed to the data density (i.e. number of the distributed observations over the Earth due to the coverage of the subsatellite tracks). Although inclinations become larger or smaller than 90°, polar gaps occur but the data density in the remaining part of the total area increases. A simple formula can be applied for quantifying the increment of date density due to the inclination variation (Kim, private communication) as

$$A = 4\pi(R_e + h)^2 \sin i, \tag{6.1}$$

where h is the orbital altitude in meter and the inclination (i) is indicated in degrees. Whereas the polar gaps may contaminate the recovery of some coefficients, the higher data density improves the recovery of the others. But this is not generally a valid characteristic since Fig. 6.2 shows gravity degradation especially in the zonal coefficients of the inclinations 95°, 85° and 80°. This may be due to the minimum wavelength of the (90×90) gravity solution of 4° (given by $360/n_{max}$, where n_{max} is the maximum spherical harmonics degree), and it is much smaller than the gap size of these inclinations (10°, 10° and 20°, respectively). The 89.5° and 89° cases provide better gravity solutions because their gap sizes of 1° and 2° are lower than the minimum gravity wavelength of 4°. This emphasizes the statement that, the improvement of the data density for gravity solutions is limited by the selected inclinations. For this reason, a selection of an inclination (e.g. i= 89.5°) that differs not too much from 90° brings small improvements and seems to be more preferable in satellite geodesy applications in order to estimate the global gravity field of the Earth.

Therefore, one can conclude that the data density has a limitation in the performance of the gravity field recovery in case of the existence of polar gaps. Although, Fig. 6.2 shows sectorial gravity improvements of some inclinations (e.g. 95° and 85°) rather than 90° due to the data density. The zonal coefficients in case of these inclinations show a worse gravity recovery result due to polar gaps, whose effect is larger than the data density improvements. The result is confirmed also for inclination 80°, whose polar gap effect is significantly larger than the minimum wavelength of 4°, and hence both sectorial and zonal harmonics show an obvious gravity degradation. This appears also in case of the cumulative geoid errors (Fig. 6.3) of the latter inclination. The tesseral degree variances were analyzed as well, but since they do not provide a significant accuracy

difference from the sectorial results, they were not presented. Therefore, in our simulation scenarios, we will select an inclination of 89.5° that provides a small polar gap of 1° and an improvement of both sectorial and zonal gravity solutions. In this sense, one can recover a gravity field up to degree n_{max}= 360 (despite the fact that, this is not achievable by the satellite gravimetry missions in case of realistic measurement errors) without obtaining any degradation since the minimum wavelength is not smaller than the polar gap size.

An important phenomena, referred as **Repeat subsatellite tracks**, has been arisen during the selection of the orbital inclination (see Fig. 6.1). Repeat subsatellite tracks occur when the satellite performs exactly β orbital revolutions, while the Earth rotates α times w.r.t. the satellite's precessing orbital plane. In other words, a repeat period of a subsatellite track means that a subsatellite track repeats after an integer number β of orbital revolutions and an integer number α of nodal days, where a nodal day is the period between the repetition of the ascending node over the same Earth-fixed meridian. Because the precession of the node is much slower than the Earth's rotation, a nodal day differs only slightly from a solar day, and in case of a sun-synchronous orbit (e.g. i= 95°) they are equal (Bezděk 2009). The repeat subsatellite track is influenced by three orbital parameters, altitude, inclination and eccentricity (as e has been selected as a fixed parameter e= 0.001, so its effect is ignored here).

If the subsatellite track shall repeat itself, the Earth must make an integer number of rotations α in the time required for the satellite to make an integral number of orbits β. This means that the precession of the satellite orbit must be taken into account. The condition of the repeat orbits is then given as (Rees 2001, p. 263)

$$P_n(\omega_e - \dot{\Omega}) = 2\pi\frac{\alpha}{\beta}, \tag{6.2}$$

using the nodal period P_n of the satellite, i.e. the time interval taken from one ascending node crossings to the next, equals $2\pi/(\dot{\omega} + \dot{M})$, so the condition can be written in terms of the classical orbital elements as

$$\alpha(\dot{\omega} + \dot{M}) \simeq \beta(\omega_e - \dot{\Omega}), \tag{6.3}$$

where,

ω_e : is the Earth's angular velocity,

$\dot{\Omega}$: is the precession rate of the satellite's RAAN angle,

$\dot{\omega}$: is the secular change in the satellite's argument of perigee,

$\dot{M}$: is the secular change in the satellite's mean anomaly.

The last three elements are calculated from the formulas (Kaula 1966, p. 39),

$$\begin{aligned}
\frac{d\Omega}{dt} &= \frac{3\mathrm{n}C_{20}R_e^2}{2(1-e^2)^2a^2}\cos i,\\
\frac{d\omega}{dt} &= \frac{3\mathrm{n}C_{20}R_e^2}{4(1-e^2)^2a^2}\left[1-5\cos^2 i\right],\\
\frac{dM}{dt} &= \mathrm{n} - \frac{3\mathrm{n}C_{20}R_e^2}{4(1-e^2)^{3/2}a^2}\left[3\cos^2 i - 1\right],
\end{aligned} \tag{6.4}$$

and ω_e is calculated using the sidereal day of about 24 hours. As the Earth takes approximately 365.25 days to orbit around the sun, so it performs exactly 1 + 1/365.25 (1.002737925 rev/day) complete turns. Thus the sidereal day becomes exactly 23.9345 hours and ω_e reads then

$$\omega_e = \frac{2\pi}{P_E} = 7.2921235 \times 10^{-05} rad/s. \tag{6.5}$$

The repeat period condition (Eq. (6.3)) is related with the mean motion of the satellite as

$$\mathrm{n} = \frac{\beta}{\alpha}(\omega_e - \dot{\Omega}) - (\dot{\omega} + \dot{M}). \tag{6.6}$$

Eq. (6.6) contains secular rates of the orbital elements Ω, ω and M that are almost completely caused by the second zonal term J_2 (where J_2 is the normalized coefficient $C_{2,0}\sqrt{5}$) which depends on the inclination. Therefore, the repeat subsatellite tracks will also change significantly with the inclination. After inserting the secular rates which are calculated from Eq. (6.4) into Eq. (6.3), the ratio β/α can be easily obtained. Eq. (6.6) reads for the first order in J_2 after taking n as $(\beta/\alpha)\omega_e$ (Bezděk 2009)

$$\mathrm{n} = \frac{\beta}{\alpha}\omega_e \left[1 - \frac{3}{2} J_2 \left(\frac{R_e}{a}\right)^2 \left(4\cos^2 i - \frac{\beta}{\alpha}\cos i - 1\right)\right]. \tag{6.7}$$

The fraction α/β is expressed in its lowest terms (i.e. that α and β have no common factors other than 1). This can be desired as an α-day repeating orbit, while the term β governs the longitudinal separation between the subsatellite tracks on the Earth's surface since there are β ascending and β descending passes. Therefore, Eq. (6.2) is referred also as the fundamental interval λ or the longitudinal spacing between sequential subsatellite tracks at the equator

$$\lambda = P_n(\omega_e - \Omega_P) = 2\pi\frac{\alpha}{\beta} \quad \text{rad.} \tag{6.8}$$

Table 6.1 shows the repeat period of the indicated inclinations discussed in this section.

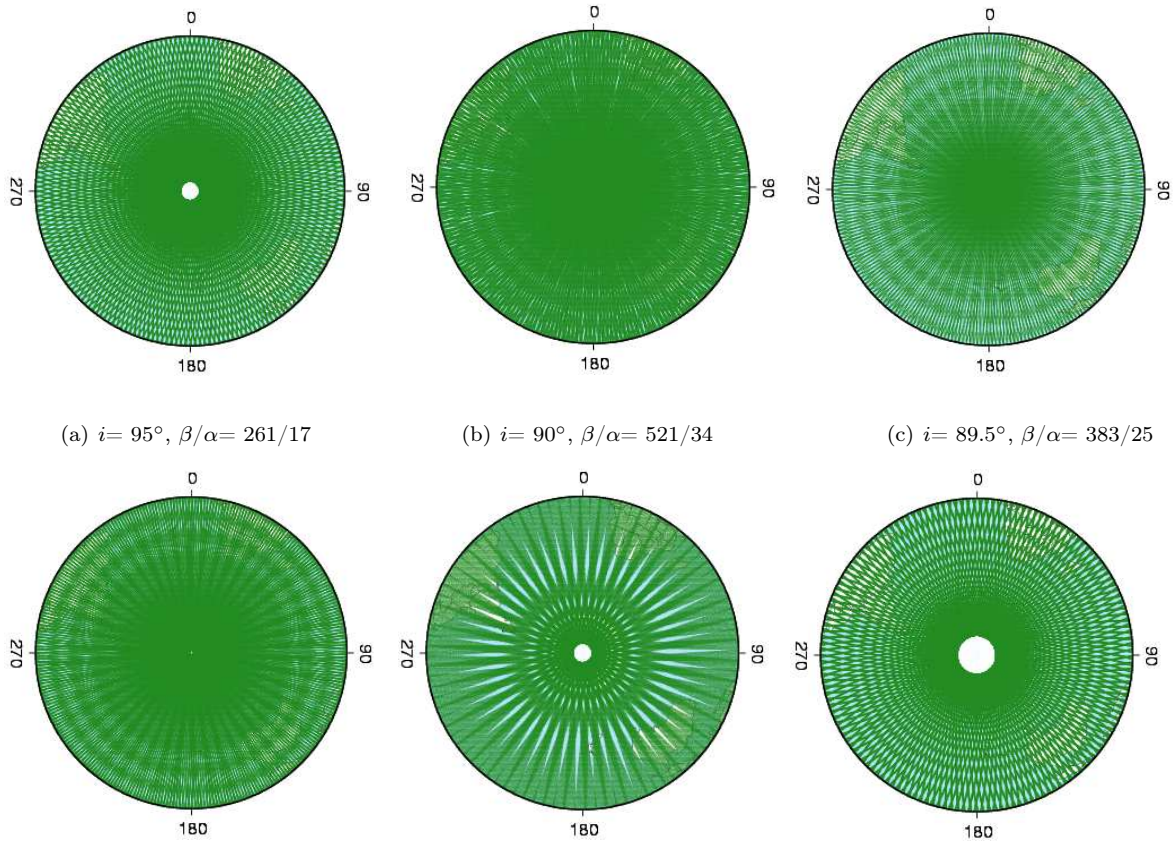

(a) i= 95°, β/α= 261/17 (b) i= 90°, β/α= 521/34 (c) i= 89.5°, β/α= 383/25

(d) i= 89°, β/α= 337/22 (e) i= 85°, β/α= 153/10 (f) i= 80°, β/α= 229/15

Fig. 6.1: Subsatellite tracks of 30 days of a simulated GRACE-like FF at the same orbital altitude of 450 km and for different inclinations.

Table 6.1: Repeat period of subsatellite tracks depending only on the inclinations with an orbital altitude of 450 km and an eccentricity of 0.001.

FF as shown in Fig. 6.1	inclination $i[deg.]$	α-day repeat-period [days]	β-orbits to repeat	Subcycle repeat-period [days]	Long. Interval $\lambda[deg.]$	Long. Interval $\lambda[km]$
(a)	95	17	261	3	1.38	153.54
(b)	90	34	521	3	0.69	76.92
(c)	89.5	25	383	3	0.94	104.63
(d)	89	22	337	3	1.07	118.92
(e)	85	10	153	3	2.35	261.93
(f)	80	15	229	4	1.57	175.00

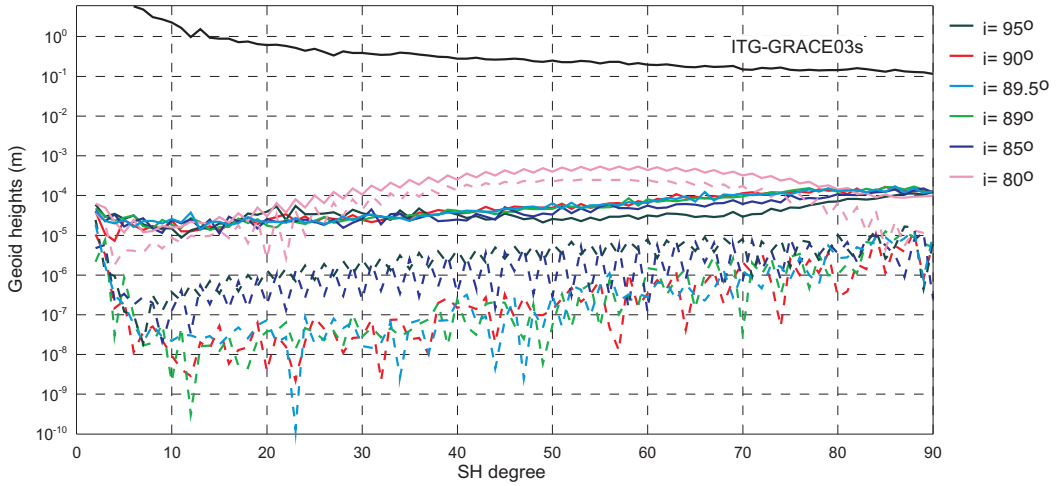

Fig. 6.2: *DDV* of geoid heights between ITG-GRACE03s and gravity field solutions of simulated GRACE-like FF at different inclinations. The solid lines represent (90 × 90) sectorial gravity coefficients and the dashed lines represent the (90 × 0) zonal gravity coefficients.

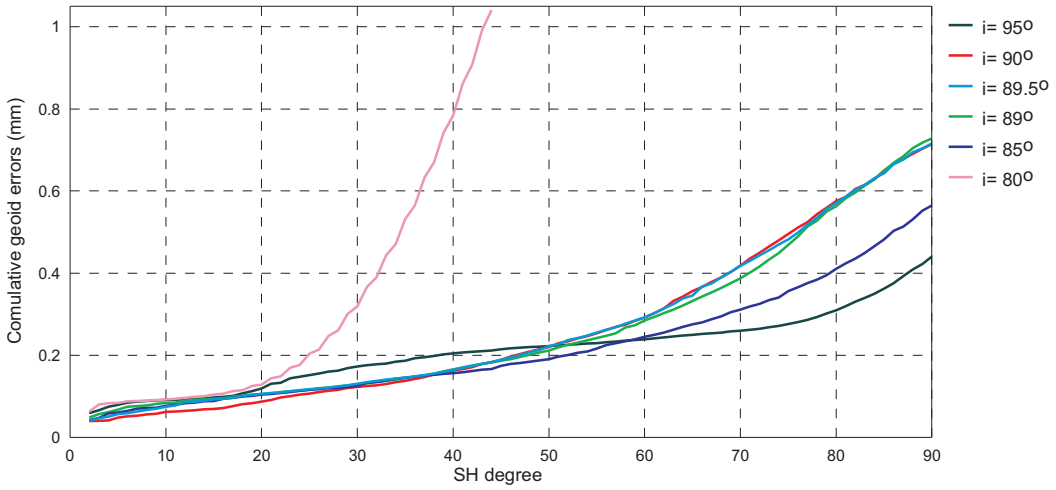

Fig. 6.3: Cumulative geoid errors between ITG-GRACE03s and gravity field solutions of simulated GRACE-like FF at different inclinations.

6.2.2 Orbit Altitude and Subsatellite Track Variability

The choice of the orbital altitude (and with this the semi-major axis) is one of the most important orbital parameter that affects the gravity estimation. The typical satellite altitude ranges for providing a sufficient gravity accuracy are around 250 km to 500 km. A selection of such low altitudes has two main shortcomings due to the residual atmosphere, which causes the air drag. First, the limitation of the mission's lifetime and the necessity for orbit maintenance manoeuvres because of the orbit decay. Second, the non-gravitational accelerations imposed on the satellite which have to be measured. Therefore, on the one hand, strengthening the accuracy of the gravity estimation requires an as low as possible altitude, while, on the other hand, this accuracy is limited by the atmospheric drag (see e.g. Kim 2000, p. 195).

The variation of the gravity error associated with the spherical harmonic degree n due to the change of the orbital altitude is reflected by the so-called inverse attenuation factor, $[r/R_e]^{2n+1}$, which is a function of the spherical harmonic degree. The exponent n indicates that the higher the orbital altitude (and consequently the larger r) is, the worse the resolution of the gravity field recovery. In other words, the gravity anomalies are attenuated as the distance from the source becomes larger (see Fig. 6.4). Higher values representing higher orbital altitudes cause an increasing degradation of the gravity solution. Also from another point of view, the satellite at the same orbital altitude is subject to a degradation in the gravity solution at higher degree coefficients due to the accumulated error of the model parameters. This will be presented in Chapter 7 when comparing the gravity field solution of e.g. degree 90 of mm accuracy level with one of e.g. 180 of cm accuracy level. This issue has no relation with the degradation arisen from the aforementioned attenuation factor effect. It is clear also that under the same level of noise, the errors of the high degree terms are seen to increase quite dramatically with a modest increase of the satellite altitude. This underlines the importance of a low altitude of satellite orbits for the recovery of high resolution gravity field rather than the relatively higher orbital altitudes.

The choice of the orbital altitude determines the Earth's coverage pattern (i.e. the variation of subsatellite tracks) and repeat modes as formerly mentioned in Sec. 6.2.1. Homogeneous and uniform subsatellite tracks are favorable and ideal for the estimation of the gravity coefficients. Therefore, when designing a mission, the orbit should be maintained to generate a uniform subsatellite track pattern and the repeat modes have to be avoided as good as possible. Fig. 6.5 shows different modes of subsatellite tracks at different orbital altitudes, noting that the inclination has already been selected to be 89.5° as recommended in Sec. 6.2.1. All simulation scenarios cover a time span of 30 days in an altitude range between 300 and 410 km. The repeat periods of these different altitudes are indicated in Table 6.2.

It is shown from Fig. 6.5 and Table 6.2 that the finest possible global coverage at inclination i= 89.5° is obtained at 400 km altitude within a time period of 49 days. Numerical simulations were performed to investigate the effect of a subsatellite tracks variability for different satellite altitude modes. As shown in Fig. 6.6 and Fig. 6.7, the lower altitudes provide better gravity estimation than higher ones, despite a not ideal subsatellite coverage. This can be attributed to the minimum wavelength of the (90×90) gravity solution of 4° which is larger than the longitudinal gaps (between the subsatellite tracks) of e.g. 300 km, 360 km and 410 km. Therefore, the non uniform subsatellite tracks do not play a significant role in the (90×90) gravity solution. The interval of 310 km does not differ much from this wavelength and hence its gravity recovery indicates a relatively better solution. The longitudinal intervals around the altitudes corresponding to short repeat cycles have to be avoided since we are seeking for a sufficient spatial sampling and for mitigating the coverage gap problem.

For such reason and also for other reasons such as a longer mission duration, which is more straightforwardly maintained by higher altitudes in addition to the relatively lower effect of the atmospheric drag at high altitudes, the altitude 400 km is desirable for our simulation analyses. Another aspect for selecting the altitude of 400 km is that the gravity solution of all altitudes as shown from Fig. 6.6 has the same accuracy at lower degrees.

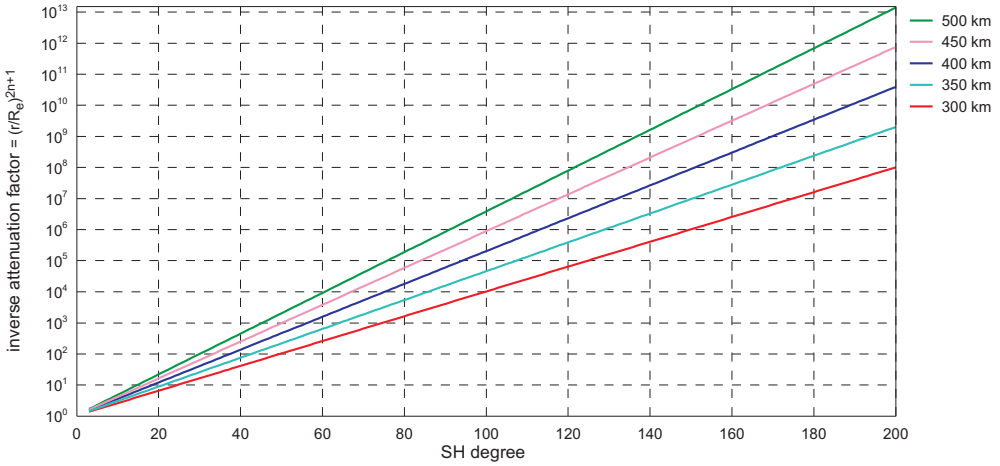

Fig. 6.4: Effect of the inverse attenuation factor as a function of spherical harmonic degree at different orbital altitudes.

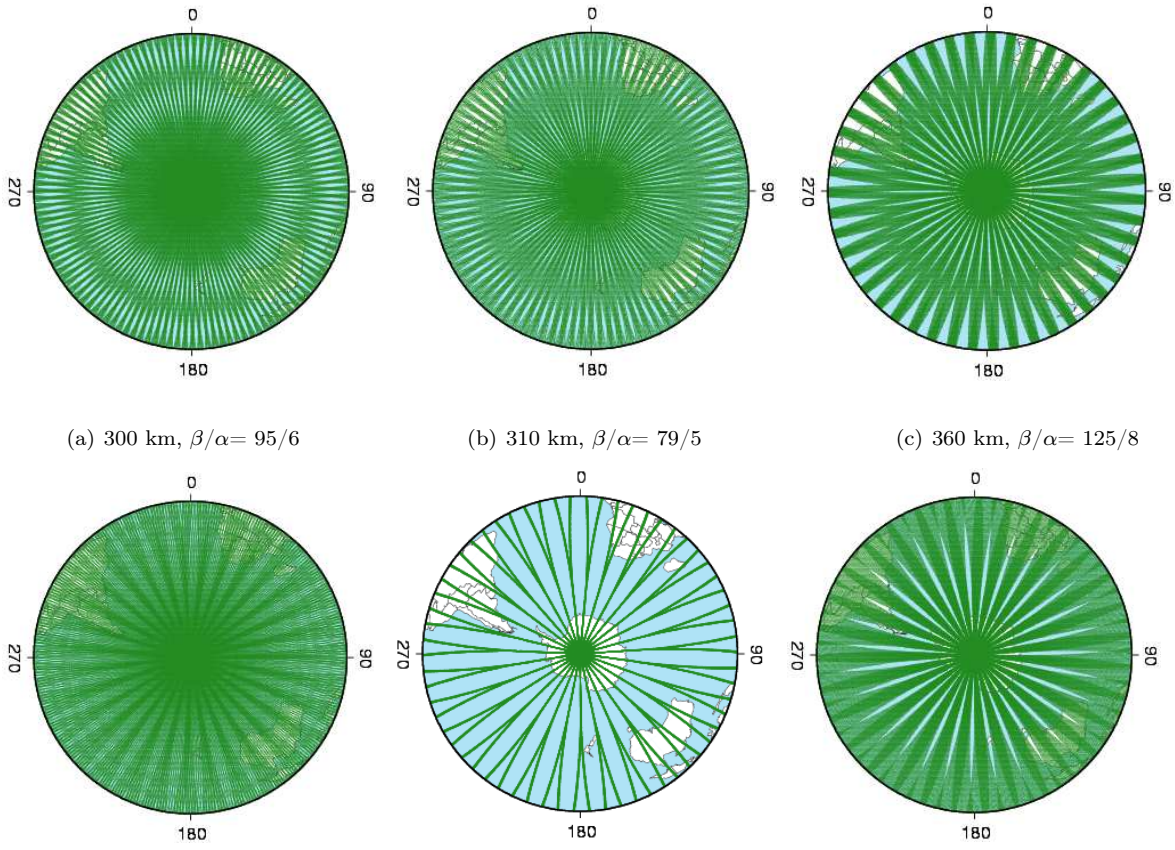

(a) 300 km, β/α= 95/6 (b) 310 km, β/α= 79/5 (c) 360 km, β/α= 125/8

(d) 400 km, β/α= 759/49 (e) 407 km, β/α= 31/2 (f) 410 km, β/α= 170/11

Fig. 6.5: Different modes of subsatellite tracks of 30 days of a simulated GRACE-like FF at the same orbital inclination of 89.5° and at different orbital altitudes.

Table 6.2: Repeat period of subsatellite tracks depending only on the orbital altitude with fixed inclination of 89.5° and an eccentricity of 0.001.

FF as shown in Fig. 6.5	Orbital altitude [km]	α-day repeat-period [days]	β-orbits to repeat	Subcycle repeat-period [days]	Long. Interval $\lambda[deg.]$	Long. Interval $\lambda[km]$
(a)	300	6	95	-	3.79	421.84
(b)	310	5	79	-	4.56	507.28
(c)	360	8	125	3	2.88	320.60
(d)	400	49	759	2	0.47	52.8
(e)	407	2	31	-	11.61	1292.74
(f)	410	11	170	2	2.12	235.74

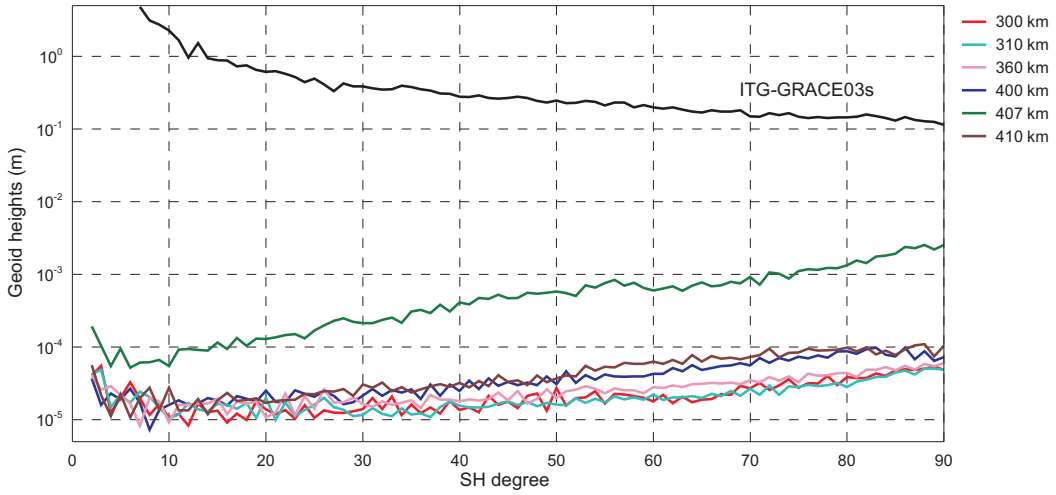

Fig. 6.6: *DDV* of geoid heights between ITG-GRACE03s and gravity field solutions of a simulated GRACE-like FF at different orbital altitudes.

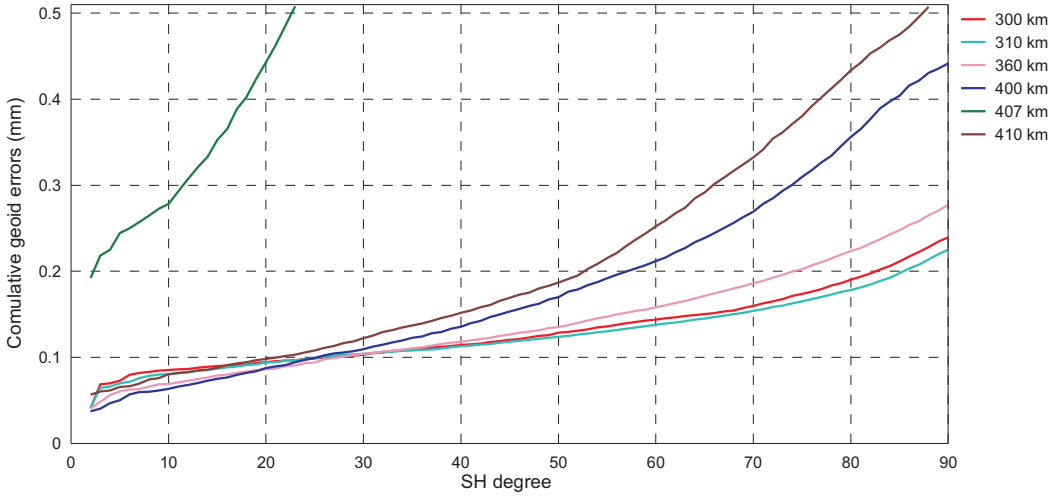

Fig. 6.7: Cumulative geoid errors between ITG-GRACE03s and gravity field solutions of simulated GRACE-like FF at different orbital altitudes.

6.2.3 Inter-satellite Range

6.2.3.1 Inter-satellite Range Geometry

Basically the performance of the SST mission is determined by three main components besides the previous mentioned parameters (especially the orbital altitude). These components include the inter-satellite range (or separation), the distance metrology and the measurement accuracy of non gravitational acceleration. The use of inter-satellite separation for the gravity field recovery is of great significance because the separation between the satellites in ll-SST mode determines in part how gravity frequencies contribute to the total signal.

The variation of the inter-satellites range affects the gravity field solution. On the one hand, as the inter-satellite range increases, the strength of the gravity signal increases especially for the lower potential harmonics (Kim 2000). However, on the other hand, the SST measurement noise levels becomes larger as the range between the satellites increases.

Some numerical simulations of the GRACE-like FF were accomplished using 30 days of observations for a complete and sufficient Earth's coverage with the previous recommended orbital inclination (i= 89.5°) and altitude (h= 400 km). The simulation scenarios include six different inter-satellite separations angles of 0.08°, 0.4°, 0.8°, 1.2°, 1.7° and 2.5° corresponding to separations of 10 km, 50 km, 100 km, 150 km, 200 km and 300 km, respectively. The results are indicated in Fig. 6.8 in terms of *DDV* of geoid heights and in Fig. 6.9 in terms of cumulative geoid errors using the same level of SST measurement noise in order to analyze only the effect of distance changes between two satellites on the gravity field recovery. It is clearly shown that the gravity error level diminishes as the inter-satellite range increases. At low degrees, the accuracy of the potential coefficients is not significantly improved, but as the separation between the two satellites increases, the coefficients of higher degree are obviously affected. As seen from the *DDV* of geoid heights, the separation angles above 1.2° (150 km) perform one to one and a half order of magnitude better than in case of an angle 0.08° (10 km).

The size of the inter-satellite distance between the satellites is restricted by the observability problem for certain gravity coefficients. In other words, if the inter-satellite separation is as same as the wavelength of a certain gravitational signal, the potential coefficients generating this signal will be hard to be observed (see Kim 2000, p. 190).

An important issue is the selection of the optimal separation considering only the along-track separation (i.e. the two satellites are in the same orbital planar) related to the frequency of such gravitational signal. Referring to the repeat period condition (Eq. (6.3)), one can write the orbital frequency as

$$N = (\dot{\omega} + \dot{M}) = \frac{2\pi\beta}{T_{rep}}, \tag{6.9}$$

and the nodal frequency as

$$\dot{L} = (\dot{\Omega} + \dot{\Theta}) = -\frac{2\pi\alpha}{T_{rep}}. \tag{6.10}$$

Where T_{rep} is the repeat period in seconds and contains exactly β orbital revolutions in α nodal days. It is clear that the term $(\dot{\omega} + \dot{M})$ will be constant and the variation $(\dot{\Omega} + \dot{\Theta})$ is also assumed linear in time. Then, the gravitational frequencies are therefore (Mackenzie 1995)

$$\begin{aligned} \dot{\psi}_{jm} &= \frac{2\pi\beta}{T_{rep}} \left(j - m\frac{\alpha}{\beta} \right) = \\ &= N \left(j - m\frac{\alpha}{\beta} \right), \end{aligned} \tag{6.11}$$

with the index $j = n - 2p$ (see Sec. 3.3.1). Assuming the along-track separation angle between the two satellites is ΔS, where $S = \omega + M$, then it can be related to the gravitational frequencies according to the condition

$$\sin\left(\dot{\psi}_{jm}\frac{\Delta S}{2N}\right) = 0, \tag{6.12}$$

and hence

$$\dot{\psi}_{jm}\frac{\Delta S}{2N} = \pm k\pi, \qquad k = 0, 1, 2, \cdots . \tag{6.13}$$

From Eq. (6.11), this condition reads

$$\left(j - m\frac{\alpha}{\beta}\right)\Delta S = \pm 2k\pi, \qquad k = 0, 1, 2, \cdots . \tag{6.14}$$

Writing $\Delta S = 2\pi/f$, where f represents the maximum frequency being measured by cycles per revolution, then for the case at hand

$$j - m\frac{\alpha}{\beta} = \pm kf, \qquad k = 0, 1, 2, \cdots . \tag{6.15}$$

This equation is used to find the critical separation at which the highest frequencies will be attenuated. By choosing an orbital inclination of 89.5° and an altitude of 400 km, the satellite pair would take to constitute β= 360 revolutions over the approximate α= 23 days, which cover all of its ground tracks.

According to the Nyquist rule, which states that the maximum degree of the gravity solution n_{max} should be smaller than half of the orbital revolutions (i.e $n_{max}<\beta/2$), then a maximum degree of 180 can be recovered. The maximum frequency, using Eq. (6.15) is

$$\left|-180 - 180\frac{23}{360}\right| = \pm kf. \tag{6.16}$$

If we put k= 1, then we get $f \approx 192$ which corresponds to a separation of ΔS= 1.875°. This means that the attenuation of the highest frequency will occur at separation 222 km. It is desirable to choose the inter-satellite range larger than the desired resolution in order to maximize the measurement signal. In summary, one can conclude that in case of a twin-satellite FF, an along-track separation of 1.8° would be the best compromise for a gravity recovery up to degree and order 180. Some coefficients would be better determined with a larger separation but only at the expense of others. This leads to the recommendation that the best overall solution would be obtained with a number of different separations within the same mission. This is due to the fact that the harmonic coefficients do not have a strong effect of high frequency orbital perturbations on the in-plane (i.e. when the satellites have the same orbital plane) for such a polar orbit (meant here by 89.5°) because their contribution to the line of sight (LOS) velocity is zero. But these coefficients cause a high frequency orbital perturbations perpendicular to the orbital plane (Mackenzie 1995).

For this reason, a multi-satellite FF with different satellite separations is demanded. For instance, by using a pair of satellites with different right ascension angles ($\Delta\Omega$), the cross-track velocities are no longer perpendicular to the line of sight and hence provide a useful contribution to the range rate signal from both higher order tesseral terms and zonal ones. This holds also for the radial separations that have different velocity directions that are also no longer perpendicular to the line of sight. The numerical test computations for different SFFs will be shown in Chapter 7 to investigate the effect of using different inter-satellite separations with different sensitivity directions of the data (along-track, cross-track and radial) on the harmonic coefficients. This issue also seems to be not desirable since changing the separation causes the inter-satellite baseline to have a non-optimal length and hence the measurement will have a non-optimal performance. But a notable exception from this rule is a setup that uses a laser interferometer that has a large signal to noise ratio (SNR).

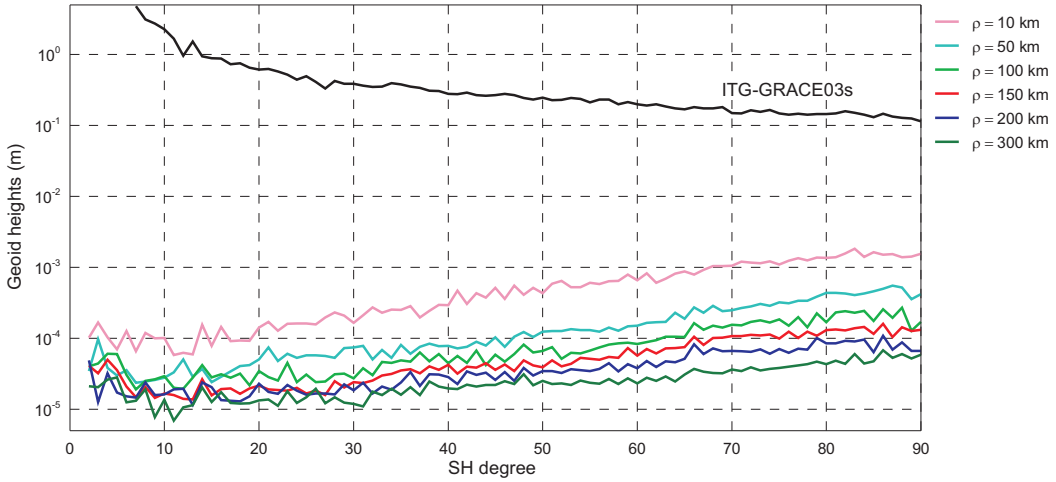

Fig. 6.8: *DDV* of geoid heights between ITG-GRACE03s and gravity field solutions of simulated GRACE-like FF at different inter-satellite baselines.

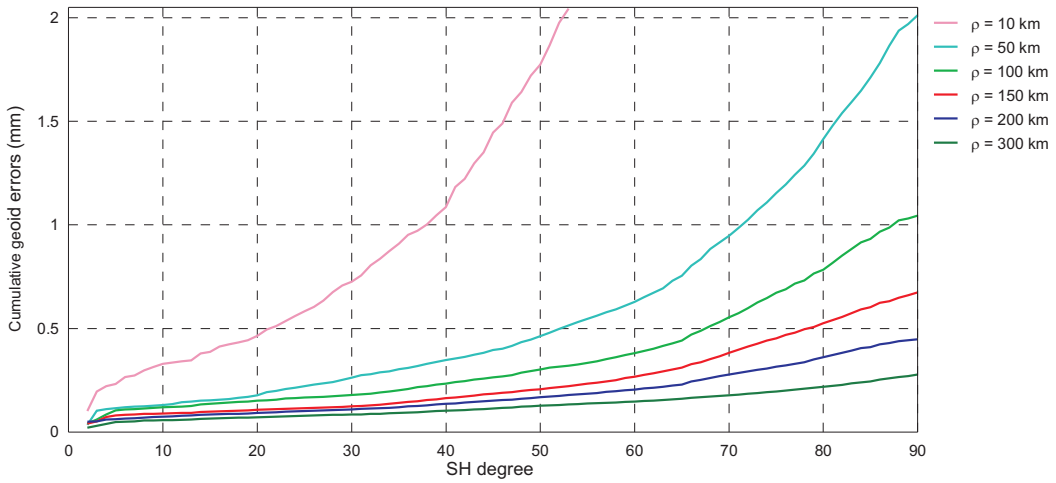

Fig. 6.9: Cumulative geoid errors between ITG-GRACE03s and gravity field solutions of simulated GRACE-like FF at different inter-satellite baselines.

6.2.3.2 Inter-satellite Range Metrology

The key SST instrumentation is the range metrology system to control the distance between the CoMs (Center-of-Mass) of the satellites. Two options are available for the future SFF for measuring the variation of the distance between the satellites' CoMs, a microwave or an optical one. The former option is already applied in the current GRACE mission and the latter option makes use of a laser interferometer which has been already tested for the coming satellite mission (e.g. GRACE-Follow on mission and LISA).

The variation of the range metrology of the satellites flying in low Earth orbits are subject to two main forces resulting from the gravitational and non-gravitational accelerations. In order to separate the two variations from each other, the latter one must be measured by an independent sensor, which is mainly provided by the accelerometer. The accelerometer measures the non-gravitational accelerations (due to the non-gravitational forces) of the CoMs of the two satellites along the line joining the CoMs. Then the difference between these accelerations is computed, from which the variation of the range between the two satellites can be obtained by double integration.

Numerous simulations were performed in order to investigate the impact of changing the metrology perfor-

mance for different accuracies ranging from microwave accuracy of 5μm till optical accuracy of 5nm. The results are shown in Fig. 6.10 and Fig. 6.11 for a simulated GRACE-like FF of inclination 89.5° and an altitude of 400 km using a satellite separation angle of 1.7° (corresponds to 200 km). As expected, a proportional improvement with improving the resolution of the range metrology can be expected except for the highest considered resolutions (5nm) which do not provide a significant improvement corresponding to the 50nm case.

One observes from Fig. 6.10 that the 50nm noise accuracy provides approximately a more than one and half order of magnitude better performance than the microwave noise accuracy. The same behavior appears also for the cumulative geoid errors indicated in Fig. 6.11, which clearly shows a larger geoid error using the microwave noise level (5μm). This demonstrates that future SST mission with a range measurement based on an optical metrology provides significantly improved gravity field solutions than the current used microwave ranging metrology. Since the concept of the range measurements of the future SFF is the optical metrology, we will apply the dominating error of the optical metrology system in the following simulation scenarios. This error is attributed to the limited frequency stability of the laser.

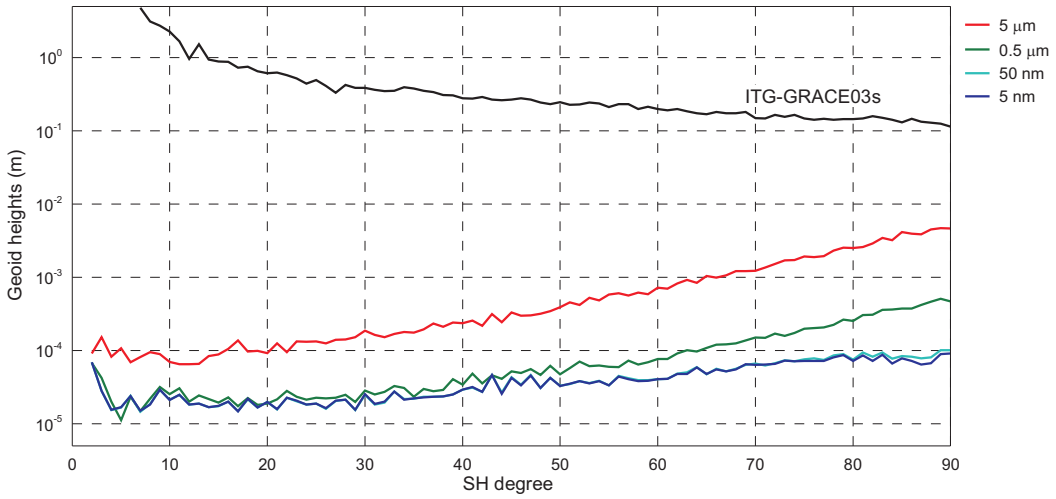

Fig. 6.10: *DDV* of geoid heights between ITG-GRACE03s and gravity field solutions of simulated GRACE-like FF at different measurement noise levels in case of an inter-satellite separation of 200 km.

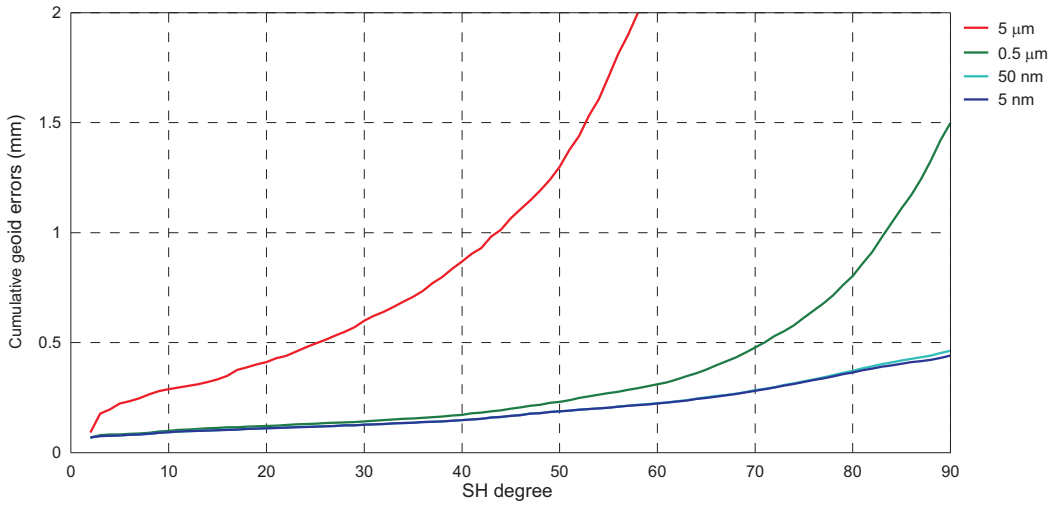

Fig. 6.11: Cumulative geoid errors between ITG-GRACE03s and gravity field solutions of simulated GRACE-like FF at different applied measurement noise levels in case of an inter-satellite separation of 200 km.

6.3 Satellite Formation Flights

6.3.1 Introduction

Satellite formation flight concepts have been studied since the beginning of the manned space program. Satellites flying in formation was not the main challenge, but the significant challenge was to have two or more satellites flying in a precise formation. Many proposals are introduced and planned from different space agencies like NASA, ESA, DLR and CNES for various satellites flying in a formation. This leads to intensively investigations that how to place these various formations in the Earth's gravity field. For example, ESA's Swarm mission, NASA's LISA mission and CNES- and DLR's micro-satellites with SAR interferometry technology and the Cartwheel concept opened the way for investigating satellite formation flights.

As satellite formation flight is composed of two or more satellites that are performing a relative motion around a common center as mentioned in Chapter 2, so that the relative motion of the satellites has to be described. Each satellite configuration composing a formation flight has been considered here to have the orbital design as described in Sec. 6.2. This is to ensure that all orbits have the same decay rates and facing approximately the same dynamics and forces.

The satellite orbits can be either circular or elliptical. The difference between the circular orbit and the elliptical one is that the inter-satellite separation will remain constant if the orbit is circular, while it will expand and contract if the orbit is elliptical. Since we consider here the satellite orbits with small eccentricities (semi-circular), the relative motion is restricted here to the circular relative motion.

In the following, we introduce the mathematical description and the analytical approximation of the relative equations of motion of different satellite formation flights in case of circular orbits.

6.3.2 Approximation of the Relative Motion

The simplest geometry type of satellite formation flight is the leader-follower type realizing a relative motion in the same orbital plane (in-plane motion as pearl string formation). In this type, the two satellites are in the same orbits with identical orbital parameters except the mean anomalies.

For the formulation of the equation of relative motion of one (e.g. follower) satellite relative to another (leader) one in circular orbits, a coordinate frame has to be introduced first of all. For that matter, we define here the so called rotating reference Hill frame. Its origin is at the leader satellite position ($\mathbf{r}_1$) and its orientation is indicated by the vector ($\boldsymbol{\epsilon}_x, \boldsymbol{\epsilon}_y, \boldsymbol{\epsilon}_z$). These orientation vectors are expressed as (Ilk and Seemüller 1977) for the case of a rigorous circular orbit as

$$\boldsymbol{\epsilon}_z = \frac{\mathbf{r}_1}{||\mathbf{r}_1||}, \qquad \boldsymbol{\epsilon}_x = \frac{\dot{\mathbf{r}}_1}{||\dot{\mathbf{r}}_1||}, \qquad \boldsymbol{\epsilon}_y = \frac{\mathbf{r}_1 \times \dot{\mathbf{r}}_1}{||\mathbf{r}_1 \times \dot{\mathbf{r}}_1||}, \tag{6.17}$$

where,

- $\boldsymbol{\epsilon}_x$ is the along-track axis and pointing in the same direction as the orbital velocity vector,
- $\boldsymbol{\epsilon}_z$ is the radial axis and oriented in radial direction (pointing to nadir),
- $\boldsymbol{\epsilon}_y$ is the out-of-plane cross-track axis and completing a right-hand system.

Since the reference frame defines a local horizon plane spanned by $\boldsymbol{\epsilon}_x$ and $\boldsymbol{\epsilon}_y$ and the local vertical direction $\boldsymbol{\epsilon}_z$, it is often referred to as a Local-Horizontal-Local-Vertical (LHLV) frame with the Cartesian coordinates (x, y, z) as shown in Fig. 6.12.

To derive the equation of relative motion, we write the follower satellite position vector using the Cartesian coordinates in the rotating Hill frame as (Schaub and Junkins 2003)

$$\begin{aligned} \mathbf{r}_2 &= \mathbf{r}_1 + \mathbf{r}_{12} = \\ &= x\boldsymbol{\epsilon}_y + y\boldsymbol{\epsilon}_x + (r_1 + z)\boldsymbol{\epsilon}_z, \end{aligned} \tag{6.18}$$

where r_1 ($=||\mathbf{r}_1||$) is the orbit radius of the leader satellite. Differentiating Eq. (6.18) twice w.r.t. the time, the follower satellite's acceleration vector reads

$$\begin{aligned}\ddot{\mathbf{r}}_2 = &\left[\ddot{x} + 2\dot{f}(\dot{r}_1 + \dot{z}) + \ddot{f}(r_1 + z) - x\dot{f}^2\right]\boldsymbol{\epsilon}_y + \\ &+ \ddot{y}\boldsymbol{\epsilon}_x + \\ &+ \left[\ddot{r}_1 + \ddot{z} - 2\dot{x}\dot{f} - x\ddot{f} - \dot{f}^2(r_1 + z)\right]\boldsymbol{\epsilon}_z,\end{aligned} \tag{6.19}$$

where f is the true anomaly of the leader satellite, $\dot{f}$ is the angular rate of the true anomaly and $\ddot{f}$ is its corresponding acceleration. The mean anomaly angular rate of the leader satellite can be obtained using the formula

$$\dot{f} = \frac{r_1\dot{r}_1}{r_1^2}. \tag{6.20}$$

Since the nominator term at the right hand side is constant for a Keplerian motion (hence $r_1^2\dot{f} = c$), then the first derivative yields the mean anomaly acceleration

$$r_1^2\ddot{f} + r_1\dot{r}_1\dot{f} = 0, \tag{6.21}$$

and, respectively,

$$\ddot{f} = -\frac{\dot{r}_1}{r_1}2\dot{f}. \tag{6.22}$$

The acceleration vector of the leader satellite can be be easily expressed in terms of the familiar Newtonian two-body equation of motion which is the most convenient approach for interpreting the motion of a satellite as

$$\ddot{\mathbf{r}}_1 = -GM\frac{\mathbf{r}_1}{r_1^3}. \tag{6.23}$$

Since we can write the position of the leader satellite as $\mathbf{r}_1 = r_1\boldsymbol{\epsilon}_z$, then Eq. (6.23) reads

$$\ddot{\mathbf{r}}_1 = -\frac{GM}{r_1^2}\boldsymbol{\epsilon}_z = (\ddot{r}_1 - r_1\dot{f}^2)\boldsymbol{\epsilon}_z. \tag{6.24}$$

From Eq. (6.24), the acceleration of the leader satellite can be expressed after equating the both sides as

$$\ddot{r}_1 = r_1\dot{f}^2 - \frac{GM}{r_1^2}. \tag{6.25}$$

When inserting Eqs. (6.22) and (6.25) into (6.19), the acceleration vector of the follower satellite can be expressed as

$$\begin{aligned}\ddot{\mathbf{r}}_2 = &\left[\ddot{x} + 2\dot{f}\left(\dot{z} + z\frac{\dot{r}_1}{r_1}\right) - x\dot{f}^2\right]\boldsymbol{\epsilon}_y + \\ &+ \ddot{y}\boldsymbol{\epsilon}_x + \\ &+ \left[\ddot{z} - 2\dot{f}\left(\dot{x} - x\frac{\dot{r}_1}{r_1}\right) - z\dot{f}^2 - \frac{GM}{r_1^2}\right]\boldsymbol{\epsilon}_z.\end{aligned} \tag{6.26}$$

The acceleration of the follower satellite can be expressed by a similar formula as Eq. (6.23)

$$\begin{aligned}\ddot{\mathbf{r}}_2 &= -GM\frac{\mathbf{r}_2}{r_2^3} = \\ &= -\frac{GM}{r_2^3}\begin{pmatrix} x \\ y \\ r_1 + z \end{pmatrix},\end{aligned} \tag{6.27}$$

with $r_2 = \sqrt{x^2 + y^2 + (r_1 + z)^2}$. Equating Eqs. (6.26) and (6.27), the nonlinear relative equations of motion are given by (Schaub and Junkins 2003)

$$\begin{aligned} \ddot{x} + 2\dot{f}\left(\dot{z} - z\frac{\dot{r}_1}{r_1}\right) - x\dot{f}^2 &= -\frac{GM}{r_2^3}x, \\ \ddot{y} &= -\frac{GM}{r_2^3}y, \\ \ddot{z} + 2\dot{f}\left(\dot{x} - x\frac{\dot{r}_1}{r_1}\right) - z\dot{f}^2 \quad -\frac{GM}{r_1^2} &= -\frac{GM}{r_2^3}(r_1 + z). \end{aligned} \tag{6.28}$$

If the relative orbit coordinates (x, y, z) are small compared to the leader orbit radius r_1, then the follower satellite can be approximated as

$$r_2 = r_1\sqrt{1 + 2\frac{z}{r_1} + \frac{(x^2 + y^2 + z^2)}{r_1^2}} \approx r_1\sqrt{1 + 2\frac{z}{r_1}}. \tag{6.29}$$

This allows to write

$$\frac{GM}{r_2^3} \approx \frac{GM}{r_1^3}\left(1 - 3\frac{z}{r_1}\right), \tag{6.30}$$

and hence the lower part of Eq. (6.27) can be simplified to

$$-\frac{GM}{r_2^3}\begin{pmatrix} x \\ y \\ r_1 + z \end{pmatrix} \approx \frac{GM}{r_1^3}\left(1 - 3\frac{z}{r_1}\right)\begin{pmatrix} x \\ y \\ r_1 + z \end{pmatrix} \approx \frac{GM}{r_1^3}\begin{pmatrix} x \\ y \\ r_1 - 2z \end{pmatrix}. \tag{6.31}$$

By substituting Eq. (6.31) into Eq. (6.28) and writing the term GM/r_1^3 in the useful form

$$\frac{GM}{r_1^3} = \dot{f}^2\frac{r_1}{p} = \dot{f}^2\frac{1}{e\cos f}, \tag{6.32}$$

then the relative equations of motion read

$$\begin{aligned} \ddot{x} + 2\dot{f}\left(\dot{z} - z\frac{\dot{r}_1}{r_1}\right) \quad -x\dot{f}^2\left(1 - \frac{r_1}{p}\right) &= f_x, \\ \ddot{y} \qquad + \qquad \dot{f}^2 y\frac{r_1}{p} &= f_y, \\ \ddot{z} - 2\dot{f}\left(\dot{x} - x\frac{\dot{r}_1}{r_1}\right) \quad +z\dot{f}^2\left(1 + 2\frac{r_1}{p}\right) &= f_z. \end{aligned} \tag{6.33}$$

Replacing the true anomaly f with the true latitude θ (where $\theta = \omega + f$) of the leader satellite, then the general equations of Eq. (6.28) w.r.t. the leader satellite read

$$\begin{aligned} \ddot{x} + z\ddot{\theta} + 2\dot{z}\dot{\theta} \quad -x\left(\dot{\theta}^2 - \frac{GM}{r_1^3}\right) &= f_x, \\ \ddot{y} \qquad + \qquad y\frac{GM}{r_1^3} &= f_y, \\ \ddot{z} - x\ddot{\theta} - 2\dot{x}\dot{\theta} \quad -z\left(\dot{\theta}^2 + 2\frac{GM}{r_1^3}\right) &= f_z. \end{aligned} \tag{6.34}$$

The forces (f_x, f_y, f_z) represent the non-Keplerian forces acting on the follower satellite that may arise from atmospheric drag or the control thrusters.

In the case of circular orbits, the eccentricity of the leader satellite is $e = 0$, $p = r_1$, where r_1 is constant and the mean orbital motion n is equal to the true anomaly rate $\dot{f}$. Therefore, the relative equations of motion

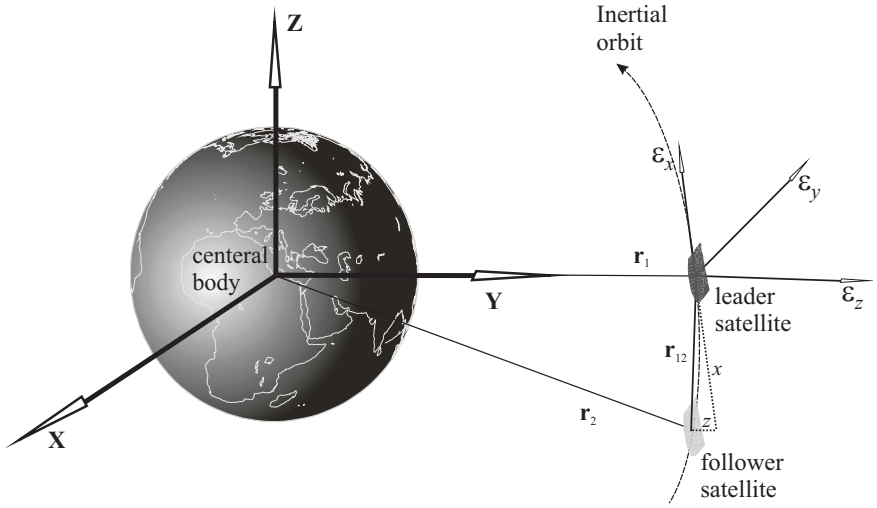

(a)

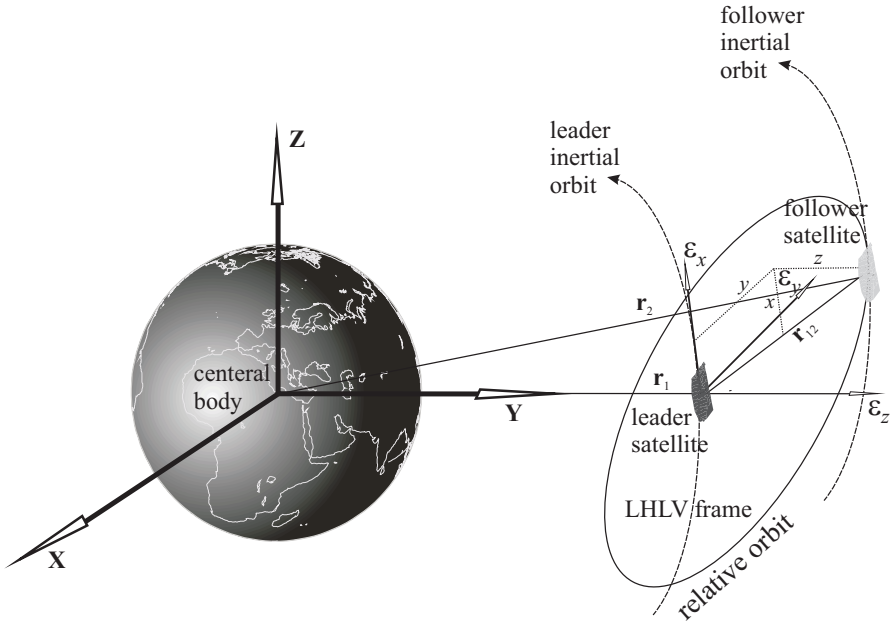

(b)

Fig. 6.12: Illustration of the relative motion of two satellites with (a) simplest in-plane leader follower geometry and with (b) an out-of-plane geometry. The motion of the two satellites referred to the inertial frame XYZ and the Earth accelerates w.r.t XYZ but does not rotate.

are simplified to the well-known linearized Hill equations, also referred to as Clohessy-Wiltshire (or CW) equations (Clohessy and Wiltshire 1960, and it will be referred as HCW in the sequel)

$$\begin{aligned} \ddot{x} + 2\mathrm{n}\dot{z} \quad\quad &= f_x, \\ \ddot{y} \quad\quad +\mathrm{n}^2 y &= f_y, \\ \ddot{z} - 2\mathrm{n}\dot{x} \quad -3\mathrm{n}^2 z &= f_z. \end{aligned} \tag{6.35}$$

Eq. (6.35) is already given before in Sec. 3.3.2 in the non-dimensional coordinates (u, v, w). The relation between the non-dimensional coordinates given in Eq. (3.57) and the one in Eq. (6.35) is given by

$$\mathrm{u} = \frac{z}{r_1}, \qquad \mathrm{v} = \frac{x}{r_1}, \qquad \mathrm{w} = \frac{y}{r_1}. \tag{6.36}$$

The HCW equations of Eq. (6.35) can be solved in a closed form, assuming that there are no perturbations present or the thrusting accelerations are switched off (i.e. $f_x = f_y = f_z = 0$) as

$$\begin{aligned} x(t) &= z_0[6(\sin(\mathrm{n}t) - \mathrm{n}t)] + x_0 + \dot{z}_0[\frac{2}{\mathrm{n}}(\cos(\mathrm{n}t) - 1)] + \dot{x}_0[\frac{1}{\mathrm{n}}(4\sin(\mathrm{n}t) - 3\mathrm{n}t)], \\ y(t) &= y_0\cos(\mathrm{n}t) + \dot{y}_0\frac{\sin(\mathrm{n}t)}{\mathrm{n}}, \\ z(t) &= z_0(4 - 3\cos(\mathrm{n}t)) + \dot{z}_0(\frac{\sin(\mathrm{n}t)}{\mathrm{n}}) + \dot{x}_0[\frac{2}{\mathrm{n}}(1 - \cos(\mathrm{n}t))]. \end{aligned} \tag{6.37}$$

The formation options are easily derived from a few principles of the relative dynamics of a circular orbit (see NG2 2009):

1. The y-component of the equations of motion is decoupled from the x- and z-components.
2. The x- and z-components are coupled with each other. Any perturbation in the xz-plane has an amplitude ratio of $x_{max} \geq z_{max}$.
3. The satellites of a formation must not have different along-track velocities $\dot{x}(z)$ at the same altitude, otherwise the formation will secularly drift apart.
4. If no secular drift $\Delta\dot{x}$ (according to item (3)) is present an along-track bias Δx is conserved on average.
5. All relative orbit motions, except the secular drift (3), oscillate described by trigonometric functions with the orbital period around the unperturbed orbit. The maxima of the amplitude can be freely chosen to lie at any point of the orbit.

The HCW equations are very convenient to explore which possible natural and unforced formation shapes are feasible. For example, in order to have a long term stable formation, the satellites must be kept apart from the secularly drifting (i.e. all orbit periods must be equal or $\Delta a = 0$, where a is the semi-major axis). This can be easily obtained from Eq. (6.37) as

$$\dot{x}_0(t) + 2\mathrm{n}z(t) = 0. \tag{6.38}$$

In addition, a trivial solution is easily identified from Eq. (6.37) as

$$x_0 = d_c, \qquad y_0 = z_0 = \dot{x}_0 = \dot{y}_0 = \dot{z}_0 = 0. \tag{6.39}$$

This corresponds to the ***GRACE-type*** formation (purely along-track configuration), which was depicted in Fig. 2.4 (see Chapter 2) and is represented in the orbital coordinates as shown in Fig. 6.13(a).

There is no solution that allows a constant distance for the x- and z-components. When the x- and z-components are coupled, there is also no solution that has a purely motion in along-radial-track or radial-cross-track or along-cross-track direction.

Apart from the GRACE-type solution, the solution with the minimal distance change in the along-radial-plane can be determined from Eq. (6.37) by setting the conditions

$$z_0 = d_c, \qquad \dot{x}_0 = -2\mathrm{n}z_0, \qquad x_0 = y_0 = \dot{y}_0 = \dot{z}_0 = 0. \tag{6.40}$$

This type of relative motion has the shape as an ellipse with axis ratio 2:1. This means that the larger axis being oriented in along-track direction is twice the shorter axis being oriented in radial-track direction. This solution is well known in this thesis as ***Radial wheel-type*** formation (with along-radial components). This type is already shown in Fig. 2.5(a) and Fig. 2.5(b) and is explained with its orbital coordinates in Fig. 6.13(d).

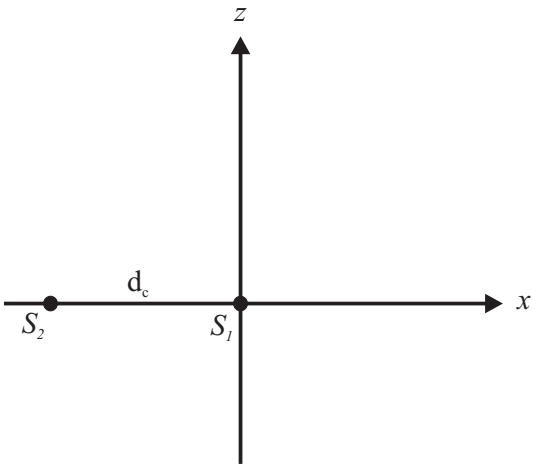

(a) GRACE-type

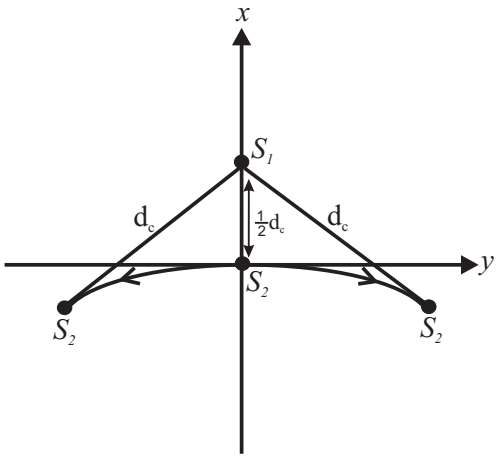

(b) Pendulum-type

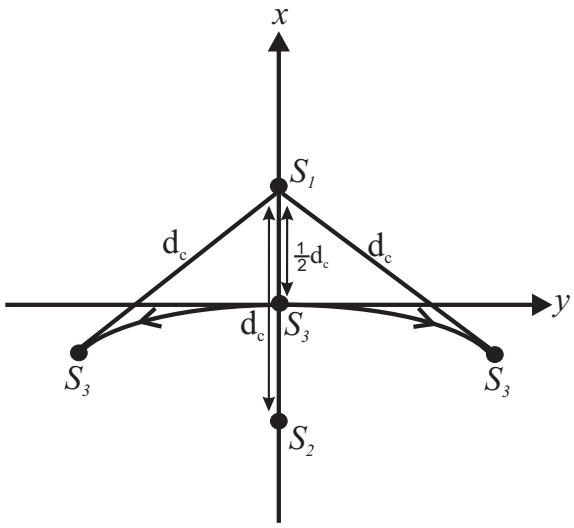

(c) GRACE-Pendulum-type

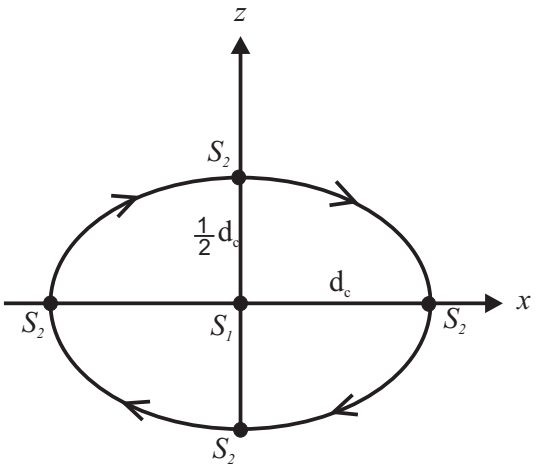

(d) Radial wheel-type

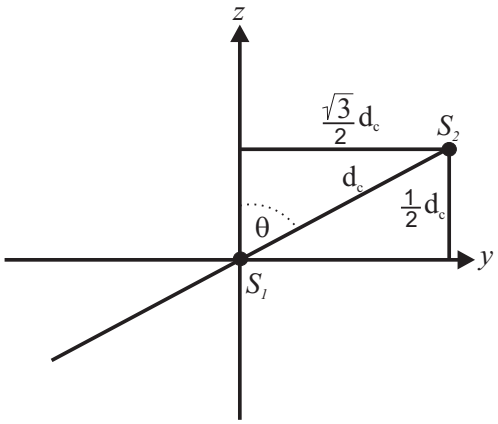

(e) Inclined wheel-type

Fig. 6.13: The relative motion of the proposed satellite formation flights.

By using the remaining freedom in the cross-track component, one can fine adjust the ellipse to a circle. This means that a solution with constant inter-satellite distance can be obtained by setting the following conditions

$$y_0 = -\frac{\sqrt{3}d_c}{2}, \qquad z_0 = d_c, \qquad \dot{x}_0 = -2\mathrm{n}z_0, \qquad x_0 = \dot{y}_0 = \dot{z}_0 = 0. \tag{6.41}$$

Where θ represents the angle of the inclined xy-plane w.r.t. the orbital plane as shown in Fig. 6.13(e). This solution is well known in this thesis as ***Inclined wheel-type*** formation (confirming all components), which is formerly indicated in Fig. 2.6.

Applying the x-bias and in addition applying a x- or y-amplitude, an along-cross-track configuration called ***Pendulum-type*** formation is obtained (see Fig. 6.13(b)). A radial x amplitude also induces an along-track motion. Hence, if one compares a solution with a x- or a y-amplitude of equal magnitude, the out-of-plane solution will lead to a lower maximal relative velocity between the satellites.

Consequently, a Pendulum formation should be defined as an out-of-plane Pendulum rather than as a radial Pendulum in order to minimize the relative velocity between the satellites for a given cross-track amplitude and an along-track bias. The condition for that is

$$x_0 = d_{c1}, \qquad y_0 = d_{c2}, \qquad z_0 = \dot{x} = \dot{y} = \dot{z} = 0, \tag{6.42}$$

where the d_{c1} and d_{c2} are the inter-satellite distances in along-track and cross-track directions, respectively. It is noting here that the inter-satellite cross-track distance can be freely chosen depending on the selected separation angle between the two satellites (i.e. $\Delta\Omega$). In this thesis, a separation angle of 1.5° has been selected producing inter-satellite cross-track distance $d_{c2} \approx 2d_{c1}$ (see Sec. 6.4.4).

6.3.3 The Use of Keplerian Parameters Difference

One obvious disadvantage when using the Hill coordinates (x, y, z) is that their differential equations (HCW) must be solved in order to obtain the relative orbit geometry. It is shown that the relative orbit is determined through the leader orbit motion and the relative orbit initial conditions (x_0, y_0, z_0, $\dot{x}_0$, $\dot{y}_0$, $\dot{z}_0$) forming six constants of the relative orbit motion. However, it is not convenient to determine the instantaneous geometry of the relative orbit motion.

Instead of using these six relative orbit constants to define the relative orbit and attain a bounded relative motion constraint, we will make use of other relative orbit parameters. These parameters would yield equivalent results without the need for the linearization assumptions and the near-circular orbit requirements. This can be done using the six Keplerian parameters to find the current satellite states. Therefore, the algebraic Kepler's equation must be numerically solved to find firstly the current mean anomaly angle. Since there is essentially only one state M, then the satellite position can be calculated and found for this M. See Appendix A for the mathematical description and for solving the Kepler equation. The benefits of using the Keplerian parameters are that they simplify the orbit description and the satellite's position computation on the one hand. On the other hand, these parameters are changing slowly even at the presence of some perturbations such as gravitational perturbations or non-gravitational ones (e.g. atmospheric drag).

6.4 Different Missions Simulation Scenarios

The aforementioned description of the different scenarios of the formation flights with their distinguished conditions gave a view of an existence of other formation possibilities. In the following, simulation scenarios concerning the study of each formation are introduced. The feasibility of these four formation flight concepts will be discussed as a step for using them in the gravity field analysis. The following sections will focus on simulation scenario analysis in terms of relative motions between the FF satellites. The analysis in terms of gravitational signal content and gravity field recovery will be introduced later in Chapter 7. But one can

generally say that it is expected from the latter three formation flight concepts in Sec. 6.3 to surpass the GRACE-type FF in terms of gravitational signal content since they have additional information in different directions. The orbit characteristics used in these simulations for the comparative study of these four types are summarized as follow:

- approximate-polar orbit (i=89.5°),
- approximate-circular orbit (small eccentricities ranging from e=0.001 to 0.01),
- orbital altitude of h=400 km, and hence all the studied formations have roughly the same orbital period due to their similar altitude,
- inter-satellite distance ranging from 100 to 200 km.

It is pointed out that in case of all simulation scenarios, the satellites constituting the formations are considered in this thesis as test masses. The motion of these satellites is considered as a free-fall motion in the Earth's gravity field. The relative motion between the satellites is measured as relative distances, relative velocities and relative accelerations.

6.4.1 GRACE-type Mission Simulation Scenario

This mission type is denominated as the along-track (or in-track) formation due to the major sensitivity direction for detecting the gravitational field. It is also considered as the simplest and realistic satellite configuration which is already successfully applied with the GRACE twin-satellite mission. One can observe immediately that this formation type is a valid formation option, in which the satellites follow each other in the orbit at a constant distance. This can be seen from the relative motion between the two satellites of GRACE-type as shown in Fig. 6.14 from different views of the observer. For the simplified case of a circular Kepler-problem, Fig. 6.14(a), Fig. 6.14(b) and Fig. 6.14(c) illustrate the motion of the two satellites in the three planes XY, YZ and XZ, respectively, in addition to the motion in plane (XYZ) as indicated in Fig. 6.14(d). The motion in these figures are referred to an inertial system with specifically selected initial conditions so that the relative motion of the GRACE-type FF is bounded. Bounded motion means that the formation does not get further away from each other and does stay at a constant distance.

For the simulation scenarios investigated in the following, a nominal inter-satellite distance between the two satellites of this type was selected to be 200 km as recommended in Sec. 6.2.3.1. The orbits of the two satellites have been integrated using a realistic ITG-GRACE03s gravity field model (a product of the real GRACE mission) up to SH (spherical harmonics) degree and order 180 for only one month time span. The selected orbital parameters are shown in Table 6.3 with identical Keplerian parameters for both satellites except for the argument of perigee and the mean anomaly. The inter-satellite distance is ranging between 199.95 km to 201 km as shown in Fig. 6.15. As expected, the last day of the orbit integration differs from the first day, which emphasizes that the relative motion is bounded as said before except for the long-term trend in the inter-satellite range. This behavior is similar to the observed real GRACE mission. The same phenomenon holds also for the range-rate and the range-rate changes. Therefore, we can say that the GRACE-type mission scenario is a quite stable formation, in principle for different types of inter-satellite distances.

This configuration is still the preferable one from the implementation point of view in spite of its strong measurements anisotropy. This anisotropy is already mentioned in Sec. 2.2.1 and at the beginning of this Chapter due to the aliasing phenomena and also due to the shape of the noise structure that is larger in the meridian direction. The error structure indicating north-south stripes of the errors in the solutions is not suitable for detecting such gravitational signals especially of high frequencies (e.g. ocean tides and atmospheric signals).

It will be shown in Chapter 7 how the gravity solution is affected by these inherent error types in the meridian (north-south) direction due to the aforementioned reasons described in Sec. 6.2 (e.g. spatial-temporal resolution due to the subsatellite-tracks variability and coverage period).

Table 6.3: Keplerian orbital parameters for the collinear GRACE-type FF.

Orbital Parameters	**GRACE-type FF**		
	GRACE A	GRACE B	Difference
a [km.]	6778.137	6778.137	Δa=0.0
e	0.001	0.001	Δe=0.0
i [deg.]	89.5	89.5	Δi=0.0
Ω [deg.]	0.0	0.0	$\Delta\Omega$=0.0
ω [deg.]	0.0	2.4	$\Delta\omega$=2.4
M [deg.]	0.0	-0.744	ΔM=0.74

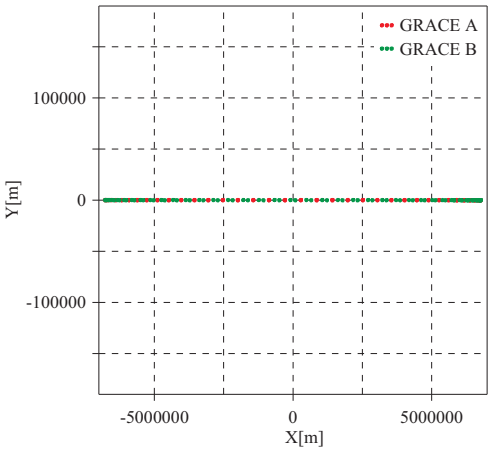

(a) XY-plane

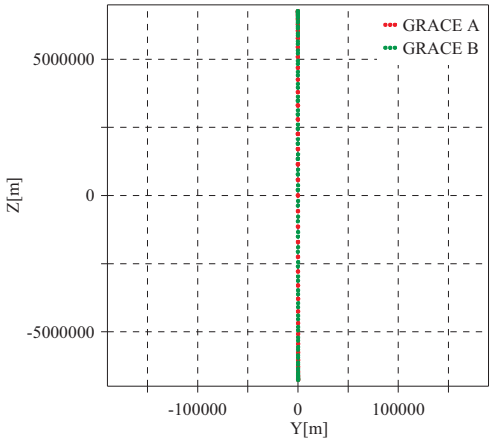

(b) YZ-plane

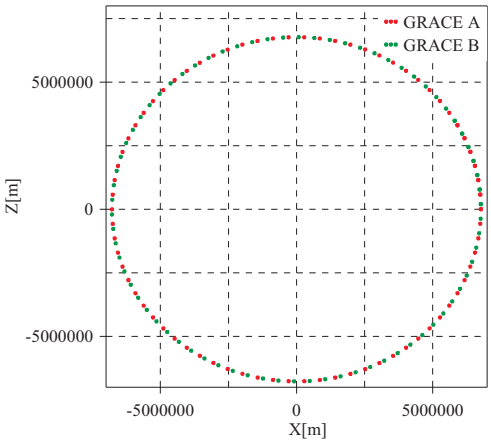

(c) XZ-plane

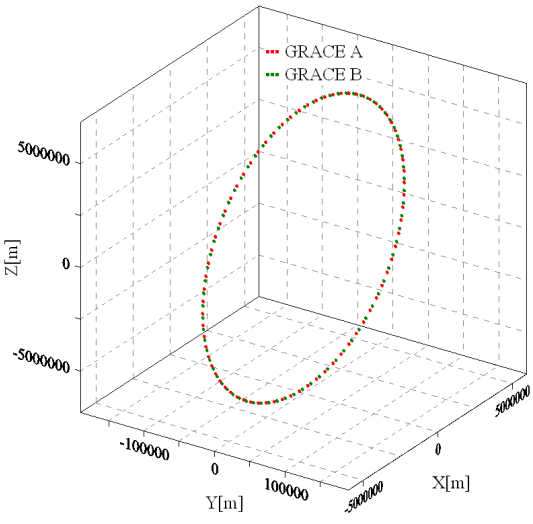

(d) XYZ-plane

Fig. 6.14: The relative motion of two GRACE-type FFs.

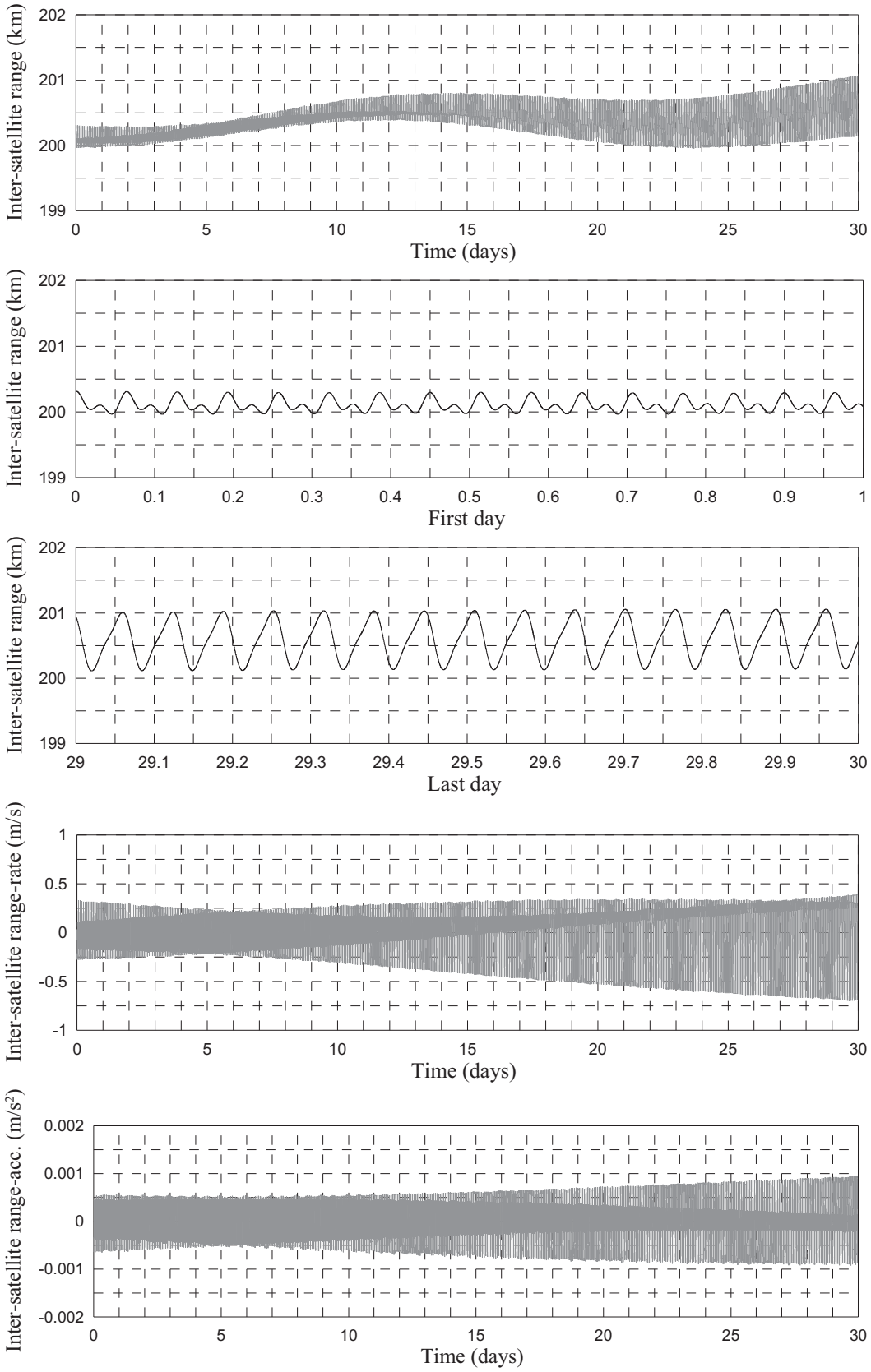

Fig. 6.15: The inter-satellite range, range-rate and range-changes of the two satellites of GRACE-type.

6.4.2 Radial wheel-type Mission Simulation Scenario

6.4.2.1 East-West Radial wheel-type FF

Alternative mission scenarios, which can improve the gravity field estimation, implies the use of multiple information of the satellite's observations. The execution of this mission type overcomes the limitations of the baseline scenario, whose inter-satellite range is restricted to only one type scale of distance, either small or large. It provides multiple and different scales of inter-satellite ranges during its satellite revolutions. The basic concept of the Radial wheel formation is already given in Fig. 6.13. It enables multiple information types of satellite observations, when considering the relative motion of the follower satellite S_2 around the leader one S_1.

Two major information types are very promising and sensitive for the gravity field recovery. One of these is obtained during the motion in the along-track direction (x), while the other motion type is performed in the radial direction (z). The inter-satellite range of the along-track direction is twice of the radial one. Therefore, this type of motion is referred to as 2:1 relative motion about their center of mass. The observations during the majority of the time are composed of a combination of the along-track and radial directions.

By considering the relative motion of the two satellites in Radial wheel-type FF as illustrated in Fig. 6.17, one realizes that the relative motion is similar to the GRACE-type as long as the two satellites of the Radial wheel-type FF are constituting a motion in the along-track direction. As the two satellites proceed towards the equator, they perform a relative motion in the radial direction as shown in Fig. 6.17(c). This means that the relative motion takes place in the same local vertical plane.

The Radial wheel formation has been chosen as study case because it provides a better global improvement of the gravity solutions among those in which the satellite's relative motion is bounded in a plane along the orbit, and thus is still relatively simple to be implemented.

6.4.2.2 Controlling the Stability of the Radial wheel-type FF

When applying a trivial solution as follow:

$$\Delta a = 0, \quad \Delta e = 0, \quad \Delta i = 0, \quad \Delta\Omega = 0, \tag{6.43}$$

and setting the two remaining Keplerian elements, argument of perigee and mean anomaly, as

$$\Delta\omega = \Delta M = 180, \tag{6.44}$$

then the Radial wheel-type FF can be designed. We have to note here that for designing a stable Radial wheel-type formation, the differences in the RAAN angle was set to be zero that follows from Eq. (6.43). The longitude of the ascending node of the satellites may differ slightly avoiding a collision of both satellites as introduced by Massonnet (1998). If the satellite orbits have a regular spacing of the argument of perigee (ω), then they will describe an ellipse around a reference point along an orbital period.

The eccentricity (e) is the most important parameter for determining the shape and the dimension of the 2:1 relative elliptical motion. If the satellite altitude is already fixed, then it holds according to the following relation between the eccentricity and the inter-satellite range (ρ) (Sneeuw et al. 2008),

$$e = \frac{\rho_{min}}{2a} = \frac{\rho_{max}}{4a}, \tag{6.45}$$

where ρ_{min} is the minimum inter-satellite range represented by the minor-axis in the radial component of the 2:1 relative ellipse and ρ_{max} is the maximum inter-satellite range represented by the major-axis in the along-track component of the 2:1 relative ellipse. The formation yields a constant angular velocity as viewed from its center when the eccentricities of the two satellites are set to be identical.

Two suggestions for performing the Radial wheel-type FF have been considered; east-west Radial wheel-type

and north-south Radial wheel-type, according to the motion of one satellite relative to the other one w.r.t. the Earth's equator. The selected initial conditions are given in Table 6.4. The two formation types satisfy the conditions in Eq. (6.43) and Eq. (6.44), but differ only in the values of the argument of perigee (ω) and the mean anomaly (M).

The nominal inter-satellite range has been selected between 100 km defining the minor diameter of the relative ellipse and 200 km defining the major one, and maintaining 150 km mean distance between the satellites. A behavior of one month simulation of east-west Radial wheel-type FF with its both first and last day satellite separations are shown in Fig. 6.18. The inter-satellite baseline between the satellites is stable for the first several revolutions producing a periodic oscillation at a frequency of 2 cycles-per-revolution. At the end of the month, the east-west Radial wheel-type FF drifted slightly only in the along-track direction but providing a still stable bounded relative motion.

Table 6.4: Keplerian orbital parameters for the Radial wheel-type FF with its both postulations. Radial wheel-type 1 depicts east-west motion and Radial wheel-type 2 depicts north-south motion.

Orbital	**Radial wheel-type FF**				
	East-West Radial wheel		North-South Radial wheel		Differene
Parameters	Radialw. 1A	Radialw. 1B	Radialw. 2A	Radialw. 2B	
a [km.]	6778.137	6778.137	6778.137	6778.137	Δa=0.0
e	0.0074	0.0074	0.0074	0.0074	Δe=0.0
i [deg.]	89.5	89.5	89.5	89.5	Δi=0.0
Ω [deg.]	0.0	0.0	0.0	0.0	$\Delta\Omega$=0.0
ω [deg.]	0.0	-180	270	90	$\Delta\omega$=180
M [deg.]	90	-90	90	-90	ΔM=180

6.4.2.3 Radial wheel-type FF as a Gravity Gradiometry

The Radial wheel-type FF provides different observables in different directions as introduced in Sec. 6.4.2.1. Each measurement type can be accounted for as a single component of the gravity gradient tensor $\mathbf{V}$. So by considering again the observations in the LOS direction, we find that the range-rate $\dot{\rho}$ in Eq. (5.35) between the two satellites is a projection of the relative vectorial velocity $\dot{\mathbf{r}}_{12}$ (where $||\dot{\mathbf{r}}_{12}|| = \dot{\rho}$) onto the LOS unit vector $\mathbf{e}$. The scalar range acceleration $\ddot{\rho}$ can be obtained from Eq. (5.36) by numerical differentiation.

If we use the Newton's equation of motion, one can set the vectorial acceleration $\ddot{\mathbf{r}}_{12}$ (where $||\ddot{\mathbf{r}}_{12}|| = \ddot{\rho}$) equal to the difference in gravitational attraction $\Delta V_{1,2}$ between the two satellites S_1 and S_2. Then the in-line gravity gradient $\mathbf{e}^T\mathbf{V}\mathbf{e}$ (with $\mathbf{V}$ the gravity gradient tensor) in the baseline direction can be obtained when dividing this vectorial acceleration by the baseline.

In this sense, the observable becomes V_{xx} as the baseline approaches to the along-track direction and becomes V_{zz} as the baseline becomes close to the radial direction. In other words, the observed gravity gradient $\mathbf{e}^T\mathbf{V}\mathbf{e}$ contains projections of multiple tensor components $V_{ij}, i, j \in [x, y, z]$. When considering a rotational angle (ξ) around the y-axis, that represents the cross-track direction, the baseline is directed in a new x'-axis and the gravity observable is then given by (Sneeuw and Schaub 2005)

$$V_{x'x'} = \cos^2\xi V_{xx} + 2\cos\xi\sin\xi V_{xz} + \sin^2\xi V_{zz}. \tag{6.46}$$

As previously mentioned that the Radial wheel-type FF contains at certain latitudes a pure along-track gravity information, a pure radial information and a combination of both components at the majority of the latitudes. Therefore, Eq. (6.46) becomes valid for the observable of this formation type providing a measurement of all three components of the gravity gradient tensor (V_{xx}, V_{xz}, V_{zz}). These three types of measurements can also be obtained using three satellites in a triangle formation or in a spoke formation of six satellites. The first option seems to be more complicated since it requires two ranging systems on board of each satellite. While the latter option seems to be too expensive for the purpose of the gravity field recovery. More details of these two options can be found in Sneeuw and Schaub (2005) and Wiese et al. (2008).

6.4.2.4 North-South Radial wheel-type FF

The geometry of the Radial wheel-type FF can be also realized as mentioned in Sec. 6.4.2.2 applying the same conditions in Eq. (6.43) and Eq. (6.44) but instead of placing the satellites in east-west direction, the two satellites are located in the north-south direction. The orbital parameters are given in Table 6.4. The argument of perigee of this formation type is shifted by 180° as ω_1=270° and ω_2=90°, but can be also set vice versa as ω_1=90° and ω_2=270° as another possibility for a north-south Radial wheel formation. In this case, the mean anomaly of the two satellites will be shifted by -180° as M_1=-90 and M_2=90, respectively.

The nominal inter-satellite range of north-south Radial wheel-type FF is as stable as the east-west one with the same periodic oscillation. But at the end of the month, the along-track of this type is drifted larger than the east-west Radial wheel-type as shown in Fig. 6.19. This occurs because the along-track oscillations are taking place at the equator regions of the Earth. Therefore, this drift can be attributed to the effect of the Earth's oblateness, represented in the zonal harmonic J_2 which causes the largest perturbation. The investigation of this thesis is based on the first east-west Radial wheel-type FF since it is considered to fly in a more stable bounded formation than the north-south type.

6.4.2.5 Combined Radial wheel-types

The previous concepts of east-west and north-south Radial wheel-type FFs can be combined together in a single mission scenario (i.e. one constellation) composed of four satellites in two formation flights (or one constellation). This concept is already considered and applied in the gravity field analysis by Wiese et al. (2008). Fig. 6.16 shows the concept of such a mission, in which the satellites 1 and 2 build a satellite pair (representing the east-west type) and the satellites 3 and 4 another pair (representing the north-south type). Satellites 1 and 2 collect observations in the along-track direction and the other two satellites 3 and 4 in radial direction (Fig. 6.16(a)) and vice versa as shown in Fig. 6.16(b). This means that at a particular time, the major diameter of the relative ellipse of satellites 1 and 2 will be compatible with the minor diameter of the relative ellipse of satellites 3 and 4. This is the advantage of this formation that provides a largely isotropic sampling than the previously mentioned Radial wheel-types.

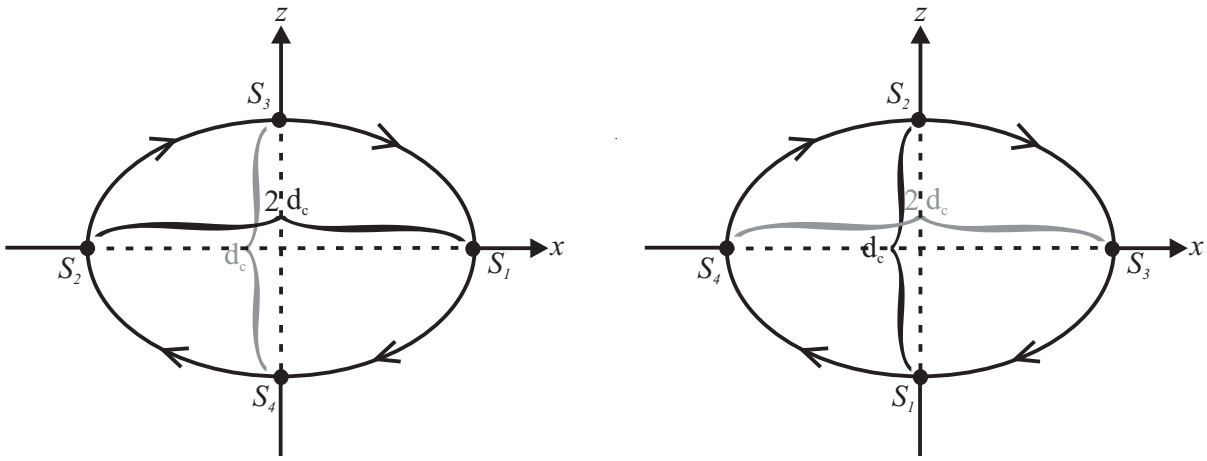

Fig. 6.16: The relative motion of four satellites of both Radial wheel-types FF.

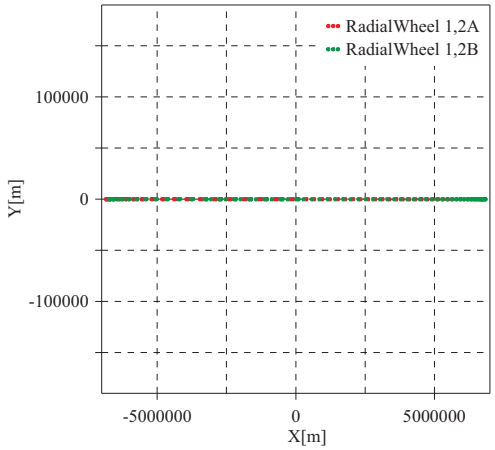

(a) XY-plane

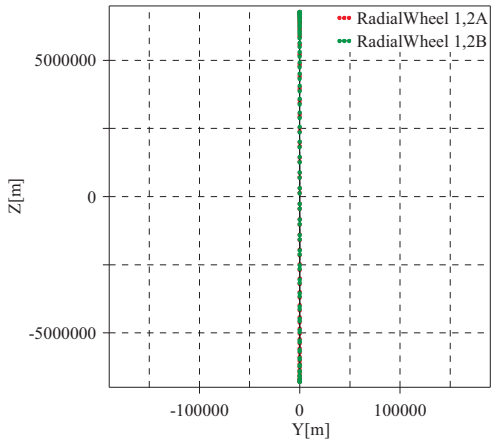

(b) YZ-plane

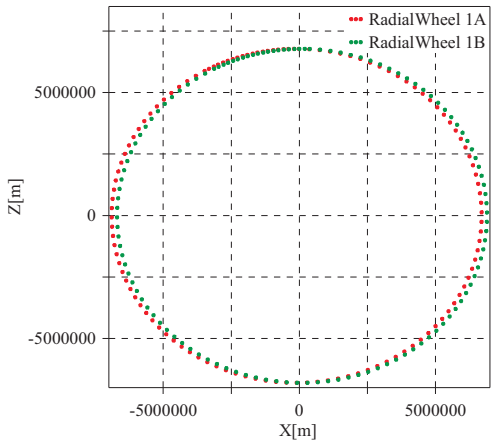

(c) XZ-plane

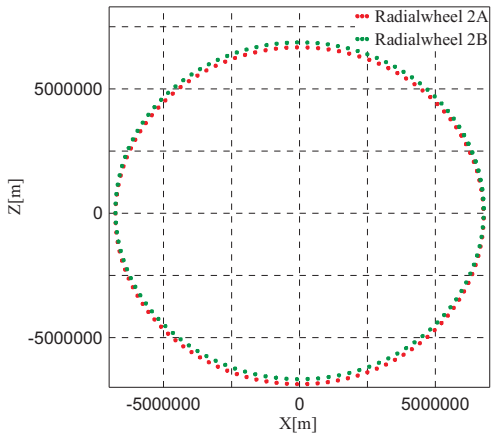

(d) XZ-plane

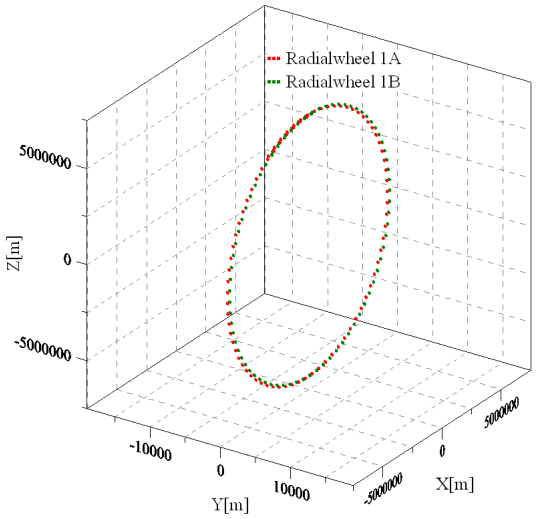

(e) XYZ-plane

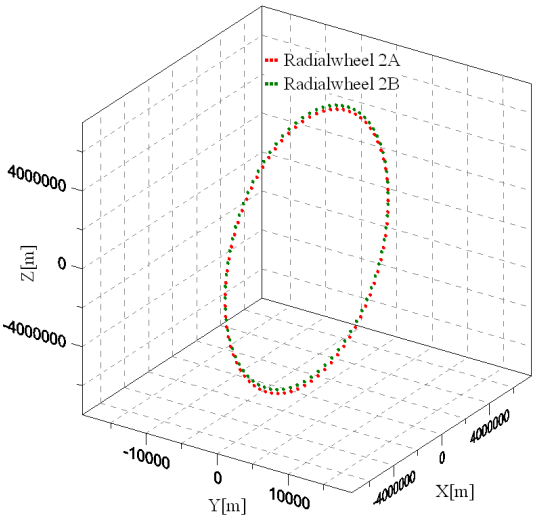

(f) XYZ-plane

Fig. 6.17: The relative motion of two Radial wheel-type FFs, (a) in the XY-plane, (b) in the YZ-plane, (c) in XZ-plane of type 1, (d) in XZ-plane of type 2, (e) in XYZ-plane of type 1 and (f) XYZ-plane of type 2.

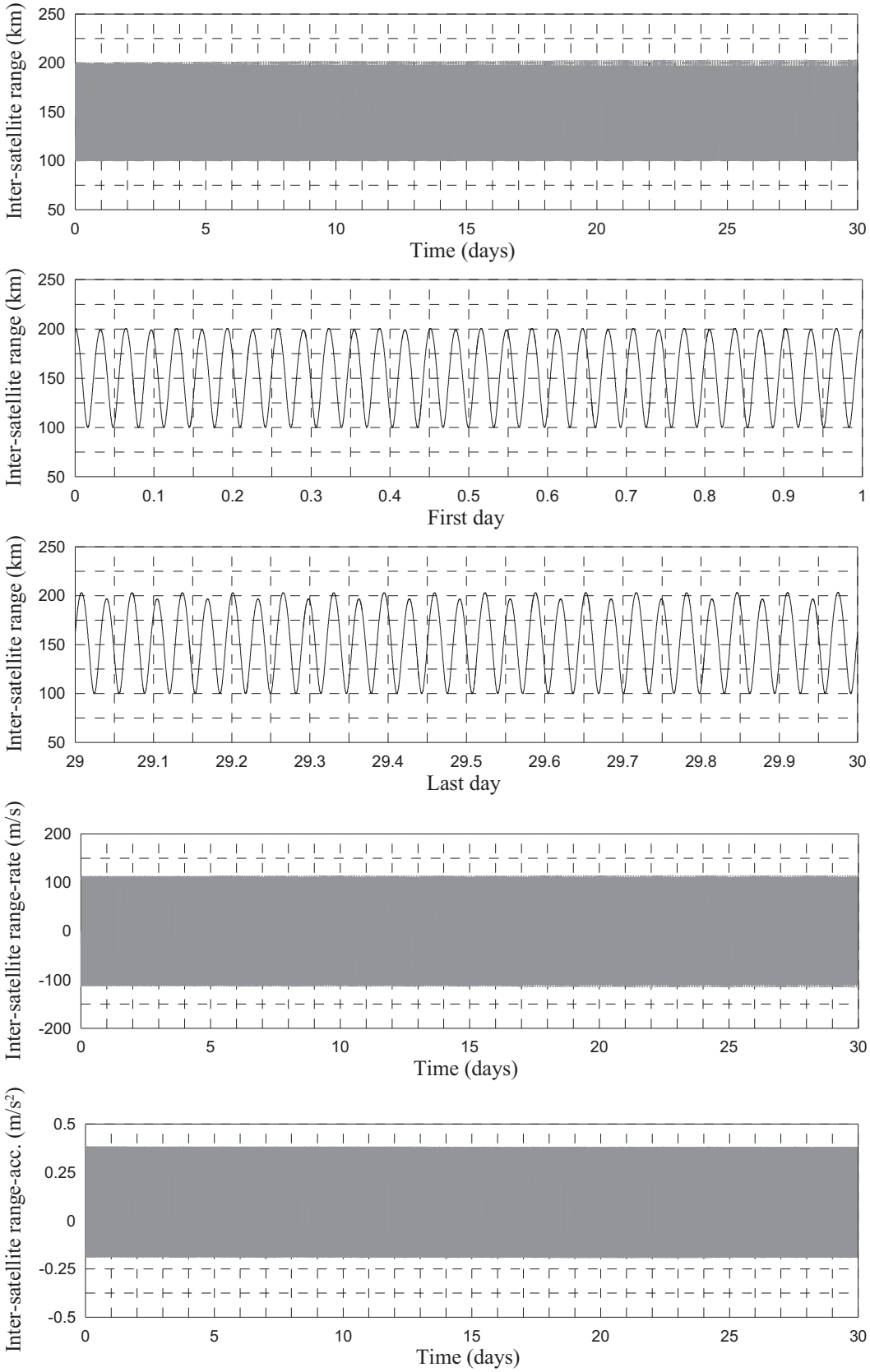

Fig. 6.18: The inter-satellite range, range-rate and range-changes of two satellites of Radial wheel-type1.

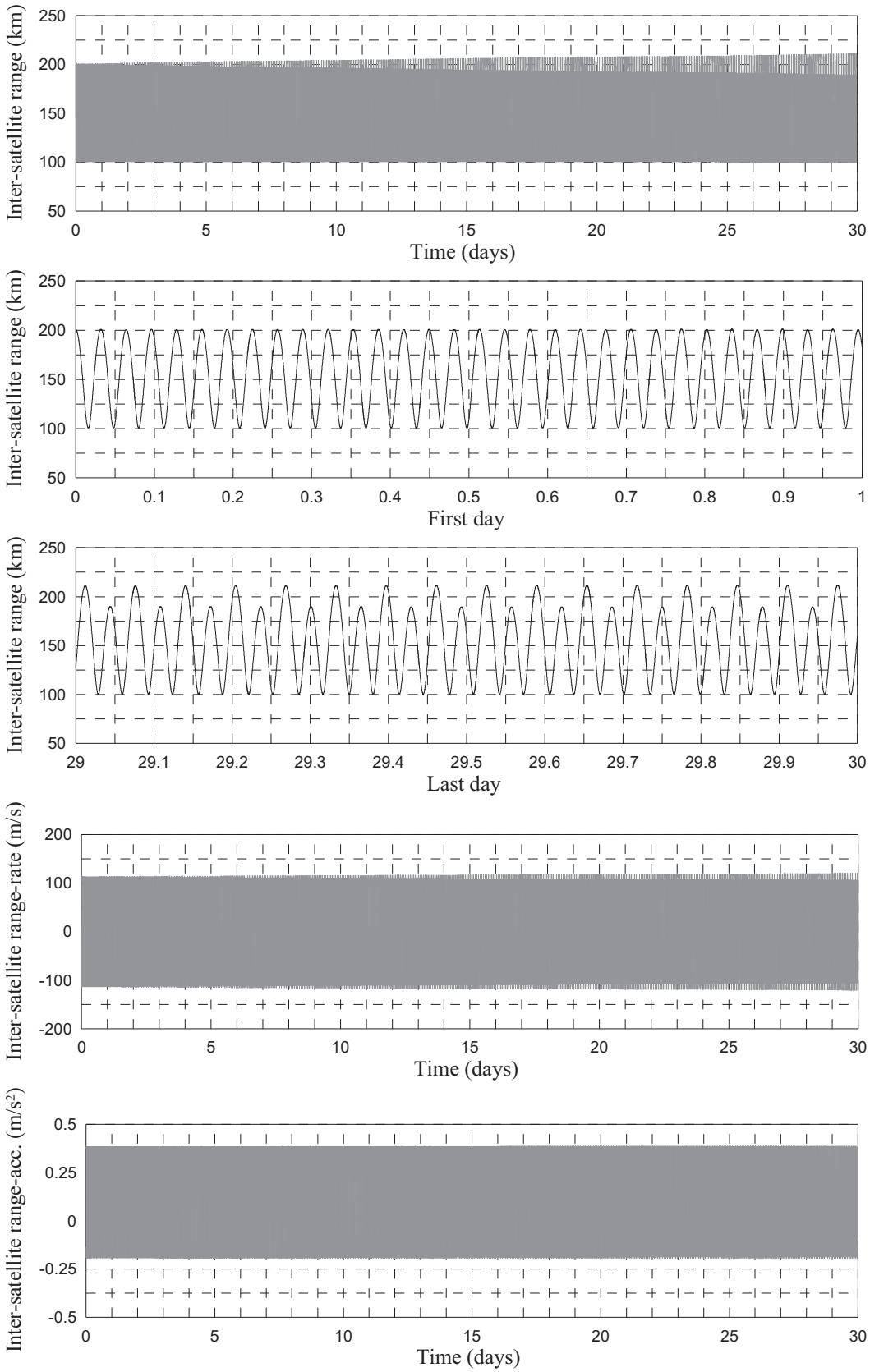

Fig. 6.19: The inter-satellite range, range-rate and range-changes of two satellites of Radial wheel-type2.

6.4.3 Inclined wheel-type Mission Simulation Scenario

An out-of-plane motion can be decoupled from the in-plane motion of the previous Radial wheel-type by selecting non zero differencing RAAN angle (Ω) or inclination (i) in Eq. (6.43). Therefore, an out-of-plane formation with a relative circular motion, known here as Inclined wheel-type, is carried out by imposing $\Delta\Omega$ and Δi. A formation with the non-zero inclination difference (Δi) results in the maximum out-of-plane separation taking place at the maximum latitude. On the contrary, a non-zero right ascension difference ($\Delta\Omega$) results in the maximum separation taking place at the equator as shown in Fig. 6.20.

A formation with a non-zero inclination difference Δi has three orbital drawbacks. It produces the follower satellite to have a slight different nodal precession rate ($\dot{\Omega}$), a slightly different orbit period and a slightly different argument of perigee rate ($\dot{\omega}$), since these elements are dependent on the inclination (refer to Eq. (6.4)). Therefore, achieving a stable SFF with Δi to investigate the recovery of the Earth's gravity field is not guaranteed. For this reason, this formation type has not been considered in this thesis.

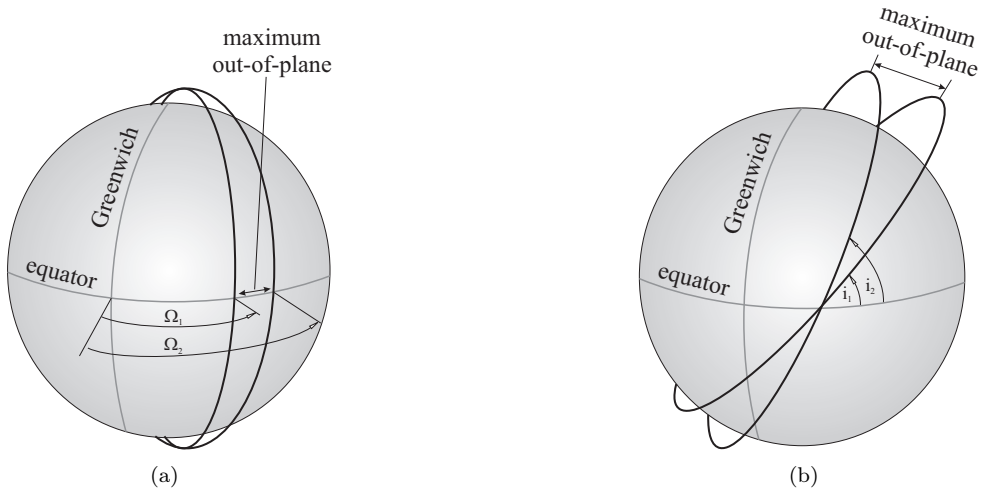

Fig. 6.20: Two satellite orbits with out-of-plane motion. (a) an out-of-plane imposed by $\Delta\Omega$, (b) an out-of-plane imposed by Δi (after Alfriend et al. 2000).

In this thesis, a selection of a non-zero RAAN angle was carried out to obtain an out-of-plane relative motion as explained in Alfriend et al. (2000), where the relative state vector can be transformed into the corresponding initial Keplerian parameters. The formation can be designed directly in terms of differential Keplerian orbital parameters as introduced by Sneeuw et al. (2008). This approach was selected by setting the argument of perigee and the mean anomaly difference $\Delta\omega = \Delta M = 180°$ for establishing the in-plane relative motion as described in the Radial wheel-type FF. Then to achieve an out-of-plane motion between the two satellites, an ascending node difference $\Delta\Omega$ was added as listed in Table 6.5. In this way, we have the satellite observations in the three along-track, cross-track and radial directions. These conditions do not guarantee that the distance between the satellites will remain constant, since the argument of perigee (ω) and the mean anomaly (M) of each satellite may drift at different rates making the lines of perigee to move apart over time. Therefore, we have chosen an eccentricity difference (Δe) to exaggerate the in-plane relative orbit.

The radial amplitude and the cross-track amplitude form an in-plane ellipse with a ratio of $1{:}\sqrt{3}$ as shown in Fig. 6.13(e). With an appropriate phasing, one obtains also a circular relative motion. Fig. 6.21 shows the circular relative motion in the LHLV frame. Fig. 6.21(a) and Fig. 6.21(b) show clearly the out-of-plane relative motion.

Fig. 6.22 represents the nominal inter-satellite distances between the two satellites. For the first revolutions,

the baseline is quite stable, but at the end of the simulated month, a significant drift is thus seen not only in the positive along-track direction (x) but also in the negative direction ($-x$). In addition, this formation type provides a variable baseline orientation. Therefore, it requires more studies from the implementation point of view. However, this formation provides the most isotropic sampling of all proposed and investigated satellite formation flights, since it provides satellite observables in all directions: the along-track, the cross-track and the radial.

Table 6.5: Keplerian orbital parameters for the Inclined wheel-type FF.

Orbital Parameters	**Inclined wheel-type FF**		
	Inc. wheel A	Inc. wheel B	Difference
a [km.]	6778.137	6778.137	Δa=0.0
e	0.005	0.01	Δe=0.005
i [deg.]	89.5	89.5	Δi=0.0
Ω [deg.]	0.0	1.5	$\Delta\Omega$=1.5
ω [deg.]	0.0	180	$\Delta\omega$=-180
M [deg.]	90	-90	ΔM=180

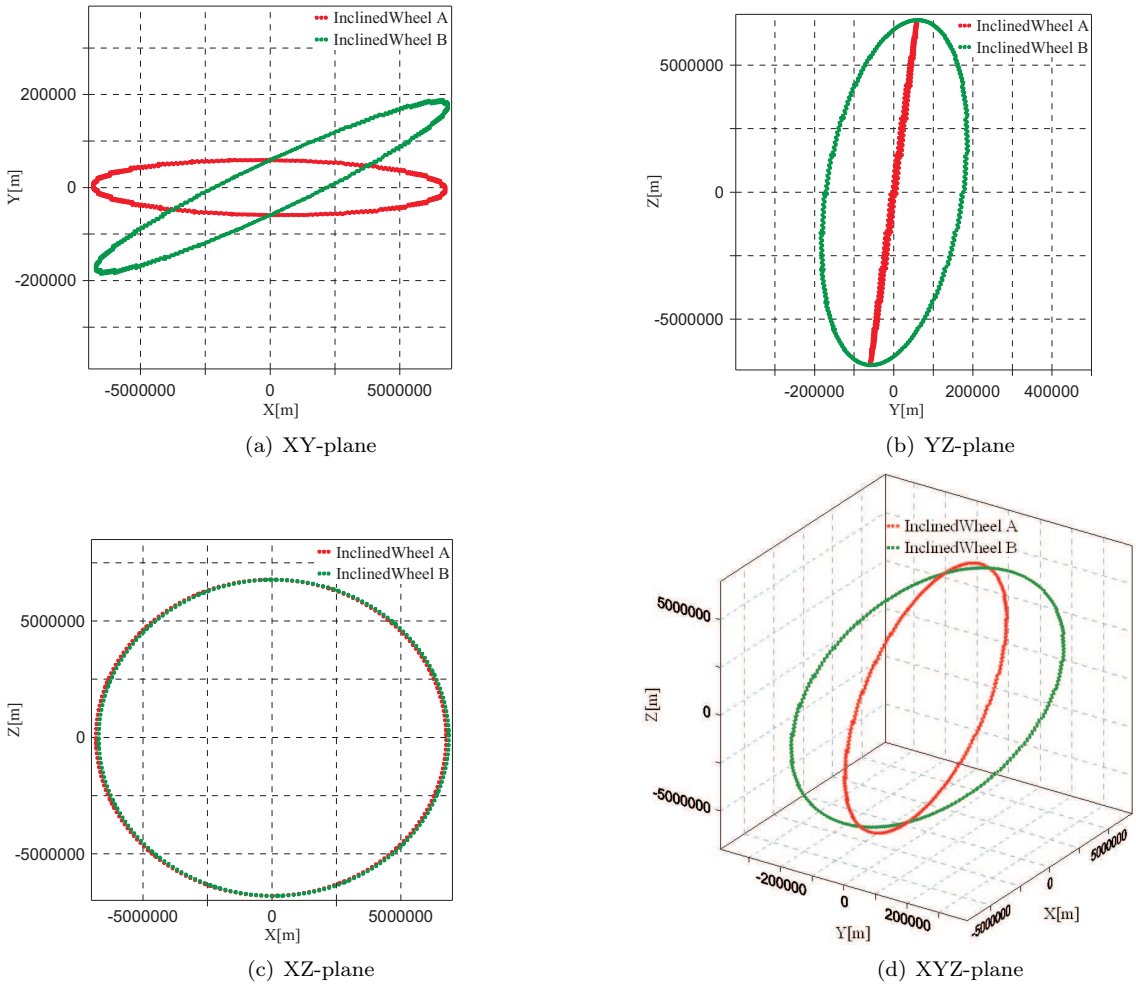

(a) XY-plane

(b) YZ-plane

(c) XZ-plane

(d) XYZ-plane

Fig. 6.21: The relative motion of two Inclined wheel-type FFs, (a) in the XY-plane, (b) in the YZ-plane, (c) in XZ-plane and (d) in XYZ-plane.

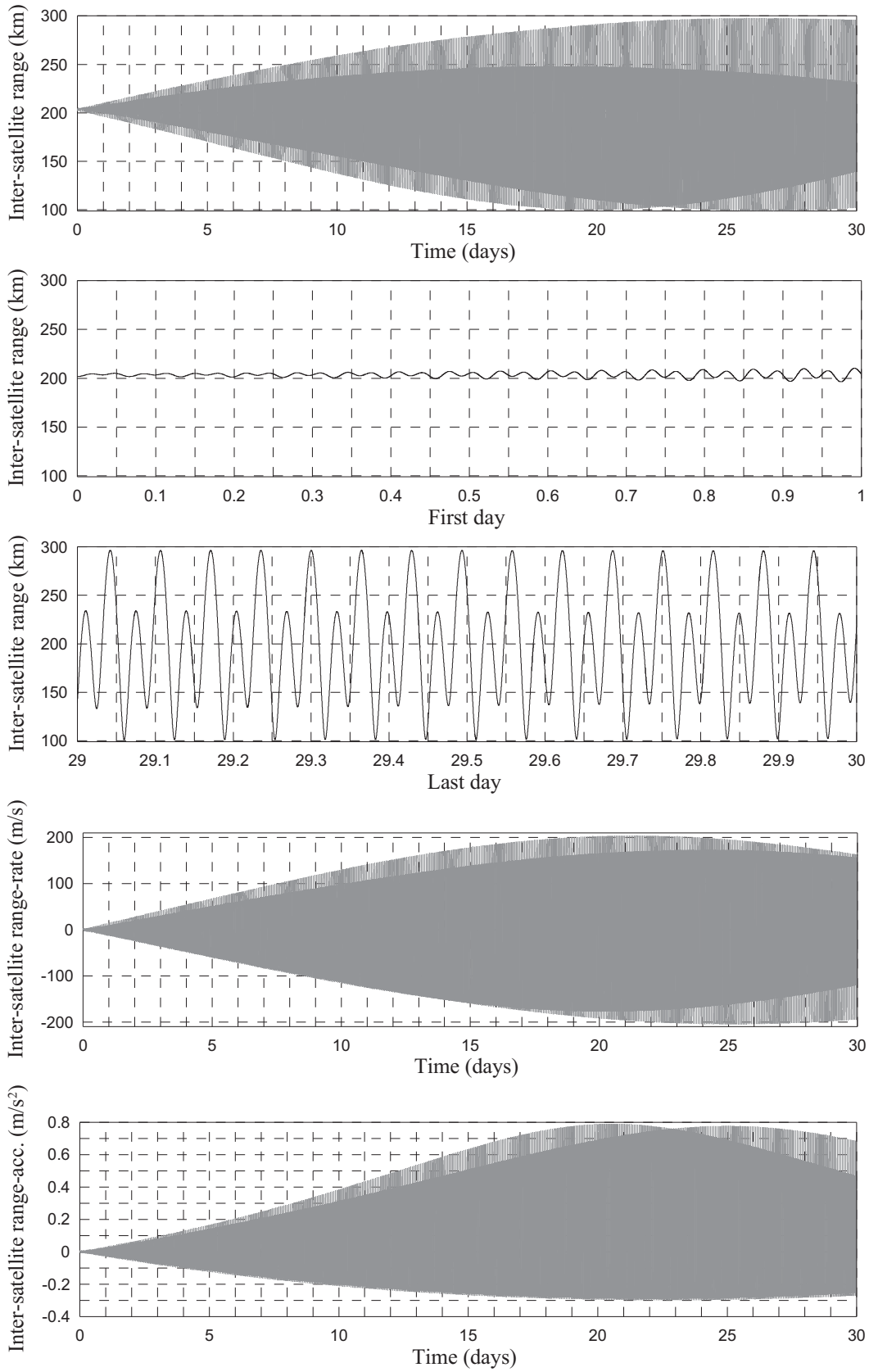

Fig. 6.22: The inter-satellite range, range-rate and range-changes of two satellites of Inclined wheel-type.

6.4.4 Pendulum-type Mission Simulation Scenario

A so called Pendulum-type formation is achieved when adding an out-of-plane motion (y-component) to the GRACE-type FF. The two satellites have slightly different orbit planes but the baseline vector is constant and orthogonal to the nadir. The ascending nodes will slightly differ, resulting in a maximum out-of-plane separation at the equator and the minimum at the pole. This is already given in Fig. 6.20(a). Therefore, no significant improvements are expected from the cross-track measurements at the pole regions, since the strongest elongation is reached at the equator.

Looking at the Table 6.6, we see that the mean anomaly M is equal to that one of the GRACE-type FF and hence the out-of-plane Pendulum will not show the secular drift in the mean anomaly contrary to the Radial wheel-type or Inclined wheel-type. This is considered as an advantage generating this out-of-plane Pendulum-type to fly in a bounded formation. This Pendulum-type was explained in Chapter 2 (see Fig. 2.7(b)). Considering only a cross-track component (without difference in the mean anomaly) yields a non-bounded formation with a very large variable inter-satellite distance due to the significant drift of the mean anomaly. This latter type was pointed out in Fig. 2.7(a).

The relative motion of both satellites (Fig. 6.23) takes place in the xy-plane. This means that the relative motion remains in the same local horizontal plane. Therefore, the in-plane (i.e. along-track) motion is similar to the GRACE-type FF in the xz-plane, while the out-of-plane motion takes place in the xy- and the yz-plane similar to the Inclined wheel-type FF. To generate a bounded relative motion, the out-of-plane amplitude should be twice the along-track amplitude (i.e. satisfies the condition of Eq. (6.42)), with no offset in the along-track direction. Note that the out-of-plane amplitude can be chosen freely.

In Fig. 6.24, the achieved inter-satellite range has been selected to realize the approximate range of the previous formations. Therefore, choosing a cross-track angle of 1.5° produces a maximum latitude separation of 200 km. We find that the inter-satellite distance varies between 85 km to 200 km due to the cross-track variation (while the along-track is constant). However, it is still a bounded formation in the gravity field. This variation needs to be controlled. This control must be mainly executed by the satellite's manoeuvres. This sort of investigation is beyond the scope of this thesis.

It should also be mentioned here that the second type (cross-track (only) Pendulum-type) shown in Fig. 2.7(a) has been also examined. But since its nominal inter-satellite distance varies (using the applied separation angle of 1.5°) between 2 km to 178 km, the gravity field recovery analysis using its SST measurements were left in this thesis.

6.4.5 GRACE-Pendulum-type Mission Simulation Scenario

A new mission scenario called GRACE-Pendulum-type is achieved when combining the two GRACE-type and Pendulum-type formation flights in one bounded formation as explained in Chapter 2 (see Fig. 2.8(a)). This formation is composed of three satellites (GR-Pend A, GR-Pend B and GR-Pend C), whose parameters are indicated in Table 6.6. It performs two inter-satellites baseline vectors in the horizontal plane, one of them is established between GR-Pend A and GR-Pend B satellites (correspond to GRACE-type FF) in the along-track direction and the other one between GR-Pend A and GR-Pend C (correspond to Pendulum-type FF) in the cross-track direction (Fig. 6.13(c)).

The combination of the third baseline between GR-Pend B and GR-Pend C has not been considered as an observation and its measurements have not been included during the set up of the observation equations for the analysis of the global gravity field recovery due to the following reasons. Firstly, the inter-satellite distance is ranging between 300 km to 400 km which means that this baseline will suffer from some problems that already mentioned in Sec. 6.2.3.1. For example, by this inter-satellite range, the potential coefficients of the gravitational signal with minimal wavelengths will be poorly detected. Secondly, the incorporation between the along-track observations and the cross-track ones is already achieved by that arm between GR-Pend A and GR-Pend C, therefore, adding the same type of cross-track measurements to the observations will be with nonsense. Another important reason is that, the extremely challenging from the technical point

of view by establishing for each satellite two on board ranging systems, which makes it hard to accomplish this formation type with three inter-satellite baselines.

Table 6.6: Keplerian orbital parameters for the out-of-plane nodal Pendulum-type FF (as seen in Fig. 2.7(b)) and GRACE-Pendulum-type FF(as seen in Fig. 2.8(a)).

Orbital	**Pendulum-type FF**			**GRACE-Pendulum-type FF**		
Parameters	Pendulum A	Pendulum B	Difference	GR-Pend A	GR-Pend B	GR-Pend C
a [km.]	6778.137	6778.137	Δa=0.0	6778.137	6778.137	6778.137
e	0.001	0.001	Δe=0.0	0.001	0.001	0.001
i [deg.]	89.5	89.5	Δi=0.0	89.5	89.5	89.5
Ω [deg.]	0.0	1.5	$\Delta\Omega$=1.5	0.0	0.0	1.5
ω [deg.]	0.0	0.0	$\Delta\omega$=0.0	0.0	2.4	0.0
M [deg.]	0.0	-0.744	ΔM=0.744	0.0	-0.744	-0.744

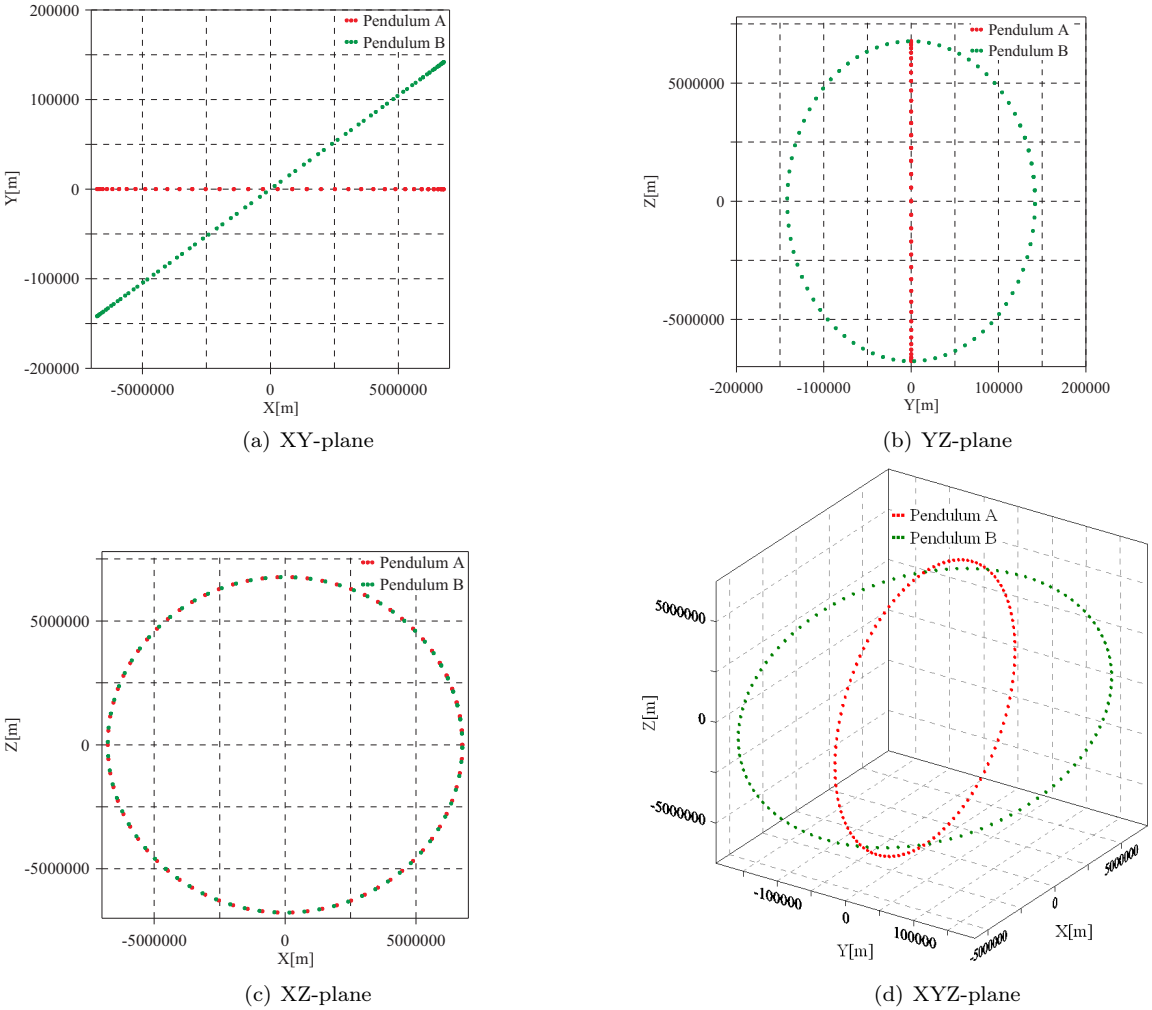

(a) XY-plane

(b) YZ-plane

(c) XZ-plane

(d) XYZ-plane

Fig. 6.23: The relative motion of two Pendulum-type FFs, (a) in the XY-plane, (b) in the YZ-plane, (c) in XZ-plane and d) in XYZ-plane.

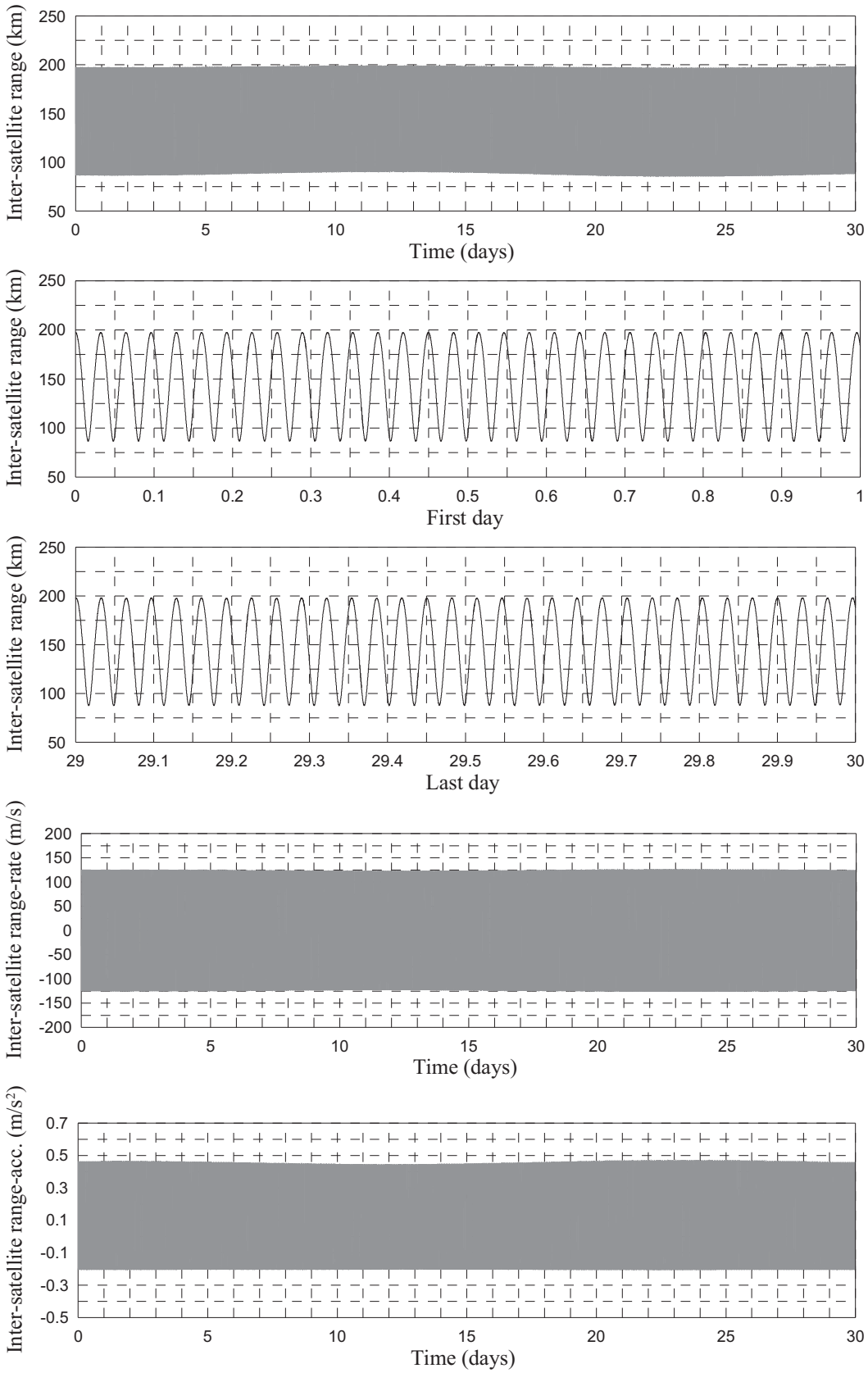

Fig. 6.24: The inter-satellite range, range-rate and range-changes of the two satellites of Pendulum-type.

6.4.6 Multi-GRACE-type Mission Simulation Scenario

All the previously discussed formation flights (GRACE-, Radial wheel-, Inclined wheel-, Pendulum- and GRACE-Pendulum-type) have a common disadvantage represented in their sampling behavior. This sampling issue is demonstrated by the well known Heisenberg-uncertainty principle of spatio-temporal sampling (Dirac 1958, p. 98) which explains the relation between the spatial and temporal sampling. The Heisenberg-theorem shows a reverse relation that the better spatial sampling is, the worse temporal sampling becomes and of course vice versa. Refer to Eq. (6.8), this rule can be proved when considering the spatial and temporal scales as

$$S_{space} = \frac{2\pi}{\beta}, \qquad S_{time} = \alpha, \tag{6.47}$$

where,

S_{space}	spatial sampling,
S_{time}	temporal sampling,
β	satellite revolutions in α days.

The product between the spatial sampling S_{space} and the temporal sampling S_{time}, taking into account the revolution time T_{rev} from the third Kepler's law ($T_{rev} = \sqrt{GM/a^3}$) reads

$$S_{space} \cdot S_{time} = \frac{2\pi\alpha}{\beta \cdot 24 \cdot 60 \cdot 60}[\mathrm{s}] = 2\pi T_{rev}[s]. \tag{6.48}$$

Indeed, for the LEO satellites, this product is very small and can be regarded as a constant

$$S_{space} \cdot S_{time} = c. \tag{6.49}$$

This relation is regarded as Heisenberg-rule of spatio-temporal sampling of a satellite (see Reubelt et al. 2009 and van Dam et al. 2008, p. 110). If we have a sufficient spatial sampling of a satellite mission of one month (e.g. real GRACE mission), the temporal resolution becomes insufficient because of the short periodic signals (e.g. daily and weekly) that will alias into the monthly signals. On the contrary, a satellite mission with an adequate temporal resolution (of e.g. one week or 10 days) provides a worse spatial sampling due to the lack of the coverage of the Earth with satellite tracks.

To overcome this sampling problem facing the current and the proposed future satellite formation flights, a straightforward solution by considering more than one formation flight is demanded. This requirement is essential due to the difficulty of simultaneous higher spatial and higher temporal resolution together with a single formation flight mission. Therefore, multiple formations (or a constellation as referred in the sequel) will have the potential to sample the globe at essentially different locations at the same time. Using a satellite constellation, e.g. two pairs of satellites on two different orbits can substantially improve the spatial and temporal sampling.

Three main constellations are proposed from the reference GRACE-type formation to investigate the spatio-temporal sampling, taking into account that all formation flights have the same orbital altitude and hence will have roughly similar orbital periods. One of these constellations is composed of two pairs of GRACE-type formations with a temporal shift. In other words, the two pairs have the sampling with same spatial resolution but differs in the temporal one and will pass a certain latitude at two different times. The maximum achievable ground track distance of one day is approximately 2600 km, achieved by a mean anomaly difference of π. Therefore, the constellation will have two formations of the same orbital elements but differs in the mean anomaly with π (i.e. ΔM=180°) as indicated in Table 6.7.

The second proposed constellation is designed with the same temporal sampling but a difference in the spatial one. This can be realized with two pairs of satellites having differences of their ascending nodes. The selection of the RAAN angle should fulfill the condition that the subsatellite-tracks of the second formation shall be placed halfway between those of the first orbit to obtain a homogeneous spatial sampling. In this case, a RAAN difference of $\Delta\Omega$=180° of the two semi-polar formations at the same altitude has been selected to

accomplish this condition. This means that the subsatellite-tracks can be tuned up to one half of the Earth's circumference.

The last proposed constellation design can be considered to have only one pair on a semi-polar orbit (i=89.5°) and the other pair on an orbit of significantly lower inclination. This idea has been already introduced by e.g. Bender et al. 2008. An advantage of this constellation is that no loss occurs in the spatial resolution due to the condensed subsatellite-tracks of the semi-polar single pair, which suffices to achieve the same sampling that require the two pairs at lower latitudes. Similarly, sufficient spatial sampling will be achieved at low latitudes due to the densely subsatellite-tracks of the one pair at relatively low latitudes. This can be used to combine the data of two non-isotropic measurements of the two pairs to an overall increased isotropic measurement. As formerly mentioned, the subsatellite-tracks of the second inclined orbit should be placed halfway between those of the first one. For this purpose, the selected lower inclination should be in the medium range between 40° and 70°. In our case, a lower inclination angle of 55° was chosen because at this angle homogeneous subsatellite-tracks will cross equi-spaced the equator.

A drawback occurs when performing the latter formation type of inclination difference related to the different repeat period of the subsatellite tracks. A different subsatellite track distance in the orbital altitude have to be carried out to overcome this problem. This means that no synchronism between the satellites takes place due to the different altitude. Therefore, this condition has not been taken into our consideration within this thesis, since we only consider the same orbital altitudes selected in the mission design.

To examine the former two constellation types, we select only 24 days of the satellite revolutions. This is because at satellite's altitude of 400 km, each satellite pair will complete a full coverage of 360 revolutions after 23.14 days. No additional subsatellite-tracks were considered to avoid a contamination of the full Earth's coverage. The maximum spacing between the subsatellite-tracks would be about 111 km (or 1 degree) at the latitude. This means that each latitude compartment will be covered by satellite observations. The reference case as shown in Fig. 6.25(b) represents the ascending and descending distribution of the subsatellite-tracks of 24 days of simulated GRACE-type FF. Fig. 6.25(a) shows only the half of satellite's observations because this type will be combined with another formation (of 12 days) to form a constellation (of 12 days) with ΔM and $\Delta\Omega$.

The last constellation design with Δi is only shown in Fig. 6.25(e), but as mentioned it was not investigated within the thesis.

Table 6.7: Keplerian orbital parameters for different constellations of GRACE-type FF with two postulations(ΔM and $\Delta\Omega$).

		Orbital Parameters					
		$a[km]$	e	i [deg.]	Ω [deg.]	ω [deg.]	M [deg.]
Constellation 1 (ΔM)	GRACE A	6778.137	0.001	89.5	0	0	0
	GRACE B	6778.137	0.001	89.5	0	0	-0.744
	GRACE C	6778.137	0.001	89.5	0	0	180
	GRACE D	6778.137	0.001	89.5	0	0	179.256
Constellation 2 ($\Delta\Omega$)	GRACE A	6778.137	0.001	89.5	0	0	0
	GRACE B	6778.137	0.001	89.5	0	0	-0.744
	GRACE C	6778.137	0.001	89.5	-180	0	0
	GRACE D	6778.137	0.001	89.5	-180	0	359.256
Constellation 3 (Δi)	GRACE A	6778.137	0.001	89.5	0	0	0
	GRACE B	6778.137	0.001	89.5	0	0	-0.744
	GRACE C	6778.137	0.001	55	0	0	0
	GRACE D	6778.137	0.001	55	0	0	-0.744

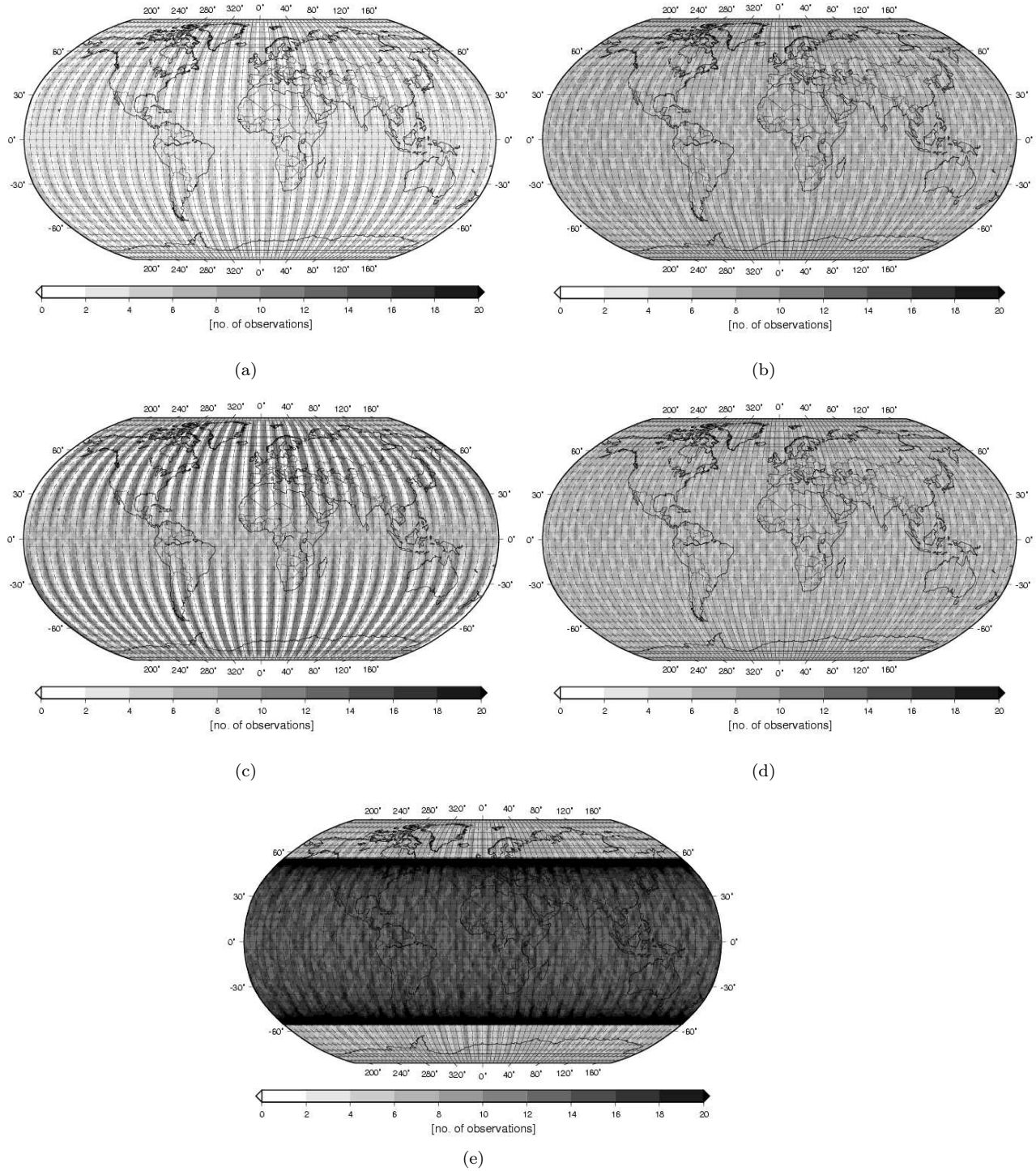

Fig. 6.25: Ascending and descending observation distribution of the proposed satellite constellations of GRACE-type FF, (a) 12 days of one GRACE-type FF, (b) 24 days of one GRACE-type FF, (c) 12 days of one constellation with a mean anomaly difference (ΔM) and (d) 12 days of one constellation with a RAAN difference ($\Delta\Omega$) and (e) 24 days of one constellation with an inclination difference (Δi).

7. Test Computations and Results

In this chapter, the numerical calculations and results of the different proposed satellite formation flights in the context of the determination of the global gravity field of the Earth are presented. A description of the numerical simulation procedures is given in the first section. In the following sections, numerical solutions of the Earth's global static gravity field are discussed for the different formation flights, which are previously described in Chapter 6. After that, time variable gravity field results are presented, where the temporal signals are caused by the ocean tides, atmosphere, ocean and hydrology. We should mention here that the investigated time variable variations of the gravity field are modeled by a forward calculation based on the data of the background physical models which are described in Sec. 5.2.2.

7.1 Simulation Scenario of Formation Flights

For examining the influence of different mission scenarios to be considered under controlled conditions, numerical simulations using the GROOPS software are performed. These simulations are fundamentally required in order to compare the expected performance of each mission formation flight in recovering the Earth's global gravity field. The procedures of these numerical simulations executed by GROOPS are already described in Chapter 5 from the orbit integration to the recovery of the Earth's gravity field. In this study, all orbits were designed to have exactly a time span of 30 days for a sufficient Earth's coverage except for the last mentioned scenarios in Sec. 6.4.6, where 24 and 12 days are selected due to the sampling issues (discussed later).

As a first step, the orbit integrator was examined for testing the systematic errors of the integrator during the integration process. Since the GRACE-type formation flight was selected as a reference mission for comparisons, its simulated orbits (with the orbital elements indicated in Table 6.3) were compared with a reference data set that referred to SC7 data set (IAG -SC7 2003). This SC7 data set has simulated data of the three satellite gravity field missions of CHAMP, GRACE and GOCE and provides a unique easily accessible data set for various comparisons. The SC7 data set covers a time period of 30 days with a sampling rate of 5 seconds and includes the absolute positions, velocities and accelerations of the GPS satellites as well as the three satellite missions and reference frame specifications. The simulation scenarios are simplified so far as no noise in the data for the GPS orbits, for CHAMP and GRACE have been considered. The satellite files contain observation epochs in Modified Julian Date (MJD). The absolute coordinates refer to a (quasi) inertial system with origin in the center of mass of the Earth and the axes directed to the principal axes of inertia (Z-axis). The relation of this quasi-inertial system to the Earth fixed coordinate system is defined by the sidereal time (GAST) as rotation angle between the two specified coordinate systems.

For testing the deviation (due to the systematic error of the integrator) of the satellites' positions through the orbit integrator rounding errors, the initial values (initial position and initial velocity vectors) of SC7 are integrated using GROOPS also at the same time interval of 5 seconds. The deviation between the output observations from the orbit integrator and SC7 observations using an interpolation polynomial degree of 10 is smaller than 20.97 μm per day as shown in Fig. 7.1.

All studied simulated scenarios of the satellite orbits were integrated using ITG-GRACE03s (a product of the GRACE mission) as a pseudo-real static gravity field model up to a SH (Spherical Harmonic) degree and order n= 180. Also background models as given in Sec. 5.2.2 were considered during the orbit integration process. Further force models related to the atmospheric air drag, solar radiation pressure and Earth albedo were not included.

The nominal inter-satellite measurements (the relative distance, the relative velocity and the computed acceleration) of each formation were then computed using Eqs. (5.34) – (5.36). Furthermore, the accelerometer measurements in addition to the star camera data for each satellite were generated as a preparation step for setting up the observation equations required to estimate the unknown parameters from the satellite-to-satellite tracking information. Subsequently, each satellite's coordinates are contaminated with white noise

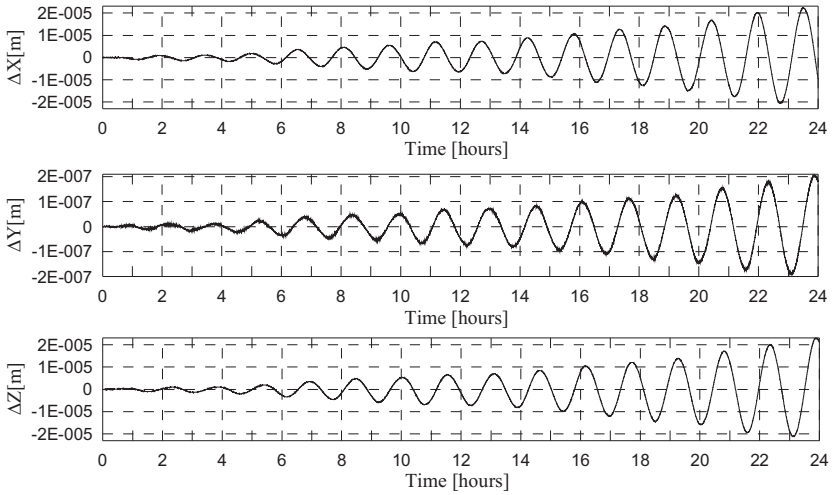

Fig. 7.1: The deviation of the positions between GRACE A satellite from SC7 data set and the simulated GRACE A satellite through the orbit integration using GROOPS.

(normal distributed and uncorrelated errors) of a standard deviation of 2 cm, since the accuracy of the estimated LEO orbit is in the size between 2 cm to 5 cm. The range measurements are contaminated with 50 nm as suggested before in Sec. 6.2.3.2. A remark should be mentioned here, that this selected noise value still has an impact on the inter-satellite observations, since the analysis is based on the short arc method. So each short arc of only 30 minutes will be affected by this noise value. This has been already seen by referring to Fig. 6.10 which shows that noise values of 5 μm, 0.5 μm and 50 nm affect the gravity field solution, while small noise value of 5 nm has no significant impact on the solution.

It is worthwhile noting here that the 5 nm noise accuracy have not provided further improvements because of the fact that the limitations of the numerical accuracy of the computers. We should also mention here, that no colored noises are assumed here in our simulation scenarios. This assumption is justified because for any real mission the correlations between the observations are not known exactly. Also when simulating the satellite orbits, the a-priori information of the correlation between the coordinates are not known, therefore, the correlations were not taken into account in this study.

Before the estimation of the unknown parameters of the gravity field, the observations were reduced by a static reference field. This step is required for refining the observation equations to be adequate with the measurements accuracy as illustrated in detail in Mayer-Gürr (2006) (p. 59-61). Therefore, the static gravity field model ITG-GRACE03s was selected as a reference field and applied up to SH degree n= 180.

As a first step to establish the system of observation equations, the total orbit is divided into short arcs. For each short arc, the partial system of observation equations is set up using the integral equation approach. This approach is considered to be the spirit of this study because of its accuracy rather than the other methods as described in Chapter 5. The satellite orbits of one month, which contain $\approx$ 518000 observations (neglecting that each observation has many measurement values of GPS-positions, range and range-rate) is divided into 1440 short arcs of 30 minutes length of each arc.

After the satellite observations were divided into short arcs, they are employed as input of the observation equations in a way that each short arc covers 360 positions (30 minutes with position's sampling rate every 5 seconds). Each position is estimated using Eq. (5.2). This produces a system of observation equations (360 equations) in the matrix form of Eq. (5.16). From these observation equations, the normal equation system is built as given in Chapter 5 in the form of Eq. (5.22). It is worthwhile noting here that the observation equations are independent of the formation and the data type (along-track, cross-track and radial).

A direct solution of the normal equations is then applied by GROOPS via a Cholesky decomposition to obtain a set of unknown parameters (Eq. (5.23)) representing the gravity field solution in terms of spherical harmonic

coefficients and their formal errors, which are calculated from the covariance matrix of the parameters (Eq. (5.24)). The gravity field functionals at given grid points are evaluated and displayed using these spherical harmonic coefficients in order to obtain the gravity field solution in terms of gravity anomalies or geoid heights. The graphical representation of the solution in the spectral and spatial domains was depicted for visualizing our results in terms of geoid heights.

7.2 Gravity Field Solutions

Static Gravity Field: The Earth's global static gravity field derived from satellite observations are caused by the total mass of the Earth as the sum of the solid Earth mass together with additional masses. These masses are the atmospheric mass, oceanic mass, continental water masses (hydrology) and the both polar ice sheet masses: the continental ice mass and the see ice masses. All these masses are reflected in the total Earth mass M (constituting the geocentric gravitational constant GM value), which is a parameter of geodetic reference systems. As the Earth's whole system is mass conserving in principle, GM should be constant over time. Any time dependency of GM could only be caused by wrong estimates for GM (or the corresponding zero degree coefficient of the spherical harmonic series). So, one must be aware of the GM value when applying different static gravity fields, because any slight change in this value yields an effect on the gravity solution. In other words, any change in the GM value produces a different scaled potential coefficients. Hence, if one applies two different static fields, the coefficients must be correspondingly scaled. For this reason, we applied one static gravity model ITG-GRACE03s for restricting the effect on the comparison between the different satellite formation using different time variable signals. It is necessary to point out that the noticeable differences between the static gravity field models is not arisen from the conserving mass of the whole Earth's system but caused by the mass distribution.

Time Variable Gravity Field: When the different mass components of the Earth's system are transported, fluctuated at various temporal and spatial scales and/or its mass density changed, then the gravity field changes during the time. Therefore, the situation is more complex for the analysis of the time variable gravity field than in case of the static field. In order to take into consideration such temporal variations for gravity field analysis, the suitable satellite configuration and the sampling pattern of the satellite mission in addition to its sensors play a crucial role. This can be a solution in order to avoid or at least mitigate the aliasing of temporal signals into the resulting fields. What we are seeking in our analyses is to find the best satellite configuration and a homogeneous sampling pattern which allows to determinate the influence of the time variable gravity field with a lower error. To achieve this, numerous simulations of the different proposed satellite formation flights are necessary.

The largest time variations of the Earth's gravity field are based on the direct tide and those of the solid Earth and of the oceans due to the gravitational interactions with the Sun and the Moon as illustrated in Sec. 4.2. Another small tidal phenomenon that was taken into consideration in our study are the pole tides caused by the pole movement. Moreover, in the atmospheric masses (wind, temperature and air pressure) underlie also these variations. Due to the atmospheric masses, a reaction on the oceanic water column takes place causing mass variations and circulations. The distribution of the continental water masses through the water cycle process is closely related to the processes in the atmosphere and the oceans. Therefore, it should be taken into consideration when investigating the time variations of the Earth's gravity field.

In the following, the influences of the temporal variations on the gravity field solutions through the study of various simulation scenarios of the different satellite formation flights are examined. In a first step, the static gravity field is analyzed and then a study of the different time variable effects from different signals will be performed. A brief summery of the procedures and the applied models used through our investigation is summarized in Table 7.1.

Table 7.1: Overview of the different applied models and parameters used for the analysis of the investigated satellite formation flights (such as GRACE, Pendulum, GRACE-Pendulum, Radial wheel, Inclined wheel) and satellite constellations (such as Multi-GRACE ΔM and Multi-GRACE $\Delta\Omega$).

Reference Static Gravity Field	Time Variable Gravity Field								Resolution		Sampling Rate	Mission Time
	Atmosphere	Ocean	De-aliasing	Hydrology	Tides				Static	Temporal		
					Direct	Pole	Earth	Ocean				
ITG-GRACE03s	ECMWF (n= 100)	OMCT, PPHA (n= 100)	AOD1B (n= 100)	WGHM, LaD (n= 100)	Ephemerides DE 405 by the JPL	IERS 2003	Anelastic Earth (IERS 2003)	FES2004, EOT08a (n= 80)	n= 60, 90, 180	n= 80, 100	Δt= 5 sec.	12, 24, 30 days, 6 months

7.2.1 Static Gravity Field Solutions of Satellite Formation Flights

In the following section, the global static gravity field will be recovered based on the simulated data of the previously mentioned SFFs. This includes two main simulation studies comprising two scenarios. The first scenario concerns with the formation flights of the identical temporal resolution (mission period of 30 days). This scenario includes the study of GRACE-type, Radial wheel-type, Inclined wheel-type, Pendulum-type and GRACE-Pendulum-type FFs. The second scenario is related to the topic of studying different spatial and temporal resolutions (less than 30 days) through the gravity field analysis of Multi-GRACE-type constellation measurements. The analysis of the gravity field was applied according to the procedures already mentioned in Sec. 7.1.

7.2.1.1 Simulation Study: Scenario 1

This section discusses the results of the Earth's global static gravity field recovery for the GRACE-type, Radial wheel-type, Inclined wheel-type, Pendulum-type and GRACE-Pendulum-type FFs. For the representation of the global static gravity field of the Earth, some moderate resolvable SH degrees have been selected. This is for corresponding comparisons and better interpretations of the different SFFs at different wavelengths of the gravity field spectrum. For example, representations of spherical harmonics up to the degrees 60, 90 and 180 have been selected for the recovery of long-to-medium, medium-to-short and short wavelength structures of the global gravity field, respectively.

The reasons for choosing different wavelength ranges are related firstly to the restriction of previous studies,

concerning the use of formation flight concepts for the gravity field recovery, up to only degree 60 (see e.g. Sharifi et al. 2007, Sneeuw et al. 2008 and Wiese et al. 2008). Secondly, the medium-to-short wavelength structure (n_{max}= 90) can detect and explain more error spectrum features that the long-to-medium one (n_{max}= 60) cannot detect or explain. The same holds also in case of the short wavelength (n_{max}= 180) w.r.t. the medium-to-short one. This provides more understanding for various error sources of the global gravity field recovery. Another reason is the variation of the accumulated errors of the applied model for each selected SH degree. In other words, when comparing the recovered solution of e.g. n_{max}= 60 to those of n_{max}= 90 and n_{max}= 180 (the same holds also for e.g. n_{max}= 90 compared to n_{max}= 180), we find that the former one indicates a solution accuracy range that is lower than those of the latter upper degrees. The same holds also for the recovered solution up to the degree 90 compared to degree 180. This is attributed to the accumulated model errors (i.e. $\sigma_{c_{nm}}$ and $\sigma_{s_{nm}}$) in case of degree 90 that is larger than those of degree 60 and also in case of accumulated errors up to degree 180 that are larger than those of 60 and 90. Therefore, the recovery of the static gravity field has not been restricted to one selection of one SH degree type.

Before investigating the static gravity field solutions from different SFFs, they have been firstly examined without contaminating the satellite observations with errors (i.e error-free case). After that, the white noises have been added to the satellite observations in order to investigate their influences on the gravity solutions. In the following section, the effects of different noises on the monthly gravity field solutions contaminating the satellite's positions and the inter-satellite ranges are discussed.

7.2.1.2 Effects of Different Noises on the Monthly Mean Gravity Field Solution

In this section, we will investigate how largely affect the observation noises the gravity field solution. Firstly, we compute the gravity field from simulated satellite observations (positions and inter-satellite distances) without consideration of any noises (i.e. error-free case). After that, we analyze again the gravity field after addition of white noises to the observations. The deviation between the error-free solution and the noisy one plays an important role to understand how the gravity field solution reacts to this applied noise. All these scenarios are applied to the Pendulum formation type as shown in Fig. 7.2. In a first step, the satellites orbits of the Pendulum-type FFs have been integrated with only the gravity field model ITG-GRACE03s as a true gravity field up to SH degree 180. The results with and without noises are represented in terms of *DDV* of geoid heights between ITG-GRACE03s and the estimated gravity solutions.

The black curve of Fig. 7.2 represents the static solution after reducing the ocean tide effects (using the same FES2004 model). When the satellites orbits are contaminated with white noise of σ_{pos}= $2cm$, the gravity solution is deviated from error-free accuracy of RMS of $0.62\mu m$ yielding worse RMS of $0.142mm$ as represented by the cyan curve of Fig. 7.2. This latter solution is affected by this noise at long and medium harmonics than the medium-to-short ones. When the inter-satellite ranges are only contaminated using different white noises (e.g. σ_{range}= $5\mu m$, $1\mu m$ and $50nm$), the gravity solution is also affected. A most refined gravity solution is indicated by the $50nm$ noise of RMS of $0.133mm$ rather than the $1\mu m$ and $5\mu m$ one of RMS of $2.73mm$ and $13.41mm$, respectively. This behavior agrees with the results indicated before in Chapter 6 for the GRACE-type FF (cf. $5\mu m$ and $0.05\mu m$ of Fig. 6.10).

Three additional scenarios have been performed considering both the position and range noises. One of them investigates the effect when σ_{pos}= $2cm$ and σ_{range}= $50nm$, whose gravity solution is given by the purple curve with circles in Fig. 7.2. Another case investigates the noise effects when σ_{pos}= $2cm$ is added with σ_{range}= $1\mu m$ (given by the pink curve). The last case investigates the noise effects when σ_{pos}= $2cm$ and σ_{range}= $5\mu m$ (given by the yellow curve). The gravity solution indicated by the purple curve is affected by σ_{pos} at long and medium harmonics. After that (up SH degree 40), the gravity solution is affected by σ_{range} yielding RMS error of $0.195mm$. In case of the other two solutions given by the pink and yellow curves, the effects of σ_{pos} are included under the effects of the σ_{range} of $1\mu m$ and $5\mu m$ which yields RMS global error of $2.73mm$ and $13.41mm$, respectively.

Therefore, white noises of σ_{pos}= $2cm$ and σ_{range}= $50nm$ have been chosen for our analysis in order to investigate the static gravity field solutions determined from the formation flight types. Fig. 7.3 shows the *DDV* in terms of geoid heights between ITG-GRACE03s and the estimated gravity solutions of all formation

flights with and without the consideration of noises. Regarding the gravity solutions of Fig. 7.3, We have to mention here that all satellites orbits have been integrated not only with the ITG-GRACE03s model, but also with almost all of the time-variable signals of the atmosphere, ocean, hydrology and tides. Obviously, the error-free case shows approximately two to three orders of magnitude better results than in the noise case

We have to mention also here that the noise signal of Pendulum solution indicated by the purple curve of Fig. 7.3 has been plotted with Pendulum solution of Fig. 7.2. This latter solution is represented in Fig. 7.3 by the yellow curve. We observe here that with or without the consideration of temporal variation elements, one obtains almost the same static gravity field solution. One can infer from these two latter gravity solutions (the purple and the yellow) that it does not matter how many time-variable signals affect the satellite observations as long as they are correctly reduced in the gravity field analysis step. An important aspect of these curves in the fact that the GRACE-type FF, containing only along-track information, does not provide the optimal gravity field solution in both cases. This emphasizes that the other SFF types should be investigated and examined towards a better gravity field.

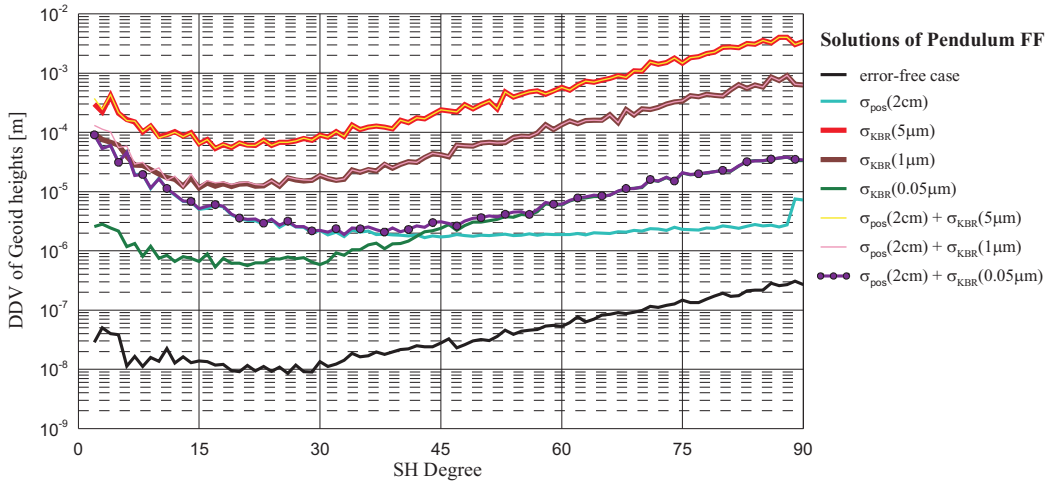

Fig. 7.2: *DDV* of geoid heights between ITG-GRACE03s and the gravity solutions of the Pendulum-type FF with and without the consideration of noises (i.e. error-free and noise cases).

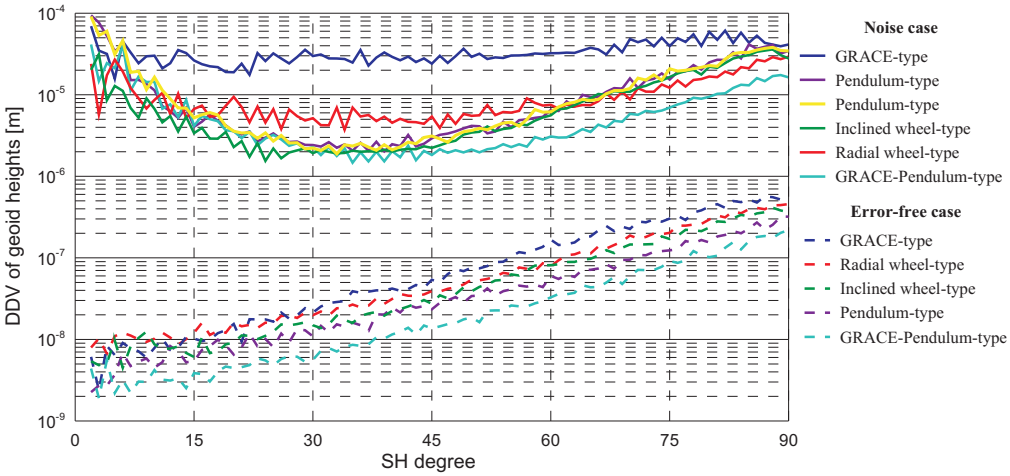

Fig. 7.3: *DDV* of geoid heights between ITG-GRACE03s and the gravity solutions of all formation flights with and without the consideration of noises (i.e. error-free and noise cases).

Degree 60: Fig. 7.4(a) illustrates the gravity field solutions of the different SFFs at a maximum recovery degree of n_{max}= 60. Two spectral analysis types of gravity field solutions are presented in this figure (and the coming figures of this type as well) in terms of difference degree variances (DDV) of geoid heights and the cumulative geoid errors. The legend at right hand side of this figure (and the coming figures of this type as well) is arranged from top to bottom representing the gravity solutions from the poorest solution to the best one, respectively, in terms of only DDV. It is clearly shown from Fig. 7.4(a) that the Pendulum-type, GRACE-Pendulum-type, Radial wheel-type and Inclined wheel-type FFs are seen to outperform the GRACE-type FF. The Inclined wheel-type FF yields the smallest global geoid errors as seen from the RMS values at degree 60 in Table 7.2. It shows approximately a full order of magnitude better result than the GRACE-type within the range of medium spherical harmonics. This is already expected since the Inclined wheel-type FF contains all components (along-track, cross-track and radial) contributed into its observations. These results correspond to the results of previous studies given by Sharifi et al. (2007) and Sneeuw et al. (2008) up to this spherical harmonics degree. However, these studies have applied another approach used for solving the observation equations for the gravity field recovery and the dimensions of the satellite formations (i.e inter-satellite baselines).

Fig. 7.5 visualizes the geoid errors after projecting them on a map of the Earth in addition to the spectral plots (Fig. 7.4(a)). GRACE-type FF (Fig. 7.5(a)) shows its longitudinal error pattern along the meridian direction. The error structure corresponds to the results of the real GRACE mission as seen not only from static GRACE solution but also from its monthly solutions (see e.g. Tapley et al. 2004a and Mayer-Gürr 2006, p. 94-97). The longitudinal error structure is basically attributed to the weakness of the observables of this configuration type which is mainly sensitive along the Line-of-Sight which is in north-south direction along the meridians.

Adding another horizontal information (an out-of-plane cross-track component) to the along-track one, the longitudinal error structures of the GRACE-type FF has been totally reduced and vanished in Pendulum-type FF yielding an east-west direction as seen in Fig. 7.5(b). Although, the higher errors are taking place at low degree harmonics (below n= 7) of Pendulum-type FF (see Fig. 7.4(a)), still Pendulum-type FF outperform the GRACE-type FF in terms of the global RMS accuracy (see Table 7.2).

When merging the two previous solutions into one solution, the GRACE-Pendulum-type gravity field solution is obtained. This allows a pure along-track information of GRACE-type FF to be merged with the horizontal information (along- and cross-track) of Pendulum-type FF. This configuration provides the least geoid errors at high harmonics as seen previously in Fig. 7.3 for both the error-free and the noisy case. The advantage of this configuration is that the longitudinal error structure (meridian stripes) is vanished in spite of involving the pure along-track observables accompanied with the gravity solutions of GRACE-type FF (see Fig. 7.5(c)).

The best performance of the gravity field solutions is obtained from the both radial configurations; Radial wheel-type FF and Inclined wheel-type FF in terms of the global geoid accuracy and the homogeneously distributed error spectrum as well. Comparing the latter both SFFs, the Inclined wheel-type exceeds only Radial wheel-type by carrying a cross-track component. Therefore, the gravity solution of the inclined wheel-type (which moves in the vertical and horizontal satellite orbital plane) outperforms the Radial wheel-type one (which moves only in the vertical plane). This performance can be seen in Fig. 7.4(a) in terms of DDV of geoid heights and the cumulative geoid errors by providing the lower error spectrum than GRACE-type FF and in Figs. 7.5(d) and 7.5(e) by reducing the longitudinal error structure of GRAC-type FF as well. Also it is clearly observed from the Inclined wheel-type global solution (Fig. 7.5(e)) that its error spectrum is homogeneous in a diagonal pattern (inclined east-west direction) due to the cross-track component that the Radial wheel-type one does not contain.

It should be noted here that the longitudinal error structure of Radial wheel-type FF shown in Fig. 7.5(d) is not to be misunderstood or not to be confused with the previous mentioned GRACE-type FF in Fig. 7.5(a). The reason for existence of this structure into its homogeneous solution is attributed to the recovery of sectorial coefficients, which represent physically the longitudinal slices of the Earth, at a poor spatial resolution of 333 km (half-wavelength). This error structure will be reduced when using different gravity solutions with sufficient spatial resolutions.

Degree 90: The previous investigation of degree 60 was examined at degree 90 to provide global gravity solutions of the investigated SFFs but with a finer spatial resolution (222 km half-wavelength). Additional Information was acquired when the global gravity analyses were carried out at this degree. GRACE-type FF still provides the poorest global gravity field solution for all degrees below n= 90.

Despite the fact that the Pendulum-type FF does not achieve the performance level of the radial configurations (Radial wheel-type and Inclined wheel-type FFs) and GRACE-Pendulum as well, it still yields a global solution better than the GRACE-type FF. The *DDV* spectral signal of the Inclined wheel-type FF has been drastically changed above degree n= 64 providing a global error larger than the Radial wheel-type and GRACE-Pendulum-type FFs as seen from Table 7.3. Nevertheless the Inclined wheel-type FF provide the smallest cumulative geoid errors below degree n= 82 (see Fig. 7.6(e)). Although GRACE-Pendulum provides a moderate cumulative geoid error curve, it shows the least error spectra of all indicated gravity solutions.

The Radial wheel-type FF still shows the same gravity accuracy obtained up to degree n= 60 ranging from a full to half-order of magnitude better performance than GRACE-type FF at the majority of the spherical harmonics degrees (see Fig. 7.4(b)). The former error structure of the Radial wheel-type FF at the SH degree n= 60 given in Fig. 7.5(d) has been clearly glowed by degree n= 90 as shown in Fig. 7.6(d). This emphasizes that the recovered error spectrum from Radial wheel-type is homogeneous for the sectorial harmonics.

Degree 180: A much finer spatial resolution (≈111 km half-wavelength) rather than the two previous investigations (60 and 90) is applied at degree n= 180. By carrying out the global gravity recovery to higher harmonics degree, the global RMS errors have been drastically increased as shown in Table 7.4. The RMS of the geoid heights at higher harmonic coefficients provides global gravity solutions three to four order of magnitude worse than those solutions of the lower harmonic coefficients as shown from the spectral signals of Fig. 7.4(c).

The Inclined wheel-type FF which was considered at low harmonics to have the most performed global gravity solution than other SFFs, it became the worst solution especially up n= 122, in addition to its complexity (from implementation point of view). When considering Fig. 7.7(e), one observes slight improvements of the geoid errors at the northern part of the Earth. This may be caused by the large variation of the inter-satellite distances between the two satellites above the northern hemisphere more than the variation occurred above the southern hemisphere. This can be seen from the last day of the orbit integration as shown in Fig. 6.22. The former large variation is better for recovering some harmonic coefficients, especially by a pair of satellites having cross-track and radial SST measurements, whose contribution is useful to higher harmonics and zonal ones as discussed before at the end of Sec. 6.2.3.1.

The second worst global gravity solutions is arisen from the out-of-plane Pendulum-type FF. It provides an improved global solution better than GRACE-type FF for long and medium wavelength ranges and for short wavelength up to only degree n= 134. This can be seen when comparing the global homogeneous distributed error structure in Fig. 7.7(b) to that one of GRACE-type FF in Fig. 7.7(a). Up degree n= 135, the global solution of GRACE-type FF begins to outperform the Pendulum-type FF above this degree and also below degree n= 7. The slight improvements between the two global gravity solutions are seen in the equatorial region of Fig. 7.7(a).

In case of GRACE-Pendulum-type FF, the obtained gravity field solution is considered as the best of all solutions of the SFF types with the best homogeneous error spectrum at different wavelength ranges of the harmonic coefficients. This is clearly shown from the spectral representation of Fig. 7.4(c) in terms of both the *DDV* and the cumulative geoid errors and from the global solution of Fig. 7.7(c) when comparing with those of Figs. 7.7(a) and 7.7(b). The RMS values are indicated in Table 7.4. This proves the importance of combining the horizontal information (i.e. along-track and cross-track measurements) with each other into the observables. Most of geoid errors accompanying all solutions of SFFs (except for GRACE-Pendulum-type FF) have been clearly reduced in the gravity solution of the Radial wheel-type FF. One can clearly observe from Fig.7.7(d) that the Radial wheel-type FF has a very prominent isotropic pattern visible with a relatively homogeneous recovered spectrum.

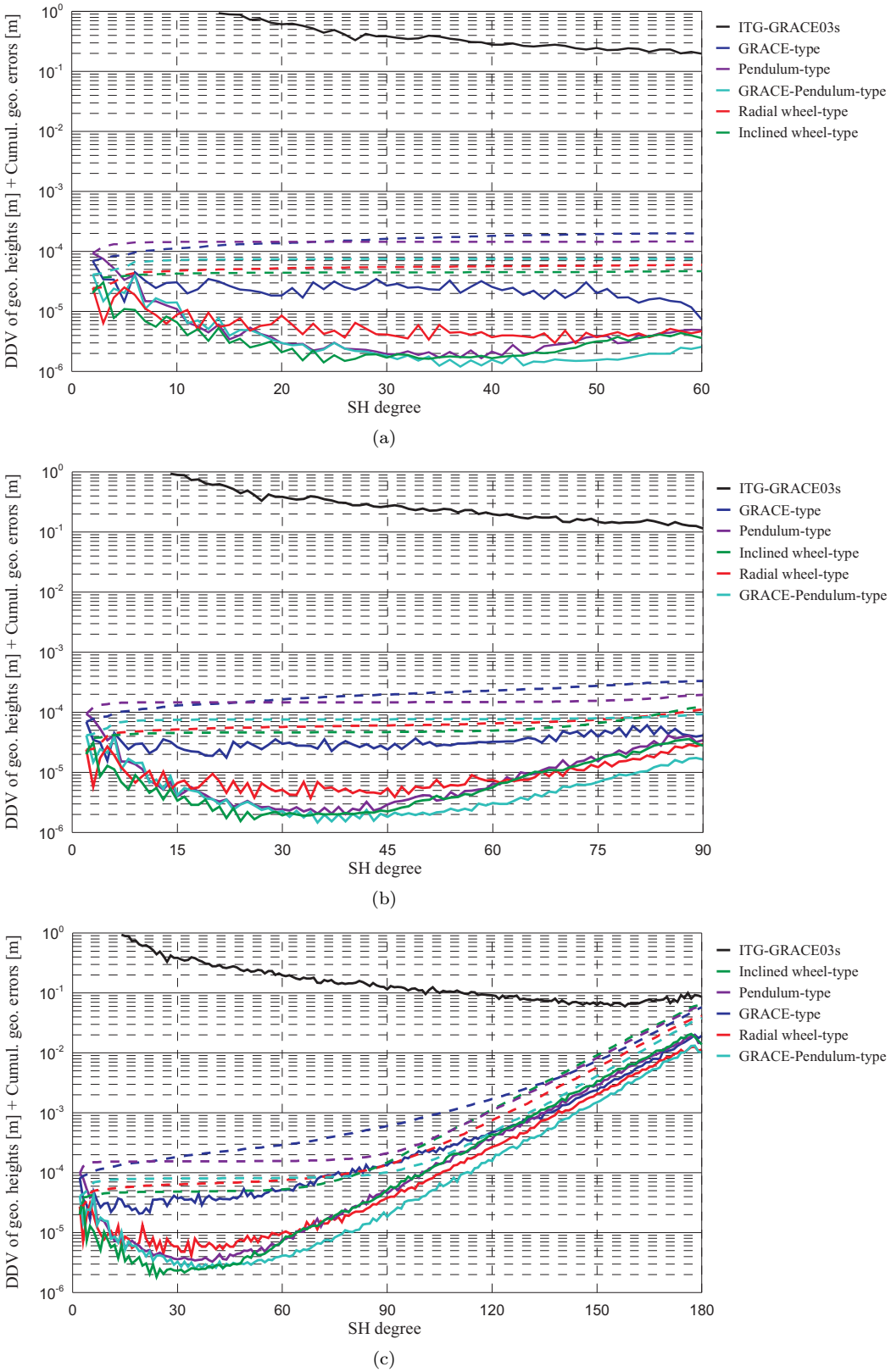

Fig. 7.4: Static gravity field solutions of the formation flights at different spherical harmonics degrees, (a) n= 60, (b) n= 90 and (c) n= 180. Solid lines represent DDV of geoid heights between ITG-GRACE03s and the gravity solutions and dashed ones represent the cumulative geoid errors.

Table 7.2: Geoidal statistical values (RMS, average, minimum and maximum) in [mm] of the different gravity solutions as determined by SFFs at degree n= 60. The gray cells represent the least geoid errors.

SH Degree & Values / FFs	n_{max}= 60			
	RMS	Avg.	Min.	Max.
GRACE-Type	0.204	0.159	-0.654	0.763
Pendulum-type	0.146	0.112	-0.490	0.550
GRACE-Pendulum-type	0.075	0.058	-0.279	0.165
Radial wheel-type	0.066	0.050	-0.295	0.236
Inclined wheel-type	0.047	0.036	-0.168	0.186

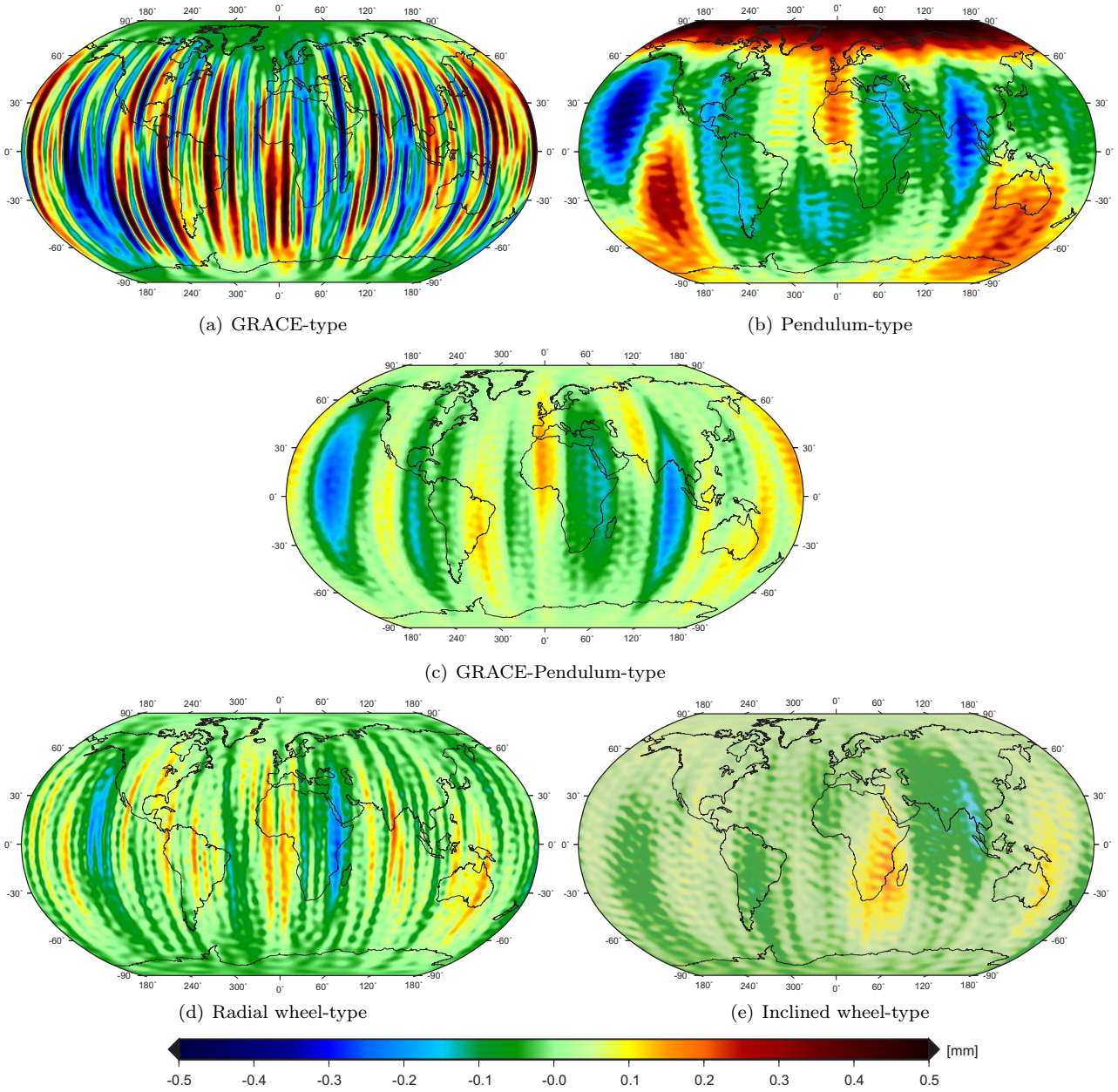

(a) GRACE-type

(b) Pendulum-type

(c) GRACE-Pendulum-type

(d) Radial wheel-type

(e) Inclined wheel-type

Fig. 7.5: Differences in geoid heights between ITG-GRACE03s and the static gravity field solutions of (a) GRACE-type, (b) Pendulum-type, (c) GRACE-Pendulum-type, (d) Radial wheel-type and (e) Inclined wheel-type, n_{max}= 60.

Table 7.3: Geoidal statistical values (RMS, average, minimum and maximum) in [mm] of the different gravity solutions as determined by SFFs at degree n= 90. The gray cells represent the least geoid errors.

SH Degree & Values / FFs	n_{max}= 90			
	RMS	Avg.	Min.	Max.
GRACE-Type	0.351	0.276	-1.375	1.433
Pendulum-type	0.202	0.160	-0.775	0.736
Inclined wheel-type	0.130	0.101	-0.575	0.570
Radial wheel-type	0.118	0.093	-0.550	0.465
GRACE-Pendulum-type	0.096	0.076	-0.412	0.318

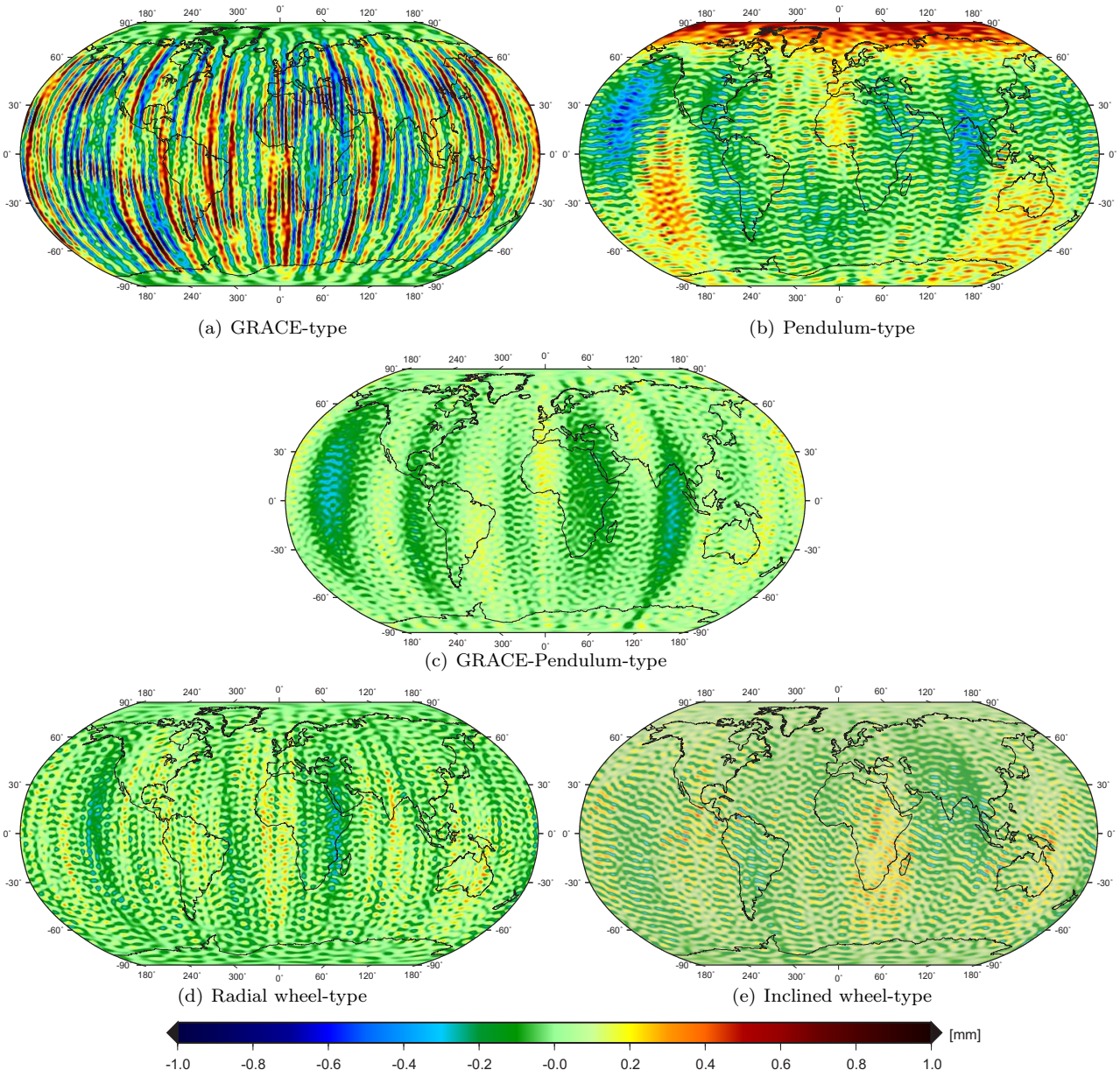

Fig. 7.6: Differences in geoid heights between ITG-GRACE03s and the static gravity field solutions of (a) GRACE-type, (b) Pendulum-type, (c) GRACE-Pendulum-type, (d) Radial wheel-type and (e) Inclined wheel-type, n_{max}= 90.

Table 7.4: Geoidal statistical values (RMS, average, minimum and maximum) in [mm] of the different gravity solutions as determined by SFFs at degree n= 180. The gray cells represent the least geoid errors.

SH Degree & Values / FFs	n_{max}= 180			
	RMS	Avg.	Min.	Max.
Inclined wheel-type	73.87	55.85	-375.0	401.0
Pendulum-type	68.94	54.57	-323.4	291.5
GRACE-Type	68.22	54.42	-293.3	268.9
Radial wheel-type	48.19	38.01	-218.7	217.8
GRACE-Pendulum-type	44.25	35.09	-169.6	178.8

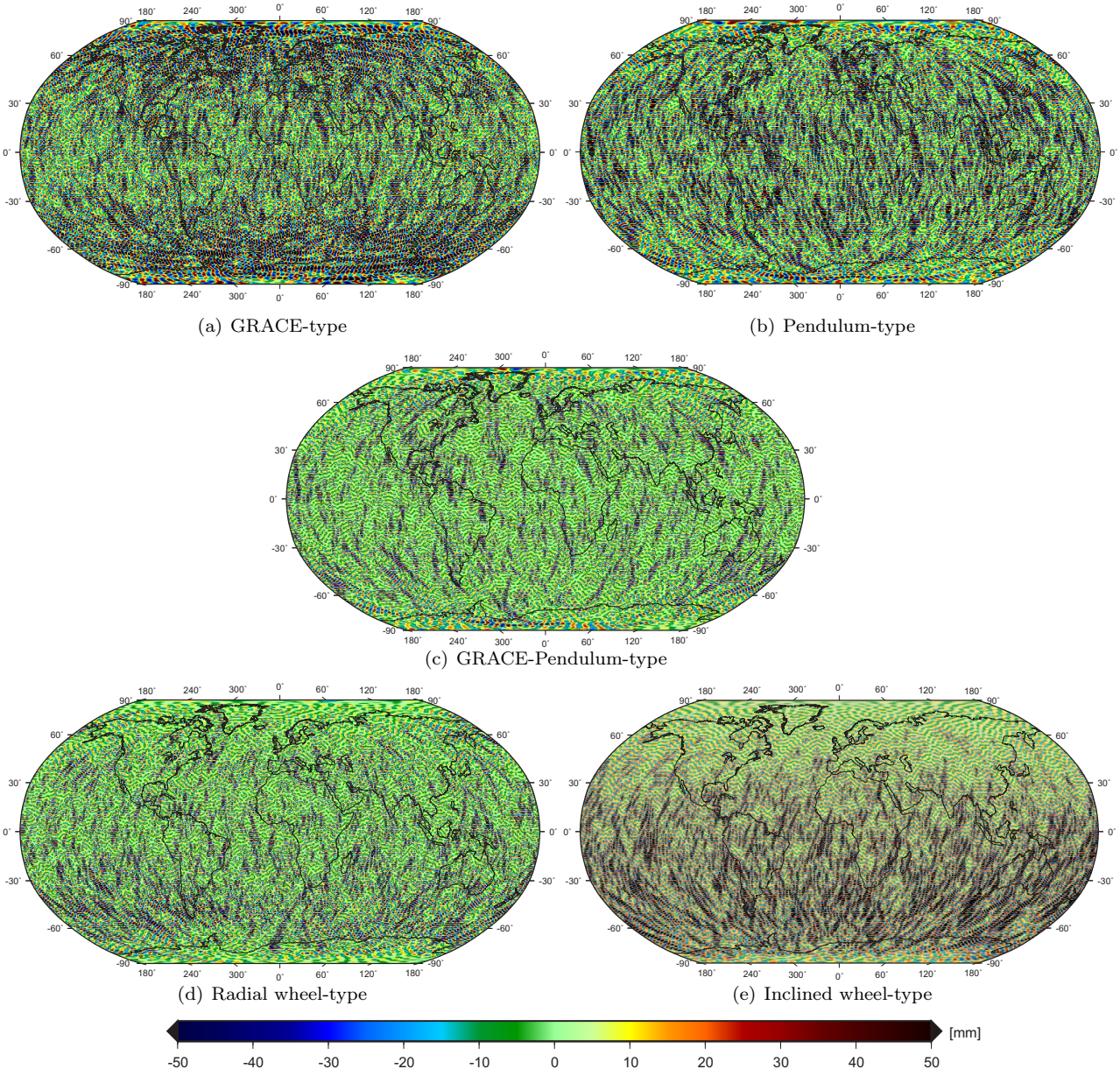

(a) GRACE-type (b) Pendulum-type

(c) GRACE-Pendulum-type

(d) Radial wheel-type (e) Inclined wheel-type

Fig. 7.7: Differences in geoid heights between ITG-GRACE03s and the static gravity field solutions of (a) GRACE-type, (b) Pendulum-type, (c) GRACE-Pendulum-type, (d) Radial wheel-type and (e) Inclined wheel-type, n_{max}= 180.

Formal Errors Analysis: Besides the errors which are already shown in Figs. 7.4(a) – 7.4(c), the formal errors were also estimated using the form of Eq. (5.46) which represent the variances of the estimated geopotential coefficients. These variances are computed from the diagonal of the covariance matrix of the parameters given in the form of Eq. (5.24). Fig. 7.8 shows the formal standard deviations (which are given by the positive root of the variances, i.e. σ_n) in terms of geoid heights. It differs from Figs. 7.4(a) – 7.4(c) in that, they represent, as previously mentioned, the errors of the estimated geopotential coefficients from their expected values not the actual errors of the estimated coefficients from the truth model (represented by ΔC_{nm} and ΔS_{nm}) as in the latter mentioned figures.

In order to visualize the full error situation of the estimated geopotential coefficients, another representation of the formal errors called the Triangle figures are generated as shown in Fig. 7.9 (page 103). This figure represents the formal standard deviations of the different SFF types (GRACE, Pendulum, GRACE-Pendulum, Radial wheel and Inclined wheel) with the studied SH degrees (60, 90 and 180). The values plotted in Fig. 7.9 are obtained by taking the log of the absolute values of the formal errors ($\sigma_{c_{nm}}$ and $\sigma_{s_{nm}}$). Therefore, the color bar is given in a log scale, in which the lower numbers indicate lower errors and the higher numbers indicate higher ones. The color bar is identical for the degrees 60 and 90 and is extended to higher values in case of degree 180 due to the higher errors.

Additional information can be inferred from this analysis. For instance, one recognizes that the formal errors in the long wavelength domain are optimistic, while the high spherical harmonic degrees are somewhat pessimistic. These plots of Fig.7.9 visualize more clearly some specific features of the solutions indicated in the spectral and spatial domains and prove that the difference degree variances and the cumulative geoid errors do not give the detailed information for such error spectra. For instance, when comparing the formal errors of the Inclined wheel-type FF with those of the GRACE-Pendulum-type FF at degree 60 (see Fig.7.9, left side), one recognizes that, in spite of the smallest RMS geoid errors of the Inclined wheel-type FF, its full error spectrum (comparing from degree 40 up to 60) is worse than that of the GRACE-Pendulum-type FF. Therefore, the formal errors analysis plays an important role for completing the whole scenario needed to visualize the gravity field results.

In conclusion, numerous gravity field solutions of the different SFFs have been recovered at different SH degrees (60, 90 and 180) correspond to different gravitational wavelengths. The gravity field results at degree n= 60 have showed an agreement with the previous studies as previously mentioned. Extending the gravity field recovery to higher SH degrees have showed that the restriction of such studies on only long wavelengths seems to be pessimistic scenarios. This is due to the fact that additional and new information has been acquired by applying the gravity recovery to medium and short gravity wavelengths. This was shown in all spectral (Fig. 7.4) and spatial (Figs. 7.5– 7.7) domains as well as the representation of the formal errors (Fig. 7.9). Despite the fact that the Radial wheel-type FF solution does not provide the best overall global gravity solutions, we recommend the Radial wheel-type as the most compatible configuration type for the recovery of the static gravity field. Some facts encourage this recommendation. First of all, the Radial wheel-type FF contains the radial observable component. This leads to a refined gravitational content and leads to improved gravity field solutions within the lower error spectrum and a better isotropy. Another reason is the relative simplicity of the configuration design from the implementation point of view in contrast to the out-of-plane configurations like Pendulum-type, Pendulum-GRACE-type and Inclined wheel-type FFs. Finally, involving only two satellites in its architecture design makes it cheaper than other SFF types having three satellites, e.g. GRACE-Pendulum-type FF.

7.2.1.3 Simulation Study: Scenario 2

Despite the significant knowledge of the Earth's gravity field has been achieved from the satellite observations of the current satellite missions (see Chapter 2), their duration plays a mission deficiency. For instance, one requires typically about 30 days until receiving a global homogeneous sampling for these missions. This deficiency is considered as the sampling problem which still facing the gravity field recovery until nowadays. The sampling with its both portions (spatial and temporal) is an important issue for the gravity field analysis because it determines if the estimation of the potential coefficients from the satellite observations are accurate and sufficient enough. New challenges for improving the modeling concepts, not only the static but

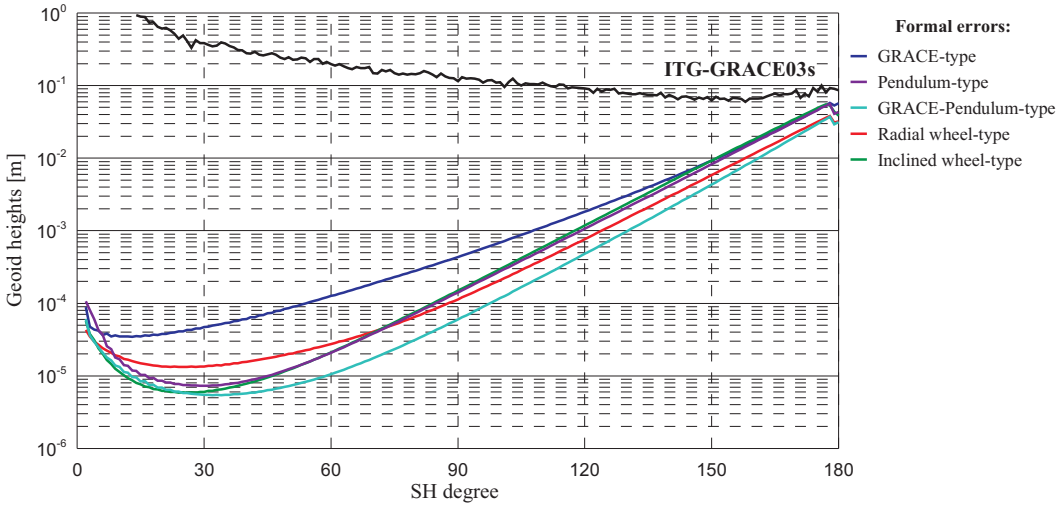

Fig. 7.8: Formal errors of the geopotential coefficients for different SFFs in terms of degree variances of geoid heights.

also the temporal, are expected by solving such this problem. This is because of the fact that, the selection of a proper sufficient sampling leads to corresponding adequate gravity field solutions.

The following section discusses a trial method for solving this sampling problem (as proposed in Sec. 6.4.6). The solution is based on multiplying two (or more) SFF types into one constellation to make the opportunity for merging the satellite observations of different spatial or temporal samplings into the same analysis process of the global gravity field. Constellations of the Multi-GRACE-type FF have been selected to this simulation study since the fact that GRACE-type FF is the successful ll-SST mission type and also because of its simple formation flight from the design point of view in addition.

The estimation of the potential coefficients from only 24 days of satellite observations were examined referred to the reason already explained in Sec. 6.4.6 (refer to page 87). The maximum spherical harmonics degree for this analysis is restricted up to only degree n=90 in consequence of Nyquist rule (refer to page 61). The same orbital parameters of the GRACE-type FF given in Table 6.3 were considered using the conditions given in Table 6.7. Four simulation scenarios for the estimation of the gravity field potential coefficients were performed. The first scenario includes two satellites with 24 days forming a full homogeneous sampling (360 satellite's orbits). The second one was applied for two satellites with a sampling of 12 days (180 satellite's orbits). The third and fourth scenarios were applied for four satellites (one constellation of two GRACE-type FFs) with a sampling of 12 days but they differ in their resolutions. The third one has different temporal resolution and same spatial one (ΔM), while the last scenario has different spatial sampling and same temporal one ($\Delta\Omega$) as indicated in Table 6.7. These four scenarios may not provide much information considering only the static part of the gravity field. However, this investigation is expected to provide valuable information and interpretations for the time variations of the gravity field concerning those signals of frequencies higher than the monthly frequencies.

The static global gravity field solutions are given in Fig. 7.10 in terms of *DDV* of the geoid heights and in terms of accumulated geoid errors as well. These actual differences (between the estimated coefficients and the reference ones, ΔC_{nm} and ΔS_{nm}) are also given in Fig. 7.12 beside the formal errors that have been discussed already in the end of Sec. 7.2.1.1. It is clearly shown that the spatial sampling plays a very important role for improving the gravity solutions when comparing the error spectrum of the 24-days solution with the 12-days solution. The 24-days solution was also compared with the 30-days solution (Fig. 7.10), which was formerly given in Fig. 7.4(b), to demonstrate the difference between both solutions. The comparison between the two latter gravity field solutions in Fig. 7.10 indicates a slightly improved gravity solution of the 30-days case. This is also seen in the standard deviation given in Table 7.5. The reason of this slightly better performance are the additional observations in case of a 30-days mission. The spatial sampling becomes poorer in case of a 12-days mission, so that a worse gravity solution is obtained.

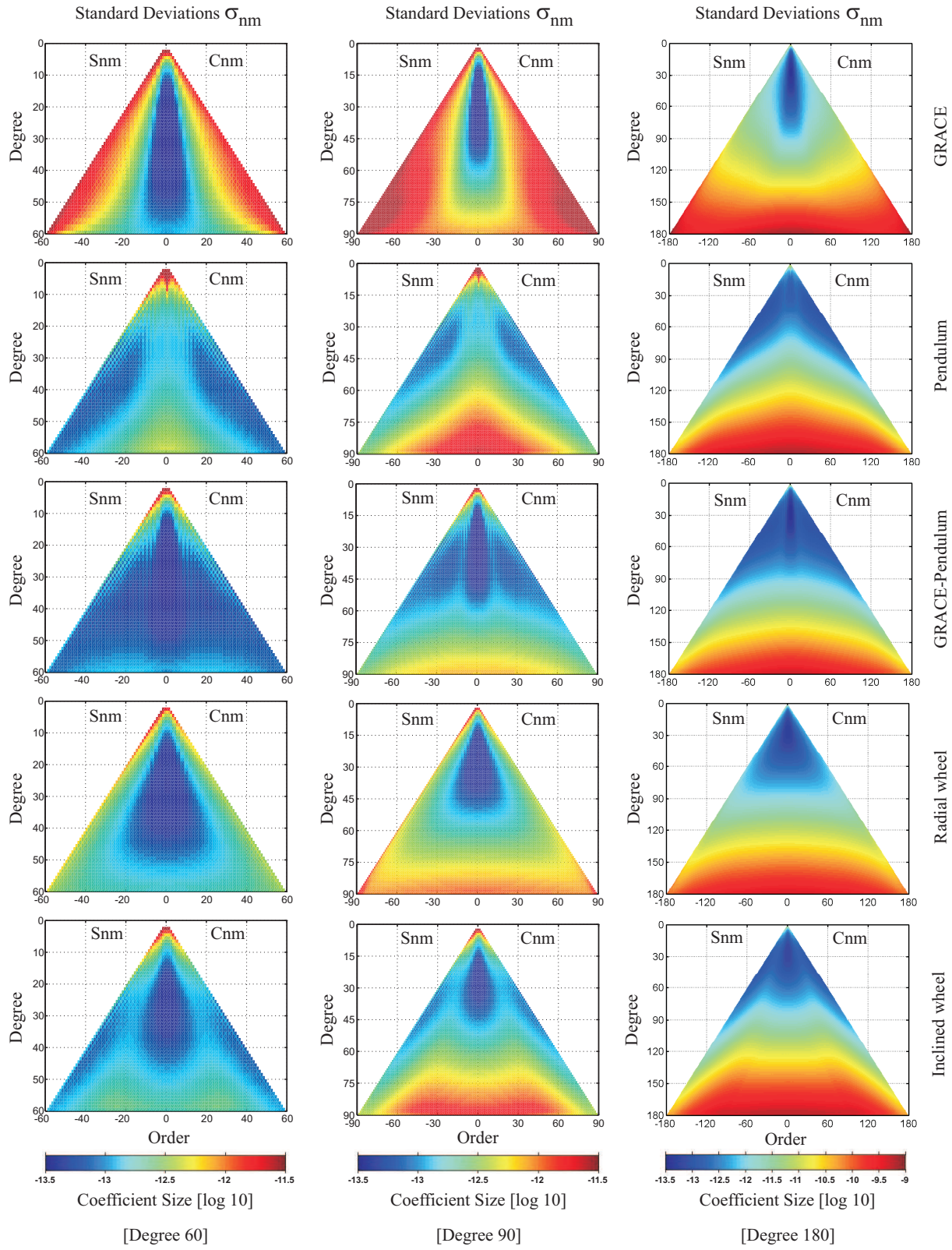

Fig. 7.9: Formal standard deviations of the recovered SH coefficients. From top to bottom: GRACE-type, Pendulum-type, GRACE-Pendulum-type, Radial wheel-type and Inclined wheel-type at different SH degrees; n= 60 (left), n= 90 (middle) and n= 180 (right).

This can also be seen if the 24-days solution in Fig. 7.11(a) is compared with the 12-days solution in Fig. 7.11(b). This fact is confirmed also by the formal standard deviations and the differences of the recovered coefficients (see Fig. 7.12). One observes a double performance in the 24-days global solution than in the 12-days solution documented in the global geoid errors expressed in the RMS and the average values in Table 7.5.

Now we consider the third and the forth cases of the Multi-GRACE-type constellations with a sampling period of 12 days. The third case (i.e. ΔM) as previously pointed out is composed of one constellation (of two SFF pairs) with the same spatial resolution of the 12-days case but with a temporal resolution twice the 12-days formation. For this reason, we find that the distribution of the subsatellite tracks as previously shown in Fig. 6.25(c) is twice the tracks in Fig. 6.25(a). Therefore, the corresponding recovered static gravity field solution of ΔM case (Fig. 7.11(c)) surpasses the 12-days solution (Fig. 7.11(b)) at all wavelength ranges of the gravity spectra and surpasses the 24-days solution at long harmonics (below n= 15). The improvement of ΔM solution is also seen from the cumulative geoid errors which were obviously improved, especially at low harmonics, when compared to the 24-days geoid errors. The formal standard deviations as well as the true SH differences emphasize these results already discussed in the spectral domains. Fig.7.12, especially the formal errors (at the left side), shows that the ΔM solution has (at the low order area) a less uncertainty (i.e errors) than the 12-days solution and approximately the same uncertainty behavior of the 24-days solution except for the medium-to-short harmonics.

The last constellation, which is composed of two GRACE-type FFs with different orbital RAAN (i.e. $\Delta\Omega$ shift), was also investigated in order to recover the gravity field. A different RAAN of $\Delta\Omega$= 180° has been selected as given before in Table 6.7 in order to have a homogeneous pattern of the satellite orbits at equatorial areas. This orbital RAAN difference corresponds to an Earth's longitudinal difference (λ) producing also a homogeneous subsatellite tracks pattern. An advantage of this constellation that it performs the same spatial coverage that the 24-days FF provides but in only 12 days. The recovered gravity field solution of the $\Delta\Omega$ constellation shows better solution (i.e geoid errors) of approximately more than half order of magnitude than the 12-days solution (see Fig. 7.10). It provides also an approximate behavior regarding the 24-days solution. This can be clearly seen from the formal errors given in Fig. 7.12 which does not show an obvious difference between the 24-days solution and the $\Delta\Omega$ solution.

When comparing the $\Delta\Omega$ solution with the aforementioned ΔM solution, we find that the former solution has less uncertainty and less geoid errors than the latter recovered solution. This can be clearly seen from Fig.7.12 rather than Fig. 7.10. From the investigation of the Multi-GRACE-type constellations applied to the determination of the static gravity field, one can conclude that a means of the retrieval of the gravity field now is possible from a 12 days mission instead of 24 (as well as 30) days of a single GRACE mission. Further investigations regarding this scenarios (or these constellations) will be examined in the following sections considering the time variable gravity field.

Table 7.5: Geoidal statistical values (RMS, average, minimum and maximum) in [mm] of the different gravity solutions as determined by the GRACE-type FFs and Multi-GRACE-type constellations at degree n= 90.

SH Degree & Values / FF types	n_{max}= 90			
	RMS	Avg.	Min.	Max.
GRACE 30-days	0.351	0.276	-1.375	1.433
GRACE 24-days	0.410	0.314	-1.566	1.601
GRACE 12-days	0.802	0.610	-3.409	4.031
Multi-GRACE (ΔM)	0.492	0.375	-2.092	2.581
Multi-GRACE ($\Delta\Omega$)	0.432	0.340	-1.678	1.630

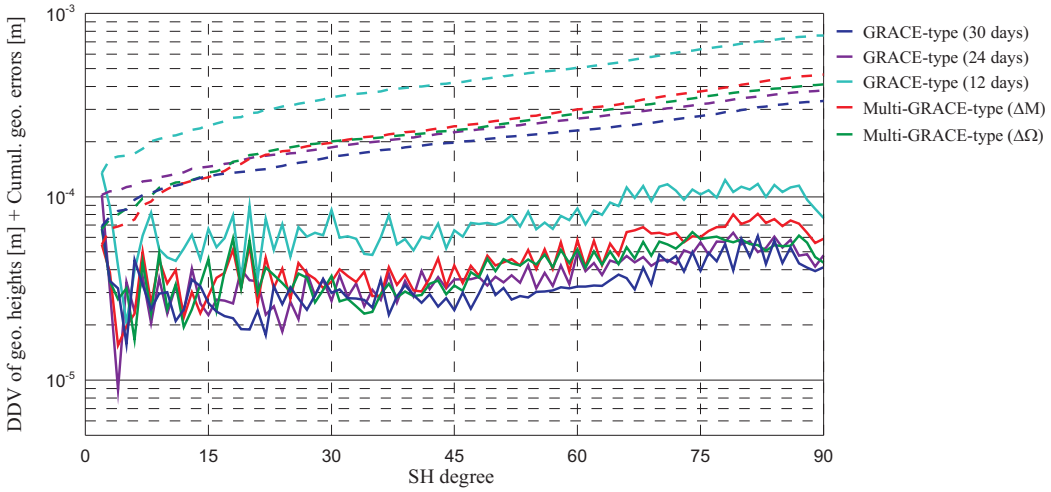

Fig. 7.10: Static gravity field solutions of the GRACE-type FFs and Multi-GRACE-type constellations. Solid lines represent *DDV* of geoid heights between ITG-GRACE03s and the gravity solutions and dashed ones represent the cumulative geoid errors.

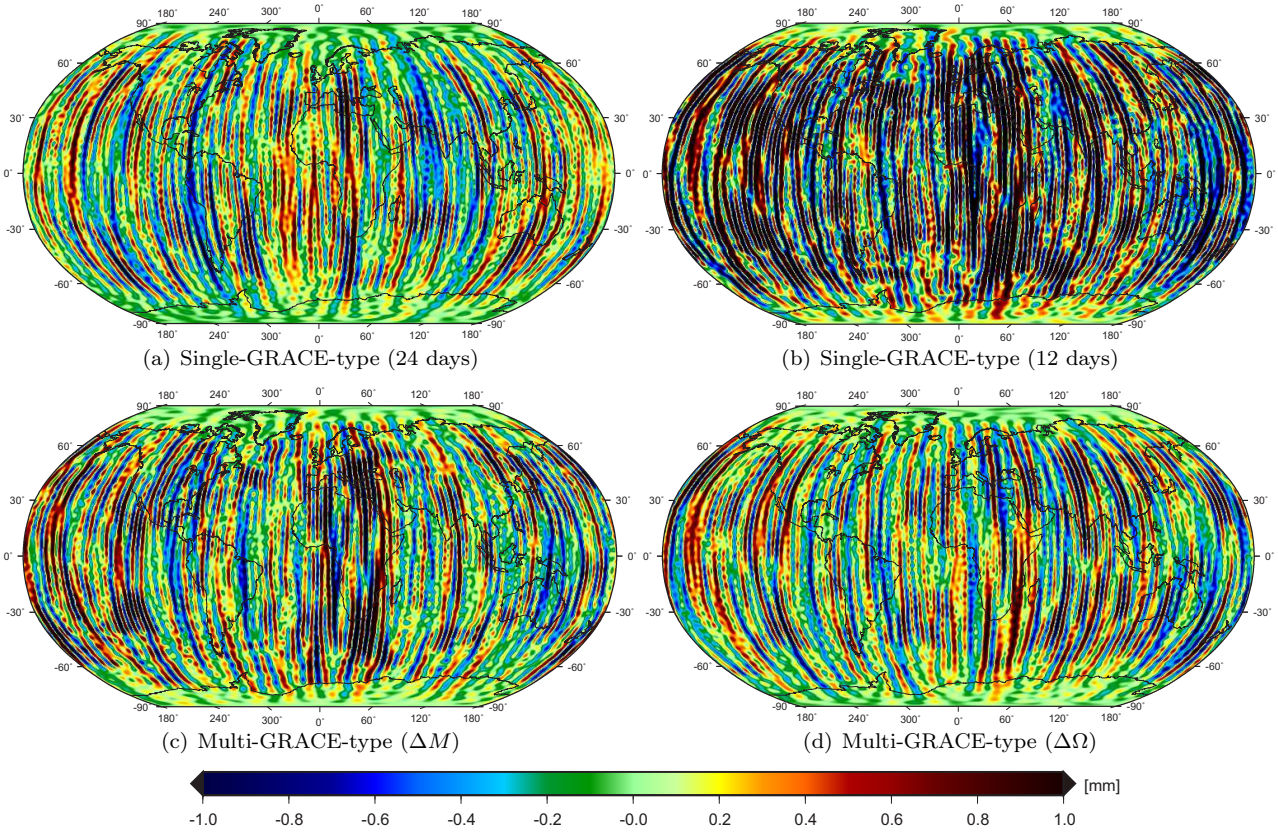

(a) Single-GRACE-type (24 days)
(b) Single-GRACE-type (12 days)
(c) Multi-GRACE-type (ΔM)
(d) Multi-GRACE-type ($\Delta\Omega$)

Fig. 7.11: Differences in geoid heights between ITG-GRACE03s and the static gravity field solutions of GRACE-type FFs and Multi-GRACE-type constellations, (a) GRACE-type 24-days, (b) GRACE-type 12-days, (c) Multi-GRACE-type (ΔM) constellation and (d) Multi-GRACE-type ($\Delta\Omega$) constellation, n_{max}= 90.

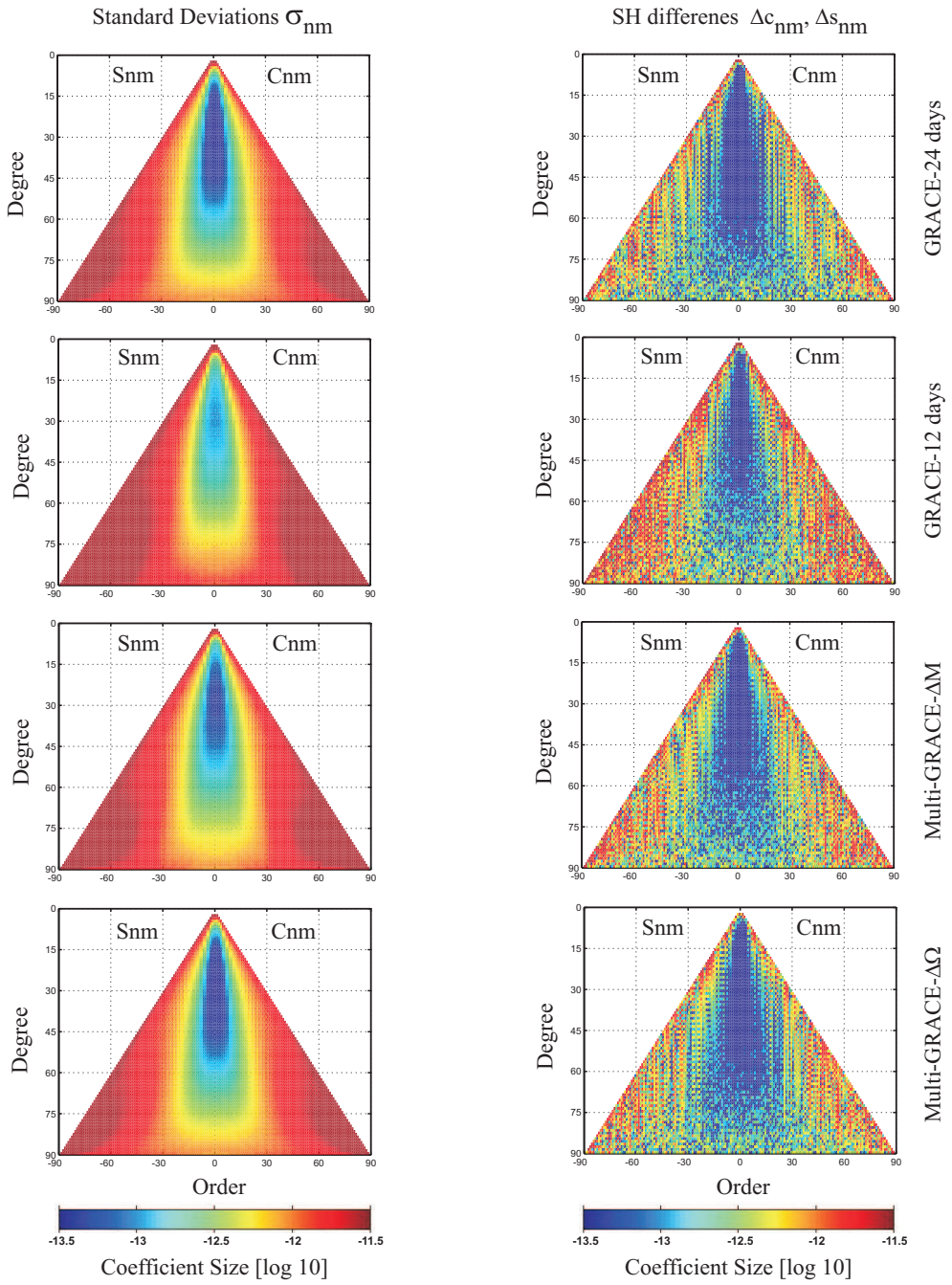

Fig. 7.12: Formal standard deviations (left) and the differences of the recovered SH coefficients (right) at degree and order 90. Solutions from top to bottom: GRACE-type 24-days, GRACE-type 12-days, Multi-GRACE-type (ΔM) constellation and Multi-GRACE-type ($\Delta\Omega$) constellation.

7.2.2 Time Variable Influences on the Gravity Field Solutions of Satellite Formation Flights

7.2.2.1 Introduction

Various processes are responsible for time variations of the Earth's gravity field (please refer to Fig. 2.3 regarding all processes with their time resolution). These variations have periods ranging from instant to very long term fluctuations. For instance, the instant variations include earthquakes and volcanos. The very long quasi-static variations include those arising from ice masses and the glacial uplift as well as the mantle convections, plate tectonic and other processes in the Earth core. The most important temporal signals having a great significance in satellite gravimetry include for example ocean tides, atmosphere, ocean and continental water mass. These phenomena induce short period temporal mass variations ranging from hourly to daily variations. As a result, they would alias into the longer period variations producing high frequency temporal aliasing effects, which distort the monthly mean gravity field estimations. This aliasing problem, which is associated with the GRACE (real mission) orbital formation, has not been investigated in the previous studies of e.g. Sharifi et al. (2007) and Sneeuw et al. (2008). Wiese et al. (2008) has investigated the aliasing effects considering satellite configurations having only two types of information: the along-track (having two and four collinear GRACE) and the radial (having two and four Cartwheel) formations.

This study intends to be comprehensive in examining nearly all satellite formations proposed to improve the Earth's gravity field. We investigate the effect of each time variable signal on the static gravity field solutions determined by different SFFs. Complementarily, our study is concerned itself also with the aliasing effects that are arising from the model errors of ocean tides, ocean and continental water hydrology. This study uses the most high frequency time variable elements that affect the gravity solutions estimated from satellite observations. These above mentioned objectives are considered as the main differences from the previous studies. Our next scenarios will investigate basically the following:

1. How largely affect the time variable signal the static gravity field solution in case of both the error-free and noisy cases (using different noises as investigated before in Sec. 7.2.1.2)?
2. How strongly are the effects of the model errors noticeable on the static gravity field solutions?
3. Which satellite formation flight provides the least errors and the refined gravity field solution?

The first item discriminates between the effect of the time variable signal and the effect of the noises on the static gravity solution. The second item investigates how far the solution affected by time variable signal and its model errors deviates from the static solution. The last item distinguishes different solutions determined from different formation flights. These mentioned items will be intensively later investigated within the next sections discussing the effects of the time-variable gravity field solutions as determined from the satellite formation flights (Sec. 7.2.2.3)

7.2.2.2 Time Variable Effects on the Gravity Field Solution at Different Noise Levels

To investigate how the time-variable signal (e.g. ocean tides) affects the gravity field solution, two simulation scenarios have been performed considering the Pendulum FF. This investigation is extended from the static scenario (Sec. 7.2.1.2) in such way that the different noises that were applied to the Pendulum FF given in Fig. 7.2 have been also applied in these scenarios. Firstly, the satellite orbits have been integrated again with the ocean tide effect using the FES2004 model beside the ITG-GRACE03s static field. In the gravity field analysis procedure, no reduction has been done to this effect. This means that the gravity solution shows the impact of the ocean tides alone as a time variable gravity field on the satellite observations. It should be mentioned here that the solutions were retrieved in this section to only SH degree n_{max}= 80 since the applied FES2004 ocean tide model is available up to this spherical degree. Fig. 7.13 shows firstly the

error-free solution indicated by the black curve after reducing the ocean tide effect. This error-free solution of RMS of $0.60\mu m$ has been also plotted with the error-free one of RMS of $0.62\mu m$ given in Fig.7.2, which indicated here with the red curve. They yield approximately the same gravity field. This emphasizes what is previously mentioned that it does not matter how many time-variable signals affect the satellite observations as long as they are correctly reduced in the gravity field analysis step.

Fig. 7.13 shows the effects of the ocean tides on the error-free gravity solution and on the noisy one indicated by error-free + FES2004 and noise + FES2004, respectively. The error-free + FES2004 case means that none of the observation noises has been added to the satellite observations in order to only observe the impact of the ocean tides on the error-free case. This is shown when comparing the error-free black curve with the black one of orange circles. The ocean tides influence the gravity solutions strongly at the long harmonics and provide a less impact at the medium harmonics yielding RMS global error of $5.98mm$. When adding white noises (noting that we applied noises of $5\mu m$ and $50nm$ only for the σ_{range}) of σ_{pos}= $2cm$ and σ_{range}= $50nm$, no further effects occurred. This is due to the fact that the impact of the ocean tides is larger than the impact of these noises. The result changes if σ_{range}= $5\mu m$ is applied which shows a worse impact in the gravity solution more than the ocean tidal effects themselves as given by the cyan curve of Fig. 7.13.

The second scenario investigates the reduction case of the ocean tide effects when another model is used to investigate how the model errors deviate from the error-free and noisy cases as well as from the ocean tide effects themselves. This was done using the ocean tide model EOT08a in the gravity analysis step. The results of this case have been indicated in Fig. 7.14 as (FES2004 – EOT08a). A detailed investigation concerning this reduction case will be given in the following sections (see Sec. 7.2.2.3.1). Firstly, the error-free solution and the impact of the ocean tides as given in Fig. 7.13 have been plotted with the FES2004 – EOT08a solutions in Fig. 7.14 to examine the deviation of the model error effects from both solutions. One can easily observe that there are no obvious differences between the gravity solutions of error-free one affected by the model errors or white noise of σ_{pos}= $2cm$ or white noise of σ_{range}= $50nm$. Slight differences began to occur up SH degree 50 to 80 because of the σ_{range} of $50nm$. When applying σ_{range}= $5\mu m$, the model errors having global RMS of $0.31mm$ are totally included under the solution of σ_{range}= $5\mu m$ which has global RMS error of $6.73mm$.

To sum up, it has been shown in this section that any selection of large white noise of the inter-satellite ranges (e.g. $5\mu m$) can blind the real effect produced by the time-variable signal as well as its model uncertainties (errors). Therefore, we will investigate in the following section the time variations of the gravity field considering the white noises of σ_{pos} of $2cm$ in orbit and σ_{range} of $50nm$ in the inter-satellite ranges, which have been already used in the static gravity field scenario.

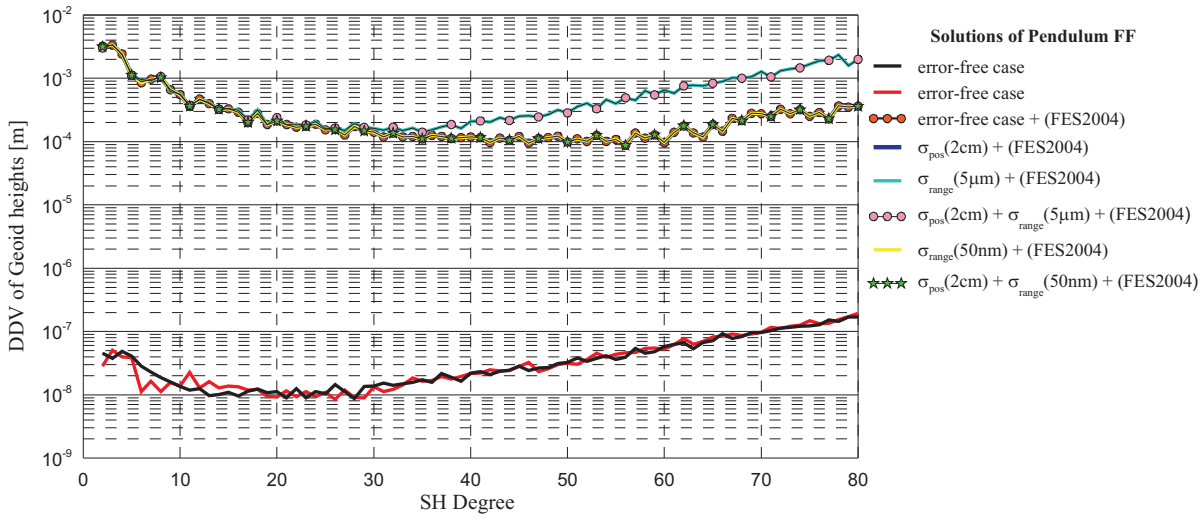

Fig. 7.13: *DDV* of geoid heights between ITG-GRACE03s and the gravity solutions of Pendulum FF affected by the ocean tides in the error-free and noise cases.

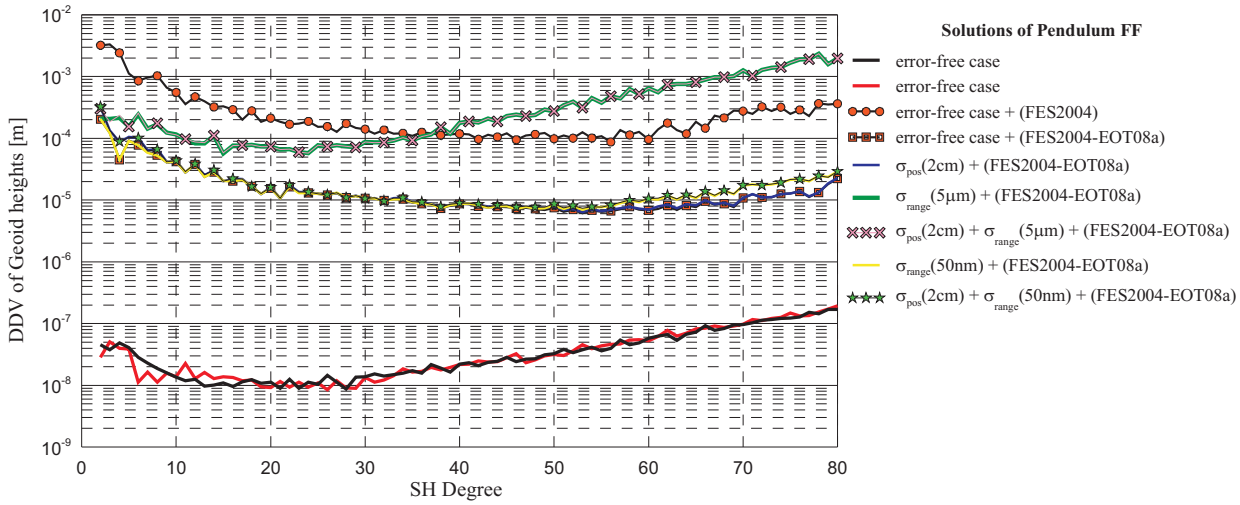

Fig. 7.14: *DDV* of geoid heights between ITG-GRACE03s and the gravity solutions of Pendulum FF affected by the ocean tides model errors in the error-free and noise cases.

7.2.2.3 Effects of Time Variable Elements on Monthly Mean Gravity Field Solutions as Determined by Satellite Formation Flights

In the following sections, the time variable gravity field attributed to mass variations of the ocean tides, atmosphere, ocean and hydrology will be investigated. This is done by numerous simulation scenarios. Each scenario includes one month (or sub-month in case of Multi-GRACE constellations) of simulated observations. These observations are integrated using the ITG-GRACE03s gravity field model (n_{max}= 180) combined with the time-variable gravity fields from the atmosphere, ocean, all tidal effects and hydrology. The temporal gravity solutions have been represented in terms of spherical harmonics up to degree and order 80 in case of the ocean tides and 100 in case of the atmosphere, the ocean and the hydrology. The following sections will also show the applied models and data used from the ocean tides, atmosphere, ocean and hydrology. The results will be given in both the spectral and spatial domains. The satellite observations have been corrupted with the white noise mentioned before (σ_{pos}= 2cm and σ_{range}= 50nm). After that, the medium-to-short wavelengths of the monthly mean field in terms of spherical harmonics were estimated.

We have to mention here that each signal of the four above mentioned phenomena has been examined alone without superimposition of other signals. Also it is important to point out that we are not tending to model or determine the time variable gravity field, but we investigate the temporal influences on the gravity field solutions. The estimates includes both the static field and the effect of time-variable gravity field or time-variable model errors. Therefore, the static gravity field was removed to obtain only these temporal effects. The obtained errors have been also compared with the temporal mean signal. The last comparison is considered as a signal-to-noise ratio (S/N ratio) which explains the possible distortion caused by the aliasing, which results from an insufficient sampling of the variation. Two Scenarios describe the obtained results given in the next sections:

1. The non-reduction case: in which the satellite observations are generated using the static and time-variable gravity field. Then in the gravity field estimation process, all these time-variables are reduced except that one, which we want to investigate its influences on the static gravity Field. This means that the time-variable element which affected the satellites orbits still remains in the gravity field estimation process.

2. The reduction case: in which the satellite observations are generated using the static and time-variable gravity field. Then in the gravity field estimation process, all these time-variables are reduced and that one, which we want to investigate is also reduced but with using another model. This explains the model inaccuracies or model errors and can also be considered as a measure of the possible aliasing of

the temporal signal. This case is a realistic one for investigating the effect of the time-variable signals on the gravity field solutions.

Fig. 7.15 shows a flowchart that explains in details these two last mentioned steps of the non-reduction and reduction cases.

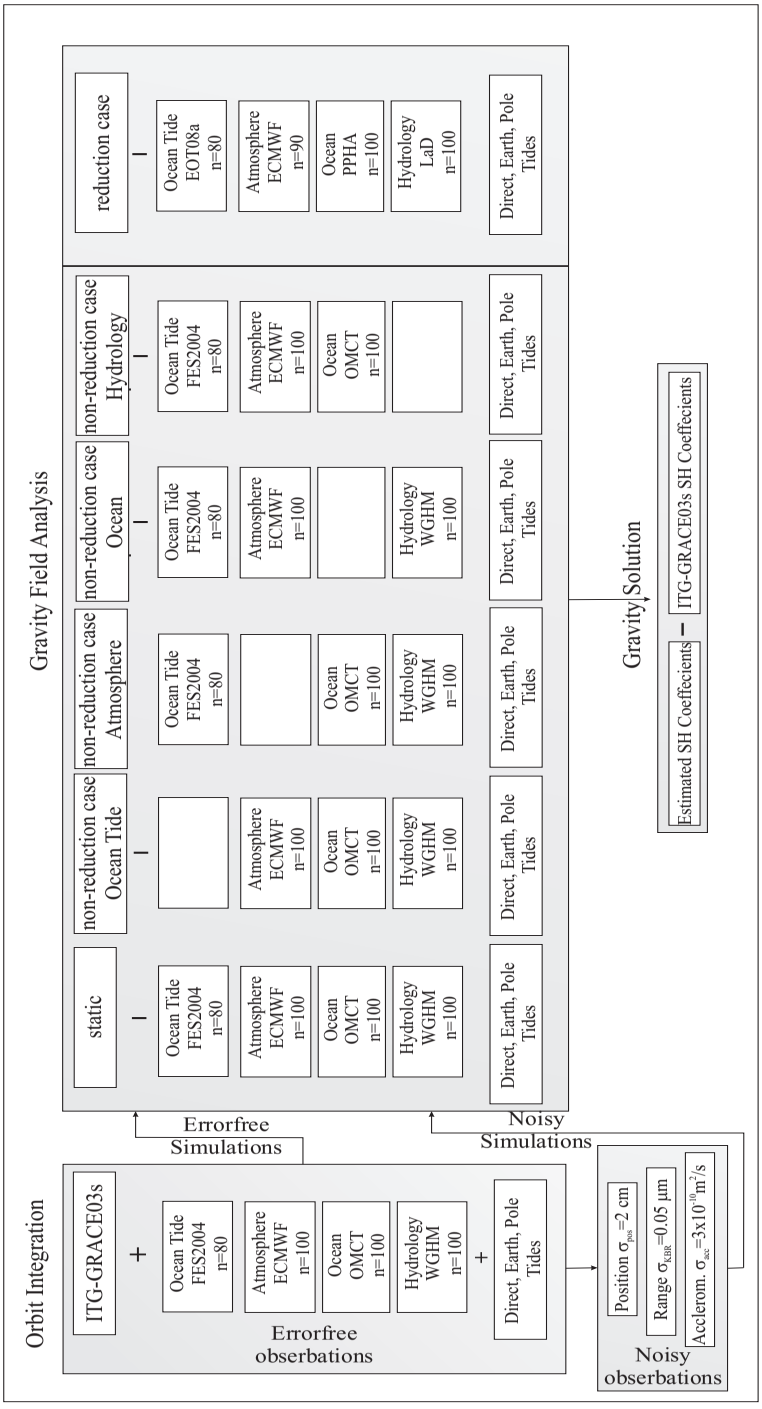

Fig. 7.15: A flowchart explains the both the non-reduction and the reduction cases.

7.2.2.3.1 Ocean Tides Effects

In this section, we examine the impact of the ocean tides on the static gravity field determined by different SFF types. The investigation is performed using the global ocean tide model FES2004 for the non-reduction case as shown in Fig. 7.15. Additionally, the effect of tidal modeling errors is also examined using another global ocean tide model EOT08a. This investigation is really significant for identifying the areas that require more improvements and further studies. This study shows also which satellite formation and which observation information provides the most refined (i.e. the least) model errors. It has to be mentioned that the effect of the temporal variations for the non-reduction and reduction cases are studied here on the mean gravity field estimates of one month of simulated observations.

The FES2004 (Finite Element Solution 2004) model (Letellier et al. 2004) is computed from the tidal hydrodynamic equations and data assimilation with a spatial resolution of $0.125° \times 0.125°$. FES2004 has better performance comparing other recent models like CSR4.0 (Center for Space Research version 4) or GOT00 (Goddard Ocean Tide model 2000). Therefore, the GRACE Science Data System processing centers at CSR, GFZ and JPL agreed to use FES2004 for GRACE gravity field solutions. The EOT08a (Empirical Ocean Tide) model (Bosch and Savcenko 2008) is a new global solution for the amplitudes and phases of the most dominant tide constituents, which is based on an empirical analysis of multi-mission satellite altimetry data of 13 years with a spatial resolution of $0.25° \times 0.25°$. It uses the combined altimeter data of the satellite missions Topex/Poseidon (using its whole life time), Jason-1, ERS-1, ERS-2, ENVISAT and GFO. This process of data combination has passed through three main pre-processing steps, which are described in detail in Savcenko and Bosch (2008).

The impact of each tidal constituent has not been investigated individually. Nevertheless, the target of this study is to investigate how much the ocean tidal effects as well as their model errors can be mitigated with different spatial samplings and proper temporal samplings. Different spatial samplings are carried out using SFFs of 30 days temporal resolution, while the proper temporal samplings are carried out using Multi-GRACE constellations of 12 days of temporal resolution. The ocean tide models FES2004 and EOT08a are applied in our investigation by using all tidal constituents. They include the semi-diurnal constituents $M2, S2, N2, K2$ and $2N2$, the diurnal constituents $K1, O1, P1, Q1$ and the long-term fortnightly M_f, monthly M_m, semi-annual S_{sa} and annual S_a constituents in addition to the non-linear tidal constituent $M4$. Each tidal constituent is decomposed into sine and cosine components and each component is expanded into spherical harmonic coefficients. So, each tidal constituent consists of 4 sets of tidal coefficients (C^C_{nm} and S^C_{nm} for cosine components and C^S_{nm} and S^S_{nm} for sine ones). The FES2004 model has been applied up to spherical harmonics degree and order $n_{max}= 80$. Therefore, the EOT08a model, whose tidal constituents are given up to spherical harmonics degree $n_{max}= 120$, has been truncated to $n= 80$ for this analysis.

The results of non-reduction and reduction cases are given in Figs. 7.16 – 7.19 spectrally and spatially, while the RMS values are given in Table 7.6. These figures are composed of two main parts that are corresponding to those scenarios given in Sec. 7.2.1.1 and Sec. 7.2.1.3. Regarding SFFs of Sec. 7.2.1.1, Fig. 7.16 shows one month (March 2004) gravity field solutions in terms of DDV of the geoid heights. The solid curves represent the impact of the FES2004 on the static gravity field solutions. This investigation is not an indication of the real state because the ocean tide effect should be removed during the gravity field analysis process. However, we examine only the influences of the ocean tides on the static gravity field solutions determined by the various satellite formation flights. The dashed curves which are corresponding to the reduction case and can also be considered as a nominal case for studying the ocean tidal aliasing error.

The ocean tides yield the largest impact of RMS errors of 2.91 cm on the GRACE-type FF gravity solution as shown in Fig. 7.16 and read in Table 7.6. The out-of-plane cross-track formations Pendulum-type and GRACE-Pendulum-type provide results approximately one full order of magnitude better than the other SFF types yielding RMS errors of 5.75 mm and 4.48 mm, respectively. The result of the GRACE-Pendulum-type FF provides an improvement of approximately factor 6 w.r.t. the GRACE-type FF. The impact of the ocean tides on the gravity field solutions determined by the radial formations Radial wheel-type and Inclined wheel-type is larger at low and medium harmonics, especially for the Radial wheel-type FF which provides the worst effect (up to n=30). At medium-to-short harmonics, the radial formations show refined results more than a half order of magnitude w.r.t. the GRACE-type FF but they do not surpass the out-of-plane

formations.

When considering the difference degree variances of the reduction case in Fig. 7.16, one observes that the GRACE-type solution behaves better from degree 2 to 30 and up degree 30 to 80 begins to behaves in a worse manner. All other formations minimized the tidal model errors as shown from their solutions providing improvement of factor 3. The solution of the Radial wheel-type descends from degree 2 up to degree 30, while in case of Inclined wheel-type it descends up to degree 40. The out-of-plane cross track Pendulum and GRACE-Pendulum formations minimized most of the ocean tide model errors since they provide the most refined solutions up to degree 60, while up degree 60 to 80 begin their solutions to be distorted. This can be clearly read from the right side of Table 7.6. We can infer from Fig. 7.16 that the the out-of-plane formations are able to solve most of model errors that the GRACE and even radial formations cannot solve. These improvements can be obviously shown in the spatial domain of Fig. 7.18 in terms of geoid heights. The model errors underlies the global ocean tide influences (the non-reduction case) of approximately factor 20 for the GRACE-type formation and of approximately factor 10 for the other formations (see Fig. 7.18). This can be seen from the global error distribution in the spatial domain of Fig. 7.18 when comparing the left figures with the right ones.

Figs. 7.17 and 7.19 show the gravity field solutions of the Multi-GRACE-type constellations with both the ($\Delta\Omega$) and (ΔM) concepts. They are also compared to the two GRACE-type 24-days and GRACE-type 12-days solutions in the spectral and spatial domains. The Multi-GRACE-type constellations with ΔM and $\Delta\Omega$ have not provided significant improvements in the static gravity field (see Fig. 7.11), but the results show significant importance in case of investigating the ocean tide effects. Similar to Fig. 7.16, Fig. 7.17 shows the retrieval of the gravity field solutions influenced by ocean tide effects and their model errors. Considering the non-reduction case, the GRACE-type 12-days FF yields the largest variances (errors). This result was expected since the GRACE-type 12 days FF suffers from poor spatial resolution. The ΔM constellation did not provide a refined solution w.r.t. the GRACE-type 12-days FF, despite its double number of satellite orbits. This may also be due to the same previous mentioned reason since the spatial coverage of the ΔM constellation is as poor as the GRACE-type 12-days FF. The slight improvements that the ΔM constellation provides are due to that some of the ocean tide constituents (especially the semi-diurnal) have been detected in a good manner because of the temporal shift (half day) of this ΔM constellation. This can be seen in Fig. 7.19 when comparing the global errors distribution of ΔM solution with that one of GRACE-type 12-days (e.g. the south of Pacific Ocean in west of South America).

On the contrary, the $\Delta\Omega$ constellation of 12-days provides a better gravity solution not only w.r.t. the two former solutions but also w.r.t. the GRACE-type 24-days solution. This is already clear when comparing the $\Delta\Omega$ solution with the latter mentioned 24-days one given in Fig. 7.19. Most of the global errors in the northern part of the Atlantic and Pacific oceans were significantly minimized in the $\Delta\Omega$ solution. The reason of this improvement is that the GRACE-type $\Delta\Omega$ constellation can detect the aliasing signals temporally at the same time which are not supported by the 12 days and 24 days formations and the ΔM constellation. In other words, when one GRACE-type FF of the $\Delta\Omega$ constellation detects such variations that take place over an area, the other GRACE-type FF of the same constellation detects temporally (as well as spatially) other variations over other areas at the same time. This means that the GRACE-type $\Delta\Omega$ constellation helps in minimizing the temporal aliasing of some signals (having smaller periods than 24 days). The slight improvement that the GRACE-type $\Delta\Omega$ constellation provides is read in Table 7.6, which shows an improvement of approximately factor 2 w.r.t. the GRACE-type FF (of 30 days). This indicates how important is GRACE-type $\Delta\Omega$ constellation not only for mitigating the influences of the ocean tide effects but also for reducing some model errors.

To sum up, the monthly mean gravity field solutions might be less corrupted by the tidal effects as well as tidal aliasing errors since they vary periodically over time at every location, and hence, will be averaged over one month. However, this study shows that the ocean tides model uncertainties can be mitigated when using some suitable spatial sampling by different satellite formations, especially the GRACE-Pendulum-type, and/or proper temporal sampling such as Multi-GRACE constellation. Yet, the factor of improvement that the GRACE-Pendulum-type provides is more convenient for investigating the ocean tide variations compared with Multi-GRACE constellation.

Table 7.6: Geoidal statistical values (RMS, average, minimum and maximum) of the different gravity solutions as determined by all SFFs due to the ocean tides effects at degree n= 80 corresponding to Fig. 7.18 (the upper five rows) and Fig. 7.19 (the lower four rows). The gray cells represent the least geoid errors.

Model / SFF types	FES2004 [cm]				FES2004 – EOT08a [mm]			
	RMS	Avg.	Min.	Max.	RMS	Avg.	Min.	Max.
GRACE (30-days)	2.919	2.007	-14.53	16.51	1.044	0.760	-6.240	6.289
Pendulum (30-days)	0.575	0.459	-2.502	1.825	0.316	0.246	-2.652	1.163
GRACE-Pendulum (30-days)	0.448	0.356	-2.306	1.880	0.241	0.179	-2.424	1.289
Radial wheel (30-days)	0.705	0.533	-3.813	4.116	0.349	0.249	-4.748	3.459
Inclined wheel (30-days)	0.758	0.608	-2.782	3.149	0.343	0.268	-2.213	2.300
GRACE 24-days	1.326	1.002	-6.509	6.611	1.082	0.747	-7.706	7.011
GRACE 12-days	3.915	2.876	-19.56	23.14	3.250	2.049	-24.34	23.97
GRACE 12-days (ΔM)	3.515	2.518	-18.79	21.72	3.112	1.921	-24.71	24.51
GRACE 12-days ($\Delta\Omega$)	1.150	0.894	-5.997	6.692	0.675	0.526	-3.142	3.302

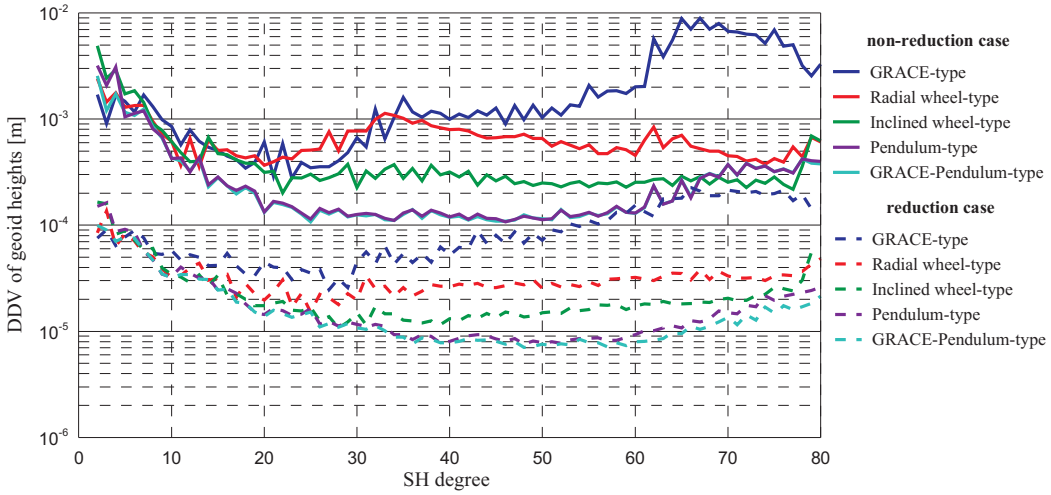

Fig. 7.16: *DDV* of geoid heights between ITG-GRACE03s and gravity field solutions as determined by different SFF types due to the ocean tide effects for both non-reduction and reduction cases.

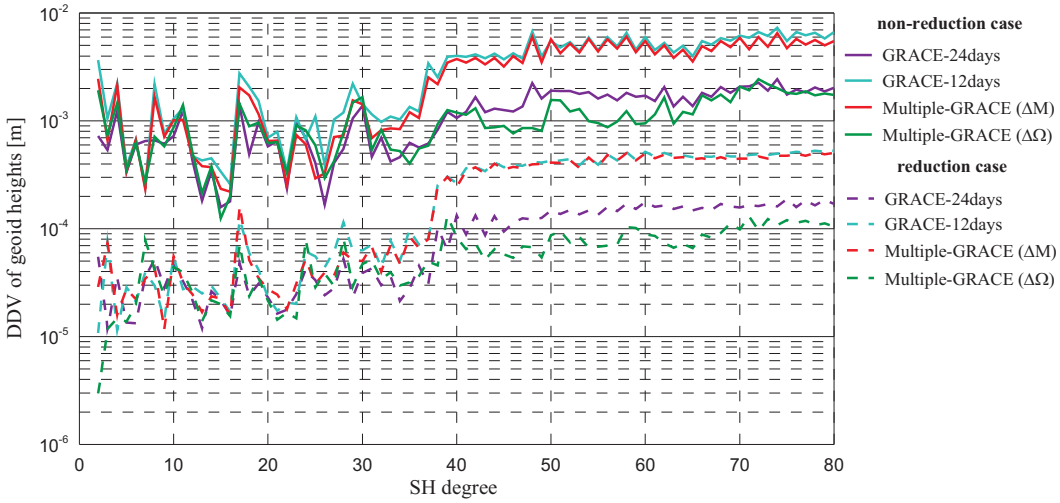

Fig. 7.17: *DDV* of geoid heights between ITG-GRACE03s and gravity field solutions as determined by by Multi-GRACE-type constellations due to the ocean tide effects for both non-reduction and reduction cases.

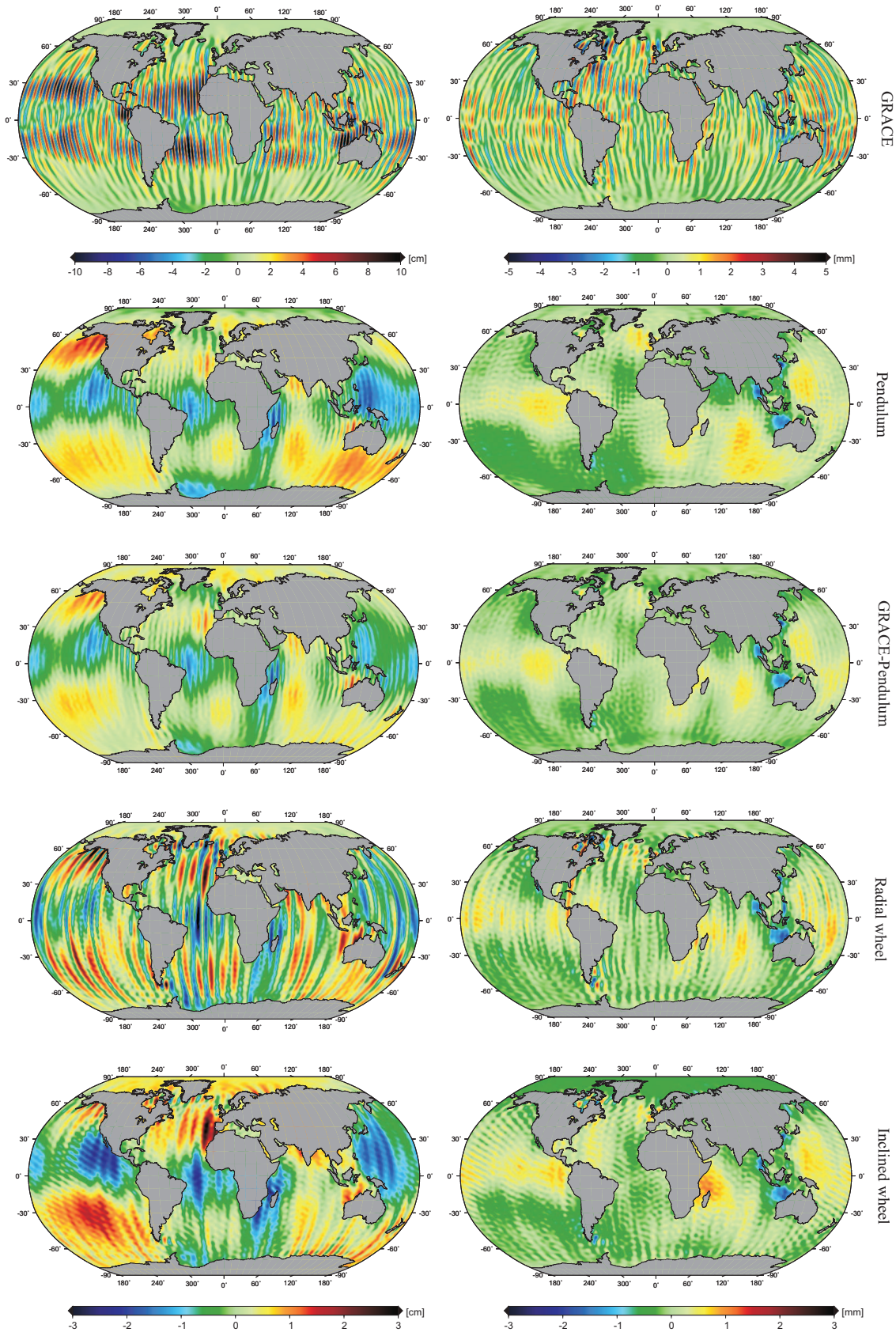

Fig. 7.18: Differences in geoid heights between ITG-GRACE03s and the gravity field solutions due to ocean tides effects as determined by SFF types. From top to bottom: GRACE, Pendulum, GRACE-Pendulum, Radial wheel and Inclined wheel. The left side represents the non-reduction case and the right side represents the reduction case, n_{max}= 80.

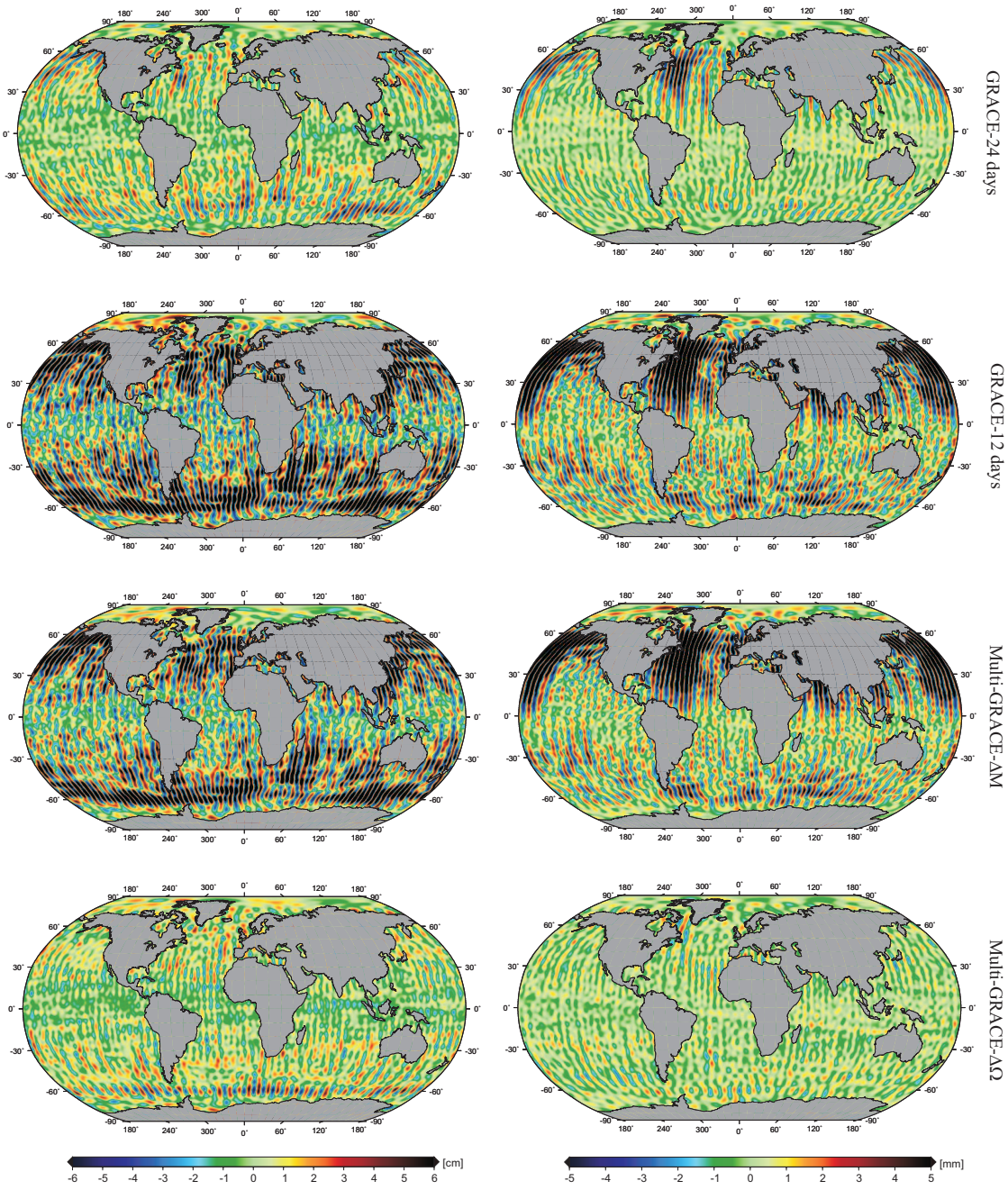

Fig. 7.19: Differences in geoid heights between ITG-GRACE03s and the gravity field solutions due to ocean tides effects as determined by GRACE-type FFs and Multi-GRACE-type constellations. From top to bottom: GRACE-type 24-days, GRACE-type 12-days, Multi-GRACE-type (ΔM) constellation and Multi-GRACE-type ($\Delta\Omega$) constellation. The left side represents the non-reduction case and the right side represents the reduction case, n_{max}= 80.

7.2.2.3.2 Processing of Atmospheric, Oceanic and Hydrological Effects

In the case of ocean tide model, the spherical harmonics have been represented by sinusoidal functions for the ocean tidal constituents. Unlike the ocean tide model, the models of the atmosphere, ocean and continental hydrology are represented here by spline base functions. This is due to the fact that the models of e.g. atmosphere and oceans are changing every 6 hours and every day w.r.t. the hydrology. So, beside the ITG-GRACE03s reference static field, these temporal models are interpolated in our simulations as a reference time variable gravity field parameterized or interpolated by time splines. This is considered as the most powerful advantage of GROOPS (Sec. 5.2) which parameterizes the time variable gravity field in the time domain and builds a set of spherical harmonic coefficients at a given time t. The advantage of this approach especially when using the short arc method is to know the temporal variations beneath the satellite formation flight in time. This means that by building the observation equation of each epoch of the short arc (of 30 minutes), the high frequency temporal resolutions of the 6 hourly atmosphere, 6 hourly ocean and daily continental hydrology are accurately handled within the analysis. The recovered gravity solutions are in terms of monthly mean spherical harmonic coefficients. The mean static field is subtracted from this mean solution producing the solution influenced by temporal variations. At the end, this solution is plotted w.r.t. the monthly and daily mean temporal signal to investigate how the mean recovered solution deviates from the mean temporal signal.

7.2.2.3.3 Atmospheric Effects

The atmospheric mass variations have always a special interest, especially when working with satellite observations. This is because the masses in the air column above each point on the Earth vary by a significantly large portion of the total Earth's mass. The Earth's atmosphere has a mean mass that corresponds to approximately 10^{-6} of the total mass of the Earth. Therefore, the atmospheric variations can be easily detected and well modeled by numerous observations having different parameters such as air pressure and air density, dry and wet air, water vapor and virtual temperature. The height (i.e. orthometric height) is also considered as a main parameter for modeling the atmospheric variations as given before in Sec. 4.2.2.1. A description of the mathematical expressions of these effects can, for example, be found in Peters (2007).

In this section, we present the simulated results of the impact of atmospheric variations on the recovered static gravity field coefficients as determined by all SFFs with the same procedures given in Sec. 7.2.2.3.1. Our analysis is based on the available atmospheric date from the de-aliasing product (Flechtner 2007) that was carried out by the GFZ. In this product, the operational analysis data at the European Center for Medium-range Weather Forecast (ECMWF) Integrated Forecast System (IFS) at synoptic times 0:00, 6:00, 12:00 and 18:00 has been extracted. The corresponding spatial resolution is 0.5° with a temporal resolution of 6 hours. For the four time steps, the gravity field spherical harmonic coefficients are given up to degree and order of n_{max}=100.

In the first step, the harmonic coefficients computed from ECMWF atmospheric data have been truncated from de-aliasing data sets (i.e. AOD1B-RL04 product). Sequentially, these coefficients have been applied as a background atmospheric model to investigate the influence of the atmospheric variations on the static gravity solutions (i.e. the non-reduction case). In our current study, there is no other atmospheric model available to investigate the model inaccuracy. However, other atmospheric models are available from e.g. NCEP (National Centers for Environmental Prediction) data. Instead, we considered 10% of signal power of the applied atmospheric model from ECMWF data as model errors. In this section, we consider this scenario as reduction case to determine the aliasing effects on the monthly mean field by considering the impact of these 10% remaining errors along one month mean solution.

The results of the atmospheric variations for one month of simulated observations (March 2004) are given in Figs. 7.20 – 7.23 in terms of *DDV* of geoid heights in the spectral domain. Figs. 7.24 and 7.25 represent the results in the spatial domain for all proposed SFF types. It is relevant to represent these spectral solutions not only by building the difference degree variances but also by comparing them with the monthly and daily mean atmospheric signals. These mean daily signals are given by the gray area in Fig. 7.21 representing

30 curves of 30 days of March 2004. Within this range of the gray curves, the monthly mean atmospheric variations (the black curve), which is the one-month average of daily atmospheric variations, is drawn to observe how far the solutions of the reduction case deviate from the monthly and daily mean solutions.

Fig. 7.20 shows the gravity field solutions of the SFF types given in Sec. 7.2.1.1 up to SH degree and order of n=100 for both the non-reduction and reduction cases. The largest atmospheric RMS error results as expected from the GRACE-type gravity field solution yielding its well-known error striping shape in the north-south direction as shown in Fig. 7.24. Table 7.7 shows RMS error of 1.5 cm, which is approximately of factor 5 to 7 worse w.r.t. the solutions of the other formation flights. Despite the worse behavior of other configurations than GRACE-type at long wavelength ranges (i.e. at low harmonics), they provide better results approximately one order of magnitude w.r.t. the GRACE-type FF at the medium and medium-to-short wavelengths (see Fig. 7.20). Considering the results of Fig. 7.24 except that one for the GRACE-type, we recognize large atmospheric effects of the Pendulum and Inclined wheel formations at the north pole (indicated by the positive geoid errors) as well as at the south pole. Most of these atmospheric effects are mitigated already by the other two formations of the GRACE-Pendulum-type and the Radial wheel-type. This can be attributed to the cross-track ranges occurring at the poles. As already investigated in the last chapter (refer to Sec. 6.2.3.1), the level of the gravity errors increases when the inter-satellite distances between the satellites diminish. These effects are reduced in case of the GRACE-Pendulum-type solution because of the incorporation of along-track information of its configuration. Moreover, most of these effects are mitigated in the Radial wheel-type because of the existence of the along-track arm at the poles, where the cross-track information is not involved within the observations of this formation. This shows how important is the along-track information for providing the least geoid errors over the pole areas when investigating the atmospheric variations.

The behavior of the reduction case did not differ much from the non-reduction case except that the reduction case provides improved results of factor 10 lower than the non-reduction case. The Pendulum and Inclined wheel formations behave in a worse manner up degree n=55 to 100 w.r.t. the non-reduction case. This can be easily observed when comparing the two signals of Pendulum and Inclined wheel formations in Fig. 7.20 (compare their solid curves with their dashed curves). The GRACE-Pendulum-type still provides the most refined recovered solution in the reduction case. To observe the deviation of the aliasing effects from the mean daily and monthly solutions, the gravity field solutions of the non-reduction and reduction cases have been plotted with the monthly and daily mean atmospheric signals as shown in Fig. 7.21. In this figure, only the gravity solutions of the GRACE-type and the GRACE-Pendulum-type FFs have been drawn since they provide the largest and least RMS errors, respectively, to avoid the confusion by representing all signals. These solutions are also compared with their corresponding static gravity field solutions, which are given before in Sec. 7.2.1.1 up to degree n=90 to consider the deviation of the aliasing effects from the static solutions. Considering the monthly mean atmospheric signal, we find that the aliasing effects are larger than the GRACE-type and GRACE-Pendulum-type FFs monthly solutions up to degree 12 and 22, respectively. This indicates how important the GRACE-Pendulum-type FF is, specifically, for detecting the aliasing effects induced by the atmospheric variations w.r.t. the GRACE-type one.

The same procedures have been applied for the Multi-GRACE-type constellations as shown in Figs. 7.22 and 7.23. The gravity field solutions have been recovered up to only degree and order n_{max}=90 according to the Nyquist rule (see Sec. 6.2.3.1). Regarding the non-reduction case, the GRACE-type 12-days FF and the Multi-GRACE-type (ΔM) constellation provide as expected the largest atmospheric effects as seen in Fig. 7.25 due to their worse spatial coverage. Albeit the latter constellation surpasses the former one at the majority of the wavelength ranges due to the double number of its satellite observations. The slight refinements that the Multi-GRACE-type (ΔM) constellation provides can be obviously observed when comparing the two latter mentioned solutions at the southern part of the Pacific Ocean. The Multi-GRACE-type ($\Delta\Omega$) constellation surpasses all solutions of the other GRACE-type FFs providing the least error level in the spectral domain as seen from its gravity solution in terms of the *DDV* and as read from Table 7.7. Most of the atmospheric variations have been reduced at the northern and southern parts of the hemispheres as shown in Fig. 7.25.

The same thing holds also for the reduction case. The gravity solutions have not differed from the non-reduction case except for the level of error accuracy, which shows the improved results of factor 10 w.r.t. the

non-reduction case as read from Table 7.7. Similar to Fig. 7.21, the gravity field solutions of GRACE-type 12-day and the Multi-GRACE-type ($\Delta\Omega$) constellation representing the largest and least RMS errors, respectively, have been plotted versus the daily and monthly mean atmospheric variations as well as the static gravity solutions in Fig. 7.23. This shows how the solutions of the non-reduction and the reduction cases are far from the atmospheric variations. We have found that the monthly mean atmospheric variations are larger than the GRACE-type 12-days and Multi-GRACE ($\Delta\Omega$) monthly solutions up to degree 12. Therefore, the atmospheric aliasing is hard to be predicted or significantly minimized in case of the Multi-GRACE-type ($\Delta\Omega$) constellation due to the fact that it contains the observations only in the along-track direction.

Comparing the results of the atmospheric variations with the ocean tide variations of the last section, one can clearly conclude that detection of the atmospheric variations are much difficult than the ocean tide ones. Comparing Figs. 7.18 and 7.19 with Figs. 7.24 and 7.25 also indicate that the impact of the ocean tide variations exceeds that one induced by the atmospheric variations (in terms of the error level of geoid heights). This agrees with the reality since the ocean tidal variations affect the satellite orbits approximately by a deviation of sub-meter level, while the atmospheric variations affect them yielding an approximate deviation of sub-cm level. This will be noticed later from Fig. 7.32.

Table 7.7: Geoidal statistical values (RMS, average, minimum and maximum) of the different gravity solutions as determined by all SFFs due to the atmospheric effects at degree n= 100 corresponding to Fig. 7.24 (the upper five rows) and Fig. 7.25 (the lower four rows). The gray cells represent the least geoid errors.

Model / SFF types	ECMWF [cm]				ECMWF 10%-aliasing [mm]			
	RMS	Avg.	Min.	Max.	RMS	Avg.	Min.	Max.
GRACE	1.503	1.126	-6.660	7.005	1.575	1.193	-6.936	6.790
Pendulum	0.215	0.164	-0.847	1.104	0.365	0.289	-1.317	1.599
GRACE-Pendulum	0.157	0.120	-0.753	0.837	0.200	0.157	-0.783	0.979
Radial wheel	0.295	0.226	-1.383	1.772	0.358	0.281	-1.626	1.978
Inclined wheel	0.251	0.194	-1.132	1.841	0.343	0.272	-1.307	1.918
GRACE 24-days	1.145	0.854	-5.902	6.063	1.207	0.898	-7.456	6.818
GRACE 12-days	1.936	1.468	-8.891	7.947	2.089	1.576	-9.396	9.064
Multi-GRACE (ΔM)	1.687	1.251	-8.610	8.422	1.766	1.300	-8.895	8.391
Multi-GRACE ($\Delta\Omega$)	1.001	0.726	-4.606	4.725	1.033	0.766	-4.916	5.100

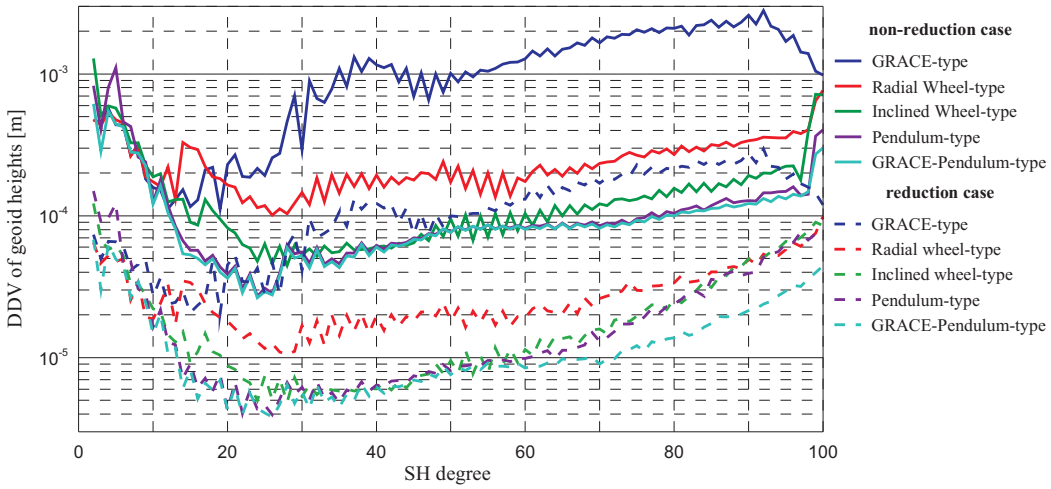

Fig. 7.20: *DDV* of geoid heights between ITG-GRACE03s and gravity field solutions as determined by different SFF types due to the atmospheric effects for both non-reduction and reduction cases.

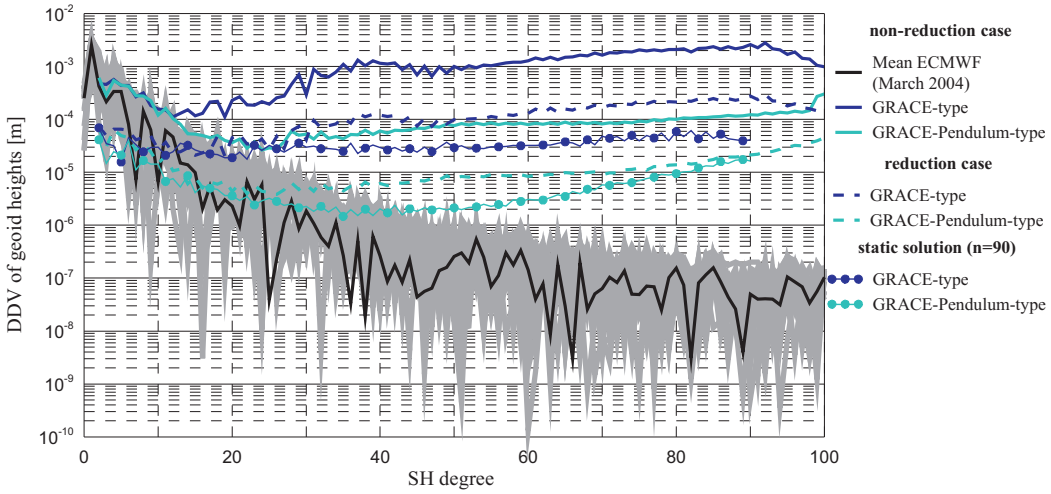

Fig. 7.21: *DDV* of geoid heights between ITG-GRACE03s and gravity field solutions as determined by GRACE- and GRACE-Pendulum-type FFs due to the atmospheric effects for both non-reduction and reduction cases compared to the mean daily and monthly atmospheric variations.

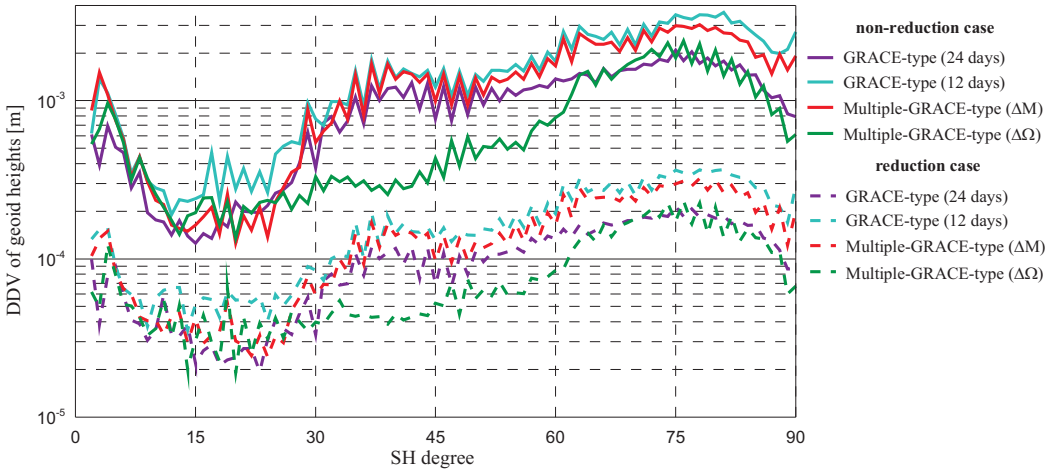

Fig. 7.22: *DDV* of geoid heights between ITG-GRACE03s and gravity field solutions as determined by GRACE-type FFs and Multi-GRACE-type constellations due to the atmospheric effects for both non-reduction and reduction cases.

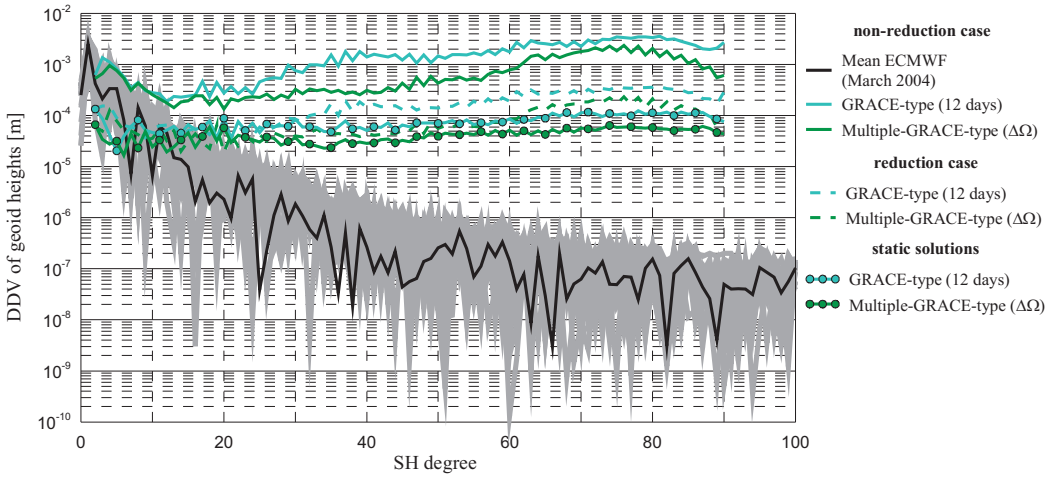

Fig. 7.23: *DDV* of geoid heights between ITG-GRACE03s and gravity field solutions as determined by GRACE-type 12-day FF and the Multi-GRACE-type ($\Delta\Omega$) constellation due to the atmospheric effects for both non-reduction and reduction cases compared to the mean daily and monthly atmospheric variations.

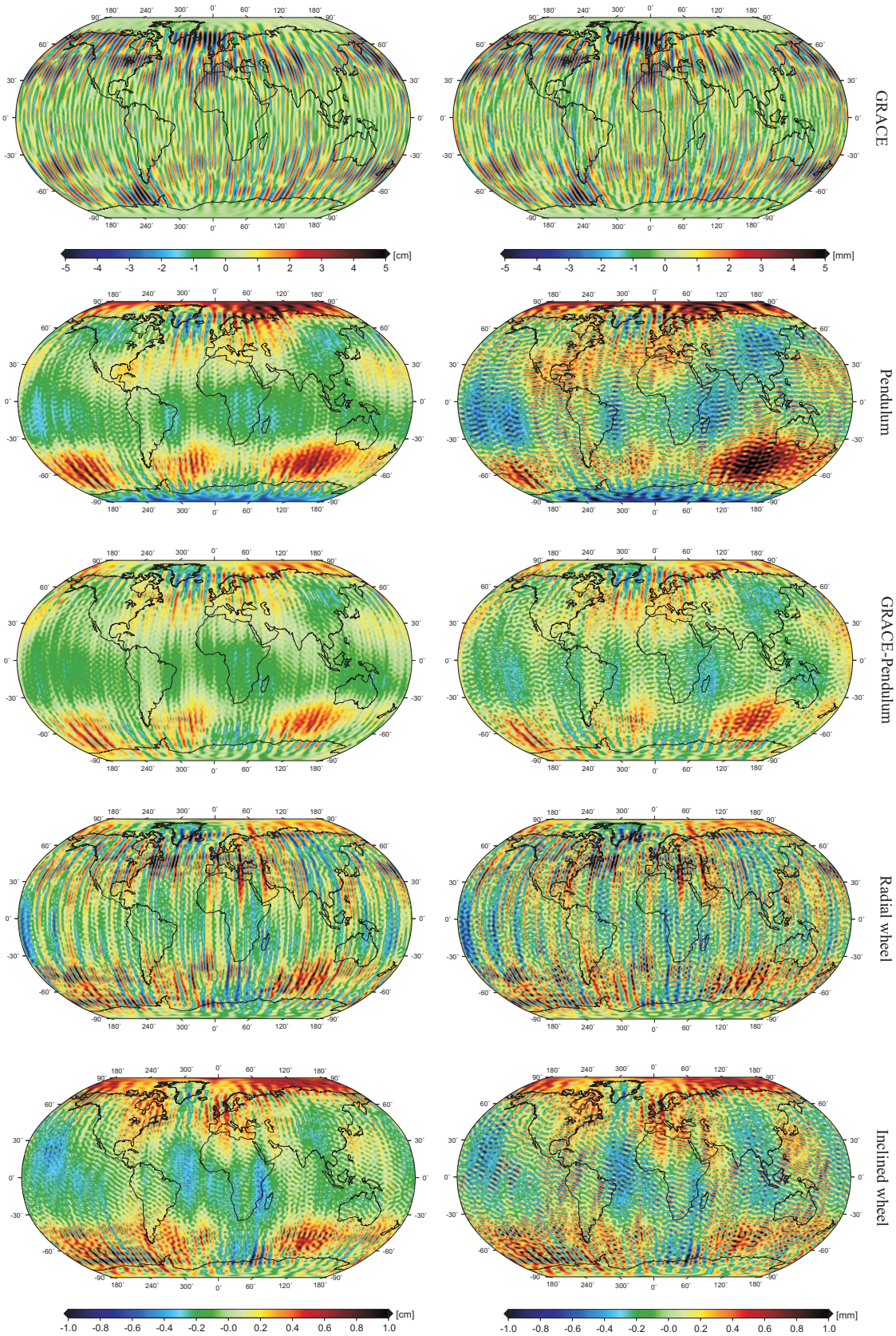

Fig. 7.24: Differences in geoid heights between ITG-GRACE03s and the gravity field solutions due to atmospheric variations as determined by SFFs. From top to bottom: GRACE, Pendulum, GRACE-Pendulum, Radial wheel and Inclined wheel. The left side represents the non-reduction case and the right side represents the reduction case, n_{max}= 100.

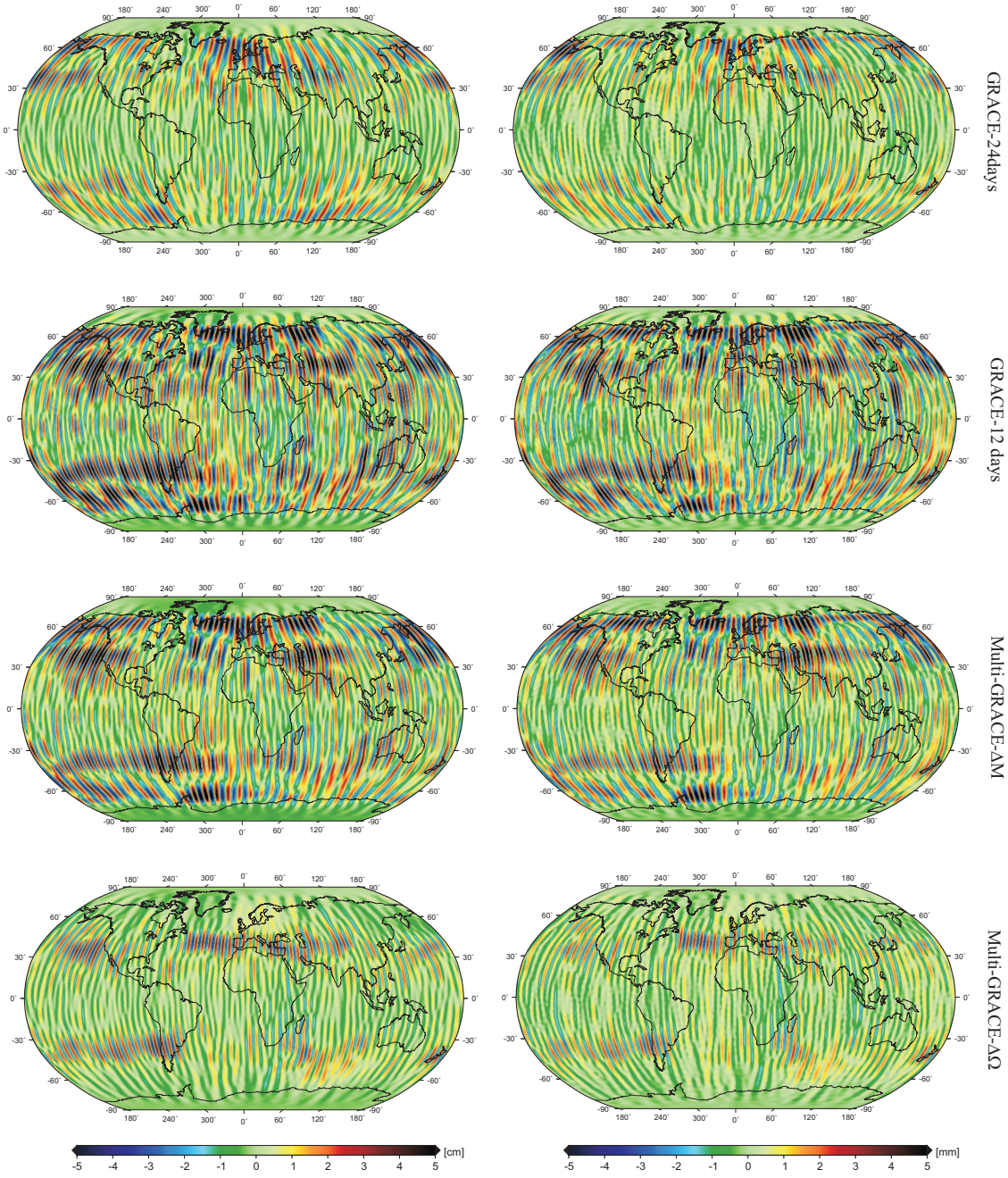

Fig. 7.25: Differences in geoid heights between ITG-GRACE03s and the gravity field solutions due to atmospheric variations as determined by GRACE-type FFs and Multi-GRACE-type constellations. From top to bottom: GRACE-type 24-days, GRACE-type 12-days, Multi-GRACE-type (ΔM) constellation and Multi-GRACE-type ($\Delta\Omega$) constellation. The left side represents the non-reduction case and the right side represents the reduction case, n_{max}= 100.

7.2.2.3.4 Oceanic Effects

The temporal variations of the oceanic water mass are dependent on the previously mentioned atmospheric mass variations. This is due to the fact that a reaction takes place over an area producing an oceanic mass variation when the mass column of the atmosphere (e.g. air pressure variations) changes over this area. Therefore, a realistic and an accurate modeling requires always a combined consideration of the atmosphere and ocean ideally with consistent data. For instance, the AOD1B product (Flechtner 2007) has the data type "glo", which is composed of the combined atmospheric data type "atm" and the oceanic one "ocn". In other words, the harmonic coefficients "atm+ocn" yield exactly those of type "glo" (e.g. AOD1B-RL04). As mentioned in Sec. 4.2.2.2, the oceanic temporally variable components are substantially smaller than those of the atmosphere. Therefore, they produce gravity field variations which are in a comparable order of magnitude lower than those of the atmosphere. This is latterly shown in Fig. 7.32 (Sec. 7.2.2.3.5) which shows besides the two temporal gravity field solutions of the atmospheric and oceanic variations as determined by e.g. GRACE-type FF the gravity solution of the "glo" variation.

In this section, we investigate both the non-reduction and reduction cases using two different ocean models, the baroclinic OMCT model and the barotropic PPHA one. The processing is similar to the ocean tides scenario given in Sec. 7.2.2.3.1. The main differences between the two OMCT and PPHA ocean models as well as their processing strategies are given in detail in Flechtner (2007). Similar to the atmospheric processing, the gravity field analysis is based here on the available oceanic data from the two de-aliasing products AOD1B-RL04 for OMCT and AOD1B-RL01 for PPHA with the same temporal resolution of synoptic times 0:00, 6:00, 12:00 and 18:00. The corresponding spatial resolution of OMCT and PPHA models are 1.875° and 1.125°, respectively. For the AOD1B computations, the two models have been interpolated to spatial resolution of 0.5° (Flechtner 2007, p. 20-22). The OMCT model has been used in the non-reduction case. In other words, the satellite observations have been generated with OMCT and then its effects have not been reduced in the gravity field estimation process. The PPHA model has been applied for the reduction case to investigate the model differences. The spherical harmonics coefficients estimated from the PPHA model have been truncated from de-aliasing data of AOD1B-RL01 product (Flechtner, private communication).

A time series of one month (March 2004) has been also applied for this analysis. The gravity field results are given in the spectral domain in Figs. 7.26 – 7.29 in terms of *DDV* of geoid heights. Figs. 7.30 and 7.31 represent the oceanic variations in the spatial domain for all SFF types. Fig. 7.26 represents the results of both the non-reduction and reduction cases of the GRACE-, Pendulum-, GRACE-Pendulum-, Radial wheel- and Inclined wheel-type FFs. Fig. 7.27 represents only the largest and least RMS errors of the GRACE-type and GRACE-Pendulum-type FF types, respectively, w.r.t. their static gravity field solutions. The daily and monthly mean oceanic variations have been also plotted in the same figure (Fig. 7.27) to investigate how the two solutions are far from the mean oceanic variations.

Regarding the non-reduction case, the spherical harmonics (of $n_{max} = 100$) concerning the OMCT oceanic model have been taken from the AOD1B-RL04 product. This shows the impact of the oceanic variations on the static gravity solutions of the SFF types. The obtained results are similar to those given in the atmospheric section (compare Fig. 7.20 with Fig. 7.26) except for the level of error variability. The RMS errors of the oceanic variations show slight refinements as given in Table 7.8 for the non-reduction case. This emphasizes how the oceanic variations depend on the atmospheric ones as discussed before. They agree with the atmospheric variations in character but not in error accuracies.

The gravity field solutions of the reduction case have been plotted together with the non-reduction solutions in Fig. 7.26. The geoid heights have been represented in the spatial domain in Fig. 7.30. Similarly, the oceanic variations have their largest influences on the GRACE-type solution and their least influences on GRACE-Pendulum-type one. Therefore, we have plotted only these two solutions with the daily and monthly mean oceanic variations. The GRACE-Pendulum-type provides an obviously significant refinement, which is clearly observed in Fig. 7.30, especially in the southern parts of the Pacific ocean and the Atlantic ocean. Moreover, most of the OMCT model errors have been reduced by applying the PPHA model regarding these oceanic regions except for the northern part of the hemisphere (i.e. the Arctic). This is due to the global coverage of the baroclinic OMCT model which is between 77°S and 90°N, while the barotropic PPHA model covers only

from 75°S to 65°N of the global oceans. Another reason is the different calculation processes that have been applied for each model. For instance, The S2 oceanic tidal constituent was included during the calculations of the AOD1B-RL01 for the PPHA model. This effect (of S2 constituent) was removed during the calculation of the spherical harmonics of AOD1B-RL04 for the OMCT model. Therefore, no improvements are obtained for the Arctic region as seen from Fig. 7.30.

The gravity solutions of the reduction case of the oceanic variations agree with those obtained by the ocean tides scenario and the atmospheric one that the GRACE-Pendulum-type FF provides. The improvement is approximately of factor 6 w.r.t. the GRACE-type FF. Moreover, most of the geoid errors induced by the GRACE and Pendulum configurations have been disappeared in the GRACE-Pendulum one. Hence, merging the cross-track information with the along-track one into the same observations mitigates the influences of the temporal variations of the ocean tides, the atmosphere and the ocean as well as their model differences.

Similarly, the oceanic variations have been investigated for the Multi-GRACE-type constellations. The results are given in the spectral domain in Figs. 7.28 and 7.29 in terms of the DDV of the geoid heights and in the spatial domain in Fig. 7.31. As same as the atmospheric scenario, the gravity field solutions of the oceanic variations have been carried out up to spherical harmonic degree and order n=90 because of the Nyquist rule. As read from Table 7.8, the results of the oceanic variations concerning the non-reduction case did not differ from those obtained from the atmospheric scenario. The Multi-GRACE-type ($\Delta\Omega$) constellation provides better results of half-order of magnitude w.r.t. the GRACE-type 12-days solution. The gravity solution influenced by the oceanic variations of Multi-GRACE-type (ΔM) constellation surpasses all three configurations up degree 14 to 28. This can be seen from the behavior of difference degree variances given in Fig. 7.28 and in terms of the geoid errors in Fig. 7.31. Regarding the reduction case, the Multi-GRACE-type ($\Delta\Omega$) constellation provides a better solution of factor 2 w.r.t. the GRACE-type 24-days solution at the medium harmonics (Fig. 7.28). This improvements can be also seen spatially in Fig. 7.31. This result agrees also with the previously obtained results (of ocean tides and atmosphere) which showed that the Multi-GRACE-type ($\Delta\Omega$) constellation provides the refined gravity solution of all Multi-GRACE formations.

Table 7.8: Geoidal statistical values (RMS, average, minimum and maximum) of the different gravity solutions as determined by all SFFs due to the oceanic effects at degree n= 100 corresponding to Fig. 7.30 (the upper five rows) and Fig. 7.31 (the lower four rows). The gray cells represent the least geoid errors.

Model / SFF types	OMCT [cm]				OMCT-PPHA [cm]			
	RMS	Avg.	Min.	Max.	RMS	Avg.	Min.	Max.
GRACE	1.385	0.988	-7.587	8.012	0.925	0.601	-7.359	7.292
Pendulum	0.167	0.121	-1.309	1.116	0.121	0.083	-1.345	1.088
GRACE-Pendulum	0.138	0.098	-1.283	1.159	0.095	0.059	-1.302	1.112
Radial wheel	0.225	0.171	-1.168	1.163	0.130	0.097	-0.924	0.933
Inclined wheel	0.228	0.175	-1.577	0.903	0.165	0.125	-1.049	0.509
GRACE 24-days	1.072	0.731	-6.450	6.375	0.761	0.485	-5.700	5.678
GRACE 12-days	1.601	1.177	-8.901	8.366	0.973	0.668	-6.336	6.506
GRACE 12-days (ΔM)	1.410	1.011	-8.028	7.669	0.872	0.558	-6.331	6.427
GRACE 12-days ($\Delta\Omega$)	0.691	0.493	-4.198	3.613	0.400	0.289	-2.206	2.131

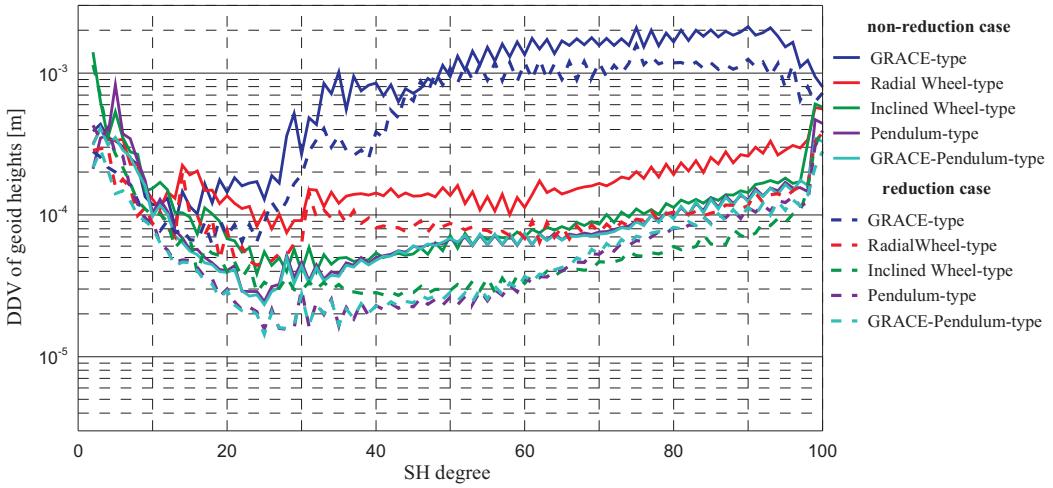

Fig. 7.26: *DDV* of geoid heights between ITG-GRACE03s and gravity field solutions as determined by different SFF types due to the oceanic effects for both non-reduction and reduction cases.

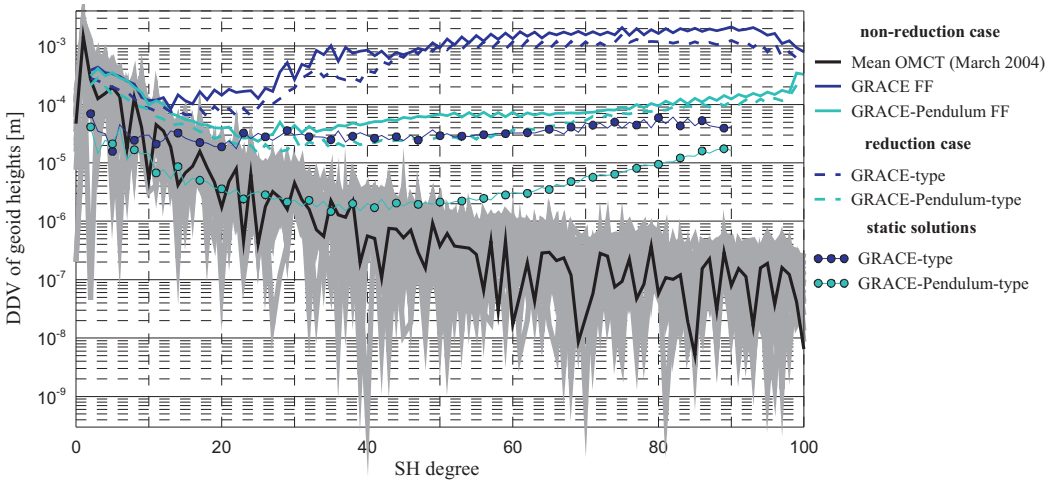

Fig. 7.27: *DDV* of geoid heights between ITG-GRACE03s and gravity field solutions as determined by GRACE- and GRACE-Pendulum-type FFs due to the oceanic effects for both non-reduction and reduction cases compared to the mean daily and monthly oceanic variations.

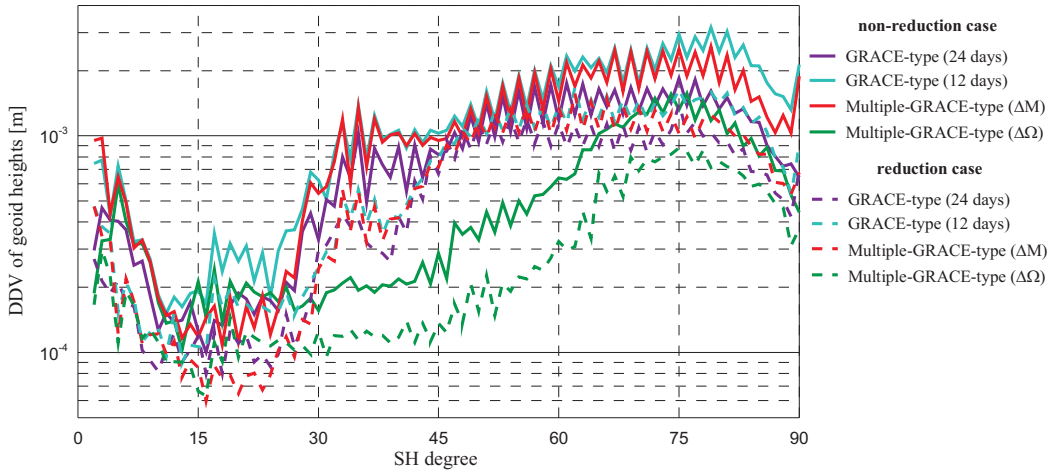

Fig. 7.28: *DDV* of geoid heights between ITG-GRACE03s and gravity field solutions as determined by GRACE-type FFs and Multi-GRACE-type constellations due to the oceanic effects for both non-reduction and reduction cases.

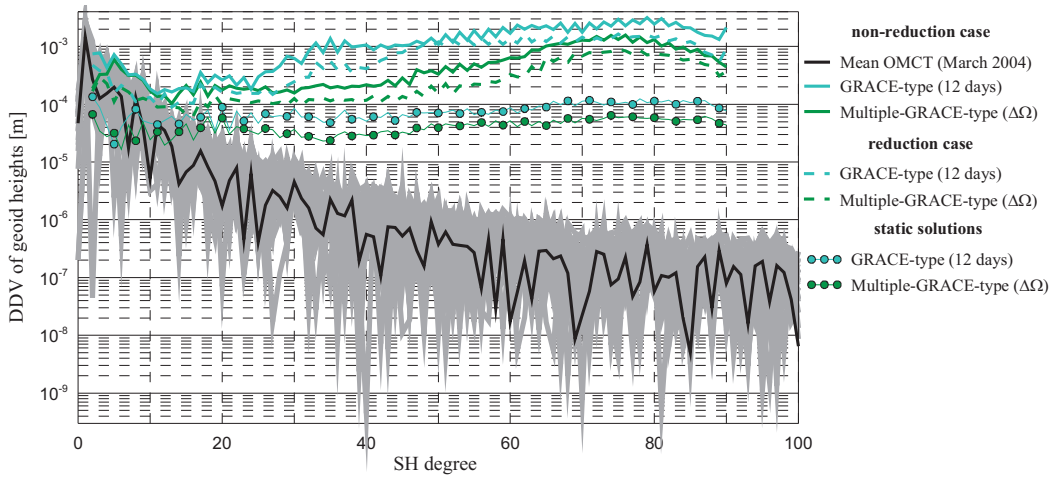

Fig. 7.29: *DDV* of geoid heights between ITG-GRACE03s and gravity field solutions as determined by GRACE-type 12-day FF and the Multi-GRACE-type ($\Delta\Omega$) constellation due to the oceanic effects for both non-reduction and reduction cases compared to the mean daily and monthly oceanic variations.

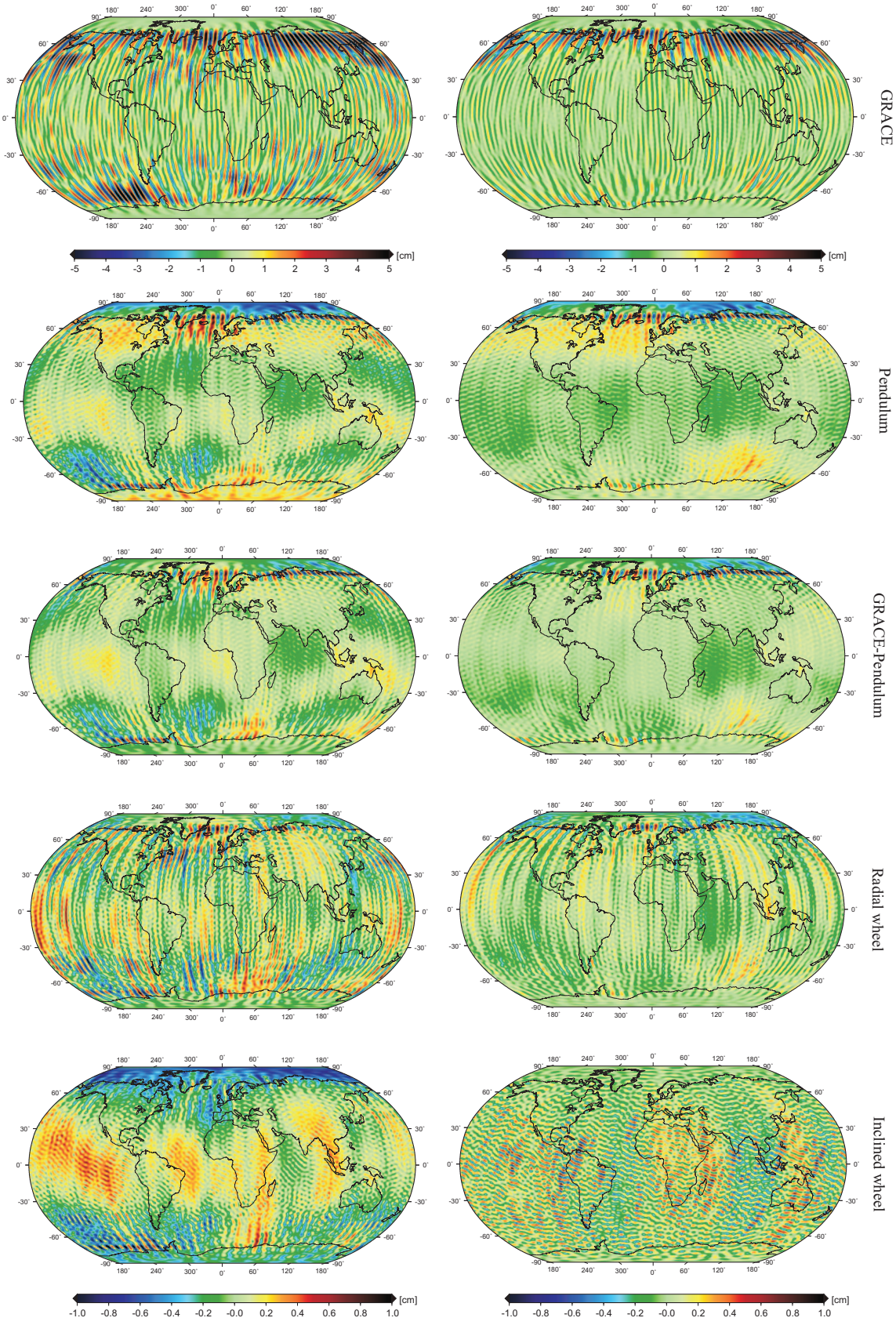

Fig. 7.30: Differences in geoid heights between ITG-GRACE03s and the gravity field solutions due to oceanic variations as determined by SFFs. From top to bottom: GRACE, Pendulum, GRACE-Pendulum, Radial wheel and Inclined wheel. The left side represents the non-reduction case and the right side represents the reduction case, n_{max}= 100.

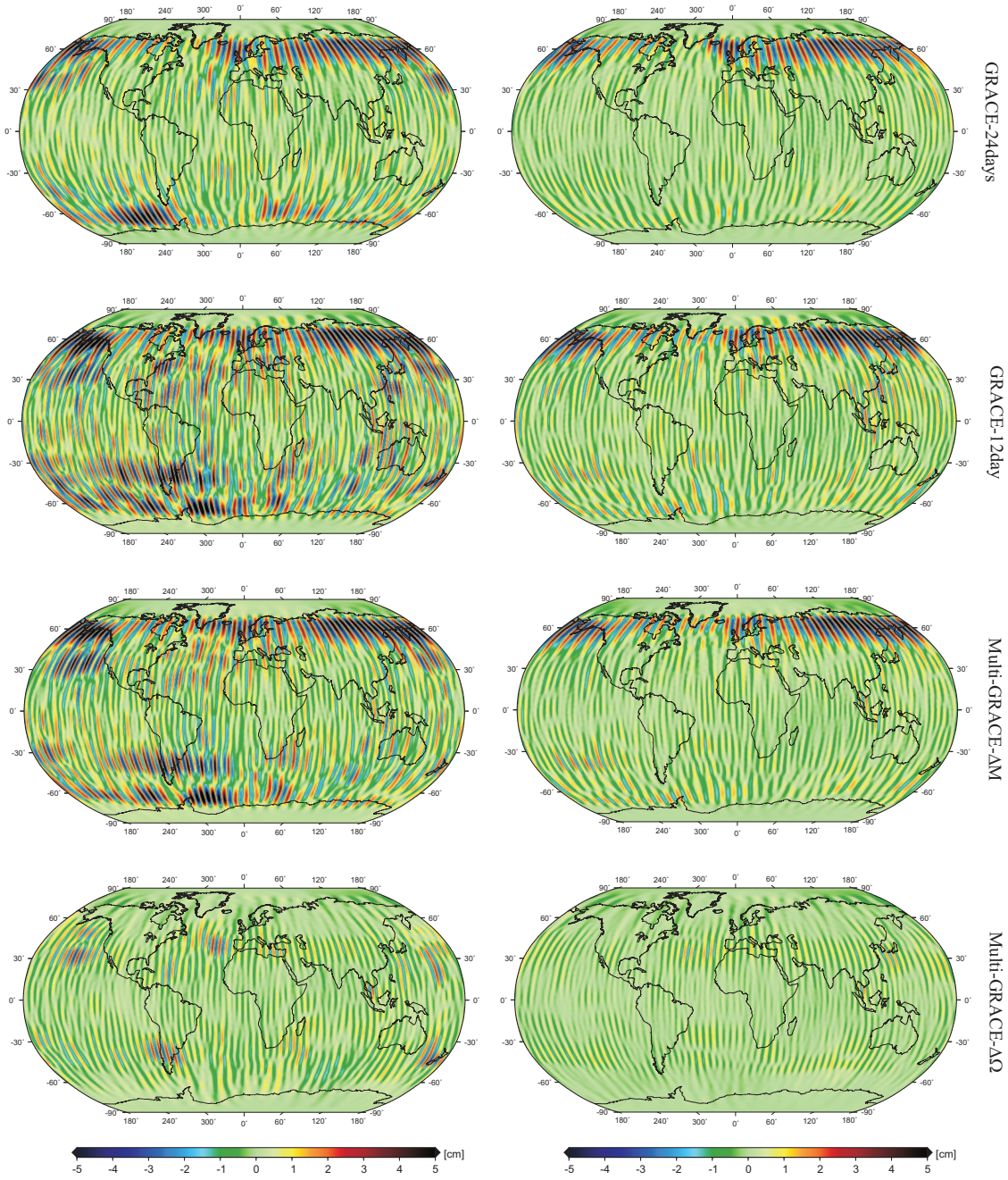

Fig. 7.31: Differences in geoid heights between ITG-GRACE03s and the gravity field solutions due to oceanic variations as determined by GRACE-type FFs and Multi-GRACE-type constellations. From top to bottom: GRACE-type 24-days, GRACE-type 12-days, Multi-GRACE-type (ΔM) constellation and Multi-GRACE-type ($\Delta\Omega$) constellation. The left side represents the non-reduction case and the right side represents the reduction case, n_{max}= 100.

7.2.2.3.5 Combined Atmospheric-Oceanic Effects

The global oceanic field can be combined with the global atmospheric field to get one global field. This combination is of a significant interest for reducing both effects together from the satellite observations such as the situation in the real observations of the GRACE mission. For this type of combination, some steps are required, which are already discussed before in Sec. 4.2.2.3 and are described in more detail by Flechtner (2007). We investigate in this section the influences of the combined atmospheric-oceanic variations on the static gravity field solution. This is done by taking the sum of the global atmospheric variability plus the oceanic pressure variability (i.e. ECMWF+OMCT) of the data type "glo" from the AOD1B-RL04 product. This scenario has been applied considering only one formation flight, the GRACE-type FF. Fig. 7.32 shows different levels of the geoid errors in terms of difference degree variances between the ITG-GRACE03s and different solutions. These solutions represent the influences of the atmospheric, oceanic and the combined atmospheric-oceanic variations, in addition to the ocean tidal and the hydrological ones on the static gravity solution of the GRACE-type FF (i.e. the non-reduction case).

Fig. 7.32 shows that an obvious improvement is obtained at all ranges of the gravity wavelengths through the combination of the atmospheric-oceanic variations. This can be easily read from Table 7.9, which shows this improvement not only for the GRACE-type FF, but also for all SFF types of Pendulum, GRACE-Pendulum, Radial wheel and Inclined wheel. Because of the similarity of the error structure that the atmospheric-oceanic solutions provide compared to the oceanic variations, we represented here only the results in terms of DDV of geoid heights in the spectral domain. The corresponding gravity field solutions are given in Fig. 7.33. The results agrees totally with the previous investigated atmospheric and oceanic variations.

Table 7.9: Geoidal statistical values (RMS, average, minimum and maximum) of the different gravity solutions as determined by all SFFs due to the combined atmospheric-oceanic variations at degree n= 100 considering only the non-reduction case.

Model / SFF types	ECMWF [cm]			OMCT [cm]			ECMWF+OMCT [cm]		
	RMS	Avg.	Max.	RMS	Avg.	Max.	RMS	Avg.	Max.
GRACE	1.503	1.126	7.005	1.385	0.988	8.012	1.089	0.791	6.752
Pendulum	0.215	0.164	1.104	0.167	0.121	1.116	0.159	0.120	1.066
GRACE-Pendulum	0.157	0.120	0.837	0.138	0.098	1.159	0.117	0.082	1.015
Radial wheel	0.295	0.226	1.772	0.225	0.171	1.163	0.190	0.143	1.395
Inclined wheel	0.251	0.194	1.841	0.228	0.175	0.903	0.145	0.113	0.843

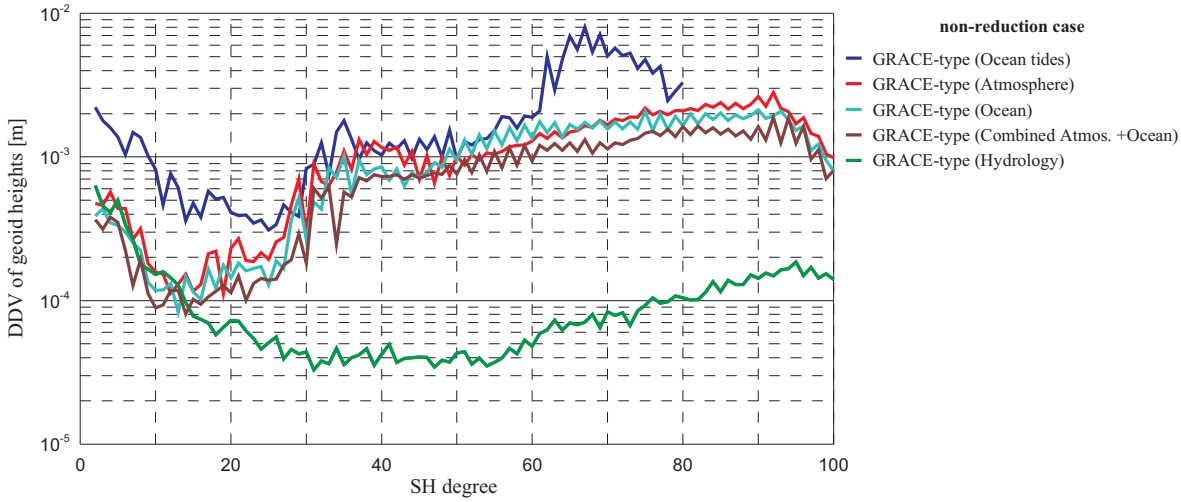

Fig. 7.32: *DDV* of geoid heights between ITG-GRACE03s and gravity field solutions of GRACE-type FF influenced by different temporal variations.

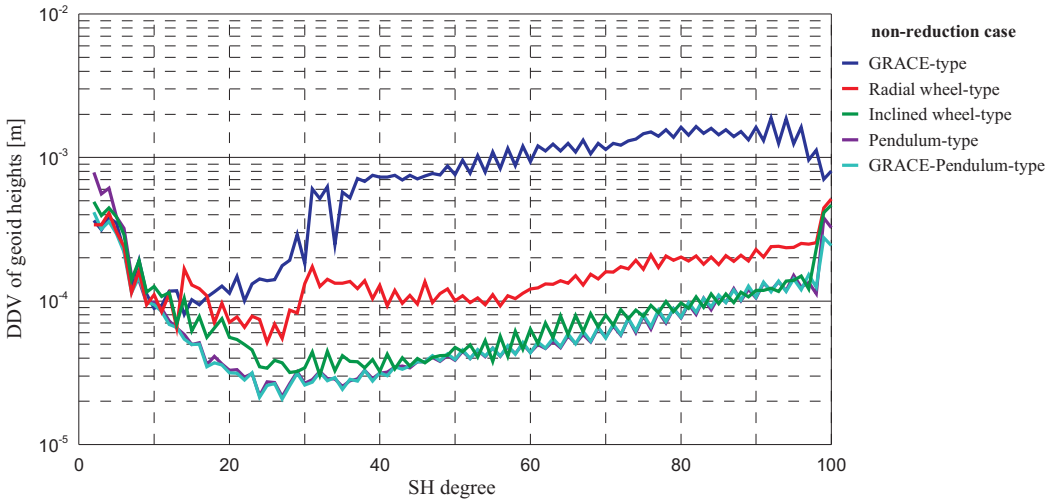

Fig. 7.33: *DDV* of geoid heights between ITG-GRACE03s and gravity field solutions as determined by different SFF types due to the combined atmospheric-oceanic variations for the non-reduction case.

7.2.2.3.6 Hydrological Effects

After the reduction of the above mentioned signals (ocean tides, atmosphere and ocean) from the GRACE satellite observations, the remaining signal is only one of the significant effects arising from the global continental water storage (or continental hydrology). A simple formula regarding the change in the continental water storage and its corresponding temporal gravity variations can be found e.g. in Peters (2007). One of our goals is to investigate how gravity solutions determined by the SFFs are influenced due to the effects of the hydrological variations as well as their model errors. Firstly, we have to mention that the error size of the hydrological signal is lower than those of the ocean tide, atmospheric and oceanic variations. This was clearly shown from Fig. 7.32, which showed that the error level for recovering the hydrological variations (e.g. from GRACE formation) is approximately of factor 10 lower than the other variations.

In this section, the effect of the hydrological variations and their model inaccuracies using two global models, WGHM and LaD (Land Dynamics Model of the US Geological Survey) are investigated. The first model, WGHM, has been applied to investigate the non-reduction case, while the other LaD model has been used to implement the model differences (i.e. the reduction case). Some differences between the two models should be firstly reviewed. These differences are caused by computational concepts, input data and spatial and temporal resolutions. The former WGHM model is based on the vertical water balance of the land areas as described in Döll et al. (2003), while LaD model is based on the energy balance approach (refer to Milly and Shmakin 2002 for more details). Some inputs were considered in WGHM model as the direct runoff, which is proportional to relative effective degree of saturation, as well as lakes, reservoirs and wetlands. The latter WGHM inputs: lakes, reservoirs and wetlands have not been considered in LaD model. The typical spatial resolution is $0.5°\times0.5°$ for WGHM with temporal resolution of daily calculation steps and $1°\times1°$ for LaD with monthly temporal resolution. Therefore, we expect large model inaccuracies and aliasing effects as well. A further valuable comparison between the two hydrological models can, for example, be found in Gruber (2009).

A simulation scenario of one month (March 2004) has been selected for this investigation. Analogously to the processing steps of the previous temporal variations, the influences of the hydrological variations on the gravity solutions determined by SFF types of 30 days temporal resolution, are investigated. This represents the non-reduction case, whose results are given in terms of DDV of the geoid heights in the spectral domain in Fig. 7.34(a) up to SH degree n=100. In this sections, we represent the reduction case in two ways, the reduction case 1 and the reduction case 2. The first case investigates the hydrological model differences between the WGHM model and the LaD one. The second case was investigated since the hydrological model differences have been found to exceed the influences of the hydrological variations themselves. Therefore, we applied the reduction case 2 which is already explained in the atmospheric section by considering only 10% of the power signal of the WGHM model as moder errors. Figs. 7.34(a) and 7.34(b) depict the non-reduction case compared with both reduction cases 1 and 2, respectively. Fig. 7.34(c) shows only the largest and least recovered gravity solutions compared with the mean monthly and daily temporal variation signals as determined from the WGHM model.

It is worthwhile noting that the results given in terms of the geoid heights can be also converted in terms of the equivalent water (EW) heights. The related mathematical conversion is expressed in details in Wahr and Molenaar (1998). Fig. 7.35 shows a comparison between the geoid heights and the EW heights for all SFF types. Significant information can be inferred from Fig. 7.35. For instance, the RMS errors of the gravity solutions influenced by the hydrological variations do not exhibit distinguishable differences in terms of geoid heights, since their error accuracies are in mm-level. Contrarily, distinguishable discrepancies are recognized by representing the results in terms of EW heights, whose accuracy are in meter-level. The discrepancies between the geoid and EW heights can be easily read from the RMS values given in Table 7.10. The EW heights are also able to provide us with additional informations more than the geoid ones. For example, the GRACE-Pendulum-type FF, which has not displayed a better solution in terms of the geoid heights, has provided the least RMS errors in terms of EW heights.

Figs. 7.36 and 7.37 represent the geoid heights for the non-reduction case compared with the reduction cases 1 and 2, respectively. One can easily observe from these figures that the largest variations are visible over the continents, particularly the seasonal effects which are clearly recognizable in the large tropical river basins

like the Amazon in South America, the Congo and the Niger in Africa and the Ganges in India. Therefore, our objective is to find which satellite formation provides the least influences of the hydrological variations on its gravity solution.

Regarding the non-reduction case, the largest impact of the hydrological variations results from the GRACE-type FF in terms of both geoid and EW heights as read from Table 7.10. In Fig. 7.34(a), we see that the GRACE-type FF solution behaves better up degree 2 to 55 and up 56 begins to distort. The difference degree variances of the radial formations and the out-of-plane Pendulum behave better up degree 2 to 69, then up degree 70 the solutions begin to distort. The GRACE-Pendulum-type FF provides the least difference degree variances up degree 2 to degree 75 and then its solution begins to behave in a worse manner. We can infer from this that if the GRACE-type FF is able to recover the hydrological variations up to SH degree 55, the other formation flight types have the ability to detect these variations up to higher degrees.

The gravity solutions concerning the reduction case 1 behave in a worse manner as shown in Fig. 7.34(a) displaying drastic changes of the DDV of geoid errors from mm-level to cm-level. Most of these changes are reflected by significant differences between the models, which take place especially over the snow areas e.g., the Antarctica, the Greenland and the Siberian basins. A main reason for these large differences between the obtained results is accounted for different storage component of both WGHM and LaD models as mentioned before. This may be due to surface water storage in the snow pack, which is accounted for in WGHM but was not accounted for the other LaD model. One finds that the geoid errors of the reduction case 1 are worse than the non-reduction case by approximately factor 10 in RMS as read from Table 7.11. We infer from this that applying a wrong model to the observations can not solve the aliasing effects in the hydrological signal but will aggravate them. For this reason, we applied another scenario to investigate the model inaccuracies by using 10% of the hydrological signal power of WGHM model as a model errors in the gravity estimation process. Figs. 7.36 and 7.37 show the gravity solutions of the non-reduction case compared with the reduction cases 1 and 2, respectively in terms of the geoid errors in the spatial domain.

It should be mentioned that the results emphasize and support the previous outcome. This means that the GRACE-type FF provides the largest effect of the hydrological variations because of distortion of its signal at medium harmonics. The radial configurations, especially the Radial wheel-type FF, provides the least RMS errors in terms of only the geoid heights in both the non-reduction and reduction cases. Considering the reduction case 2, the GRACE-Pendulum surpasses all configurations yielding the least RMS geoid errors of factor 2.5 w.r.t. the GRACE-type and factor 1.5 w.r.t the radial formations. Finally, we can conclude that the other formation flights having radial and cross-track information into their observables can detect the variations to a moderate degree better than GRACE-type.

According to the least RMS errors that the GRACE-Pendulum-type solution provides in terms of EW heights in the non-reduction case and in terms of the geoid heights in the reduction case 2, it has been plotted versus the GRACE-type FF gravity solutions as shown in Fig. 7.34(c). These solutions are plotted with the mean monthly and daily hydrological variations determined by the WGHM model as well as the static gravity solutions (up to only n=90) to consider the deviations of the both solutions as mentioned in the last sections. It is clear that the GRACE signal deviates away from the mean signals at the long wavelengths up to n=15, while the GRACE-Pendulum signal agrees with the mean solution till the medium wavelength ranges up to n=50. This indicates how important is the latter configuration for solving the aliasing effects of the hydrological signal better than the GRACE-type FF.

Table 7.10: Comparison between the geoid heights [in mm] and the equivalent water heights [in m] of the gravity solutions as determined by the different SFF types corresponding to Fig. 7.35. The gray cells represent the least values.

Model / SFF types	Geoid Heights [mm]				Equivalent Water Heights [m]			
	RMS	Avg.	Min.	Max.	RMS	Avg.	Min.	Max.
GRACE	1.448	1.003	-10.24	10.59	0.2538	0.1723	-2.0951	2.2944
Pendulum	1.363	0.993	-6.777	6.241	0.0905	0.0712	-0.4385	0.5048
GRACE-Pendulum	1.224	0.859	-6.487	6.173	0.0543	0.0394	-0.4350	0.5431
Radial wheel	1.159	0.781	-6.803	5.789	0.0829	0.0618	-0.9605	0.9650
Inclined wheel	1.188	0.813	-6.380	5.847	0.0901	0.0694	-0.5338	0.6227

Table 7.11: Geoidal statistical values (RMS, average, minimum and maximum) of the different gravity solutions as determined by SFFs due to the hydrological variations at degree n= 100 corresponding to Fig. 7.37 and Fig. 7.36. The gray cells represent the least geoid errors.

Model / SFF types	WGHM [mm]			WGHM-LaD [mm]			WGHM 10%-aliasing [mm]		
	RMS	Avg.	Max.	RMS	Avg.	Max.	RMS	Avg.	Max.
GRACE	1.448	1.003	10.590	10.75	7.385	57.92	0.489	0.384	2.135
Pendulum	1.363	0.993	6.241	13.06	8.590	74.49	0.314	0.251	1.397
GRACE-Pendulum	1.224	0.859	6.173	11.81	8.291	61.40	0.178	0.136	0.797
Radial wheel	1.159	0.781	5.789	9.195	6.019	53.22	0.239	0.188	1.062
Inclined wheel	1.188	0.813	5.847	9.857	6.587	55.66	0.271	0.211	1.233

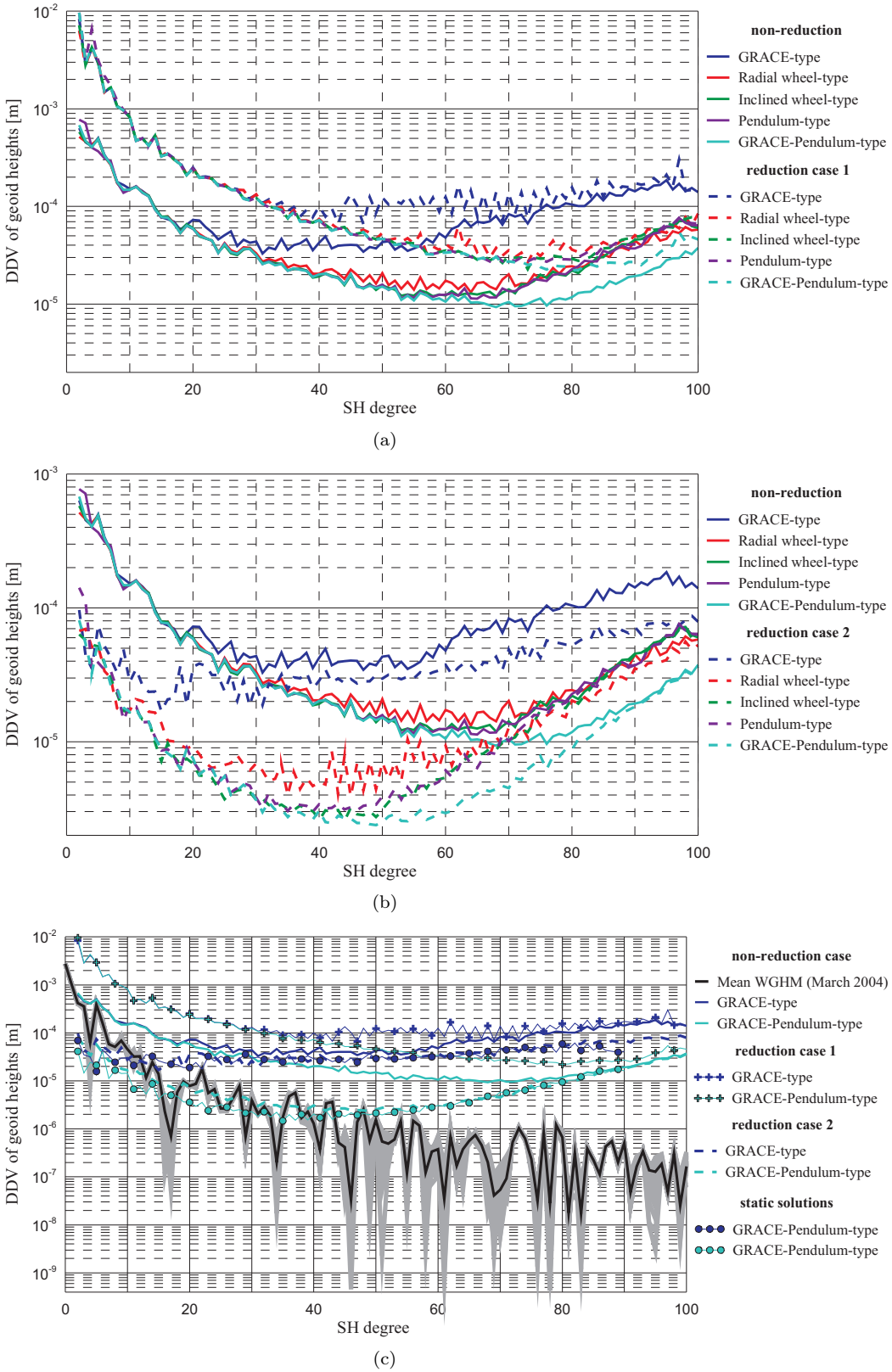

Fig. 7.34: Gravity field solutions of the SFFs affected by the hydrological variations for the non-reduction case compared with a) the reduction case, b) the aliasing case and c) the mean daily and monthly hydrological variations and the static solutions.

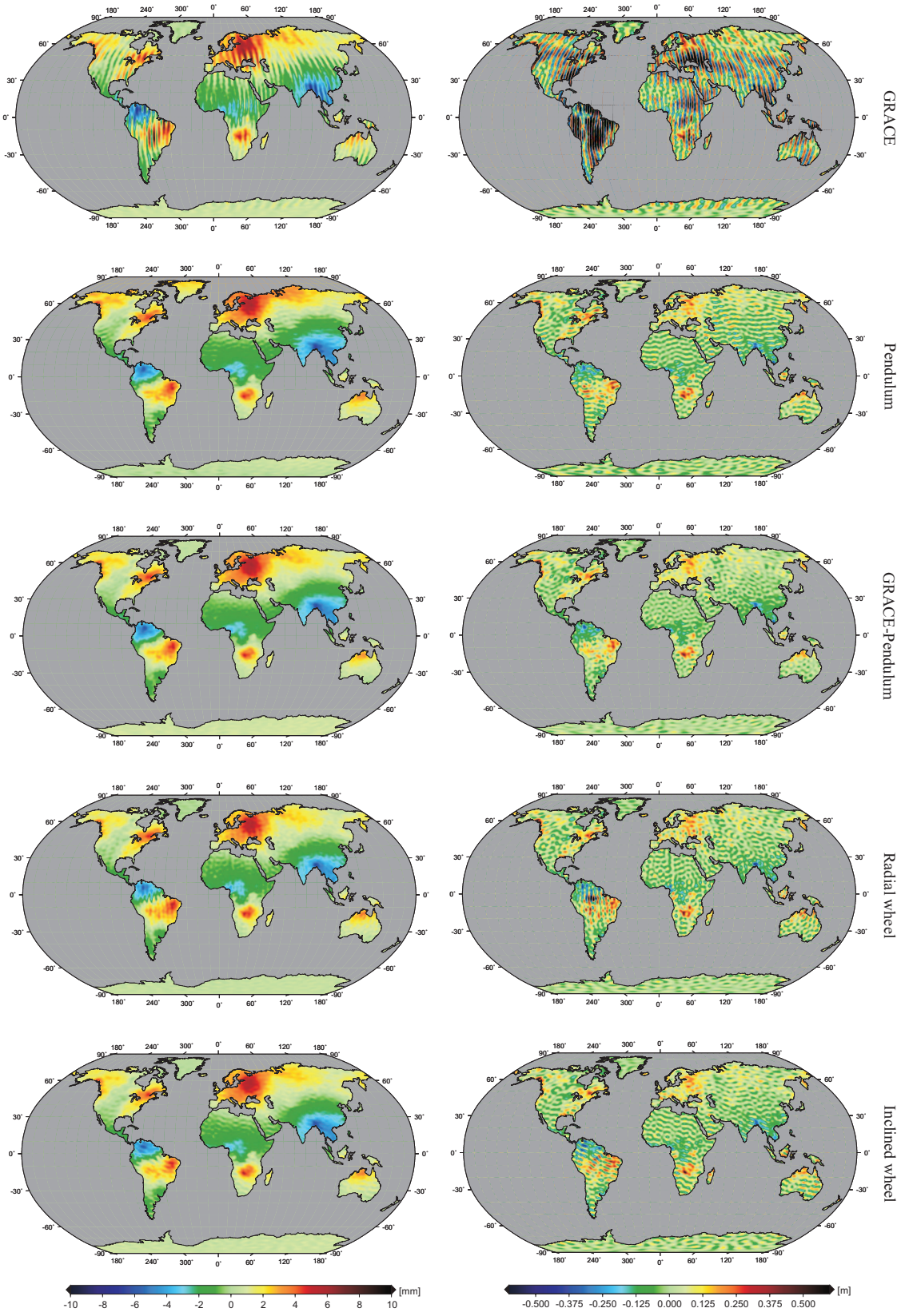

Fig. 7.35: Differences in geoid heights between ITG-GRACE03s and the gravity field solutions due to hydrological variations as determined by SFFs. From top to bottom: GRACE, Pendulum, GRACE-Pendulum, Radial wheel and Inclined wheel. The left side represents the gravity solution in terms of geoid heights in $[mm]$ and the right side represent the equivalent water heights in $[m]$ in the non-reduction case, n_{max}= 100.

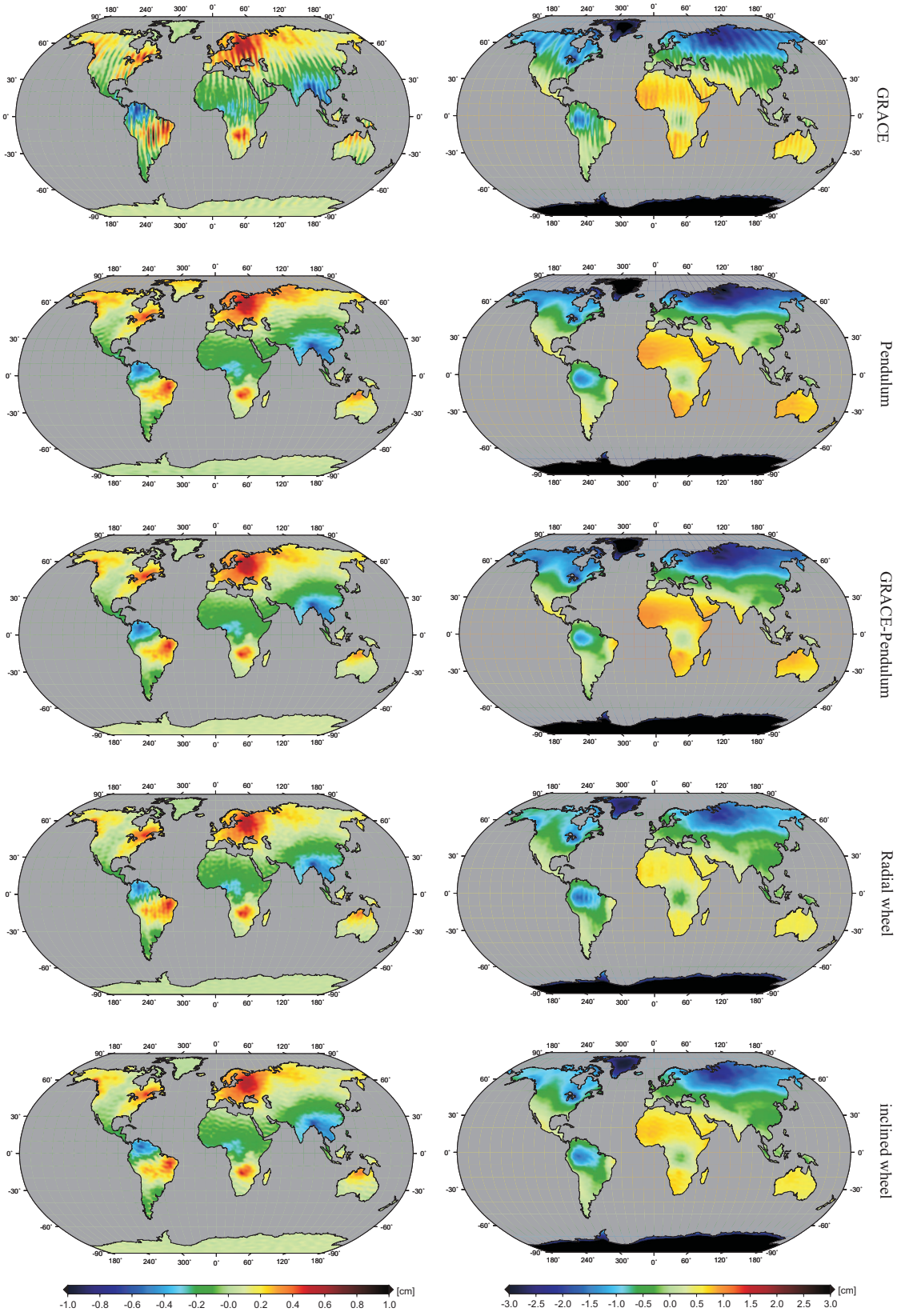

Fig. 7.36: Differences in geoid heights between ITG-GRACE03s and the gravity field solutions due to hydrological variations as determined by SFFs. From top to bottom: GRACE, Pendulum, GRACE-Pendulum, Radial wheel and Inclined wheel. The left side represents the non-reduction case and the right side represents the reduction case 1, n_{max}= 100.

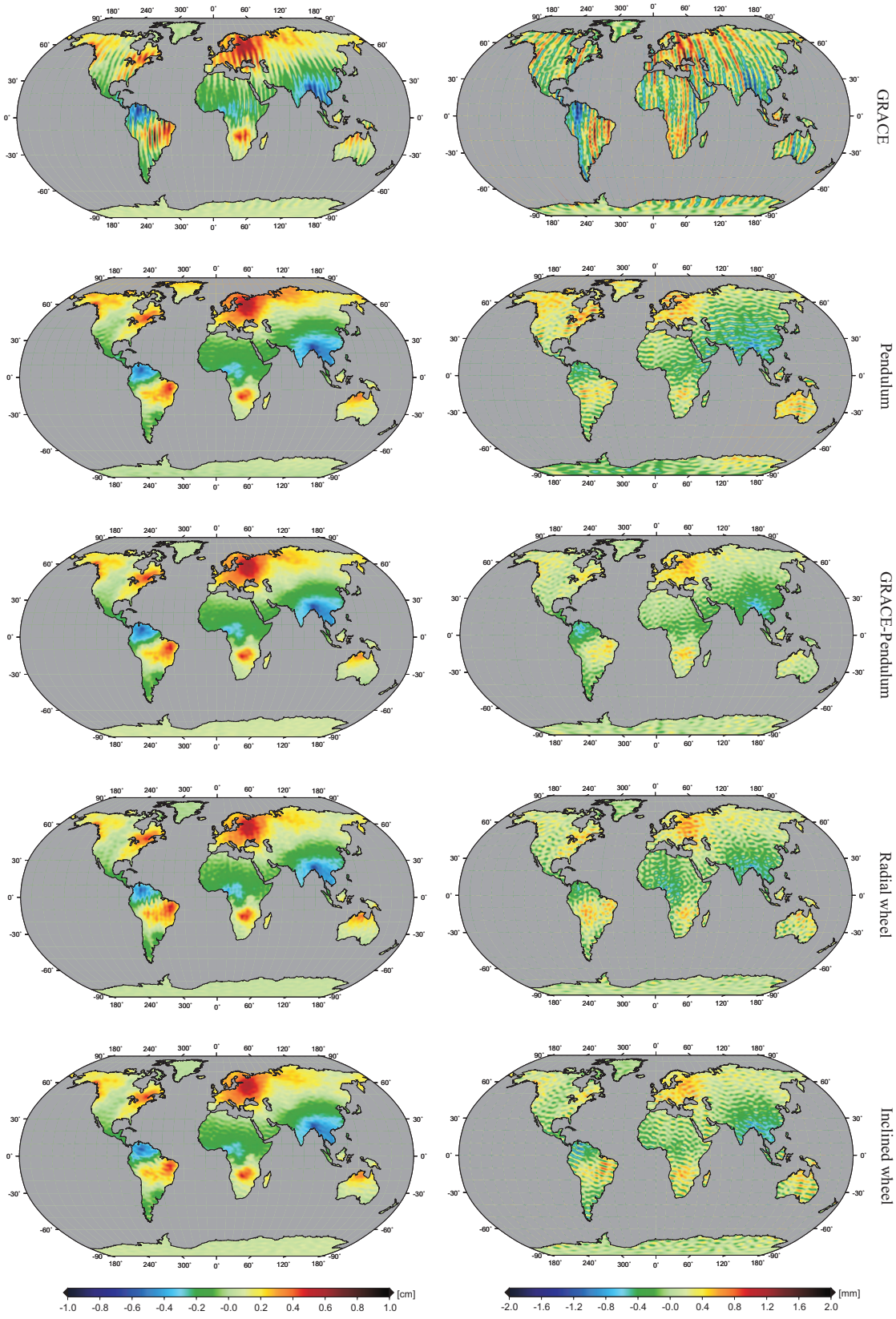

Fig. 7.37: Differences in geoid heights between ITG-GRACE03s and the gravity field solutions due to hydrological variations as determined by SFFs. From top to bottom: GRACE, Pendulum, GRACE-Pendulum, Radial wheel and Inclined wheel. The left side represents the non-reduction case and the right side represents the reduction case 2, n_{max}= 100.

7.2.2.3.7 Monthly Hydrological Influences on the SFFs gravity solutions

In this section, the influences of the monthly hydrological variations on the static gravity solutions determined by the satellite formation flights are investigated. This means that we investigate only the non-reduction case as described in Sec. 7.2.2.3. All SFF types have been firstly examined to fly in a bounded stable formation for a long mission duration. For this purpose, a time span of 6 months, beginning from 01-01-2006 till 30-06-2006, has been selected. The satellite orbits of all SFFs have been integrated and the SST measurements have been generated with the same procedures described in Sec. 7.1.

Table 7.12 shows the inter-satellite ranges of the SFF types along the mission period of 6 months. This investigation considers the satellite configurations of GRACE, Pendulum, GRACE-Pendulum and Radial wheel. We have to mention here that the gravity field solutions of the Inclined wheel-type FF have been excluded from our analyses. This is due to the large variabilities of its inter-satellite distances from the first to the sixth month as read in Table 7.12. The rest SFF types are flying in a stable bounded formation in the time variable gravity field.

The results are given in the spatial domain in Figs. 7.38 and 7.39 in terms of the geoid heights. The corresponding geoid errors are read in Table 7.13. The results of this scenario still agree with all time variable results given in the previous sections in such way that the hydrological signal has the largest influences on the gravity solution the GRACE-type FF as shown from its RMS errors. The impact on the gravity solutions of the other three configurations Pendulum, GRACE-pendulum and Radial wheel FFs becomes smaller w.r.t. the GRACE-type FF. The Radial wheel-type FF provides the best solution that shows the least geoid errors in terms of only RMS values from the period of 01-01-2006 till 30-04-2006. The GRACE-Pendulum-type FF yields the least errors in the fifth and sixth months of the year 2006. The Pendulum-type FF also has an obvious improvement as read from its minimum and maximum values given in Table 7.13. This can be clearly indicated when we compare Pendulum and GRACE-Pendulum solutions in Figs. 7.38 and 7.39 with each other. We find that most of the amplitudes of the hydrological variations in the Amazon basin in South America, the Congo and the Niger in Africa and the Ganges in India have been minimized by the out-of-plane cross-track configurations.

Due to the valuable information that the equivalent water heights offer, the previous results have been also represented in the spatial domain in terms of the equivalent water heights as shown in Figs. 7.40 and 7.41. Their corresponding EW heights are read from Table 7.14. These results differ from those given in geoid heights in that the GRACE-pendulum-type FF provides the least water heights in all period of the six months. This emphasizes how important is the GRACE-pendulum-type configuration for mitigating the error structure associated with the hydrological variations.

Table 7.12: Inter-satellite distances of the SFF types for a mission period of 6 months.

SFF types / Month	GRACE-range [km]	Pendulum-range [km]	Radial wheel-range [km]	Inclined wheel-range [km]
Jan. 2006	200 – 202	85 – 199	100 – 204	100 – 299
Feb. 2006	202 – 206	87 – 200	100 – 205	100 – 305
Mar. 2006	206 – 210	90 – 201	100 – 210	75 – 350
Apr. 2006	210 – 213	93 – 202	100 – 220	65 – 405
May 2006	213 – 217	95 – 204	100 – 225	10 – 425
Jun. 2006	217 – 221	97 – 206	100 – 232	50 – 465

Table 7.13: Geoidal statistical values (RMS, average, minimum and maximum) in [mm] of the different gravity solutions as determined by GRACE-type and Pendulum-type FFs (top) and GRACE-Pendulum-type and Radial wheel-type FFs (bottom) due to the hydrological variations of 6 months at degree n= 100 corresponding to Figs. 7.38 and 7.39, respectively.

SFF types / Months	GRACE-type				Pendulum-type			
	RMS	Avg.	Min.	Max.	RMS	Avg.	Min.	Max.
Jan. 2006	1.508	1.006	-13.18	16.50	1.031	0.750	-4.158	6.948
Feb. 2006	1.536	1.066	-7.10	16.18	1.431	1.041	-5.236	12.59
Mar. 2006	1.671	1.153	-6.379	18.10	1.600	1.119	-5.696	14.06
Apr. 2006	1.775	1.191	-8.248	19.07	1.663	1.136	-5.667	15.72
May 2006	1.636	1.069	-8.322	20.55	1.305	0.829	-3.801	14.23
Jun. 2006	1.688	1.050	-10.79	23.33	0.975	0.569	-3.270	10.86
SFF types / Months	GRACE-Pendulum-type				Radial wheel-type			
	RMS	Avg.	Min.	Max.	RMS	Avg.	Min.	Max.
Jan. 2006	0.967	0.693	-4.502	6.696	0.932	0.615	-4.226	9.338
Feb. 2006	1.305	0.923	-5.290	12.32	1.232	0.806	-4.809	12.77
Mar. 2006	1.510	1.050	-5.606	13.942	1.450	0.949	-5.831	14.51
Apr. 2006	1.556	1.063	-5.682	15.53	1.473	0.922	-5.692	16.44
May 2006	1.209	0.719	-3.421	14.23	1.222	0.703	-3.568	14.52
Jun. 2006	0.967	0.533	-3.257	11.26	1.068	0.625	-3.500	11.99

Table 7.14: Equivalent water statistical values (RMS, average, minimum and maximum) in [m] of the different gravity solutions as determined by GRACE-type and Pendulum-type FFs (top) and GRACE-Pendulum-type and Radial wheel-type FFs (bottom) due to the hydrological variations of 6 months at degree n= 100 corresponding to Figs. 7.40 and 7.41, respectively.

SFF types / Months	GRACE-type				Pendulum-type			
	RMS	Avg.	Min.	Max.	RMS	Avg.	Min.	Max.
Jan. 2006	0.313	0.178	-4.414	4.366	0.093	0.073	-0.479	0.803
Feb. 2006	0.237	0.149	-2.575	2.777	0.097	0.076	-0.481	1.271
Mar. 2006	0.205	0.138	-2.121	2.705	0.094	0.073	-0.459	1.313
Apr. 2006	0.247	0.158	-2.066	2.637	0.091	0.070	-0.400	1.448
May 2006	0.300	0.196	-3.245	3.050	0.089	0.068	-0.364	1.113
Jun. 2006	0.369	0.218	-4.047	4.561	0.084	0.065	-0.391	0.818
SFF types / Months	GRACE-Pendulum-type				Radial wheel-type			
	RMS	Avg.	Min.	Max.	RMS	Avg.	Min.	Max.
Jan. 2006	0.051	0.038	-0.439	0.689	0.084	0.058	-0.875	1.565
Feb. 2006	0.056	0.039	-0.421	1.138	0.076	0.057	-0.470	1.208
Mar. 2006	0.057	0.039	-0.407	1.290	0.081	0.058	-0.608	1.730
Apr. 2006	0.059	0.040	-0.347	1.323	0.79	0.057	-0.427	1.444
May 2006	0.056	0.038	-0.344	1.147	0.081	0.060	-0.371	1.042
Jun. 2006	0.052	0.037	-0.279	0.825	0.086	0.062	-0.686	1.206

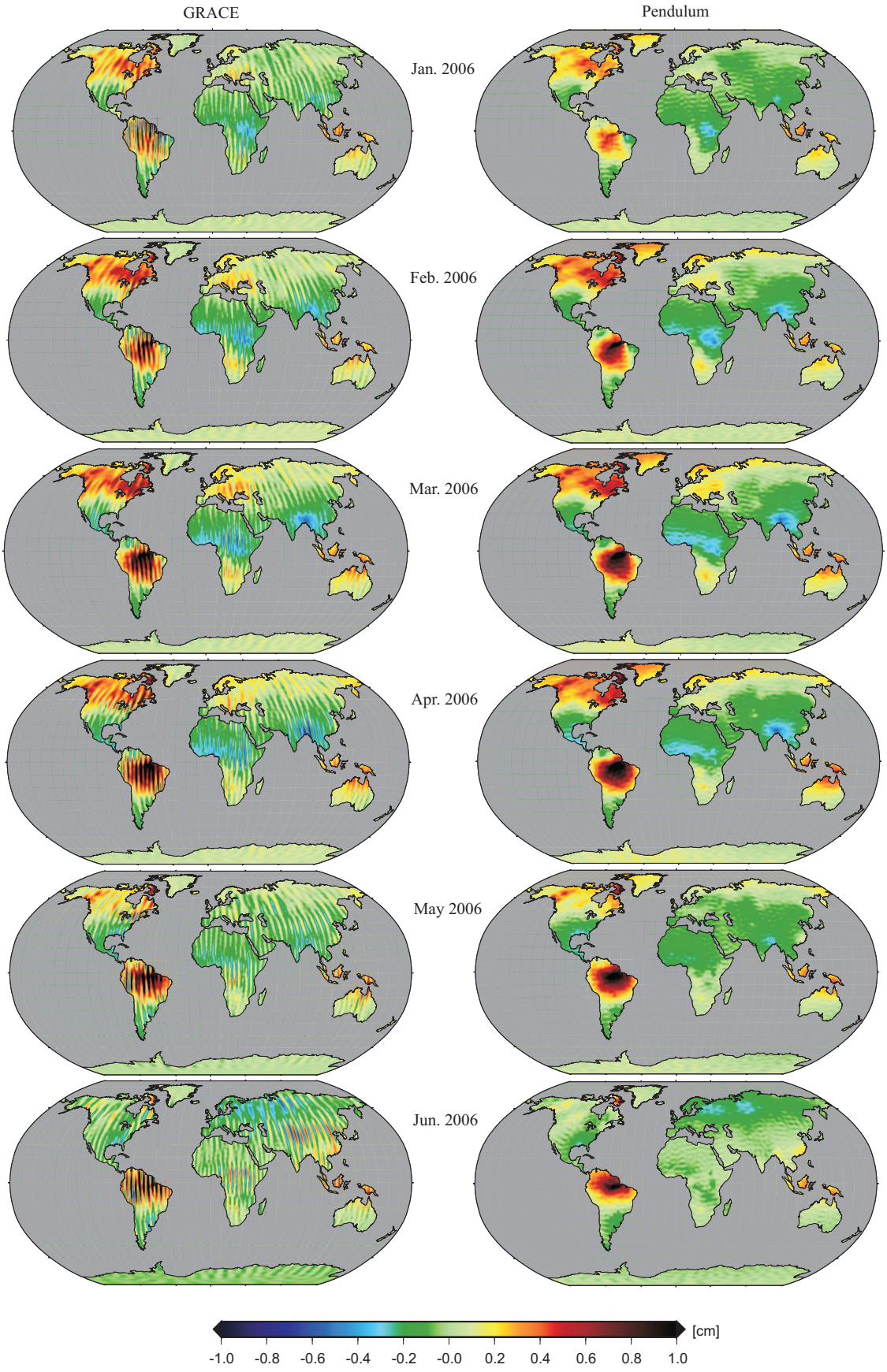

Fig. 7.38: Monthly Gravity variations for GRACE-type FF (left) and Pendulum-type-FF (right) in terms of geoid heights.

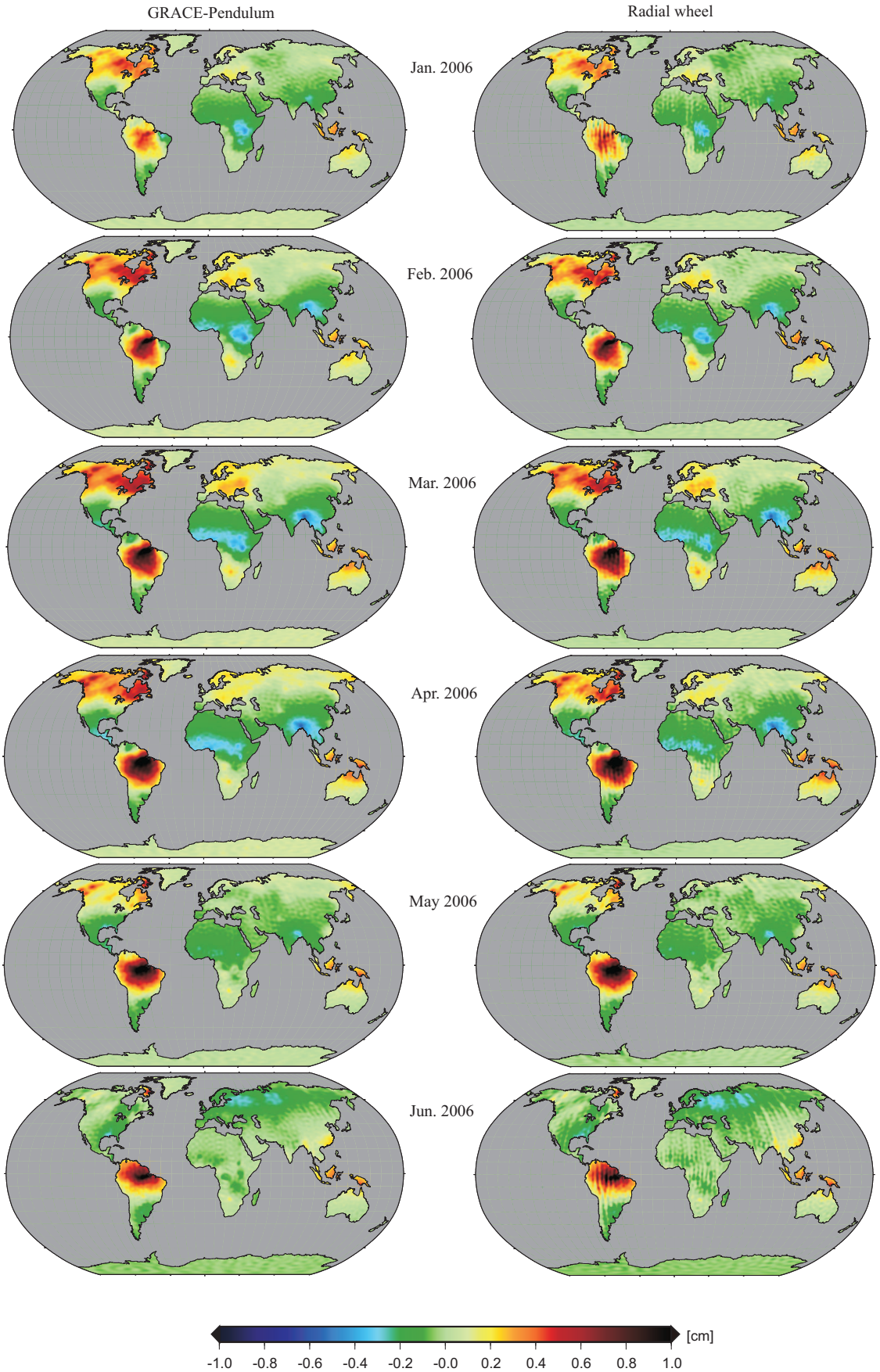

Fig. 7.39: Monthly Gravity variations for GRACE-Pendulum-type FF (left) and Radial wheel-type FF (right) in terms of geoid heights.

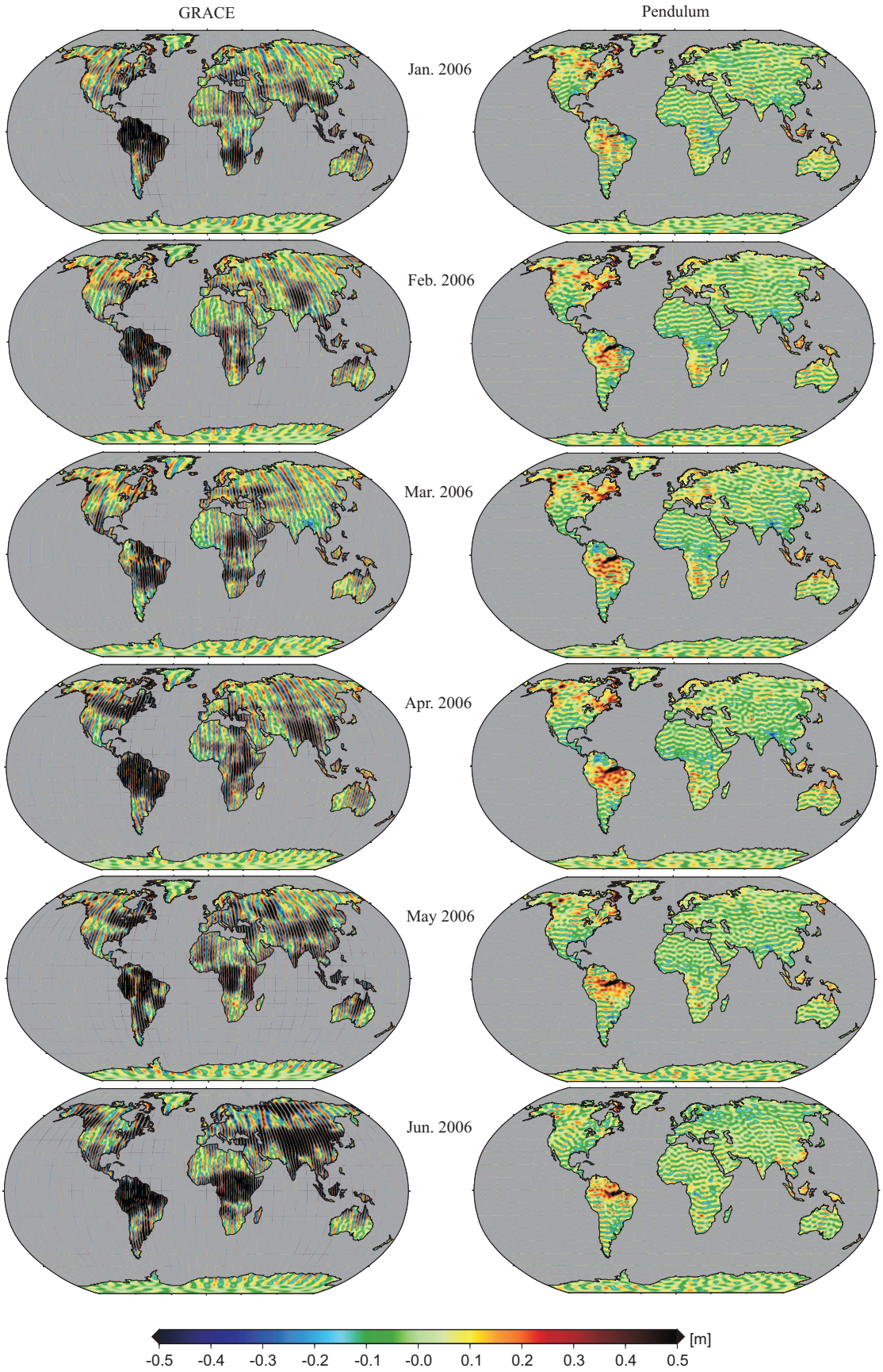

Fig. 7.40: Monthly Gravity variations for GRACE-type FF (left) and Pendulum-type-FF (right) in terms of water heights.

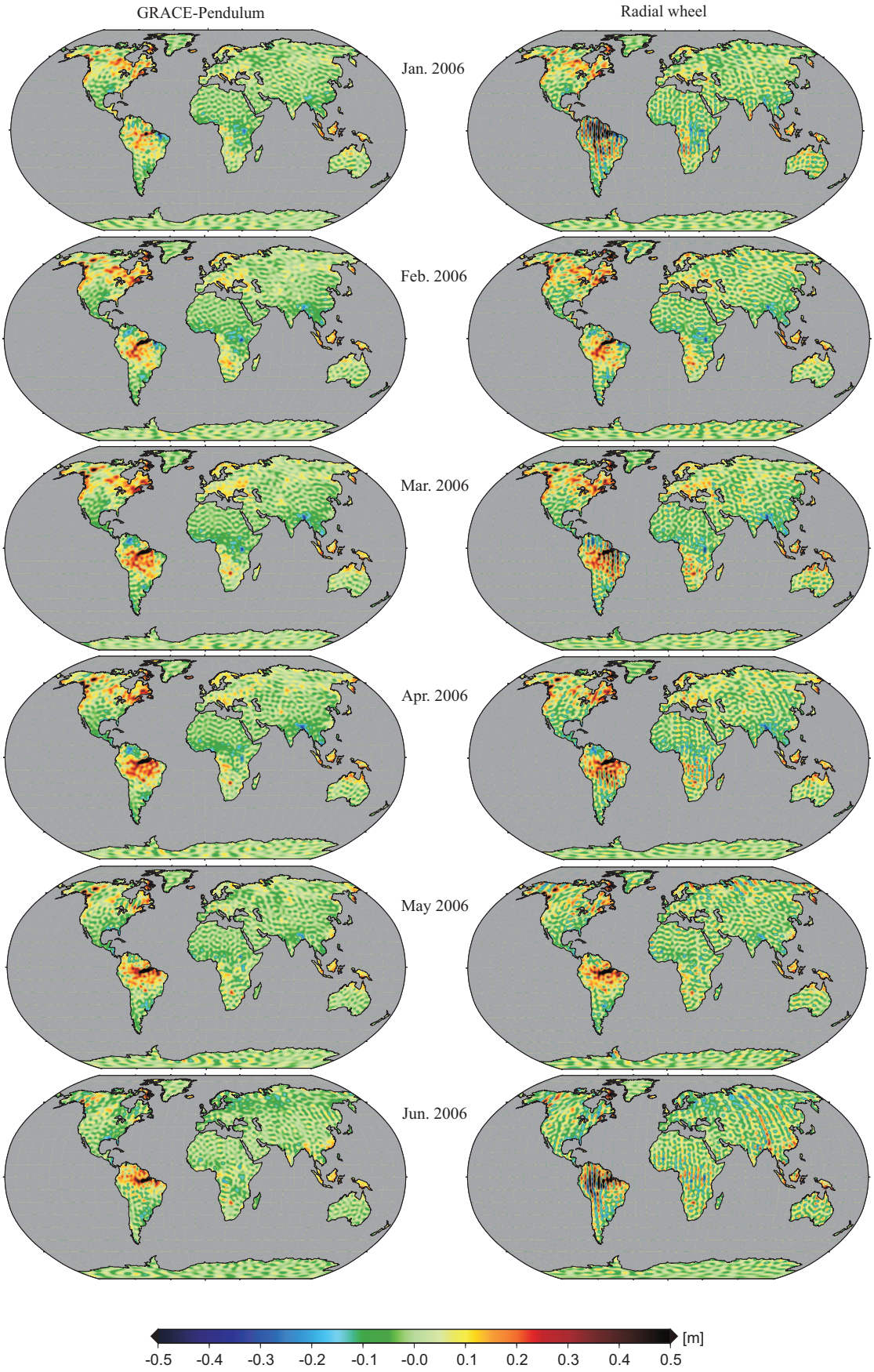

Fig. 7.41: Monthly Gravity variations for GRACE-Pendulum-type FF (left) and Radial wheel-type FF (right) in terms of water heights.

8. Summary and Conclusions

8.1 Summary

This thesis has focused on the improvement of the global static gravity field by examining different satellite formation flight (SFF) types. The satellites have been applied as test masses based on the satellite-to-satellite tracking concept in the low low mode (ll-SST). The gravity potential is assessed for detecting the temporal variations of the time-variable gravity field. It has to be mentioned that some issues have been investigated in our study while others have not taken into our consideration. First of all, the short-arc approach has been applied to the satellite formation flights (SFF). Second, the gravity field analysis has not been restricted to the long and medium wavelength ranges of the recovered gravity field, but also has been applied to the short wavelengths. Third, this study has taken into consideration most of the time-variables of the gravity field to detect the influences of the temporal variations on the gravity field solutions. The latter objective has been considered as one of the major goals of this thesis. Last but not least, an innovative satellite formation flight has been developed by merging two formations into one constellation to significantly improve the gravity field recovery. To implement our goals, different satellite configurations with different satellite information (along-track, cross-track and radial) as well as different orbital options have been investigated. The issues which have not taken into consideration will be latterly shown in the recommendations section.

The analysis of the global gravity field was performed based on the classical Newton-Euler's equation of motion using the short arcs method of approximately 30 minutes arc length. Numerous scenarios were simulated for this purpose to generate and analyze the satellite observations of the different formation flights. The observation equations are set up for each short arc as applied for the calculation of the ITG-GRACE03s gravity field model. The numerical simulations have been performed with the Gravity Recovery Object Oriented Programming System (GROOPS) software package, which has been developed at the Department of Astronomical, Physical and Mathematical Geodesy, Institute of Geodesy and Geoinformation (IGG), University of Bonn.

To sum up, Chapter 1 introduced the objectives of this thesis and the demand of an improvement of the gravity field based on satellite missions of SFFs in addition to the thesis's architecture. The current satellite missions applied in satellite geodesy to determine the gravity field such as the three successful satellite missions CHAMP, GRACE and GOCE have been introduced in Chapter 2. Moreover, the concept of satellite formation flight using various proposals of satellite configurations, which contain observations in different directions (e.g. along-track, cross-track and radial) was sketched. A review of the satellite motion in the static gravity field based on Kaula's solution of the disturbed Keplerian motion and the Hill solution of satellite motion in a circular plane has been reviewed in Chapter 3. Moreover, this chapter introduced the potential theory and the spherical harmonics (SH) analysis in geodetic applications. The most time variable elements affecting the satellite's motion in the gravity field have been described in Chapter 4 in addition to some other effects (e.g. the relativistic effects). To conclude the procedure used for our gravity field analysis, Chapter 5 described the theoretical steps required for solving the unknown gravity field parameters from satellite observations via the functional physical model and linearized deterministic one. The physical model is based on the formulation of the Newton-Euler's equation of motion formulated as a boundary value problem for two satellites of ll-SST mission type. The deterministic model is used for connecting the satellite's observations to the unknown parameters via the well-known Gauss-Markov matrix form for setting up a linear system of observation equations for the satellite's short arcs and then solved by the least-squares adjustment. The steps of numerical simulation and several processes performed via GROOPS software have been illustrated in Chapter 5.

In Chapter 6, the shortcomings that confine the current satellite missions and the importance of the formation flights for solving them have been discussed. Subsequently, the essential features of the design of the satellite orbits constituting the SFF were reviewed. This overview took into consideration the most adequate orbital parameters for the optimal recovery of the gravity field. For instance, we have designed all satellite orbits in our study away from the short repeat period, which was represented by satellite revolutions divided by

satellite nodal days (i.e. β/α). The required conditions were to select small eccentricities (e.g. 0.001, 0.005 and 0.01), an orbital inclination of 89.5 and a satellite altitude of 400 km for providing better global gravity field solutions. Furthermore, desirable inter-satellite ranges have been selected larger than the desired spatial resolution in order to maximize the measurement signal. Inter-satellite distances between 100 km – 200 km were selected, which provided a gravity field solution more than one full-order of magnitude better w.r.t. distances of 10 km. Moreover, the inter-satellite range metrology was one of the performance factors that has been investigated within this thesis. We applied an accuracy of 50 nm (an optical metrology) for all investigated SFF types. The gravity solution determined using this accuracy level surpasses the microwave accuracy of 5 μm by factor 100.

The relative motion between the satellites as well as their formation options have been easily derived from solution of Hill equations. For instance, a trivial solution by keeping the satellites apart from the secular drifting (i.e $\Delta a = 0$) yields the GRACE-type formation. When setting a type of relative motion to have the shape of an ellipse with an axis ratio 2:1, the Radial wheel-type formation is obtained. The larger axis of this formation being oriented in the along-track direction is twice the shorter axis being oriented in the radial direction. An Inclined wheel-type formation has been obtained by modifying the last mentioned Radial wheel-type adding an out-of-plane cross-track component to contain observations in all directions (along, cross and radial). A cross-track component has been added to the GRACE-type formation to yield an out-of-plane Pendulum-type formation. In this thesis, an innovative formation type, the GRACE-Pendulum-type FF, has been developed from the last two mentioned formations by combining the along-track axis of the GRACE-type with the cross-tack one of the Pendulum-type in one bounded formation. This combination performs two inter-satellite baseline vectors both in the horizontal plane. For a simple orbit description and position computation, all satellites orbit have been represented by Kepler parameters. This is due to the fact that the Keplerian parameters are changing slowly even under the presence of some perturbations. This reason was very important for maintaining the formation stability under the influence of the gravitational forces (e.g. tides, atmosphere, ocean and hydrology).

In Chapter 7, test computations and gravity field solutions of the different investigated satellite formation types have been represented and discussed. All satellite formations in this thesis have been divided into two main types depending on different temporal sampling rates. The first type includes formations of 30 days of satellite orbits. These formation are the GRACE-type as a reference formation, Pendulum-type, GRACE-Pendulum-type, Radial wheel-type and Inclined wheel-type. The other type includes formation missions having 12 days of satellite orbits. These missions include Multi-GRACE $\Delta\Omega$ and Multi-GRACE ΔM constellations. Chapter 7 included two major investigations that are applied for all satellite formations. The first investigation concerned with the static gravity field and the other investigates the influences of the temporal variations and the model errors on the static solutions. The static gravity field solutions have been represented at different SH degrees up to $n_{max} = 60$, 90 and 180 to recover different wavelength ranges of the gravity field features. The ITG-GRACE03s model has been applied, as a reference (truth) gravity field, to estimate the static gravity field determined by different types of SFF. To investigate the influences of the time variable signals as well as their model errors on the static gravity field solutions, different background models have been applied. For the oceanic tides, the models FES2004 and EOT08a have been used to detect the oceanic tidal variations as well as the model differences. The applied models are given for the atmosphere in terms of spherical harmonics derived from the ECMWF data and for the ocean from the OMCT and the PPHA models. For the continental hydrology, the WGHM and LaD models have been applied. The gravity field solutions have been represented in terms of spectral domain, e.g. difference degree variances (DDV) of the geoid heights, accumulated geoid errors, formal standard errors and the actual differences of the recovered SH coefficients in addition to the spatial domain.

8.2 Conclusions

All test computations and results of this study has demonstrated obviously how important are the satellite formation flights to improve the gravity field solutions. All results showed the benefits of incorporating additional information into the observable of along-track component like adding radial and cross-track components. It has been found that the GRACE-type is a non-optimal satellite configuration not only for the

recovery of static gravity field but also for detecting the time variations of different temporal signals. This is due to the fact that the GRACE-type FF collects satellite observations in solely one direction (along-track). The incorporation of other information provides significant improvements in terms of the error levels and identical distribution of the errors in all directions (i.e isotropy). The improvements have been performed by the cross-track configurations like Pendulum-type and GRACE-Pendulum-type FFs and the radial configurations like Radial wheel-type and Inclined wheel-type FFs. Although, refined gravity solutions have been achieved from the along-track configuration by merging two collinear GRACE-type FFs as performed by Multi-GRACE-type constellations.

Regarding the static scenario, three scenarios have been analyzed at SH degrees and orders of 60, 90 and 180 representing long-to-medium, medium-to-short and short wavelength ranges, respectively. We can conclude that restricting the static gravity field solutions to only long or medium wavelengths are not sufficient for drawing the full picture and acquiring all information to interpret the results. The results of the static part demonstrate that satellite formation flights can provide not only gravity field improvements in the medium wavelength band but they can also contribute to higher degrees. This can help in understanding the spatial aliasing, which might be caused by restricting the solutions at only low SH degrees.

Regarding the temporal scenario, the influences of four time dependent signals of the ocean tides, the atmosphere, the ocean and the hydrology have been investigated. The influences of the combined atmospheric-oceanic variations on the static gravity field solution have been also discussed. Each scenario considered two main cases of study, the non-reduction and reduction cases. The non-reduction case has depicted the influences of the temporal variations of each signal on the static gravity solutions. The reduction case has described the aliasing effects due to the model differences. The applied data and models for these two cases of each temporal signal have been already described in the preceding section.

The investigation of **the ocean tides** influences has identified firstly the areas that require more improvements and further studies and has showed secondly which satellite formation and which observable types provide the most refined (i.e. the least) model differences. We can conclude that the ocean tidal aliasing effects can be minimized using a proper spatial and temporal sampling as determined by GRACE-Pendulum FF and Multi-GRACE ($\Delta\Omega$) constellation, respectively. The results obtained by proper spatial sampling (from GRACE-Pendulum FF) have surpassed those having temporal sampling and have provided better results than GRACE-type FF in terms of aliasing effects.

Unlike the ocean tides, the influences and model errros of the **the atmospheric and oceanic** variations have been also mitigated by the SFFs but not as much as ocean tides because of their shorter periods. The results' behavior of the oceanic variations were similar to those of atmospheric variations in character (but not in level of errors) due to the fact that the former variations depend on the latter ones. For both temporal signals, the radial and cross-track configurations reduced the influences of the atmospheric and oceanic variations on the static gravity solutions as well as their model errors. The Pendulum-type and the GRACE-Pendulum-type FFs provided RMS errors less than the Radial wheel-type and Inclined wheel-type FFs. Regarding the improvements of the temporal sampling, the impact and the aliasing errors of the atmospheric and oceanic variations have been also mitigated with the Multi-GRACE ($\Delta\Omega$) providing refined gravity solutions in only 12 days.

The influences due to the temporal variations of **the hydrological** signal have been investigated only for the formations of different spatial resolutions represented by GRACE, Pendulum, GRACE-Pendulum, Radial wheel and Inclined wheel FF types. The influences of the temporal hydrological variations have been studied not only for one month but also for 6 months (first half of the year 2006). The gravity solutions have been represented in terms of geoid heights and equivalent water heights. Regarding the one month investigation, the refined solutions have been obtained from the Radial wheel-type and the GRACE-Pendulum-type FFs for the non-reduction and reduction cases. For the 6 months investigation, the gravity solutions of the out-of-plane Inclined wheel formation have been excluded from our investigation due to the large variability of its inter-satellite ranges. The Radial wheel FF has displayed the least RMS geoid errors for the first 4 months and the GRACE-Pendulum FF for the last 2 months. Nevertheless, the latter formation has provided the most refined gravity results with the least RMS errors in terms of equivalent water heights.

We can conclude from the temporal scenario that the radial and cross-track configurations can detect tem-

poral variations and reduce their model differences up to higher spherical degrees than the the along-track configuration. All implemented numerical computations have proved that a progress in the recovery of the global static gravity field and the detection of its temporal variations are achieved from the formation flights.

8.3 Recommendations

Some advancements support further investigations of satellite formations, e.g. Pendulum, GRACE-Pendulum and Radial wheel formation flights in addition to the Multi-GRACE $\Delta\Omega$ constellation. They provide bounded satellite formation flight for a long mission period to recover the global static gravity field. The Radial wheel should be considered as a candidate mission for future gravity field. This is back to some reasons already mentioned in the last chapter (see Sec. 7.2.1.1). One reason is that the radial observations provide more isotropic gravity solutions w.r.t. other configurations (e.g. the GRACE-type and out-of-plane Pendulum-type). A satellite mission of pure along-track is sub-optimal and of pure cross-track is still to be technically challenging. Another reason is that the Radial wheel configuration seems to be more simpler from the design perspective by having only two satellites than other configurations, which have three satellites like the GRACE-Pendulum-type FF. Furthermore, the lower cost of the Radial wheel formation, since its formation has only two satellites, makes its satellite mission more cheaper than a mission of three (e.g. GRACE-Pendulum formation) or four (e.g. Multi-GRACE $\Delta\Omega$ constellation) satellites. Our recommendation is based on the fact that the mission design of the GRACE-Pendulum-type on the spacecraft level demands more challenging than other configurations as in a relative ranging metrology scenario. Concerning the optical metrology itself, more detailed evaluation of the utilized components are required, especially on the specific mission demands for the metrology system. Also the inter-satellite baseline orientation in case of the Pendulum-, GRACE-Pendulum- and Inclined wheel-mission types makes the out-of-plane configurations highly technically challenging.

Regarding the temporal variations of the gravity field, the impact of each tidal constituent and its aliasing effect should be individually investigated. Another atmospheric model should be applied in order to obtain the real atmospheric model residuals using the different formation flights. A further investigation concerning all obtained results of the satellite formation flights should be implemented with consideration of filtering techniques. This is back to the fact that the filtering approaches (e.g. isotropic or non-isotopic) can reduce the error structures of the obtained results of the satellite formation flights and will increase the factor of improvement of the gravity results. As a final remark, however these satellite formations except GRACE-type will be realized or not, we believe that these analyses reveal significant advantages from the scientific point of view. This study has displayed that the satellite formation flights improve the knowledge of the global gravity field of the Earth. This will help definitely in understanding the time variable elements of gravity field, which are responsible for the mass transportation and mass changes in the Earth's system.

A. Keplerian Motion, Keplerian Anomalies and Kepler's Equation

A.1 Kepler Motion

Johannes Kepler (1571-1630) formulated the three Laws of Planetary Motion. These laws give a description but not an explanation of the planetary motion. They provide a very good approximation of the real motion of a planet considered as a mass point within the solar system because the planetary masses can be neglected when compared to the mass of the Sun which is considered as a point mass as well. For this reason, the undisturbed gravitational motion of point mass is also called *Keplerian motion*. It is well known from celestial mechanics that the simplest form of the motions of celestial bodies moving under the influence of mutual mass attraction is the motion of two bodies (two-body problem). This means that, given at a specific time the positions and velocities of two bodies (initial conditions) moving under their mutual gravitational force, we can derive their positions and velocities at any other time.

For artificial satellites, their mass inhomogeneities can be neglected compared with the Earth's masses formulating a two-body problem, can be empirically described by Kepler's laws and can be analytically solved based on Newtonian mechanics. Because of the tiny satellite mass compared to the Earth's masses, the two-body problem becomes a one-body problem or a Kepler-problem.

In the following sections, we are going to deal with such parameters that are required to describe and define the orbit of any satellite. These parameters are called Keplerian elements or satellite orbital elements (also called orbital coordinates). Fig. A.1 shows the basic orbital parameters and also explains the relation between the equatorial and orbital planes with their corresponding vectors systems. Orbital elements are itemized as follows:

Semi-major Axis (a): The ellipse is characterized geometrically by the long axis (semi-major axis). This axis is very important because it tells us the size of the orbit ellipse.

Eccentricity (e): The satellite orbit of the Kepler-problem model is an ellipse, i.e. $0 \leq e < 1$. Eccentricity tells us the shape of the satellite's orbit. In case of e=0, the orbit's shape becomes a circle.

Inclination (i): Is the angle between the orbital plane and the equatorial plane. Inclination is a number between 0° and 180°. Orbits with an inclination of 0° are called equatorial orbits, and those with inclination of 90° are called polar orbits. When $i < 90°$ and $i > 90°$, the orbits are referred as prograde (i.e. the satellite orbits is in the direction of the Earth's rotation) and as retrograde (i.e. the satellite orbits is opposite to the direction of the Earth's rotation), respectively.

Right Ascension of Ascending Node (Ω): This is the second number after inclination that orients the orbital plane in space. The line of nodes is the intersection of the equatorial plane and the orbital plane. This line nudges two places, one is called the ascending node, where the satellite crosses the equator from south to north. The other is called the descending node, where the satellite crosses the equator from north to south. Ω is in the range from 0° to 360°.

Argument of Perigee (ω): This angle orients the orbit ellipse in the orbital plane. Perigee means a point, where the satellite is nearest to the Earth. When the satellite is farthest from the Earth, this point is called apogee.

True Anomaly (ν): It is an angle which specifies the position of the satellite along the orbit. It varies periodically around the satellite orbit from 0° to 360° during one revolution. Instead, the **Mean Anomaly** (M) is used since it relates to the true anomaly (see Sec. A.2) because M calculates the time of satellite between two points on the orbit very easily. Like ω, perigee always occurs at $M = 0°$, and apogee always occurs at $M = 180°$. Alternately, we could use **Time of Perigee Passage** τ, at

which a satellite passed perigee.

To sum up, the parameters (a,e,i,Ω,ω,τ) are required to describe the satellite's motion orbiting around the Earth in case of the simplified Kepler-problem. Two of them (a and e) describe the form of the orbit, two elements (M and τ) define the position and time along the orbit and the rest three elements (i, Ω, ω) define the orientation of the orbit in space.

In satellite orbits, the motion of the satellites is governed by the universal law of gravitation that had been formulated by Newton. If there was no atmosphere or ocean or other external perturbing forces, then the orbit of the satellites could be determined, at least numerically. However, in practice the situation is more complicated because not all the effects of relevance are accurately known or predictable. Some of these complicating perturbing forces arise from the indirect tide effects, atmospheric drag, impact of the Sun (solar wind) on the atmosphere and the gravitational attraction of other planetary objects, whose coordinates must be known. This leads to the use of the term osculating orbit for describing the motion of the satellite. The osculating orbit means simply an unperturbed Keplerian orbit, whose initial parameters, position vector and velocity vector, coincide with the true perturbed state vectors (position, velocity) at a certain epoch. Hence, the true satellite orbit can be considered as the envelope of all successive osculating orbits with osculating orbital parameters. From this follows, the perturbed satellite motion can be interpreted to be a Keplerian motion with time variable parameters.

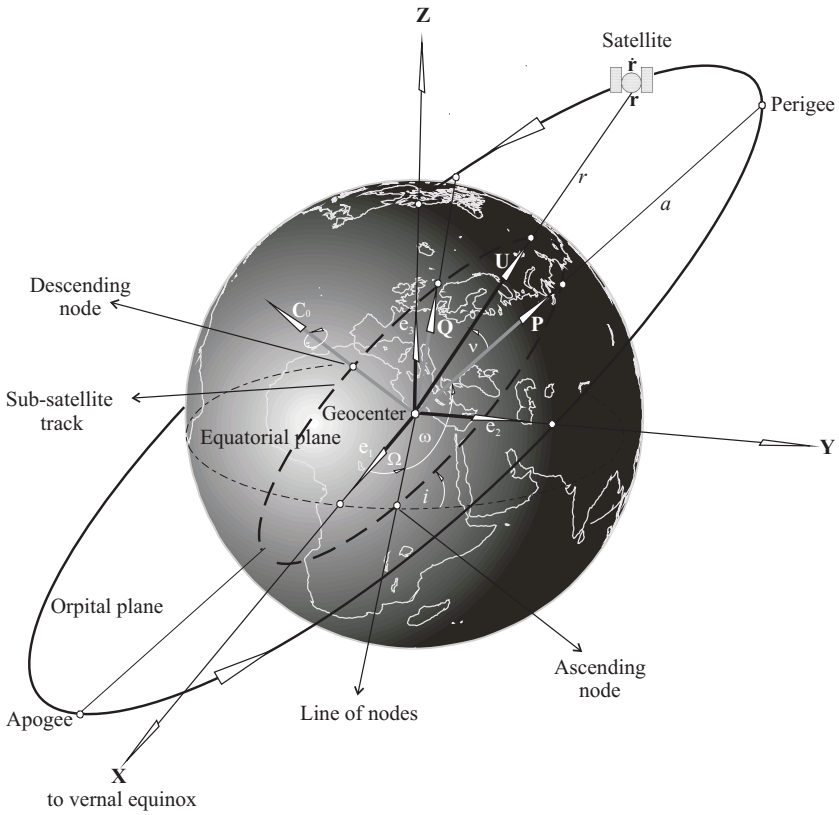

Fig. A.1: Keplerian elements with the orbit vector system.

A.1.1 Kepler Problem and the Gravity Field

In the following, a review of the Kepler problem and the classical way for solving this problem is introduced. When investigating the gravity field of the Earth, considered as a point mass, or as extended body with radial-symmetric density function from a point outside or on the Earth's surface, then the force functions of the gravitational field at distance r from the center is

$$\mathbf{g}(\mathbf{r}) = \frac{GM}{r^2}\frac{\mathbf{r}}{r}, \tag{A.1}$$

Under such conditions a satellite in orbit around the Earth can be considered to follow a Keplerian motion. But the satellite's motion is slightly perturbed because it of various effects. These are due to the heterogeneous shape of the Earth and also the other gravitational effects (see Section 3.3.1). Therefore, satellite's trajectories are not Keplerian orbits. In the following, we shall examine the satellite motion under the Keplerian laws and review the practical solution of Kepler's problem to be able to compute the satellite's positions from Kepler elements and also vice versa.

A.1.2 The Motion of a Satellite

The vector product of position and velocity vectors ($\mathbf{r}$, $\dot{\mathbf{r}}$) satisfy an indefinite integration over time t, the following conservation law

$$\mathbf{C} = \mathbf{r} \times \dot{\mathbf{r}}. \tag{A.2}$$

This conservation law states that any central motion happens in a constant plane, whose normal direction is determined by the integration vector $\mathbf{C}$. This means that, the cross product of the position and velocity vectors is a vector orthogonal to both of them. Therefore, the position vector $\mathbf{r}$ and velocity vector $\dot{\mathbf{r}}$ are always perpendicular to $\mathbf{C}$. The unit vector $\mathbf{C}_0$ (with $\mathbf{C}_0 = \mathbf{C}/\,|\mathbf{C}|$) can be represented by the two keplerian angles, the inclination i and the right ascension of ascending node Ω (see Fig. A.1) as

$$\mathbf{C}_0 = \sin i \sin\Omega \mathbf{e}_1 - \sin i \cos\Omega \mathbf{e}_2 + \cos i \mathbf{e}_3. \tag{A.3}$$

Due to this relation, it follows that the closer the satellite is to the Earth, the higher is the velocity of the satellite. In the following, we will define an orthogonal set of unit vectors spanning the orbital planr, $\vec{\mathbf{P}}$,$\vec{\mathbf{Q}}$. When introducing planar polar coordinates r, ν in the orbital plane, then the unit vector $\mathbf{U}$ of the position vector of a satellite with the true anomaly ν can be written as

$$\mathbf{U} = \cos\nu \mathbf{P} + \sin\nu \mathbf{Q}. \tag{A.4}$$

By building $\mathbf{C} = C\mathbf{C}_0$, with C=$|\mathbf{C}|$ and replacing this in Eq. (A.2), then it follows

$$\mathbf{r} \times \dot{\mathbf{r}} = C\mathbf{C}_0 = r^2\dot{\nu}\mathbf{C}_0 \qquad \rightarrow \qquad r^2\dot{\nu} = C. \tag{A.5}$$

If we define two parameters P and A,

$$P = \frac{C^2}{GM}, \qquad e := \frac{A}{GM} = AP, \tag{A.6}$$

with the semi-latus rectum P and A an integration constant, then the polar equation for the orbit reads,

$$r = \frac{P}{1 + e\cos\nu}. \tag{A.7}$$

This equation relates the satellite's distance r to the angle between its position vector and the reference direction given by A, and thus defines the satellite's path in the orbital plane.

A.2 The Relationship between the Three Keplerian Anomalies

In the interesting case of elliptical orbits ($0 \leq e < 1$), one substitutes r in Eq. (A.5) with Eq. (A.7) to obtain the relation

$$\frac{\dot{\nu} P^2}{(1 + e\cos\nu)^2} = C, \tag{A.8}$$

correspondingly,

$$\frac{P^2}{(1 + e\cos\nu)^2} d\nu = C dt. \tag{A.9}$$

With an indefinite integration on both sides, one gets

$$\int_{\nu_0}^{\nu} \frac{P^2 d\nu}{(1 + e\cos\nu)^2} = C(t - t_0). \tag{A.10}$$

The integral can easily be estimated through an auxiliary angle E, the eccentric anomaly. For this, one accomplishes a variable change $\nu \rightarrow E$ for the estimation of the integral (A.10). One takes the equation

$$r\cos\nu = a\cos E - ae, \tag{A.11}$$

and replaces r in the polar equation (A.7), so one obtains

$$\frac{P\cos\nu}{1 + e\cos\nu} = a(\cos E - e). \tag{A.12}$$

For an ellipse, $P = a(1 - e^2)$, so one can obtain a relationship between the true anomaly ν and the eccentric anomaly E as

$$\cos\nu = \frac{\cos E - e}{1 - e\cos E}. \tag{A.13}$$

Hence, one gets directly

$$\sin\nu = \frac{\sqrt{1 - e^2}\sin E}{1 - e\cos E}. \tag{A.14}$$

A relationship between the eccentric anomaly E and the mean anomaly M can be derived by considering firstly the relation between the eccentric anomaly E and the time t. This preliminary step can be achieved by building the derivation

$$\frac{d\sin\nu}{dE} = \frac{d\sin\nu}{d\nu}\frac{d\nu}{dE}, \tag{A.15}$$

so one obtains

$$\frac{d\nu}{dE} = \frac{\sqrt{1 - e^2}}{1 - e\cos E}. \tag{A.16}$$

The integral of the left side of Eq. (A.10) can be written after changing the variable ν as

$$\int_{\nu_0}^{\nu} \frac{P^2}{(1 + e\cos\nu)^2} d\nu = \int_{E_0}^{E} \frac{P^2}{(1 + e\cos\nu)^2}\frac{d\nu}{dE} dE. \tag{A.17}$$

One transforms the integral to become

$$\frac{P^2}{(1 + e\cos\nu)^2}\frac{d\nu}{dE} = \frac{P^2}{(1 + e\cos\nu)^2}\frac{1 - e^2}{1 - e\cos E} = a^2\sqrt{1 - e^2}(1 - e\cos E), \tag{A.18}$$

this yields finally by indefinite integration

$$\int_{E_0}^{E} a^2\sqrt{1-e^2}(1-e\cos E)dE = a^2\sqrt{1-e^2}(E-e\sin E)\Big|_{E_0}^{E}. \tag{A.19}$$

If one inserts this solution of the integral into Eq. (A.10), then a relationship between the time and the eccentric anomaly can be produced as

$$(E-e\sin E)|_{E_0}^{E} = \frac{C}{a^2\sqrt{1-e^2}}(t-t_0). \tag{A.20}$$

By considering the relation

$$P = a(1-e^2) = \frac{C^2}{GM}, \tag{A.21}$$

and transforming the right side of Eq. (A.20) as follows:

$$\frac{C}{a^2\sqrt{1-e^2}} = \frac{C}{a\sqrt{a^2(1-e^2)}} = \frac{C}{a\sqrt{aP}} = \frac{C}{\sqrt{a^3\frac{C^2}{GM}}} = \sqrt{\frac{GM}{a^3}}, \tag{A.22}$$

then, one obtains a relationship between the time and the eccentric anomaly, which describes the position of the satellite in the orbit:

$$(E-e\sin E)\Big|_{E_0}^{E} = \sqrt{\frac{GM}{a^3}}(t-t_0). \tag{A.23}$$

Since the mean motion n of the satellite can be found by writing orbital period

$$T = 2\pi\sqrt{\frac{a^3}{GM}}, \tag{A.24}$$

to become

$$\mathrm{n} := \sqrt{\frac{GM}{a^3}}, \tag{A.25}$$

and since the mean anomaly is simply defined as the product of n and t, that determines the chronology of the satellite in a uniform motion as

$$M := \mathrm{n}(t-t_0). \tag{A.26}$$

Finally one can get the relation between the eccentric anomaly E and the mean anomaly M at a given time as the so-called **Kepler's equation** as

$$M = E - e\sin E. \tag{A.27}$$

The last relation between the true anomaly ν and the mean anomaly M can be obtained by rewriting Eq. (A.10) as

$$t = t - t_0 = \frac{P^2}{C}\int \frac{d\nu}{(1+e\cos\nu)^2}. \tag{A.28}$$

This type of function can be integrated according to Capderou (2005) as

$$\int \frac{d\nu}{(1+e\cos\nu)^2} = -\frac{e\sin\nu}{(1-e^2)(1+e\cos\nu)} + \frac{1}{(1-e^2)}\int \frac{d\nu}{1+e\cos\nu}, \tag{A.29a}$$

$$\int \frac{d\nu}{1+e\cos\nu} = \frac{2}{\sqrt{1-e^2}}\arctan\left(\sqrt{\frac{1-e}{1+e}}\tan\frac{\nu}{2}\right). \tag{A.29b}$$

Using the property of the elliptical trajectory (see Eq. (A.6))

$$1 - e^2 = \frac{P}{a} = \frac{C^2}{GMa}, \tag{A.30}$$

then we have

$$\frac{P^2}{C} = \sqrt{\frac{a^3}{GM}}(1-e^2)^{3/2} = \frac{(1-e^2)^{3/2}}{\mathrm{n}}. \tag{A.31}$$

By inserting Eq. (A.29) and Eq. (A.31) into Eq. (A.28), the relationship between the mean anomaly and true anomaly reads

$$M = \mathrm{n}(t - t_0) = 2\arctan\left(\sqrt{\frac{1-e}{1+e}}\tan\frac{\nu}{2}\right) - \frac{e\sin\nu\sqrt{1-e^2}}{1+e\cos\nu}. \tag{A.32}$$

A.3 Solution of Kepler's Equation

The Kepler's equation can be solved e.g. by iterative methods. In order to solve it, a common way is to start with an approximation of (see Schneider 1992, p.45)

$$E_0 = \begin{cases} M & \text{for small eccentric orbits} \\ \pi & \text{for highly eccentric orbits (e.g. } e{>}0.8) \end{cases}, \tag{A.33}$$

and

$$E_{i+1} = M + e\sin E_i, \tag{A.34}$$

then to employ Newton's method to calculate successive refinements E_i until the result changes by less than a specified amount between subsequent iterations. In satellite geodesy, the satellite orbits are chosen to be near-circular or circular. This generates a constant distance from the Earth's center or a constant relative velocity.

As practical numerical solution for deriving the positions and velocities from Kepler parameters, let us consider Fig. A.1. The two unit vectors $\mathbf{C}_0$ and $\mathbf{P}$ define obviously the position of the elliptical orbit in the space-fixed (inertial) system. A general expression can be obtained by introducing the unit vector $\mathbf{P}$, which directs the perigee and the perpendicular unit vector $\mathbf{Q}$, corresponding to a true anomaly $\nu = 90°$. Position and velocity vectors can be represented as linear combinations of the orbit system vectors $\mathbf{P}$ and $\mathbf{Q}$ by the following transformation:

$$\begin{pmatrix} \mathbf{r} \\ \dot{\mathbf{r}} \end{pmatrix} = \begin{pmatrix} r\cos\nu & r\sin\nu \\ -\frac{C}{P}\sin\nu & \frac{C(\cos\nu+e)}{P} \end{pmatrix} \begin{pmatrix} \mathbf{P} \\ \mathbf{Q} \end{pmatrix}. \tag{A.35}$$

In order to explain the orientation of the orbital plane and the perigee with respect to the equatorial coordinate system[1], three angles are commonly employed (see Fig. A.1); inclination (i), the right ascension of ascending nodes (Ω) and the argument of perigee (ω). With these three angles, the satellite's position in the space can be determined. This is done by relating the unit vectors in the orbital plane system with these angles as

$$\begin{pmatrix} \mathbf{P} \\ \mathbf{Q} \\ \mathbf{C}_0 \end{pmatrix} = \begin{pmatrix} \cos\omega & \sin\omega & 0 \\ -\sin\omega & \cos\omega & 0 \\ 0 & 0 & 1 \end{pmatrix} \begin{pmatrix} 1 & 0 & 0 \\ 0 & \cos i & \sin i \\ 0 & -\sin i & \cos i \end{pmatrix} \begin{pmatrix} \cos\Omega & \sin\Omega & 0 \\ -\sin\Omega & \cos\Omega & 0 \\ 0 & 0 & 1 \end{pmatrix} \begin{pmatrix} \mathbf{e}_1 \\ \mathbf{e}_2 \\ \mathbf{e}_3 \end{pmatrix}. \tag{A.36}$$

[1]It is the common coordinate system for describing the Earth's satellite orbits, which is aligned with the Earth's rotation axis and equator.

The first three matrices at the right side represent the three elementary transformations that are primarily required for expressing the satellite's position in the equatorial coordinate system. After multiplying these right-side matrices of (A.36) and substituting them in (A.35), one obtains the final expression of the satellite's position and velocity in equatorial coordinates

$$\begin{pmatrix} x \\ y \\ z \end{pmatrix} = \begin{pmatrix} r\cos\nu\left(\cos\omega\cos\Omega - \sin\omega\sin\Omega\cos i\right) + r\sin\nu\left(-\sin\omega\cos\Omega - \cos\omega\sin\Omega\cos i\right) \\ r\cos\nu\left(\cos\omega\sin\Omega + \sin\omega\cos\Omega\cos i\right) + r\sin\nu\left(-\sin\omega\sin\Omega + \cos\omega\cos\Omega\cos i\right) \\ r\cos\nu\left(\sin\omega\sin i\right) + r\sin\nu\left(\cos\omega\sin i\right) \end{pmatrix}, \quad \text{(A.37)}$$

and

$$\begin{pmatrix} \dot{x} \\ \dot{y} \\ \dot{z} \end{pmatrix} = \begin{pmatrix} -\frac{C}{P}\sin\nu\left(\cos\omega\cos\Omega - \sin\omega\sin\Omega\cos i\right) + \frac{C(\cos\nu+e)}{P}\left(-\sin\omega\cos\Omega - \cos\omega\sin\Omega\cos i\right) \\ -\frac{C}{P}\sin\nu\left(\cos\omega\sin\Omega + \sin\omega\cos\Omega\cos i\right) + \frac{C(\cos\nu+e)}{P}\left(-\sin\omega\sin\Omega + \cos\omega\cos\Omega\cos i\right) \\ -\frac{C}{P}\sin\nu\left(\sin\omega\sin i\right) + \frac{C(\cos\nu+e)}{P}\left(\cos\omega\sin i\right) \end{pmatrix}. \quad \text{(A.38)}$$

An Inverse approach is also possible by deriving the orbital elements from the position and velocity vectors of the satellite numerically. First of all, one considers the vector product of (A.2)

$$\mathbf{C} = \mathbf{r} \times \dot{\mathbf{r}} = \begin{pmatrix} x \\ y \\ z \end{pmatrix} \times \begin{pmatrix} \dot{x} \\ \dot{y} \\ \dot{z} \end{pmatrix} = \begin{pmatrix} +(y\dot{z} - z\dot{y}) \\ -(x\dot{z} - z\dot{x}) \\ +(x\dot{y} - y\dot{x}) \end{pmatrix}, \quad \text{(A.39)}$$

and back to Eq. (A.36), it is easy to calculate the orbit inclination i and hence the right ascension of ascending nodes (Ω) numerically from the orbit normal vector $\mathbf{C}_0$ as follows:

$$\mathbf{C}_0 = \frac{\mathbf{C}}{|\mathbf{C}|} = \frac{\mathbf{r} \times \dot{\mathbf{r}}}{|\mathbf{r} \times \dot{\mathbf{r}}|} = \begin{pmatrix} \sin\Omega\sin i \\ -\cos\Omega\sin i \\ \cos i \end{pmatrix}, \quad \text{(A.40)}$$

then the orbit inclination

$$i = \arccos\left((x\dot{y} - y\dot{x})/\sqrt{(y\dot{z} - z\dot{y})^2 + (z\dot{x} - x\dot{z})^2 + (x\dot{y} - y\dot{x})^2}\right), \quad \text{(A.41)}$$

and the right ascension angle

$$\Omega = \arctan\left(\frac{y\dot{z} - z\dot{y}}{x\dot{z} - z\dot{x}}\right). \quad \text{(A.42)}$$

The semi-latus rectum is computed from (A.6) as

$$P = \frac{(y\dot{z} - z\dot{y})^2 + (x\dot{z} - z\dot{x})^2 + (x\dot{y} - y\dot{x})^2}{GM}. \quad \text{(A.43)}$$

The semi-major axis relates to the distance and the velocity vectors of the satellite with the relationship

$$\begin{aligned} a &= \left(\frac{2}{r} - \frac{\dot{\mathbf{r}}^2}{GM}\right)^{-1} \\ &= \left(\frac{2}{\sqrt{x^2 + y^2 + z^2}} - \frac{(\dot{x}^2 + \dot{y}^2 + \dot{z}^2)}{GM}\right)^{-1}. \end{aligned} \quad \text{(A.44)}$$

By substitution in (A.25), the satellite's mean motion n can be derived easily. From the fundamentals of the orbit geometry of the elliptical form, the numerical eccentricity is computed from the relation

$$e = \sqrt{1 - \frac{P}{a}}. \quad \text{(A.45)}$$

The true anomaly can be derived from (A.7) as

$$\nu = \arccos\left(\frac{P - r}{er}\right). \quad \text{(A.46)}$$

Eq. (A.35) can be written as the inverse transformation

$$\begin{pmatrix}\mathbf{P}\\ \mathbf{Q}\end{pmatrix} = \begin{pmatrix} (e+\cos\nu)/P & -(r\sin\nu)/C \\ -(\sin\nu)/P & (r\cos\nu)/C \end{pmatrix} \begin{pmatrix}\mathbf{r}\\ \dot{\mathbf{r}}\end{pmatrix}. \tag{A.47}$$

The nodal vector $\mathbf{K}$ in Fig. A.1, which is related to the right ascension of ascending node Ω, can be written as

$$\mathbf{K} = \begin{pmatrix}\mathbf{K}_1\\ \mathbf{K}_2\\ \mathbf{K}_3\end{pmatrix} = \begin{pmatrix}\cos\Omega\\ \sin\Omega\\ 0\end{pmatrix} \begin{pmatrix}\mathbf{e}_1\\ \mathbf{e}_2\\ \mathbf{e}_3\end{pmatrix}, \tag{A.48}$$

and hence, the argument of perigee can be calculated from the relations

$$\cos\omega = \mathbf{K}\cdot\mathbf{P}, \qquad \sin\omega = -\mathbf{K}\cdot\mathbf{Q}. \tag{A.49}$$

Reformulating Eq. (A.11), then the eccentric anomaly is then computed from

$$E = \arccos\left(\frac{r\cos\nu + ae}{a}\right) \tag{A.50}$$

Finally, applying the ***Kepler-Equation*** to obtain the mean anomaly in radians at time t

$$M(t) = E(t) - e\sin E(t). \tag{A.51}$$

Acronyms

AOD	**A**tmospheric-**O**ceanic **D**e-aliasing
CHAMP	**CHA**llenging **M**inisatellite **P**ayload
CNES	**C**entre **N**ational d'**E**tudes **S**patiales
DDV	**D**ifference **D**egree **V**ariances
DLR	**D**eutscheszentrum für **L**uft- und **R**aumfahrt (German Aerospace Center)
ECMWF	**E**uropean **C**enter for **M**edium-range **W**eather **F**orecast
EGM96	**E**arth **G**ravitational **M**odel 19**96**
EOT08a	**E**mpirical **O**cean **T**idal model 20**08a**
ESA	**E**uropean **S**pace **A**gency
FES2004	**F**inite **E**lement **S**olution **2004** (Ocean Tidal Model)
FF	**F**ormation **F**light
GAST	**G**reenwich **A**pparent **S**idereal **T**ime
GFZ	**G**eo**F**orschungs**Z**entrum Potsdam
GLONASS	**GLO**bal **NA**vigation **S**atellite **S**ystem
GNSS	**G**lobal **N**avigation **S**atellite **S**ystems
GOCE	**G**ravity field and steady-state **O**cean **C**irculation **E**xplorer
GPS	**G**lobal **P**ositioning **S**ystem
GRACE	**G**ravity **R**ecovery **A**nd **C**limate **E**xperiment
GROOPS	**G**ravity **R**ecovery **O**bject **O**riented **P**rogramming **S**ystem
HCW	**H**ill-**C**lohessy-**W**iltshire equations
IAU	**I**nternational **A**ssociation **U**nion
ICRF	**I**nternational **C**elestial **R**eference **F**rame
IERS	**I**nternational **E**arth rotation and **R**eference systems **S**ervice
ITG	**I**nstitute of **T**heoretical **G**eodesy, University of Bonn
ITRF	**I**nternational **T**errestrial **R**eference **F**rame
JPL	**J**et **P**ropulsion **L**aboratory
KBR	**K**-**B**and **R**anging system
LaD	**La**nd **D**ynamics Hydrology Model
LEO	**L**ow **E**arth **O**rbiter
LISA	**L**aser **I**nterferometer **S**pace **A**ntenna
LLR	**L**unar **L**aser **R**anging
LOS	**L**ine **O**f **S**ight
MJD	**M**odified **J**ulian **D**ay
NCEP	**N**ational **C**enters for **E**nvironmental **P**rediction
OMCT	**O**cean **M**odel for **C**irculation and **T**ides
POD	**P**recise **O**rbit **D**etermination
RAAN	**R**ight **A**scension of **A**scending **N**ode
RMS	**R**oot **M**ean **S**quare
SFF	**S**atellite **F**ormation **F**light
SGG	**S**atellite **G**ravity **G**radiometry
SH	**S**pherical **H**armonics
SLR	**S**atellite **L**aser **R**anging
SST	**S**atellite-to-**S**atellite **T**racking
UT1	**U**niversal **T**ime **1**
UTC	**U**niversal **T**ime **C**oordinated
UTCSR	**U**niversity of **T**exas at Austin/**C**enter for **S**pace **R**esearch
VLBI	**V**ery **L**ong **B**aseline **I**nterferometry
WGHM	**W**aterGap **G**lobal **H**ydrology **M**odel
w.r.t.	**w**ith **r**espect **t**o

List of Figures

2.1 Satellite-to-Satellite Tracking by GNSS satellites: high low-SST combined with low low-SST concept (left) and SGG with high low-SST concept (right). 5

2.2 The current applied satellites' missions (from left to right: CHAMP, GRACE and GOCE). . . 6

2.3 The requirements for future FF missions for different scales of geophysical processes at both scales; resolution and mission duration (after Rummel 2007). 8

2.4 GRACE-type FF as a reference configuration in this study. 12

2.5 Radial wheel-type FF, (a) East-West Radial wheel-type and (b) North-South Radial wheel-type. 12

2.6 Inclined wheel-type FF. 13

2.7 Pendulum-type FF, (a) cross-track Pendulum-type and (b) cross-along-track Pendulum-type. 13

2.8 (a) Combined GRACE-Pendulum-type FF and (b) Multi-GRACE-type with different temporal resolution and same spatial one. 14

2.9 (a) Multi-GRACE-type constellation with different spatial resolution and same temporal one and (b) Multi-GRACE-type with different inclinations. 14

3.1 The universal law of gravitation as described by Newton. 17

3.2 Representation of spherical coordinates 18

3.3 Relation between Kepler orbital parameters and Hill orbital parameters (u, Ω, i, r). The coordinates (u, v, w) represent the Hill coordinates. 26

5.1 Flowchart describing the procedures of the simulation scenarios by GROOPS. 47

6.1 Subsatellite tracks of 30 days of a simulated GRACE-like FF at the same orbital altitude of 450 km and for different inclinations. 55

6.2 *DDV* of geoid heights between ITG-GRACE03s and gravity field solutions of simulated GRACE-like FF at different inclinations. The solid lines represent (90 × 90) sectorial gravity coefficients and the dashed lines represent the (90 × 0) zonal gravity coefficients. 56

6.3 Cumulative geoid errors between ITG-GRACE03s and gravity field solutions of simulated GRACE-like FF at different inclinations. 56

6.4 Effect of the inverse attenuation factor as a function of spherical harmonic degree at different orbital altitudes. 58

6.5 Different modes of subsatellite tracks of 30 days of a simulated GRACE-like FF at the same orbital inclination of 89.5° and at different orbital altitudes. 58

6.6 *DDV* of geoid heights between ITG-GRACE03s and gravity field solutions of a simulated GRACE-like FF at different orbital altitudes. 59

6.7 Cumulative geoid errors between ITG-GRACE03s and gravity field solutions of simulated GRACE-like FF at different orbital altitudes. 59

6.8 *DDV* of geoid heights between ITG-GRACE03s and gravity field solutions of simulated GRACE-like FF at different inter-satellite baselines. 62

6.9 Cumulative geoid errors between ITG-GRACE03s and gravity field solutions of simulated GRACE-like FF at different inter-satellite baselines. 62

6.10 *DDV* of geoid heights between ITG-GRACE03s and gravity field solutions of simulated GRACE-like FF at different measurement noise levels in case of an inter-satellite separation of 200 km. 63

6.11 Cumulative geoid errors between ITG-GRACE03s and gravity field solutions of simulated GRACE-like FF at different applied measurement noise levels in case of an inter-satellite separation of 200 km. 63

6.12 Illustration of the relative motion of two satellites with (a) simplest in-plane leader follower geometry and with (b) an out-of-plane geometry. The motion of the two satellites referred to the inertial frame XYZ and the Earth accelerates w.r.t XYZ but does not rotate. 67

6.13 The relative motion of the proposed satellite formation flights. 69

6.14 The relative motion of two GRACE-type FFs. 72

6.15 The inter-satellite range, range-rate and range-changes of the two satellites of GRACE-type. . 73

6.16 The relative motion of four satellites of both Radial wheel-types FF. 76

6.17 The relative motion of two Radial wheel-type FFs, (a) in the XY-plane, (b) in the YZ-plane, (c) in XZ-plane of type 1, (d) in XZ-plane of type 2, (e) in XYZ-plane of type 1 and (f) XYZ-plane of type 2. 77

6.18 The inter-satellite range, range-rate and range-changes of two satellites of Radial wheel-type1. 78

6.19 The inter-satellite range, range-rate and range-changes of two satellites of Radial wheel-type2. 79

6.20 Two satellite orbits with out-of-plane motion. (a) an out-of-plane imposed by $\Delta\Omega$, (b) an out-of-plane imposed by Δi (after Alfriend et al. 2000). 80

6.21 The relative motion of two Inclined wheel-type FFs, (a) in the XY-plane, (b) in the YZ-plane, (c) in XZ-plane and (d) in XYZ-plane. 81

6.22 The inter-satellite range, range-rate and range-changes of two satellites of Inclined wheel-type. 82

6.23 The relative motion of two Pendulum-type FFs, (a) in the XY-plane, (b) in the YZ-plane, (c) in XZ-plane and d) in XYZ-plane. 84

6.24 The inter-satellite range, range-rate and range-changes of the two satellites of Pendulum-type. 85

6.25 Ascending and descending observation distribution of the proposed satellite constellations of GRACE-type FF, (a) 12 days of one GRACE-type FF, (b) 24 days of one GRACE-type FF, (c) 12 days of one constellation with a mean anomaly difference (ΔM) and (d) 12 days of one constellation with a RAAN difference ($\Delta\Omega$) and (e) 24 days of one constellation with an inclination difference (Δi). 88

7.1 The deviation of the positions between GRACE A satellite from SC7 data set and the simulated GRACE A satellite through the orbit integration using GROOPS. 90

7.2 *DDV* of geoid heights between ITG-GRACE03s and the gravity solutions of the Pendulum-type FF with and without the consideration of noises (i.e. error-free and noise cases). 94

7.3 *DDV* of geoid heights between ITG-GRACE03s and the gravity solutions of all formation flights with and without the consideration of noises (i.e. error-free and noise cases). 94

7.4 Static gravity field solutions of the formation flights at different spherical harmonics degrees, (a) n= 60, (b) n= 90 and (c) n= 180. Solid lines represent *DDV* of geoid heights between ITG-GRACE03s and the gravity solutions and dashed ones represent the cumulative geoid errors. 97

7.5 Differences in geoid heights between ITG-GRACE03s and the static gravity field solutions of (a) GRACE-type, (b) Pendulum-type, (c) GRACE-Pendulum-type, (d) Radial wheel-type and (e) Inclined wheel-type, n_{max}= 60. 98

7.6 Differences in geoid heights between ITG-GRACE03s and the static gravity field solutions of (a) GRACE-type, (b) Pendulum-type, (c) GRACE-Pendulum-type, (d) Radial wheel-type and (e) Inclined wheel-type, n_{max}= 90. 99

7.7 Differences in geoid heights between ITG-GRACE03s and the static gravity field solutions of (a) GRACE-type, (b) Pendulum-type, (c) GRACE-Pendulum-type, (d) Radial wheel-type and (e) Inclined wheel-type, n_{max}= 180. 100

7.8 Formal errors of the geopotential coefficients for different SFFs in terms of degree variances of geoid heights. 102

7.9 Formal standard deviations of the recovered SH coefficients. From top to bottom: GRACE-type, Pendulum-type, GRACE-Pendulum-type, Radial wheel-type and Inclined wheel-type at different SH degrees; n= 60 (left), n= 90 (middle) and n= 180 (right). 103

7.10 Static gravity field solutions of the GRACE-type FFs and Multi-GRACE-type constellations. Solid lines represent *DDV* of geoid heights between ITG-GRACE03s and the gravity solutions and dashed ones represent the cumulative geoid errors. 105

7.11 Differences in geoid heights between ITG-GRACE03s and the static gravity field solutions of GRACE-type FFs and Multi-GRACE-type constellations, (a) GRACE-type 24-days, (b) GRACE-type 12-days, (c) Multi-GRACE-type (ΔM) constellation and (d) Multi-GRACE-type ($\Delta\Omega$) constellation, n_{max}= 90. 105

7.12 Formal standard deviations (left) and the differences of the recovered SH coefficients (right) at degree and order 90. Solutions from top to bottom: GRACE-type 24-days, GRACE-type 12-days, Multi-GRACE-type (ΔM) constellation and Multi-GRACE-type ($\Delta\Omega$) constellation. 106

7.13 *DDV* of geoid heights between ITG-GRACE03s and the gravity solutions of Pendulum FF affected by the ocean tides in the error-free and noise cases. 108

7.14 *DDV* of geoid heights between ITG-GRACE03s and the gravity solutions of Pendulum FF affected by the ocean tides model errors in the error-free and noise cases. 109

7.15 A flowchart explains the both the non-reduction and the reduction cases. 110

7.16 *DDV* of geoid heights between ITG-GRACE03s and gravity field solutions as determined by different SFF types due to the ocean tide effects for both non-reduction and reduction cases. 113

7.17 *DDV* of geoid heights between ITG-GRACE03s and gravity field solutions as determined by by Multi-GRACE-type constellations due to the ocean tide effects for both non-reduction and reduction cases. 113

7.18 Differences in geoid heights between ITG-GRACE03s and the gravity field solutions due to ocean tides effects as determined by SFF types. From top to bottom: GRACE, Pendulum, GRACE-Pendulum, Radial wheel and Inclined wheel. The left side represents the non-reduction case and the right side represents the reduction case, n_{max}= 80. 114

7.19 Differences in geoid heights between ITG-GRACE03s and the gravity field solutions due to ocean tides effects as determined by GRACE-type FFs and Multi-GRACE-type constellations. From top to bottom: GRACE-type 24-days, GRACE-type 12-days, Multi-GRACE-type (ΔM) constellation and Multi-GRACE-type ($\Delta\Omega$) constellation. The left side represents the non-reduction case and the right side represents the reduction case, n_{max}= 80. 115

7.20 *DDV* of geoid heights between ITG-GRACE03s and gravity field solutions as determined by different SFF types due to the atmospheric effects for both non-reduction and reduction cases. 119

7.21 *DDV* of geoid heights between ITG-GRACE03s and gravity field solutions as determined by GRACE- and GRACE-Pendulum-type FFs due to the atmospheric effects for both non-reduction and reduction cases compared to the mean daily and monthly atmospheric variations.119

7.22 *DDV* of geoid heights between ITG-GRACE03s and gravity field solutions as determined by GRACE-type FFs and Multi-GRACE-type constellations due to the atmospheric effects for both non-reduction and reduction cases. 120

7.23 *DDV* of geoid heights between ITG-GRACE03s and gravity field solutions as determined by GRACE-type 12-day FF and the Multi-GRACE-type ($\Delta\Omega$) constellation due to the atmospheric effects for both non-reduction and reduction cases compared to the mean daily and monthly atmospheric variations. 120

7.24 Differences in geoid heights between ITG-GRACE03s and the gravity field solutions due to atmospheric variations as determined by SFFs. From top to bottom: GRACE, Pendulum, GRACE-Pendulum, Radial wheel and Inclined wheel. The left side represents the non-reduction case and the right side represents the reduction case, n_{max}= 100. 121

7.25 Differences in geoid heights between ITG-GRACE03s and the gravity field solutions due to atmospheric variations as determined by GRACE-type FFs and Multi-GRACE-type constellations. From top to bottom: GRACE-type 24-days, GRACE-type 12-days, Multi-GRACE-type (ΔM) constellation and Multi-GRACE-type ($\Delta\Omega$) constellation. The left side represents the non-reduction case and the right side represents the reduction case, n_{max}= 100. 122

7.26 *DDV* of geoid heights between ITG-GRACE03s and gravity field solutions as determined by different SFF types due to the oceanic effects for both non-reduction and reduction cases. . . 125

7.27 *DDV* of geoid heights between ITG-GRACE03s and gravity field solutions as determined by GRACE- and GRACE-Pendulum-type FFs due to the oceanic effects for both non-reduction and reduction cases compared to the mean daily and monthly oceanic variations. 125

7.28 *DDV* of geoid heights between ITG-GRACE03s and gravity field solutions as determined by GRACE-type FFs and Multi-GRACE-type constellations due to the oceanic effects for both non-reduction and reduction cases. 126

7.29 *DDV* of geoid heights between ITG-GRACE03s and gravity field solutions as determined by GRACE-type 12-day FF and the Multi-GRACE-type ($\Delta\Omega$) constellation due to the oceanic effects for both non-reduction and reduction cases compared to the mean daily and monthly oceanic variations. 126

7.30 Differences in geoid heights between ITG-GRACE03s and the gravity field solutions due to oceanic variations as determined by SFFs. From top to bottom: GRACE, Pendulum, GRACE-Pendulum, Radial wheel and Inclined wheel. The left side represents the non-reduction case and the right side represents the reduction case, n_{max}= 100. 127

7.31 Differences in geoid heights between ITG-GRACE03s and the gravity field solutions due to oceanic variations as determined by GRACE-type FFs and Multi-GRACE-type constellations. From top to bottom: GRACE-type 24-days, GRACE-type 12-days, Multi-GRACE-type (ΔM) constellation and Multi-GRACE-type ($\Delta\Omega$) constellation. The left side represents the non-reduction case and the right side represents the reduction case, n_{max}= 100. 128

7.32 *DDV* of geoid heights between ITG-GRACE03s and gravity field solutions of GRACE-type FF influenced by different temporal variations. 130

7.33 *DDV* of geoid heights between ITG-GRACE03s and gravity field solutions as determined by different SFF types due to the combined atmospheric-oceanic variations for the non-reduction case. 130

7.34 Gravity field solutions of the SFFs affected by the hydrological variations for the non-reduction case compared with a) the reduction case, b) the aliasing case and c) the mean daily and monthly hydrological variations and the static solutions. 134

7.35 Differences in geoid heights between ITG-GRACE03s and the gravity field solutions due to hydrological variations as determined by SFFs. From top to bottom: GRACE, Pendulum, GRACE-Pendulum, Radial wheel and Inclined wheel. The left side represents the gravity solution in terms of geoid heights in $[mm]$ and the right side represent the equivalent water heights in $[m]$ in the non-reduction case, n_{max}= 100. 135

7.36 Differences in geoid heights between ITG-GRACE03s and the gravity field solutions due to hydrological variations as determined by SFFs. From top to bottom: GRACE, Pendulum, GRACE-Pendulum, Radial wheel and Inclined wheel. The left side represents the non-reduction case and the right side represents the reduction case 1, n_{max}= 100. 136

7.37 Differences in geoid heights between ITG-GRACE03s and the gravity field solutions due to hydrological variations as determined by SFFs. From top to bottom: GRACE, Pendulum, GRACE-Pendulum, Radial wheel and Inclined wheel. The left side represents the non-reduction case and the right side represents the reduction case 2, n_{max}= 100. 137

7.38 Monthly Gravity variations for GRACE-type FF (left) and Pendulum-type-FF (right) in terms of geoid heights. 140

7.39 Monthly Gravity variations for GRACE-Pendulum-type FF (left) and Radial wheel-type FF (right) in terms of geoid heights. 141

7.40 Monthly Gravity variations for GRACE-type FF (left) and Pendulum-type-FF (right) in terms of water heights. 142

7.41 Monthly Gravity variations for GRACE-Pendulum-type FF (left) and Radial wheel-type FF (right) in terms of water heights. 143

A.1 Keplerian elements with the orbit vector system. 149

List of Tables

6.1 Repeat period of subsatellite tracks depending only on the inclinations with an orbital altitude of 450 km and an eccentricity of 0.001. 56

6.2 Repeat period of subsatellite tracks depending only on the orbital altitude with fixed inclination of 89.5° and an eccentricity of 0.001. 59

6.3 Keplerian orbital parameters for the collinear GRACE-type FF. 72

6.4 Keplerian orbital parameters for the Radial wheel-type FF with its both postulations. Radial wheel-type 1 depicts east-west motion and Radial wheel-type 2 depicts north-south motion. . 75

6.5 Keplerian orbital parameters for the Inclined wheel-type FF. 81

6.6 Keplerian orbital parameters for the out-of-plane nodal Pendulum-type FF (as seen in Fig. 2.7(b)) and GRACE-Pendulum-type FF(as seen in Fig. 2.8(a)). 84

6.7 Keplerian orbital parameters for different constellations of GRACE-type FF with two postulations(ΔM and $\Delta\Omega$). 87

7.1 Overview of the different applied models and parameters used for the analysis of the investigated satellite formation flights (such as GRACE, Pendulum, GRACE-Pendulum, Radial wheel, Inclined wheel) and satellite constellations (such as Multi-GRACE ΔM and Multi-GRACE $\Delta\Omega$). 92

7.2 Geoidal statistical values (RMS, average, minimum and maximum) in [mm] of the different gravity solutions as determined by SFFs at degree n= 60. The gray cells represent the least geoid errors. 98

7.3 Geoidal statistical values (RMS, average, minimum and maximum) in [mm] of the different gravity solutions as determined by SFFs at degree n= 90. The gray cells represent the least geoid errors. 99

7.4 Geoidal statistical values (RMS, average, minimum and maximum) in [mm] of the different gravity solutions as determined by SFFs at degree n= 180. The gray cells represent the least geoid errors. 100

7.5 Geoidal statistical values (RMS, average, minimum and maximum) in [mm] of the different gravity solutions as determined by the GRACE-type FFs and Multi-GRACE-type constellations at degree n= 90. 104

7.6 Geoidal statistical values (RMS, average, minimum and maximum) of the different gravity solutions as determined by all SFFs due to the ocean tides effects at degree n= 80 corresponding to Fig. 7.18 (the upper five rows) and Fig. 7.19 (the lower four rows). The gray cells represent the least geoid errors. 113

7.7 Geoidal statistical values (RMS, average, minimum and maximum) of the different gravity solutions as determined by all SFFs due to the atmospheric effects at degree n= 100 corresponding to Fig. 7.24 (the upper five rows) and Fig. 7.25 (the lower four rows). The gray cells represent the least geoid errors. 119

7.8 Geoidal statistical values (RMS, average, minimum and maximum) of the different gravity solutions as determined by all SFFs due to the oceanic effects at degree n= 100 corresponding to Fig. 7.30 (the upper five rows) and Fig. 7.31 (the lower four rows). The gray cells represent the least geoid errors. 125

7.9 Geoidal statistical values (RMS, average, minimum and maximum) of the different gravity solutions as determined by all SFFs due to the combined atmospheric-oceanic variations at degree n= 100 considering only the non-reduction case. 130

7.10 Comparison between the geoid heights [in mm] and the equivalent water heights [in m] of the gravity solutions as determined by the different SFF types corresponding to Fig. 7.35. The gray cells represent the least values. 133

7.11 Geoidal statistical values (RMS, average, minimum and maximum) of the different gravity solutions as determined by SFFs due to the hydrological variations at degree n= 100 corresponding to Fig. 7.37 and Fig. 7.36. The gray cells represent the least geoid errors. 133

7.12 Inter-satellite distances of the SFF types for a mission period of 6 months. 138

7.13 Geoidal statistical values (RMS, average, minimum and maximum) in [mm] of the different gravity solutions as determined by GRACE-type and Pendulum-type FFs (top) and GRACE-Pendulum-type and Radial wheel-type FFs (bottom) due to the hydrological variations of 6 months at degree n= 100 corresponding to Figs. 7.38 and 7.39, respectively. 139

7.14 Equivalent water statistical values (RMS, average, minimum and maximum) in [m] of the different gravity solutions as determined by GRACE-type and Pendulum-type FFs (top) and GRACE-Pendulum-type and Radial wheel-type FFs (bottom) due to the hydrological variations of 6 months at degree n= 100 corresponding to Figs. 7.40 and 7.41, respectively. 139

References

Abrikosov, O., F. Jarecki, J. Müller, S. Petrovic and P. Schwintzer (2006) The Impact of Temporal Gravity Variations on GOCE Gravity Field Recovery. Flury, J., R. Rummel, Ch. Reigber, M. Rothacher, G. Boedecker and U. Schreiber (Eds.), *Observation of the Earth System from Space*, Springer, Berlin Heidelberg, 255–269.

Aguirre-Martinez, M. and N. Sneeuw (2002) Needs and tools for future gravity measuring missions. *Space Science Reviews*, Vol. 108(1–2):409–416.

Alfriend, K. T., H. Schaub and D.W. Gim (2000) Gravitational Perturbations, Nonlinearity and Circular Orbit Assumption Effects on Formation Flying Control Strategies. In Proc. *The 23rd Annual AAS Guidance and Control Conference*. Breckenridge, CO, AAS, 00–012.

Balmino, G., E. Schrama and N. Sneeuw (1996) Compatibility of first-order circular orbit perturbations theories; consequences for cross-track inclination functions. *Journal of Geodesy*, Vol. 70:554–561.

Bender, P. L., J. L. Hall, J. Ye and W. M. Klipstein (2003) Satellite-Satellite Laser Links for Future Gravity Missions. *Space Science Reviews*, Vol. 108, Issue 1:377–384.

Bender, P.L., D. N. Wiese and R. S. Nerem (2008) A Possible Dual-GRACE Mission With 90 Degree And 63 Degree Inclination Orbits. In Proc. *Proceedings of the 3rd International Symposium on Formation Flying, Missions and Technologies*. Noordwijk, Netherlands, 59–64.

Berry, M. (2004) *A Variable-Step Double-Integration Multi-Step Integrator*. Ph.D. Thesis, Faculty of the Virginia Polytechnic Institute and State University, Blacksburg, Virginia.

Bezděk, A., Klokočník J. Kostelecký J. Floberghagen R. Gruber Ch. (2009) Simulation of free fall and resonances in the GOCE mission. *Journal of Geodynamics*, Vol. 48, Issue 1:47–53.

Bosch, W. and R. Savcenko (2008) EOT08a – ein neues Gezeitenmodell. *Geodätische Woche Bremen, Germany, 30.9.–2.10. (Poster)*.

Capderou, M. (2005) *Satellites Orbits and Missions*. Springer, France.

Clohessy, W. H. and R. S. Wiltshire (1960) Terminal guidance system for satellite rendezvous. *Journal of the Aerospace Sciences*, Vol. 27(9):653–658.

Dirac, P. A. M. (1958) *The principles of quantum mechanics, 4th edition*. The international series of monographs on physics 27, Oxford Science, Publications, Oxford University Press, Oxford, England.

Döll, P., F. Kaspar and B. Lehner (2003) A global hydrological model for deriving water availability indicators: model tuning and validation. *Journal of Hydrology*, Vol. 270:105–134.

Doodson, A. T. (1921) The harmonic development of tide generating potential. *Proceedings of the Royal Society*, Vol. A(100):305–329.

Elsaka, B. and K. H. Ilk (2008a) Global Gravity Field Solutions from Simulated Satellite Formation Flight Missions. *NRIAG Journal of Geophysics, Special Issue (2008)*.

Elsaka, B. and K. H. Ilk (2008b) Gravity Field Recovery of the Earth from Simulated Multiple GRACE-Type Missions. *Geodätische Woche Bremen, Germany, 30.9.–2.10. (Poster)*.

Elsaka, B., K. H. Ilk and J. Kusche (2009) Multiple Simulated Formation Flights for Future Gravity Field Recovery. *EGU General Assembly, Vienna, Austria, 19.–23.4. (Poster)*.

ESA (1999) *Gravity Field and Steady-State Ocean Circulation Explorer Mission.* Report of European Space Agency for mission selection, the fourth canditate Earth explorer core missions, SP-1233, Nordwijk, Netherlands.

Feucht, U., A. Nitsch and O. Wagner (2003) Attitude Impact on the GRACE Formation Orbit. *Third International Workshop on Satellite Constellations and Formations, Pisa, Italy, 24-26 Feb.*

Flechtner, F. (2007) AOD1B Product Description Document for Product Releases 01 to 04. Technical Report GRACE 327-750, GeoForschungsZentrum Potsdam. Rev. 3.0, Feb. 23, 2007.

Flechtner, F., R. Schmidt and U. Mayer (2006) De-aliasing of Short-term Atmospheric and Oceanic Mass Variations for GRACE. Flury, J., R. Rummel, Ch. Reigber, M. Rothacher, G. Boedecker and U. Schreiber (Eds.), *Observation of the Earth System from Space*, Springer, Berlin Heidelberg, 83–97.

Gruber, Th. (2009) The Global Water Cycle from a Geodetic Point of View. In Proc. *3rd Workshop SPP1257.* Eitorf, Germany, 29.6.-1.7.2009.

Heiskanen, W. A. and H. Moritz (1979) *Physical Geodesy.* By Helmut Moritz, Reprint of the original edition published by W.H. Freeman and Company San Francisco, 1967, Institute of Physical Geodesy, Graz.

Helmert, F. R. (1880) *Die mathematischen und physikalischen Theorien der höheren Geodäsie.* Vol. I, Minerva Gmbh. reprint, 1962.

Hill, G. H. (1878) Researches in the Lunar Theory,. *American Journal of Mathematics I*, 5–26, 129–147, 245–260.

IAG -SC7 (2003) Satellite Gravity Field Missions: Simulation Scenarios, IAG - Special Commission VII (Section II), Satellite Gravity Field Missions, http://www.geod.uni-bonn.de/SC7/index.html, administrated by K.-H. Ilk and J. Kusche, Bonn, 04.11.2003.

Ilk, K. H. (1984) On the analysis of satellite–to–satellite tracking data. In Proc. *The International Symposium on Space Techniques for Geodesy.* Sopron, 59–64.

Ilk, k. H. and W. Seemüller (1977) Zur Bewegung künstlicher Erdsatelliten in benachbarten Umlaufbahnen. *Veröffentlichung der Bayerischen Kommission für Internationale Erdmessung der Bayerischen Akademie der Wissenschaften*, Heft Nr. 38.

Ilk, K. H., R. Rummel and M. Thalhammer (1995) Refined Method for the Regional Recovery from GPS/SST and SSG. CIGAR III/2, ESA contract No. 10713/93/F/FL. European Space Agency.

Ilk, K.H., J. Flury, R. Rummel, P. Schwintzer, W. Bosch, C. Haas, J. Schröter, D. Stammer, W. Zahel, H. Miller, R. Dietrich, P. Huybrechts, H. Schmeling, D. Wolf, H. Götze, J. Riegger, A. Bardossy, A. Güntner and Th. Gruber (2005) *Mass Transport and Mass Distribution in the Earth System – Contribution of the New Generation of Satellite Gravity and Altimetry Missions to Geosciences, Proposal for a German Priority Research Program.* GOCE-Projektbüro Deutschland, Technische Universität München, GeoForschungsZentrum Potsdam. 2nd edition.

Jekeli, C. (1981) Alternative methods to smooth the Earth's gravity field. *Report 327, Department of Geodetic Science and Surveying, Ohio State Univ., Columbus, December 1981.*

Kaula, W. M. (1966) *Theory of Satellite Geodesy.* Blaisdell Puplishing Company, Waltham, Massachusetts. Toronto. London. Republished, 2000 by Dover Puplications, Inc. Mineola, New York.

Kim, J. (2000) *Simulation Study of A Low-Low Satellite-to-Satellite Tracking Mission.* Ph.D. Thesis, University of Texas at Austin, Austin, Texas, USA.

Koch, K. R. (1988) *Parameter Estimation and Hypothesis Testing in Linear Models.* Springer-Verlag, Berlin Heidelberg.

Koop, R. (1993) *Global Gravity Field Modeling Using Satellite Gravity Gradiometry.* Netherlands Geodetic Commission, Publication on Geodesy, New Series, No. 38. Delft.

Kusche, J. (2007) Approximate decorrelation and non-isotropic smoothing of time-variable GRACE-type gravity field models. *Journal of Geodesy*, Vol. 81:733–749.

Le Provost, C. (2001) Ocean tides. In Proc. Fu, L.L. and A. Cazenave (Eds.), *Satellite Altimetry and Earth Sciences.* Springer, 267–303.

Letellier, T., F. Lyard and F. Lefebre (2004) The new global tidal solution: FES2004. *Presented at: Ocean Surface Topography Since Team Meeting, St. Petersburg, Florida, Nov. 4-6.*

Mackenzie, R. A. (1995) *Gravity Field Recovery Using Two Low Satellites in Different Orbital Planes.* Ph.D. Thesis, The University of Aston in Birmingham, England.

Massonnet, D. (1998) Roue interférométrique. *French patent no 339920D17306RS.*

Mayer-Gürr, T. (2006) *Gravitationsfeldbestimmung aus der Analyse kurzer Bahnbögen am Beispiel der Satellitenmissionen CHAMP und GRACE.* Ph.D. Thesis, University of Bonn, Germany.

Mayer-Gürr, T., K. H. Ilk, A. Eicker and M. Feuchtinger (2005) ITG-CHAMP01: A CHAMP Gravity Field Model from Short Kinematical Arcs of a One-Year Observation Period. *Journal of Geodesy*, Vol. 78:462–480.

Mayer-Gürr, T., A. Eicker and K. H. Ilk (2006) Gravity Field Recovery from GRACE-SST Data of Short Arcs. Flury, J., R. Rummel, Ch. Reigber, M. Rothacher, G. Boedecker and U. Schreiber (Eds.), *Observation of the Earth System from Space*, Springer, Berlin Heidelberg, 131–148.

Mayer-Gürr, T., A. Eicker and K. H. Ilk (2007) ITG-GRACE02s: a GRACE gravity field derived from short arcs of the satellite's orbit. In Proc. *The 1st International Symposium of the International Gravity Field Service 'Gravity Field of the Earth'.* Istanbul, 193–198.

McCarthy, D. D. and G. Petit (Eds.) (2004) *IERS Conventions 2003.* Number 32 in IERS Technical Notes. Verlag des Bundesamts für Kartographie und Geodäsie, Frankfurt am Main.

Milly, P. and A. Shmakin (2002) Global Modeling of Land Water and Energy Balances. Part I: The Land Dynamics (LaD) Model. *Journal of Hydrometeorology*, Vol. 3:283–299.

Munk, W. H. and G. J. F. MacDonald (Eds.) (1960) *The Rotation of the Earth.* Cambridge Univ. Press, New York.

NG2 (2009) Next Generation Gravity Variation Monitor Study. Technical Proposal. Astrium Proposal No.: A.2009-4028-0-1, April 2009.

Peters, T. (2007) *Modellierung zeitlicher Schwerevariationen und ihre Erfassung mit Methoden der Satellitengravimetrie.* Ph.D. Thesis, Technical University of Munich, Germany.

Rees, W. G. (2001) *Physical Principles of Remote Sensing.* Cambridge University Press. 2nd edition., Cambridge, United Kingdom.

Reigber, Ch. (1969) *Zur Bestimmung des Gravitationsfeldes der Erde aus Satellitenbeobachtungen*, Vol. Vol. 137,C. Deutsche Geodätische Kommission, München.

Reigber, Ch. (1989) Gravity Field Recovery From Satellite Tracking Data. Sansò, F. and R. Rummel (Eds.), *Lecture Notes in Earth Sciences*, Springer, Berlin Heidelberg, 197–234.

Reigber, Ch., P. Schwintzer and H. Lühr (1999) The CHAMP geopotential mission. *Bolletino di Geofisica Teorica ed Applicata*, Vol. 40:285–289.

Reigber, Ch., H. Lühr, L. Grunwaldt, C. Förste, R. König, H. Massmann and Falck. C. (2006) CHAMP Mission 5 Years in Orbit. Flury, J., R. Rummel, Ch. Reigber, M. Rothacher, G. Boedecker and U. Schreiber (Eds.), *Observation of the Earth System from Space*, Springer, Berlin Heidelberg, 3–15.

Reubelt, T., N. Sneeuw and M. Sharifi (2009) Future mission design options for spatio-temporal geopotential recovery. In Proc. *Gravity, Geoid and Earth Observation*. June 23-27, 2008, Chania, Crete, Greece.

Rummel, R. (2007) The future of Satellite Gravimetry. *Presentation given at the Workshop on The Future of Satellite Gravimetry*, 12-13 April 2007, ESA/ESTEC, Noordwijk, Netherlands.

Rummel, R., J. Flury, R. Haagmans, C. Hughes, P. Le Grand, J. Riegger, E. Schrama, N. Sneeuw, B. Vermeersen and P. Woodworth (2003) Scientific Objectives for Future Geopotential Missions. Technical Report. Draft Version 6 from the ESA contract No: 16668/02/NL/MM 'Enabling Observation Techniques for Future Solid Earth Missions'.

Savcenko, R. and W. Bosch (2008) EOT08a – empirical ocean tide model from multi-mission satellite altimetry. *Report No. 81. Deutsches Geodätisches Forschungsinstitut (DGFI), München, Germany.*

Schaub, H. and J. L. Junkins (2003) *Analytical Mechanics of Space Systems.* AIAA Education Series, Reston, VA.

Schneider, M. (1968) A General Method of Orbit Determination. *Library Translation*, Vol. Vol. 1279, Royal Aircraft Establishment, Ministry of Technology, Farnborough, England.

Schneider, M. (1992) *Himmelsmechanik Band I: Grundlagen, Determinierung.* B.I. Wissenschaftsverlag, Mannheim.

Schneider, M. and Ch. Reigber (1969) On the Determination of field parameters using a generalized Fourier-analysis. In Proc. Morando, B. (Eds.), *Dynamics of Satellites, Symposium Prague COSPAR - IAG/IUGG - IUTAM.* Springer-Verlag Berlin 1970.

Schönenberg, A., R. Haagmans, A. Regan, A. Ginati and Y. Menard (2005) Swarm – Three Explorers of the Earth Magnetic Field and its Environment. *5th IAA Symposium on Small Satellites for Earth Observation*, Berlin, Germany, April 4-8, 2005.

Schrama, E. J. O. (1989) *The Role of Orbit Errors in Processing of Satellite Altimeter Data.* Ph.D. Thesis, Delft University of Technology, The Netherlands.

Seeber, G. (2003) *Satellite Geodesy.* Walter de Gruyter GmbH & Co. KG, Berlin.

Sharifi, M., N. Sneeuw and W. Keller (2007) Gravity Recovery capability of four generic satellite formations. In Proc. Kilicoglu, A. and R. forsberg (Eds.), *Gravity Field of the Earth.* General Command of Mapping, ISSN 1300-5790, Special issue 18, 211–216.

Sneeuw, N. and H. Schaub (2005) Satellite clusters for future gravity field missions. Jekeli, C., L. Bastos and J. Fernandes (Eds.), *Gravity, Geoid and Space Missions*, Vol. Vol. 129, Springer, Berlin Heidelberg, 12–17.

Sneeuw, N., M. Sharifi and W. Keller (2008) Gravity Recovery from Formation Flight Missions. Xu, Peiliang, Jingnan Liu and Athanasios Dermanis (Eds.), *VI Hotine-Marussi Symposium on Theoretical and Computational Geodesy*, Vol. Vol. 132, Springer, Berlin Heidelberg, 29–34.

Standish, E. M. (1998) *JPL Planetary and Lunar Ephemerids DE405/LE405.* Jet Propulsion Labratory, Pasadena.

Tapley, B. D. (1989) Fundamentals of Orbit Determination. Sansò, F. and R. Rummel (Eds.), *Lecture Notes in Earth Sciences*, Springer, Berlin Heidelberg, 235–260.

Tapley, B. D., S. Bettadpur, J.C. Ries, P. F. Thompson and M. M. Watkins (2004a) GRACE Measurements of Mass Variability in the Earth System. *Sience*, Vol. 305: 503-505.

Tapley, B. D., S. Bettadpur, M. M. Watkins and Ch. Reigber (2004b) The Gravity Recovery and Climate Experiment: Mission Overview and Early Results. *Geophysical Research Letters*, Vol. 31, 10.1029/2004GL019920.

van Dam, T., P. Visser, N. Sneeuw, M. Losch, T. Gruber, J. Bamber, M. Bierkens, M. King and M. Smit (2008) Monitoring and Modeling Individual Sources of Mass Distribution and Transport in the Earth System by Means of Satellites. Final Report. ESA Contract No. 20403, November 2008.

Vaníček, P. and E. J. Krakiwsky (1986) *Geodesy: The Concepts*. 2. rev. ed. Elsevier Science Publ., Amsterdam-New York.

Visser, P. N. A. M. (1992) *The Use of Satellites in Gravity Field Determination and Model Adjustment*. Ph.D. Thesis, Delft University of Technology, The Netherlands.

Wahr, J. (1985) Deformation Induced by Polar Motion. *Journal of Geophysical Research*, Vol. 90:9363–9368.

Wahr, J. and M. Molenaar (1998) Time variability of the Earth's gravity field: Hydrological and oceanic effects and their possible detection using GRACE. *Journal of Geophysical Research*, Vol. 103, No. B12:30,205–30,229.

Wiese, D. N., W. M. Folkner and R. S. Nerem (2008) Alternative mission architectures for a gravity recovery satellite mission. *Journal of Geodesy*, First Online, DOI 10.1007/s00190-008-0274-1.

Xiang, W. and J. Jørgensen (2005) Formation flying: a subject being fast unfolding in space. *Small Satellites for Earth Observation*, Wissenchaft & Technik Verlag, 85–89.

Xu, G. (2007) *GPS: Theory, Algorithms and Applications, 2nd edition*. Springer Verlag, Berlin.

Zink, M., G. Krieger and T. Amiot (2003) Interferometric performance of a cartwheel constellation for TerraSAR-L. In Proc. *FRINGE Workshop 2003*. Frascati, Italy, December 2003.